

# From polymers to gene regulation: A bottom up approach to the bacterial chromatin

THÈSE N° 6785 (2015)

PRÉSENTÉE LE 12 NOVEMBRE 2015  
À LA FACULTÉ DES SCIENCES DE BASE  
LABORATOIRE DE PHYSIQUE DE LA MATIÈRE VIVANTE  
PROGRAMME DOCTORAL EN PHYSIQUE

ÉCOLE POLYTECHNIQUE FÉDÉRALE DE LAUSANNE

POUR L'OBTENTION DU GRADE DE DOCTEUR ÈS SCIENCES

PAR

Aleksandre JAPARIDZE

acceptée sur proposition du jury:

Prof. F. Mila, président du jury  
Prof. G. Dietler, directeur de thèse  
Prof. A. Stasiak, rapporteur  
Prof. G. Muskhelishvili, rapporteur  
Prof. P. De Los Rios, rapporteur



ÉCOLE POLYTECHNIQUE  
FÉDÉRALE DE LAUSANNE

Suisse  
2015



*To Nutsa,  
for her love and support.*



*"We must find time to stop and thank the people who make a difference in our lives"- John F. Kennedy*

## Acknowledgements

It is very hard for me to acknowledge all the people whom I'm grateful for, for all their support during my PhD.

First, I would like to express my deepest gratitude to Giovanni (i.e. Prof. Dietler). I remember, the first time I met him in the lab, back in 2006. Being a bachelor student, it was like science fiction for me; seeing DNA images, visiting a dark room with the giant UHV microscope, seeing a tall cylinder filled with unknown (by that time) liquid, with floating knots inside and with Giovanni explaining things to me with a huge smile. I still remember this feeling, as if I knew him since long.

Several years later, in 2011, I was accepted in LPMV. This was the start of a great journey, with great memories and great people around me. Giovanni was always supportive, optimistic and helpful. Always finding something hidden and interesting in the data, which I thought was completely wasted and ruined. He always encouraged me to be independent and free in my work, while always being there to help, when not being able to solve a problem. His intelligence, generosity and character made me a fortunate student to have worked in his group.

During my stay in Lausanne, I was extremely lucky to meet wonderful people, who helped me a lot to grow as a person as well as a scientist (if I can call myself this way). I would like to specially thank Gianni (Dr. Giovanni Longo), for his support, interesting scientific discussions, coffee breaks on 7<sup>th</sup> floor and great sense of humour. I would like to thank Andrzej (Dr. Kulik), Sergey (Dr. Sekatskii) and Sandor (Dr. Kasas) for their patience towards me, for answering many of my numerous questions. A special thank goes to all past and present members of LPMV; Dusan, Andrea, Simone, Sunny, Ula, Livan, Fabrizio, Petar, Carine, Ewelina, Wojtek, Andrey, Karolina, Katja, David and Anton, for being great colleagues and good friends. I would also like to thank my master students Kathleen, Sylvain and Robert, for putting up with me and for so long. Special thanks to Caroline, without whom I wouldn't be able to perform most of my experiments.

Any activity in LPMV wouldn't be possible without Christine Vuichoud and Michel Kessous. Their skills and experience, their kindness and helpfulness are irreplaceable.

LPMV gave me a great opportunity to collaborate with wonderful scientists. I would like to thank Prof. Cristian Micheletti and Prof. Enzo Orlandini for their collaboration on polymer physics problems; Prof. Cole and members of his group, Dr. Florence Pojer, Dr. Benjamin Blasco and Dr. Jeremie Piton for their collaborations on *Mycobacterium tuberculosis* ; Prof. Andrzej Stasiak for valuable discussion on DNA biophysics. I also thank Prof. De Los Rios and his group members, Salvo, Michele, Alessandro, Duccio, Alberto and Andrea for their discussions and suggestions. A special thank to Prof. Georgi Muskhelishvili for his scientific and personal support during my PhD.

Needless to say, many thanks to my whole family, for their endless support.

*Lausanne, 31<sup>th</sup> August, 2015.*

**A.J.**

# Abstract

DNA molecule is the fundamental component of every living organism, since it encodes the hereditary information. Although the genetic code of almost 200 species has been sequenced, the direct connection between gene sequence, DNA structure and biological function remains poorly understood.

The aim of this thesis was to investigate the connection between DNA function and structure. Throughout the thesis we will discuss experiments testing the link between different physical properties of DNA with its biological function. For this purpose we used atomic force microscopy (AFM), a high resolution imaging technique.

The first chapter is devoted to explain the basic concepts of AFM technique, as well as the composition and structure of DNA molecules. We also describe some of the polymer physics models of DNA, defining basic quantities like the persistence and the critical exponent.

After the introduction, in chapter 2 we discuss experiments, in which we studied changes in the physical properties of DNA molecules, when bound to the substrate surface with various methods. We show that, when DNA is strongly bound to the surface, it retains its physiological B-form. On contrary, when weakly bound, a conformational B-to-A-form transition takes place. In chapter 2, we also discuss a novel experimental method, for studying DNA in geometrical confinement. By combining nanometer sized PDMS slits with AFM, we study DNA properties under confinement. When DNA is weakly confined in space, the DNA persistence length increases, molecules tend to elongate and adopt more anisotropic shapes. When molecules are under stronger confinement, DNA defects in forms of hairpins are formed. The position of the hairpins is over-posed with nicked regions in the molecule. We propose that geometrical confinement *in vivo* can promote the formation of localized defects at thermodynamically weak sites in DNA, which could bear biological function.

In chapter 3 we studied binding of staining dyes, proteins and DNA transcription machinery to DNA molecules. First we show that DNA physical properties, such as the contour length and the persistence length are significantly affected when stained with dyes. Depending on the binding mode of the dye, either the contour length, or the persistence length or both simultaneously change. Therefore, when performing experiments on stained DNA, one must take these changes into account.

In chapter 3, we move further and investigate the role of protein amino acids and DNA sequence in the formation of nucleoprotein complexes. On the example of EspR protein, a key virulence regulator in *Mycobacterium tuberculosis* (MTB), we show that single amino acid mutations, lead to lower DNA binding affinity. These key mutations also partially or complete disrupt the formation of higher order protein-DNA complexes. This leads to silencing of the MTB virulence, indicating possible drug targets.

Afterwards, on the examples of RNA polymerase (RNAP) and H-NS protein, we show the importance of DNA sequence for the binding and higher order oligomerization. By introducing DNA mutations disrupting the helical phasing between distinct RNAP binding sites in the *fis* promoter sequence, we significantly lower the RNA binding affinity to the promoter. The helical phasing of the binding sites somehow coordinates the cooperative binding of RNAP to the promoter, indicating the role of geometry in transcription regulation.

Finally on the model of H-NS protein, we show how different spatial arrangements of DNA sequences containing strong binding sites for an architectural protein determine the final 3D structure of the assembled nucleoprotein complex.

The final chapter of the thesis, is fully devoted to the study of a completely new type of DNA organisation, which we call Hyperplectonemes. Hyperplectonemes are very ordered DNA structures, formed by large supercoiled molecules, in the presence of attractive DNA-DNA potential. First, we describe in detail their structure and its dependence on various environmental factors, than their binding to nucleoid associated proteins. We argue that this emerging DNA organisation is the basic structure of the bacterial chromatin, which is further modulated by numerous DNA binding and condensing proteins *in vivo*.

**Keywords** : DNA; AFM; Bacterial chromatin; NAPs; H-NS; DNA structure; Polymer physics; DNA in confinement; Hyperplectonemes; DNA dyes.



# Zusammenfassung

Das DNA-Molekül ist die grundlegende Komponente von jedem lebenden Organismus, da sie die genetische Information kodiert. Obwohl der genetische Code von fast 200 Arten sequenziert wurde, bleibt die Frage offen, was die direkte Verbindung zwischen Gen-Sequenz, DNA-Struktur und biologischer Funktion ist.

Das Ziel dieser Arbeit war es, den Zusammenhang zwischen der DNA-Funktion und der Struktur zu untersuchen. Im Laufe der Arbeit werden wir Ergebnisse von Experimenten besprechen, die die Verbindung zwischen den verschiedenen physikalischen Eigenschaften der DNA mit ihrer biologischen Funktion behandeln. Zu diesem Zweck haben wir Atomkraftmikroskopie (AFM) verwendet, eine hochauflösende bildgebende Technik. Wir verwendeten die Fähigkeit von AFM Messungen, dass sie unter verschiedenen Bedingungen, wie beispielsweise in Luft, Flüssigkeit und Ultrahochvakuum durchführbar ist. Spezielle Bedingungen wurden ausgewählt, um Eigenschaften von nackten DNA-Molekülen als auch DNA-Komplexe mit verschiedenen Chemikalien und Proteinen zu untersuchen.

Das erste Kapitel widmet sich den grundlegenden Konzepten der AFM-Technik sowie der Erklärung von Zusammensetzung und Struktur der DNA-Moleküle. Wir beschreiben auch einige der Polymerphysik-Modelle der DNA, definieren grundlegende Größen wie die Persistenzlänge und den kritischen Exponent der DNA.

Nach dem ersten Kapitel diskutieren wir Experimente, in denen wir die Änderungen in den physikalischen Eigenschaften von DNA-Molekülen untersuchen, wenn sie mit verschiedenen Methoden an die Substratoberfläche gebunden sind. Wir zeigen, dass die DNA ihre physiologische B-Form behält, wenn sie stark an die Oberfläche gebunden ist. Wenn die DNA wiederum schwach gebunden ist, findet eine Konformationsänderung statt und es erfolgt eine Reorganisierung von B- nach A-Form.

In Kapitel 2 sprechen wir auch von einer neuen experimentellen Methode zur Untersuchung von DNA in geometrischer Begrenzung. Durch die Kombination von nanometergroßen PDMS Schlitzen mit AFM konnten wir die DNA-Eigenschaften unter geringer Begrenzung studieren. Wir zeigen, dass sich beschränkte DNA Moleküle verlängern und mehr anisotrope Formen annehmen. Die Persistenzlänge nimmt zu und die Form der Korrelationsfunktion ändert sich auch. Wenn die DNA starken Begrenzungen unterliegt, bilden sich DNA- Defekte in Form von Haarnadeln und verknüpften Regionen. Die Position der Haarnadeln ist mit DNA-Einzelstrangbrüchen im Molekül überlappt. Wir behaupten, dass die geometrischen Begrenzungen *in vivo* der Bildung von lokalisierten Defekten an thermodynamisch schwachen DNA-Stellen hilft.

In Kapitel 3 diskutieren wir über Experimente, in denen wir Bindung zwischen DNA und Farbstoffen, Proteinen und dem DNA-Transkriptionsapparat untersuchten. Zuerst zeigen wir, dass physikalischen Eigenschaften von DNA, wie zum Beispiel die Konturlänge und die Persistenzlänge, erheblich beeinträchtigt werden, wenn DNA mit Farbstoffen gefärbt ist. Je nach der Bindung des Farbstoffes ändern sich entweder die Konturlänge oder die Persistenzlänge oder beides gleichzeitig. Daher muss man diese Änderungen berücksichtigen, wenn man Experimente mit gefärbter DNA durchführt.

Im Kapitel 3 untersuchen wir auch die Rolle von Protein-Aminosäuren und der DNA-Sequenz in der Bildung von Nucleoproteinkomplexen. Am Beispiel von EspR Protein, einem Schlüsselregulator der Virulenz in *Mycobacterium tuberculosis* (MTB), zeigen wir, dass einzelne Aminosäuremutationen die DNA-Bindung stark senken. Dies führt zum Schweigen der MTB Virulenz und gilt als mögliches Arzneimittel für die Krankheit.

Im Kapitel 3 zeigen wir anhand der Beispiele der RNA-Polymerase (RNAP) und H-NS-Proteine die Bedeutung der DNA-Sequenz für die Bindung und Oligomerisierung der DNA Komplexe. Durch die Einführung von DNA-Mutationen, die die Phasierung zwischen verschiedenen RNAP-Bindungsstellen in der FIS-Promotorsequenz stören (Promotor, der den Regulatorprotein FIS kodiert), haben wir deutlich die RNA-Bindungsaffinität an den Promotor gesenkt. Obwohl die Bindungssequenzen selbst nicht betroffen sind, koordiniert die Phasierung zwischen den Bindungsstellen die kooperative Bindung von RNAP. Dieses Experiment zeigt uns die Rolle der Geometrie in der Transkriptionsregulation.

Schließlich zeigen wir in Kapitel 3, wie verschiedene Anordnungen von DNA-Sequenzen, die starke Bindungsstellen für das H-NS Protein enthalten, die endgültige 3D-Struktur der Nucleoproteinkomplexe bestimmen.

In dem letzten Kapitel der Dissertation, Kapitel 4, besprechen wir eine völlig neue Art der DNA-Organisation, die wir Hyperplectonemes nennen. Hyperplectonemes sind sehr geordnete DNA-Strukturen, die durch große (Größen > 20kb) superspiralisierende Moleküle in der Präsenz von attraktivem DNA-DNA-Potenzial gebildet werden. Wir beschreiben im Detail die Struktur in der Luft als auch in der Flüssigkeit. Wir untersuchen ihre strukturelle Abhängigkeit von verschiedenen Umweltfaktoren und ihre Bindung an verschiedene Proteine. Wir behaupten, dass diese neue DNA-Organisation die Grundstruktur des bakteriellen Chromatins, ist die weiter von zahlreichen DNA Proteinen *in vivo* moduliert wird.

**Stichwörter** : DNA; AFM; Bakteriellies Chromatin; *E.coli* NAPS; H-NS; EspR; FIS; DNA-Struktur; Polymeren Physik; DNA in der Begrenzung; Hyperplectonemes; DNA Farbstoffe.

# Table of contents

Acknowledgements .....	v
Abstract .....	vii
Zusammenfassung .....	ix
<b>Chapter 1: Introduction .....</b>	<b>4</b>
<b>1.1 DNA .....</b>	<b>5</b>
1.1.1 DNA composition and structure .....	5
1.1.2 DNA Topology.....	8
1.1.3 DNA as a polymer.....	9
1.1.3.1 <i>The Freely Jointed Chain model</i> .....	9
1.1.3.2 <i>The Freely Rotating Chain model</i> .....	11
1.1.3.3 <i>The persistence length <math>l_p</math></i> .....	12
1.1.3.4 <i>The Flory model</i> .....	12
<b>1.2 Atomic Force Microscopy .....</b>	<b>14</b>
1.2.1 Introduction to atomic force microscopy.....	14
1.2.2 Basic principles of AFM.....	15
1.2.3 Operating modes of AFM.....	15
1.2.4 DNA sample preparation .....	17
1.2.5 AFM resolution .....	19
1.2.6 Short review of AFM application in DNA imaging .....	19
<b>Chapter 2: Physical properties of DNA .....</b>	<b>20</b>
<b>2.1 Towards an effective control of DNA's sub-molecular conformation on a surface</b>	
DNA .....	20
2.1.1 Indruction .....	21
2.1.2 Materials and methods .....	22
2.1.3 Results .....	25
2.1.3.1 <i>251bp DNA: The Contour length measurements in air</i> .....	25
2.1.3.2 <i>Calculating the amount of base pairs undergoing the B-to-A transition</i> .....	26
2.1.3.3 <i>500 bp DNA : The Contour length measurements in air</i> .....	27
2.1.3.4 <i>500 bp DNA : Equilibration time vs. conformational transition</i> .....	28
2.1.3.5 <i>845 bp DNA : Effect of nicked sites on conformational transition</i> .....	31
2.1.3.6 <i>500bp DNA: Tip enhanced raman spectroscopy measurements</i> .....	33
2.1.3.7 <i>Thermodynamic Model describing the B-to-A transition</i> .....	34
2.1.4 Conclusions .....	36

<b>2.2</b>	<b>Conformational properties of DNA inside narrow slits</b>	<b>38</b>
2.2.1	Indruction	39
2.2.2	Materials and methods	40
2.2.3	Results	45
2.2.3.1	<i>Metric properties of circular DNA in confinement</i>	46
2.2.3.2	<i>Computer simulations</i>	48
2.2.3.3	<i>Using AFM resolution to investigate DNA structure: DNA hairpins</i>	50
2.2.3.4	<i>Dynamic properties of DNA in confinement</i>	53
2.2.4	Conclusions	54
<b>Chapter 3:</b>	<b>DNA-protein complexes</b>	<b>56</b>
<b>3.1</b>	<b>Influence of DNA Binding Dyes on Bare DNA Structure Studied with Atomic Force Microscopy</b>	<b>56</b>
3.1.1	Indruction	57
3.1.2	Materials and methods	58
3.1.3	Results	62
3.1.3.1	<i>PicoGreen</i>	62
3.1.3.2	<i>Dapi</i>	65
3.1.3.3	<i>DRAQ5</i>	67
3.1.4	Conclusions	69
<b>3.2</b>	<b>Functional Dissection of Intersubunit Interactions in the EspR Virulence Regulator of Mycobacterium tuberculosis</b>	<b>71</b>
3.2.1	Indruction	72
3.2.2	Materials and methods	73
3.2.3	Results	76
3.2.3.1	<i>Wild type EspR binding to PespACD</i>	76
3.2.3.2	<i>Wild type EspR concentration dependent binding</i>	78
3.2.3.3	<i>EspR mutants binding to PespACD</i>	79
3.2.4	Conclusions	82
<b>3.3</b>	<b>DNA sequence directs the assembly of H-NS filament</b>	<b>83</b>
3.3.1	Indruction	84
3.3.2	Materials and methods	85
3.3.3	Results	88
3.3.3.1	<i>Global organisation of the DNA by H-NS</i>	88
3.3.3.2	<i>Properties of the H-NS filaments</i>	91

3.3.3.3 <i>H-NS filament height</i> .....	95
3.3.3.4 <i>H-NS binding distinctly constrains the DNA on different constructs</i> .....	96
3.3.3.5 <i>Periodic structure of H-NS filaments</i> .....	97
3.3.4 Conclusions .....	99
<b>3.4 Upstream Binding of Idling RNA Polymerase Modulates Transcription Initiation from a Nearby Promoter</b> .....	<b>103</b>
3.4.1 Introduction .....	104
3.4.2 Materials and methods .....	105
3.4.3 Results .....	107
3.4.3.1 <i>RNAP-linear fis promoter complexes</i> .....	107
3.4.3.2 <i>RNAP-circular fis promoter complexes</i> .....	109
3.4.3.3 <i>Modified linker DNA-RNAP complexes</i> .....	111
3.4.4 Conclusions .....	114
<b>Chapter 4: Hyperplectonemes</b> .....	<b>115</b>
4.1 Introduction .....	116
4.2 Materials and methods.....	117
4.3 Results .....	120
4.3.1 <i>The formation of hyperplectonemes</i> .....	120
4.3.2 <i>The persistence length of hyperplectonemes</i> .....	125
4.3.3 <i>The distribution of hyperplectonemes</i> .....	127
4.4 Hyperplectoneme - NAP complexes .....	127
4.4.1 <i>Nicked DNA - NAP complexes</i> .....	127
4.4.2 <i>Hyperplectoneme - NAP complexes</i> .....	129
4.4.3 <i>FIS + H-NS pairwise nucleoprotein complexes</i> .....	131
4.5 Conclusions .....	132
<b>Chapter 5: Conclusions and future perspectives</b> .....	<b>133</b>
 Bibliography .....	 137
Curriculum Vitae .....	156



*“At lunch Francis (Crick) winged into the Eagle pub (1953) to tell everyone within hearing distance that we found the secret of life” (purported remark made at The Eagle pub in Cambridge, to celebrate the fact that, Crick and Watson, had unravelled the structure of DNA).* James Watson, *The Double Helix* (1998)

## Chapter 1: Introduction

The deoxyribonucleic acid molecule, DNA, is the core building block of every living organism. Due to its complexity and importance, it has been intriguing humanity since many decades. The history of the discovery of the DNA dates back to 1869, when the substance was first isolated from the nuclei of white blood cells. It was the Swiss biologist Johann Friedrich Mischer (1), who discovered the new acidic substance, that he called nuclein by that time. He realized that the new substance was very different from proteins, because of its unusually high content in phosphorus. However, it was not immediately understood that this molecule was the carrier of the genetic information. More than 80 years later, in 1953 at the Cavendish Laboratory in Cambridge, James Watson and Francis Crick, proposed the structure of the DNA (2) based on the X-Ray diffractograms taken by Rosalind Franklin (3), making one of the biggest scientific discoveries of the twentieth century.

Due to its shape and physical properties, DNA is a fascinating object of interest for different scientific fields. It is known that DNA molecules *in vivo* appear not only in linear and circular, but also in supercoiled and knotted forms. These features make DNA an ideal object for mathematicians to experimentally study topology, a domain describing the spatial properties of continuously deformable objects. For physics, DNA is an excellent object for testing polymer physics models and investigating statistical properties of polymers. Finally, for biological sciences, DNA is the most important molecule, due to its role as the carrier of the genetic information.

The aim of this Thesis was to investigate both physical and biological properties of DNA molecules of various sequences, sizes and topologies, by means of atomic force microscopy (AFM). Our aim was to bridge polymer physics description of DNA molecules with their biological function, to quantitatively describe phenomena such as DNA-dye interaction, protein-DNA binding, or DNA compaction into ordered filaments.

In order to give a clear framework to the studies discussed in this Thesis, in the first chapter I will first introduce the essential concepts about DNA structure, basic polymer physics models and discuss the working principles behind the AFM.

Later I will focus on the physical property changes that DNA undergoes when bound with different strength to a surface or when it is confined in three dimensional space (Chapter 2). Afterwards I will discuss the binding of staining dyes, proteins, and DNA transcription factors to DNA (Chapter 3). We investigated the role of proteins, their amino acid sequence and DNA sequence in the formation of

nucleoprotein complexes in this chapter. Finally, I will describe a completely new type of DNA organisation, which we call hyperplectonemes (Chapter 4). We argue that these novel structures represent a good model for studying bacterial chromatin *in vitro* and for addressing the role of nucleoid associated proteins in DNA structuring and modulating its dynamics.

In addition, I hope that this Thesis might be helpful for researchers starting in the field. For these reasons, the present introductory chapter is written on a relatively basic and general level.

## 1.1 DNA

### 1.1.1 DNA composition and structure

DNA molecules are fundamental components of all living organisms. In order to understand their function, we have to first know their structure and composition.

Every DNA molecule is made up of repeating blocks called the nucleotides. Nucleotides consist of three building blocks, namely: a sugar (2'-deoxyribose), a phosphate and one of four bases. There are two purine bases, adenine (A) and guanine (G), and two pyrimidine bases, thymine (T) and cytosine (C) (Figure 1.1.1). These bases are connected by hydrogen bonds (adenine pairs with thymine, and cytosine pairs with guanine), which together with the base-stacking interactions among the bases give stability to the DNA molecule, forming the so-called double stranded DNA (Figure 1.1.2).

Typically DNA molecules have a very specific structure, called the double-helix. It is formed by two DNA strands forming a helix, by winding around each other. The so-called Watson-Crick model of the DNA, describes this helix structure (Figure 1.1.2b), with the following simple rules. (a) The sugar-phosphate forms a backbone which is on the outside, while the bases are positioned inside the double-helix; (b) the plane of the bases is perpendicular to the helical axis; (c) the backbone runs in chemically opposite directions from free 5' to the 3'- end (5' → 3' indicates the directionality in the carbon numbering of a the DNA's sugar backbone); (d) the pairing between bases of opposite strands occurs only between A-T or G-C by hydrogen bonding (Figure 1.1.2). Adenine pairs with thymine by two hydrogen bonds, while cytosine bonds to guanine with triple hydrogen bonding (Figure 1.1.2a). In the model, the width of the DNA double helix is 2nm, 10 base pairs (bp) form a full turn of the helix, separated by 3.4nm. The helices formed by the two single-strands are out of phase, so that the space between the backbones in the double helix structure is alternatively wider and narrower, forming so-called major and minor grooves (Figure 1.1.2b).

The Watson-Crick model of the DNA, or the B-form DNA, is the predominant form of the DNA *in vivo*. Interestingly, this is not the only stable form of the double helix.



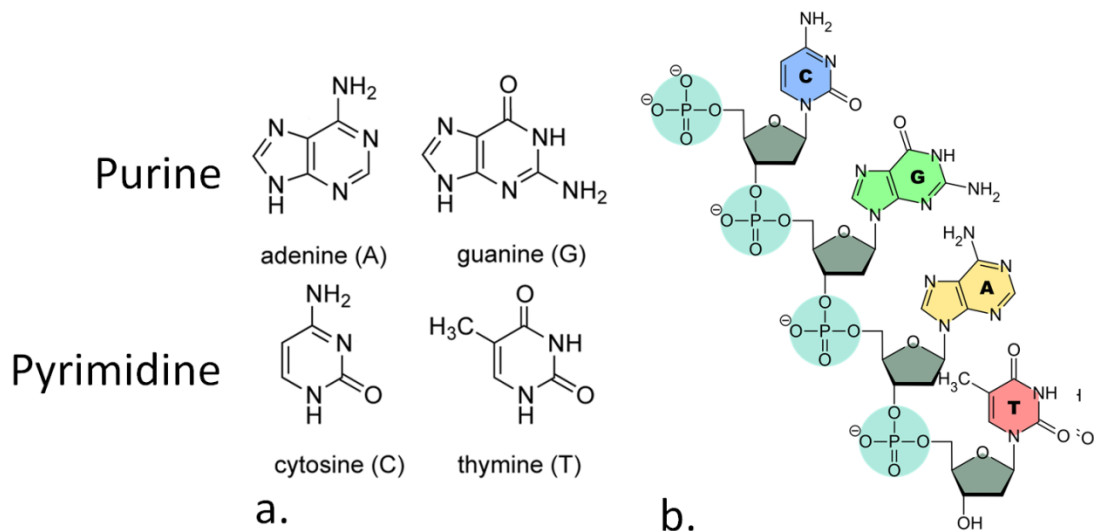


**Figure 1.1.1:** Chemical representation of nucleotides (4) and single stranded DNA. **a)** Chemical representation of all the four different bases, adenine, thymine, guanine and cytosine. **b)** Arrangement of the building blocks into a chain of single-stranded DNA.

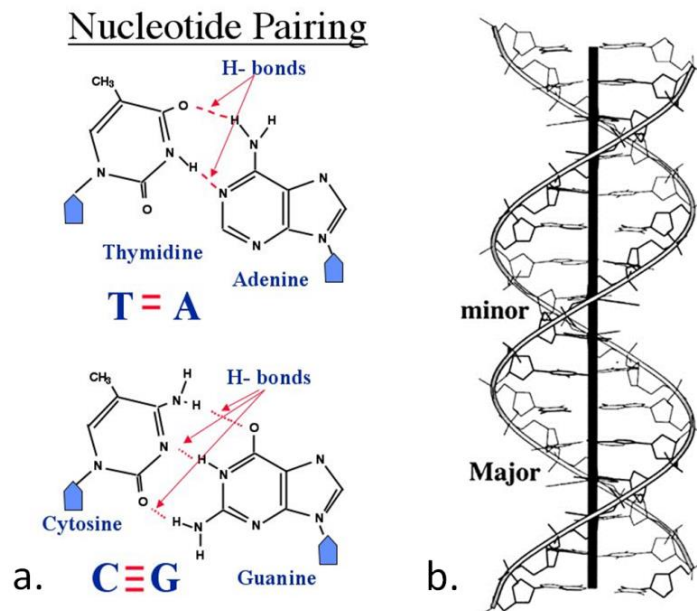


**Figure 1.1.2:** Base-pairing and structure of the DNA double-helix. **a)** The picture represents the hydrogen bonds between A and T, and G and C bases. A and T have two hydrogen bonds whereas G and C have three, making thus G-C base-pairs thermodynamically more stable. **b)** Structure of the B-form DNA double helix.

X-Ray measurements performed by Franklin and Gosling on calf thymus DNA at different humidity, revealed different diffraction patterns for the dry and wet DNA fibres (3) (they referred to it as A-form and B-form DNA). Watson and Crick, based on these data, developed their double helical model of DNA and published their work in parallel with the experimental results by Wilkins, Franklin and Gosling in the now famous Nature article (2) in 1953 (6,7).

In the following issue of Nature journal, Watson and Crick published a second article discussing the possible implications of the DNA structure and its mechanism of replication (5). It was already clear from these early structural studies that there was no single and unique DNA sub-molecular structure. The structure that the DNA would adopt was dependent on several environmental parameters, making DNA a

highly polymorphic molecule. Parameters such as the relative humidity, the composition of the solution in which DNA was submerged (presence of ethanol), as well as the DNA base pair composition, were playing a fundamental role in determining the final DNA structure.

So far, over thirty different DNA polymorphisms have been found (8-10). Among them, the so-called A, B and Z forms have been recognized as the configurations relevant in biology (Figure 1.1.3). B-DNA is thought to be the most common form of DNA present in living organisms, while A-DNA represents the configuration obtained from B-DNA when dehydrated. Both forms are right-handed double helices, in contrast to the Z-DNA, which is left-handed. The biological role of Z-DNA is still under debate, but it seems that this configuration facilitates the binding of certain classes of proteins to DNA (11). The main structural parameters for these three DNA forms are summarized in Table 1.1.

**Figure Table 1.1:** Structural parameters of the A, B and Z DNA (2,6,9)

<b>Geometry attribute</b>	<b>A-DNA</b>	<b>B-DNA</b>	<b>Z-DNA</b>
Helix sense	right-handed	right-handed	left-handed
Rotation/bp	32.7°	34.3°	30°
bp/turn	11	10.5	12
Rise/bp along axis	0.26 nm	0.34 nm	0.38 nm
Pitch/turn of helix	2.86 nm	3.57 nm	4.56 nm
Diameter	2.3 nm	2.0 nm	1.8 nm

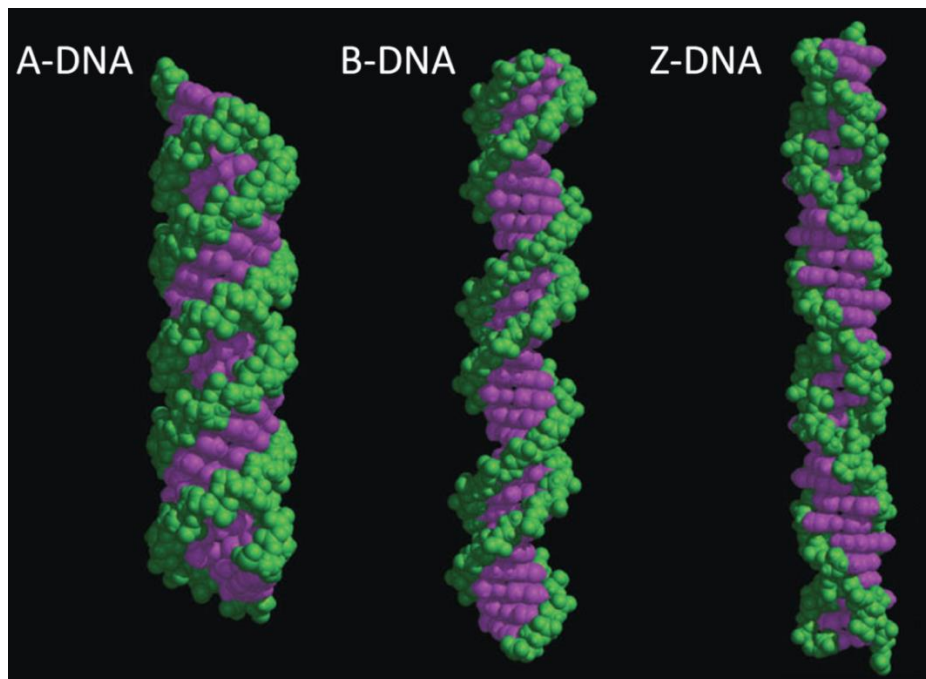


**Figure 1.1.3:** Reconstructed images of different sub-molecular structures of DNA: A, B and Z form DNA (12)

### 1.1.2 DNA Topology

Although the hereditary information is encoded in the linear sequence of the genetic code, the topological features of the DNA, such as the level of DNA supercoiling (supercoiled refers to a form of DNA in which the double helix is further twisted about itself, forming a coiled structure), play an important regulatory function. In 1963, Weil and Vinograd noticed that purified DNA specimens, despite having the same molecular weight, sedimented into three different forms during centrifugation (13,14). These forms corresponded to linear double-stranded, relaxed circular and supercoiled DNA forms, showing for the first time the existence of supercoiled DNA conformations (15). In other studies, Liu and co-workers observed the presence of DNA knots after the incubation of bacterial topoisomerase with single-stranded DNA rings (16) and double-stranded DNA extracted from P4 phage (17,18). The presence of knots was also confirmed in DNA plasmids (circular DNA) isolated from *Escherichia coli* DNA with Topo I deletion mutant during cell division (19). Topo I is an important enzyme, whose primary function is to relax supercoiling in DNA.

Development of high resolution microscopy techniques opened door to new studies investigating structural properties of DNA. For example, early measurements with Electron microscopy (20,21) confirmed the supercoiled nature of the bacterial DNA *in vivo*. Later, by using AFM several groups studied the structures of different DNA topologies with high accuracy and under physiological conditions (22-24). In particular, DNA supercoiling has been extensively studied (22) for its importance for the global DNA shape and chromatin reconstitution (25,26). Typical AFM images of DNA molecules of various topology are shown below, in Figure 1.1.4.

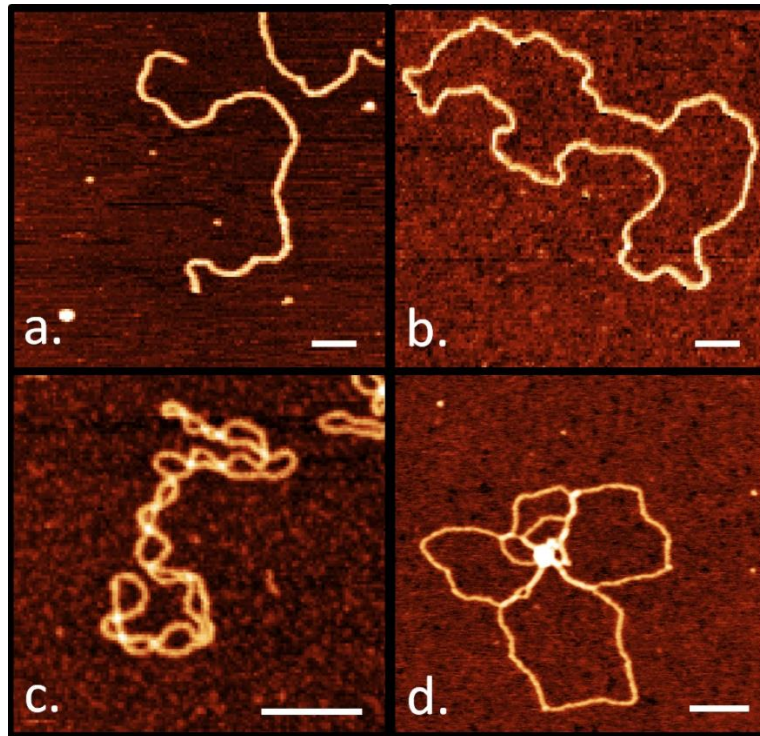


**Figure 1.1.4:** AFM images of DNA of different topologies: **a)** Linear **b)** Circular relaxed **c)** Circular supercoiled and **d)** Knotted DNA. Scale bars 100nm.

### 1.1.3 DNA as a Polymer

A polymer is a large molecule made up by a sequence of repeating building blocks, monomers. If one neglects the detailed molecular structure of the DNA, it can be considered as an elastic and homogeneous polymer, whose mechanical properties are implicitly given by its chemical structure and its interactions with the solvent. From this perspective, DNA can be considered as a model system for studying polymer physics problems. It is a stable molecule which can be produced in well-defined sizes, therefore it has often been used to test polymer theories by experimental techniques such as light scattering (27), fluorescence microscopy (28,29), optical tweezers (30,31) and atomic force microscopy (32,33).

In this chapter, I will briefly discuss some basic entities in polymer physics, based on text books by de Gennes (34), Grosberg and Khokhlov (35) and Rubinstein and Colby (36).

#### 1.1.3.1 The Freely Jointed Chain model

For simplicity, let's consider a model of an ideal polymer. Imagine a flexible chain made of  $n+1$  backbone atoms  $A_i$  (with  $0 \leq i \leq n$ ) as sketched on Figure 1.1.5. The vector  $\vec{r}_i$  connects the  $A_{i-1}$  and  $A_i$  backbone atoms. A polymer can be considered as ideal, if there are no net interactions between any pairs of monomers  $A_i$  and  $A_j$ , which are separated by sufficiently large number of bonds ( $|i-j| \gg 1$ ) (35).

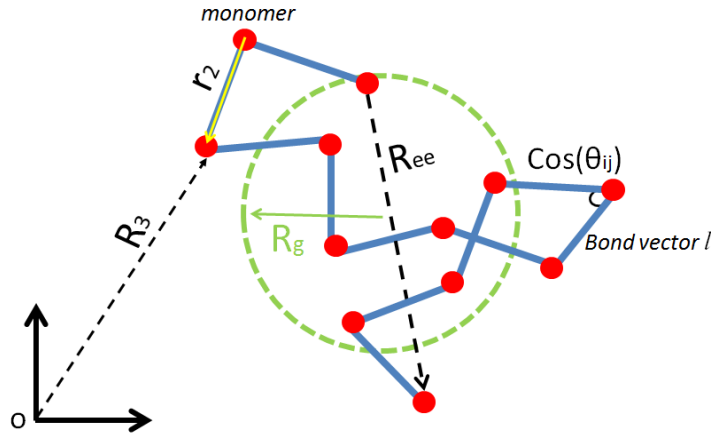


**Figure 1.1.5:** Sketch of an ideal polymer model, made out of connected segments of fixed length ( $l$ ). The position of each monomer is given by  $R_i$ , while the direction of each segment is given by  $r_i$ . The size of the polymer is described by the end-to-end distance ( $R_{ee}$ ) and the radius of gyration ( $R_g$ ).

A question arises, how can we describe such system?

To answer this question, first let us define the end-to-end vector  $\vec{R}_{ee}$  as the sum of all  $n$  bond vectors in the chain :  $\vec{R}_{ee} = \sum_{i=1}^N \vec{r}_i$ . Individual chains with different bonds will have different end-to-end vectors and

what is more useful to study is the average end-to-end vector  $\langle \vec{R}_{ee} \rangle$ .

Since the position of each monomer is "random" and does not depend on the position of the other monomers, one has:

$$\langle \vec{R}_{ee} \rangle = \left\langle \sum_{i=1}^N \vec{r}_i \right\rangle = \sum_{i=1}^N \langle \vec{r}_i \rangle = 0 \quad (1.1)$$

Here, the ensemble average  $\langle \rangle$  indicates the average over an ensemble of chains of  $n$  bonds with all possible bond orientation. First simple non-zero average is the mean-square end-to-end distance  $\langle \vec{R}_{ee}^2 \rangle$ :

$$\langle \vec{R}_{ee}^2 \rangle = \langle \vec{R}_{ee} \cdot \vec{R}_{ee} \rangle = \sum_{i=1}^N \sum_{j=1}^N \langle \vec{r}_i \cdot \vec{r}_j \rangle \quad (1.2)$$

If all bond vectors have the same length  $l = |\vec{r}_i|$ , than we can rewrite the scalar product in the following way:

$$\vec{r}_i \cdot \vec{r}_j = l^2 \cdot \cos(\theta_{ij}) \quad (1.3)$$

where  $\theta_{ij}$  is the angle between bond vectors  $\vec{r}_i$  and  $\vec{r}_j$ . If we plug the (1.3) expression into the formula (1.2), we get:

$$\langle \vec{R}_{ee}^2 \rangle = l^2 \sum_{i=1}^N \sum_{j=1}^N \langle \cos(\theta_{ij}) \rangle \quad (1.4)$$

In the simplest polymer model, in the freely jointed chain model, there are no directional correlations between the different bond vectors, meaning that  $\langle \cos(\theta_{ij}) \rangle = 0$  if  $i \neq j$ . Therefore the expression for the mean-square end-to-end distance becomes:

$$\langle \vec{R}_{ee}^2 \rangle = N \cdot l^2 \quad (1.5)$$

Equation 1.5 describes the growth of the ideal chain. One can rewrite it in a more general way in the form of:

$$\langle \vec{R}^2_{ee} \rangle \sim N^{2\nu} \quad (1.6)$$

where  $\nu$  is the so-called scaling exponent, or the Flory exponent. For the ideal polymer case it is equal to  $\nu=1/2$ . Experimental finding showed that, due to the excluded volume effects (DNA chains can not cross themselves), the value of the exponent is dependent on the dimensionality of the polymer and is equal to  $\nu=1; 0.75$  and  $0.588$ , for dimensions  $d = 1; 2$  and  $3$  (34). Therefore, this simplistic model is not suitable for describing the actual DNA in high details. The model can only describe DNA on a very coarse-grained level, for segments of  $\sim 100$  nm length, where the directional correlation between two consecutive segments is completely lost. If one wants to describe a DNA molecule on the length scale of tens of nanometers, a bending penalty between consecutive segments has to be introduced.

### 1.1.3.2 The Freely Rotating Chain model

In order to describe DNA better, we have to introduce a bending rigidity in our model. The simplest model taking it into account is the freely rotating chain model (FRC). In this model all consecutive segments have a fixed length ( $l$ ) and a fixed bending angle ( $\theta$ ) (Figure 1.1.6). All torsional angles ( $\varphi_i$ ) are equally like and independent. This induces an orientational correlation between segments leading to rigidity on length scales larger than just the length of one segment. For two consecutive segments, this correlation is constant and equal to:  $\langle \vec{r}_i \cdot \vec{r}_j \rangle = l^2 \cos(\theta)$ . It is easy to show that for segments separated longer than one monomer, the correlation between the monomers will decay in the following form:

$$\langle \vec{r}_i \cdot \vec{r}_j \rangle = l^2 \cos(\theta)^{|j-i|} \quad (1.7)$$

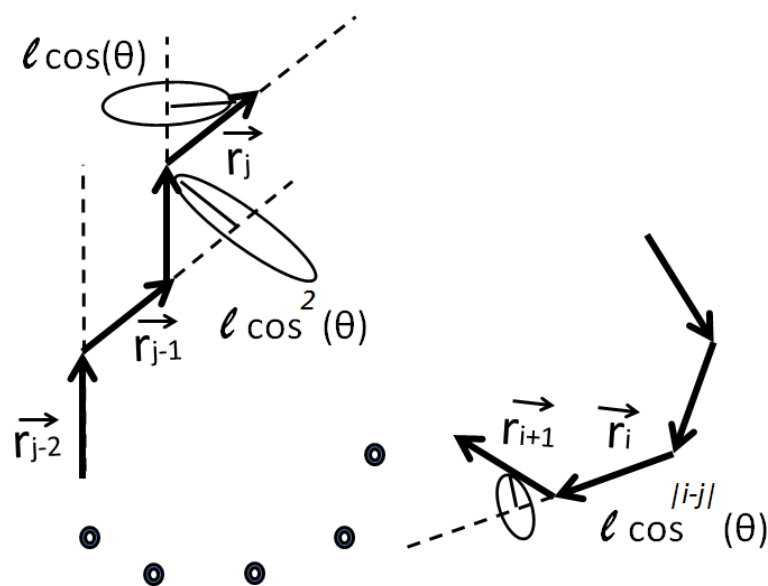


**Figure 1.1.6:** Sketch of a freely rotating chain model. All torsion angles are equal

This is because the only form of correlation that gets transmitted along the chain length is the component of vector  $\vec{r}_j$  along the bond vector  $\vec{r}_{i-1}$ . The component of  $\vec{r}_j$  normal to  $\vec{r}_{i-1}$  is zero, due to the free rotational angle  $\varphi_j$  (Figure 1.1.6).

### 1.1.3.3 The persistence length $l_p$

By using the formula (1.7) we can now define a basic property of polymer physics, the persistence length ( $l_p$ ). Since the  $\cos(\theta)^{|j-i|}$  decays very rapidly with the growing distance between  $i$  and  $j$  bonds, we can rewrite it in the form of an exponential decay :

$$\cos(\theta)^{|j-i|} = e^{(|j-i| \ln(\cos(\theta)))} = e^{\left(-\frac{|j-i|}{l_p}\right)} \quad (1.8)$$

Based on (1.8), we define the persistence length  $l_p$  as the number of chain-bonds in a persistence segment, over which the correlation decays exponentially. The persistence length is directly linked to the intrinsic properties of the polymer and the thermal energy. It can be also expressed as:

$$l_p = \frac{B_s}{k_B T} \quad (1.9)$$

where  $B_s$  is the bending stiffness of the polymer,  $T$  the temperature and  $k_B$  the Boltzmann constant. This creates an important link between statistical properties of polymers, their intrinsic physical properties and the temperature.

### Scaling of $R_{ee}$

Logically one can assume that a polymer with a bending rigidity will have a larger spatial extension compared to a flexible chain with the same number of segments. One can estimate this extension by calculating the end-to-end vector for the *FRC* model:

$$\langle \vec{R}^2_{ee} \rangle = \sum_{i=1}^N \vec{r}_i \sum_{j=1}^N \vec{r}_j = N \cdot l^2 + \sum_{i=1}^N \sum_{k=1}^{N-i} \cos^k(\theta) \simeq N \cdot l^2 + 2l^2 \sum_{i=1}^N \frac{\cos(\theta)}{1 - \cos(\theta)} = N \cdot l^2 + 2l^2 \cdot \frac{\cos(\theta)}{1 - \cos(\theta)} \quad (1.10)$$

We still recover previous scaling relation between the end-to-end distance and the number of bonds:

$\langle R^2_{ee} \rangle \sim N$ ; with the critical exponent  $\nu=1/2$ . This means that introduction of simple short-range correlations in the polymer chain does not change the scaling law for large  $N$ . By a simple re-scaling procedure the chain still behaves as an ideal polymer.

### 1.1.3.4 The Flory model

The most important missing ingredient to describe a real polymer is the interaction between the monomers. In an ideal polymer, two segments can cross each other, which is an unrealistic process. To correct this, we can introduce a monomer-monomer interaction potential  $U(\mathbf{r})$ , which can have the shape of a Lennard-Jones potential. At short distances it should have a strongly repulsive part due to the impenetrability of the monomers and an attractive one at intermediate lengths. As a consequence, if the

attractive potential is larger than the thermal energy  $k_B T$ , the monomers aggregate, otherwise, the repulsive part of the potential dominates and the entire polymer swells. The statistical properties of the chain can be than calculated using its free energy  $F$ , which will be composed of two components, the interaction energy  $F_{int}$  arising from interactions between monomers and the entropic energy  $F_{ent}$ .

To treat this kind of a system, Flory developed an approximation and considered the polymer as a dilute gas of monomers. Let's consider a swollen polymer of size  $R > R_0 = l \cdot N^{1/2}$  consisting of  $N$  monomers. The Flory approximation assumes that the monomers are uniformly distributed in the volume  $R^3$  and don't interact with each other. The probability of one monomer being in the excluded volume  $v$  of another one is the product of excluded volume  $v$  and the number density of monomers per chain volume,  $N/R^3$ . So the energetic cost of excluded volume is  $k_B T$  times the probability:  $k_B T v N / R^3$ . If we calculate the same energy cost for all  $N$  monomers in the chain we get:

$$F_{int} \approx k_B T v N^2 / R^3 \quad (1.11)$$

Flory estimated the entropic energy  $F_{ent}$ , as the energy needed to stretch an ideal chain to a given the end-to-end distance  $R$ :

$$F_{ent} \approx k_B T R^2 / N \cdot l^2 \quad (1.12)$$

If we sum this two expressions in (1.11) and (1.12) we will get the total Free energy of the polymer:

$$F = F_{int} + F_{ent} = k_B T v N^2 / R^3 + k_B T R^2 / N \cdot l^2 \approx k_B T \left( v N^2 / R^3 + R^2 / N \cdot l^2 \right) \quad (1.13)$$

It is simple to show that, by taking the minima of the free energy in respect to the size  $R$  ( $\partial F / \partial R = 0$ ), we get the equilibrium size of the polymer:  $R \approx v^{1/5} l^{2/5} N^{3/5}$ . If we extend the same calculations to  $d$  dimensions ( $d = 1$  to  $4$ ) we can write the general expression:

$$R_{Flory} \sim N^{3/d+2} \quad (1.14)$$

With the critical exponent reaching values  $\nu=1; 0.75; 0.6$  and  $0.5$  for scaling dimensions  $d = 1; 2; 3$  and  $4$ . Although the interaction energy as well as the elastic energy are poorly estimated, model is very useful since it is simple and gives a reasonable answer.



## 1.2 Atomic force microscopy

### 1.2.1 Introduction to atomic force microscopy

The best resolution achievable with conventional light microscopy techniques is of the same order of magnitude as the wavelength of the incident light (~few hundreds of nanometers). This is based on the so-called Abbe's principle (37) stating that the highest achievable resolution  $R$  of a microscope is of the order of:

$$R = \frac{\lambda}{2 \cdot N_A} \quad (1)$$

where  $\lambda$  is the wavelength of the incident light and  $N_A$  is the numerical aperture of the microscope. This limitation creates a theoretical limit for the achievable resolution, impossible to overcome with conventional microscopy techniques. Therefore, objects with dimensions comparable or less than few hundreds of nanometers cannot be imaged with an optical microscope. To overcome this limitation, various new techniques were developed. One of them is Electron Microscopy, which uses an accelerated electron beam with shorter wavelengths (38). Recently developed super high resolution techniques, e.g. Stochastic optical reconstruction microscopy (STORM) (39), STimulated Emission Depletion (STED)(40) and Photoactivated Localization Microscopy (PALM)(41), were capable of achieving resolution of ~10-20 nm.

Another high resolution technique, the Scanning Probe Microscopy (SPM), developed in 1980's was a conceptual revolution in the field of microscopy. In 1986 Binnig and Rohrer were awarded with the Nobel Prize in Physics for developing the first SPM technique, namely the Scanning Tunneling Microscope (STM) (42). The main part of the microscope is a sharp tip interacting with the sample while scanning its surface. The working principle of the microscope is based on the quantum tunnelling effect. When a metallic tip is brought very close to the sample surface, a bias voltage applied between the two allows electrons to tunnel through the vacuum between them. The resulting tunneling current is a function of tip distance, bias voltage, and the sample type. Information about the sample is acquired by monitoring the current as the tip's position scans across the sample surface. With a STM, a sub-nanometer resolution can be achieved. The main disadvantage though of STM techniques remains the fact that only conductive or semiconductive samples can be imaged. This makes an STM unsuitable for investigating biological samples.

In order to overcome the difficulties of studying dielectric samples, in the 1986, Binnig, Quate and Gerber invented the atomic force microscope (AFM)(43). AFM is a versatile tool which can function in a wide range of environmental conditions (liquid, dry, vacuum) and contrary to STM, can image both conductive and dielectric samples. Nowadays, AFM is used in many different fields of research that span from biology to nanotechnology and material science. In this chapter, I will discuss the basic working principles behind AFM microscopy. Since its original invention as a tool to investigate topography of samples at nanometer scale, the AFM technique has developed in many directions (46), from a molecular stretching device (44), to magnetism sensor and stiffness tomography tool (45). Since in this Thesis, we only used the imaging capabilities of the AFM, we will briefly present this technique below.

### 1.2.2 Basic principles of AFM

An AFM is composed of several basic components, depicted in Figure 1.2.1. A nanometer sharp tip is fixed at the end of a reflective cantilever typically made of silicon or silicon nitride (Figure 1.2.1.b). A laser beam is focused on the extremity of the cantilever which back-reflects it onto a four quadrant photodiode. The difference in light intensity on the four quadrants of the photodiode is used to determine the position of the spot on the photodiode. When the tip is brought into close proximity with the sample surface, forces between the tip and the sample lead to vertical deflection and/or axial rotation of the cantilever. These changes are amplified and detected as vertical and horizontal displacements of the reflected laser spot on the photodiode.

The sample of interest is deposited on a flat substrate (typical substrates are mica, glass, gold and highly oriented pyrolytic graphite) which than is fixed on a piezoelectric tube moving in  $x$ ,  $y$  and  $z$  directions. The  $x$  and  $y$  displacements allow for raster scanning, while the  $z$  displacement serves to adjust the distance between tip and the sample surface (Figure 1.2.1.c).

### 1.2.3 Operation modes of AFM

In order to understand operation modes of AFM, we must focus on the forces acting between the AFM tip and the sample surface. The interactions between the tip and the surface can generally be described by a Lennard-Jones-type potential (Figure 1.2.2.a), a long-range attractive potential and a short-range repulsive one. When the AFM tip and the sample surface are far apart, weak attractive forces exist between the atoms on the sample surface and the apex of the tip. This attractive interactions increase with decreasing separation, until the electron clouds of the atoms begin to overlap and repel each other.

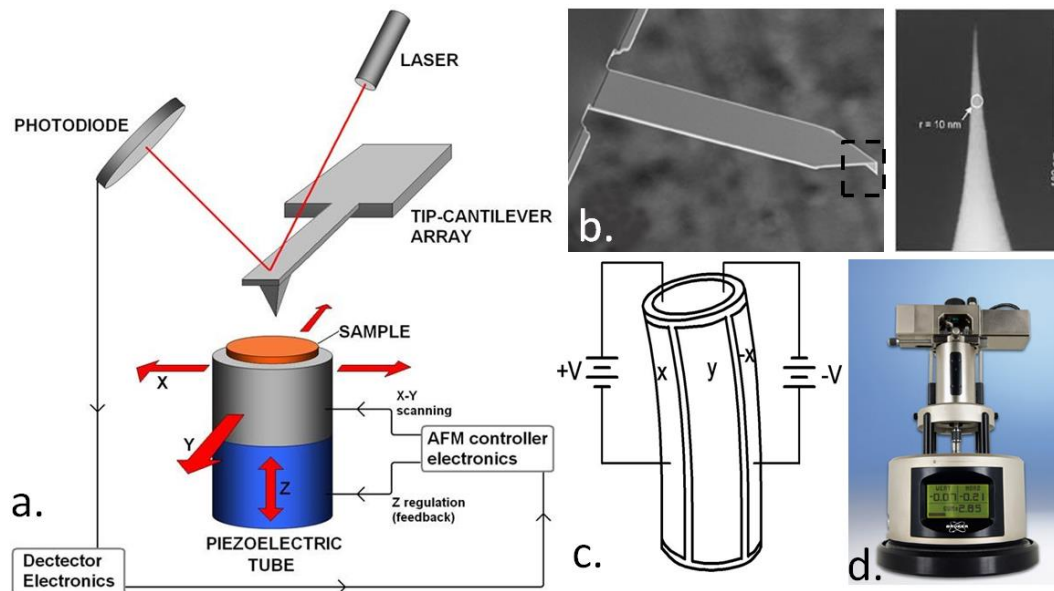


**Figure 1.2.1:** Schematic representation of basic components of an atomic force microscope. **a)** Sketch of an AFM microscope (48) **b)** Electron microscopy images of a cantilever and nanometer sharp tip (49) **c)** Representation of the movements of the cylindrical piezoelectric tube when the voltage is applied (50) **d)** image of an AFM (15).

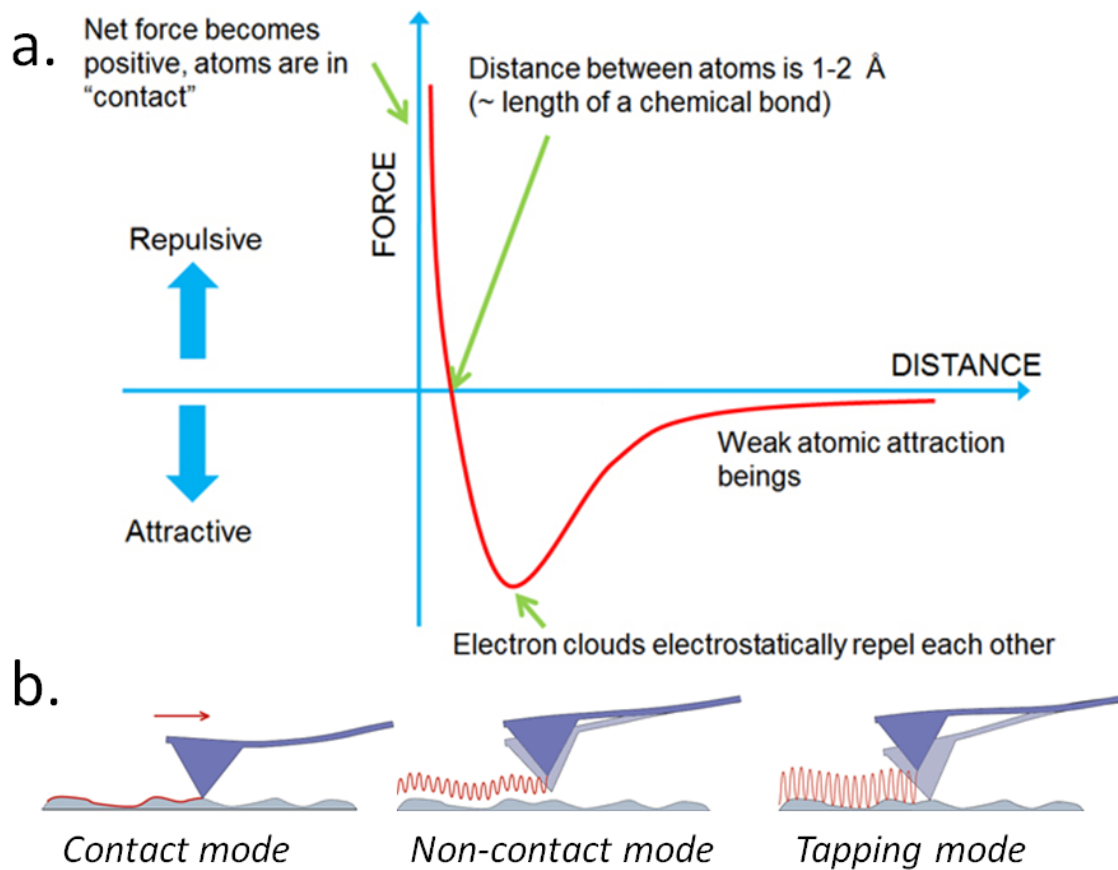


**Figure 1.2.2:** a) Lennard-Jones potential of tip-sample interaction (51) b) Different modes of AFM operation (52)

The repulsive force eventually dominates the attractive force and the net force becomes positive (repulsive), the so called “contact” region. In the case with AFM, when the tip pushes against the sample, the cantilever deflects like a linear spring described by the Hooke’s law:  $F = k \cdot \Delta x$ , where  $k$  is the elastic constant of the lever. This enables to measure forces ranging from  $10^{-13}$  to  $10^{-4}$  Newton (47).

Depending on the tip-sample interaction, different modes of AFM operation exist (Figure 1.2.2.b):

**Contact mode:** Historically, the first AFM technique that was developed was operating in the contact mode, where the tip-sample interaction is in the repulsive part of the potential. The basic working concept is based on the tip, which is approaching sample surface until it feels repulsion forces, translated into deflection of the cantilever (Figure 1.2.2b). A feedback loop then maintains a constant deflection by moving the  $z$ -position of the sample when the tip scans the surface in the  $x, y$  plane. The topographical image of the sample is reconstructed from the  $z$ -displacement readout at each scanning position. The main drawback of this method is the strong interaction of the tip with the sample, and the resulting risk of damaging the sample surface, in particular when working with biological matter.

**Non-contact mode:** A ‘simple’ solution to avoid damage or displacement of the sample is to operate the AFM in the attractive region of the tip-sample interaction potential. This method is called the non-contact mode. In this case, the cantilever is kept oscillating near its resonance frequency with low amplitudes

(typically <5 nm). Bringing the tip close to the sample surface results in the frequency shift of the cantilever oscillation due to the attractive potential (Figure 1.2.2b). This frequency shift is then used as a feedback signal to control the tip-sample distance. However, this technique often is unstable because of the small distance range in which it is operational and because of problems associated with the tip getting trapped by the attractive forces on the surface.

**Tapping mode:** The drawbacks of the 'contact' and 'non-contact' AFM modes are circumvented by the development of the so-called 'tapping mode' AFM (53). In tapping mode the cantilever oscillates near its resonant frequency with large amplitudes (typically ~20 to 100 nm), resulting in the tip periodically moving between the repulsive and attractive regimes (see Figure 1.2.2b). When the cantilever is close to the sample surface, its amplitude is reduced compared to its free oscillation. This change serves as a signal for the feedback loop to adapt the z-position of the piezo during scanning. The energy of the oscillation is sufficient to prevent the tip from getting trapped on the surface due to the attractive potential applied during each oscillation cycle. Even though the tip taps the surface, the force exerted on the sample at each strike is much smaller compared to the contact mode. The lateral forces are absent because the contact time between tip and sample is much shorter compared to the lateral displacement of the tip.

#### 1.2.4 DNA sample preparation

In order to reproducibly image with AFM, the sample of interest needs to be strongly attached to the substrate surface. For nanometer sized objects like DNA, it is vital to use ultra-flat surfaces with very low roughness, otherwise the molecule signal gets submerged in the background, and it becomes impossible to distinguish the sample from the substrate. In this Thesis, we used mica (a crystal) as a substrate.

##### **Mica**

Mica is a mineral from the family of the silicates. There are different types of mica, and the one used as an AFM substrate, is called muscovite mica (Figure 1.2.3). It is composed of (Si<sub>3</sub>Al)-silica sheets and Al<sub>2</sub> linked by oxygen atoms with the intercalated K<sup>+</sup> cations. After each cleavage step, the surface exposes K<sup>+</sup> cations which partially dissociates from the mica once the surface is in contact with water, resulting in negative surface charge. Since the DNA backbone is also negatively charged, in order to attach the DNA to mica, one needs either to treat the surface chemically (with 3-Aminopropyl-triethoxysilane (APTES) or poly-l-lysine), or to add divalent cations (Mg<sup>2+</sup>, Ni<sup>2+</sup>, Mn<sup>2+</sup>) to the DNA solution which will bridge DNA and substrate surface. Mica has several major advantages: it is composed of large atomically flat regions; it is possible to repeatedly cleave it by removing surface layers; it is relatively easy to handle and it is cost efficient.

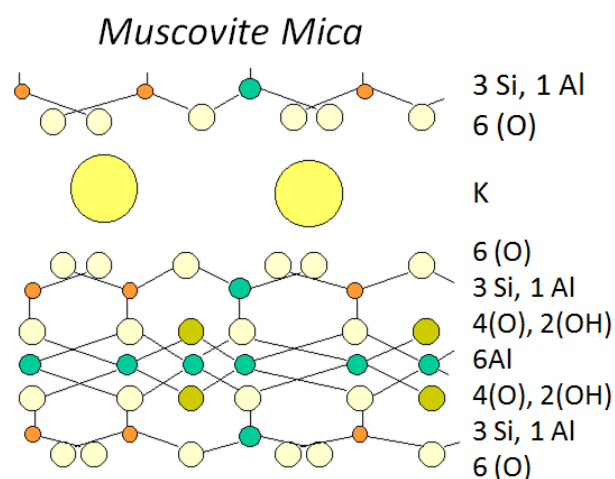


**Figure 1.2.3:** Structure of muscovite mica (54)

**DNA deposition by  $MgCl_2$ :** DNA can be bound to the mica surface by solutions containing  $MgCl_2$ ,  $NiCl_2$  or  $MnCl_2$ . To deposit DNA certain amount of  $MgCl_2$  (typically in the mM range) is added to the DNA solution in order to obtain  $Mg^{2+}$  ions. These ions bridge the negative charge of DNA molecules with the negative charges on the mica surface, thus inducing DNA adsorption on the surface.

**DNA deposition by APTES:** Another method to deposit DNA is to functionalize first the mica surface with a layer of APTES molecules (22). When APTES solution is deposited on the mica, molecules attach to the surface through silanization process, while the amino groups on the other side of the APTES molecules become positively charged (Figure 1.2.4). Subsequently, the positive amino groups bind to the backbone of the DNA molecules.

There are important differences between the two methods. The interaction between DNA and  $Mg^{2+}$  ions at typical concentration (1-5mM  $MgCl_2$ ) is relatively weak, allowing DNA molecules to relax on the surface. On the contrary, deposition with APTES molecules leads to strong DNA adsorption, preventing DNA from relaxation in 2D.

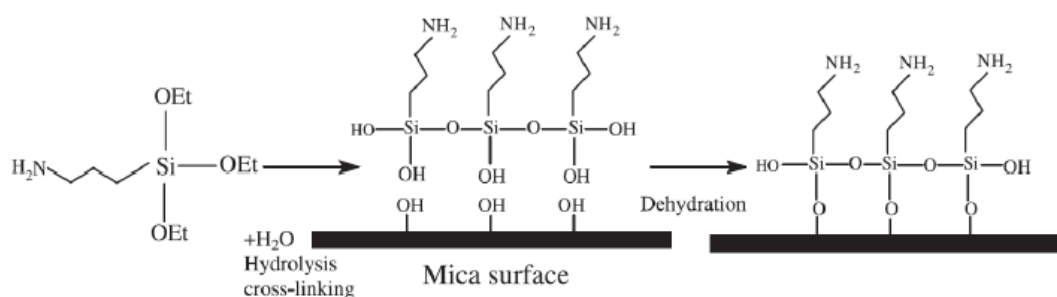


**Figure 1.2.4:** A scheme showing water mediated APTES silanization of the mica surface (55)

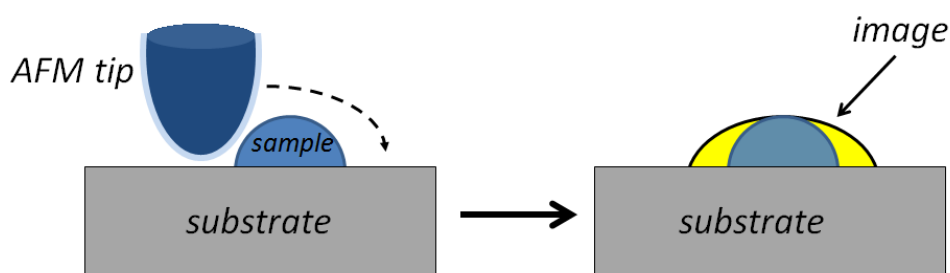


**Figure 1.2.5:** AFM imaging convolution effect. When an AFM tip with a high radius of curvature with respect to the sample is scanning, the sample appears broader on the image.

### 1.3.5 AFM resolution

AFM is an exceptional technique when it comes to imaging resolution. Unlike electron microscopy, it can generate three-dimensional image of the sample surface. When we talk about AFM resolution, we have to separately discuss the vertical and the lateral resolution.

Vertical resolution of the AFM is limited by the noise from the detection system and thermal fluctuations of the cantilever. Generally, the thermal noise is the dominant source of noise in AFM (56,57). For a cantilever with a force constant of  $\sim 40$  N/m, the thermal noise is below 0.01 nm. This results in AFM having a vertical resolution in the sub-nanometer range. Often when imaging with AFM in air, objects appear to have smaller heights than their nominal ones. This effect is mainly due to processes such as dehydration, sample deformation by tip-sample interaction and differential tip-surface-sample interaction.

The lateral resolution of the microscope is influenced by three main factors: the 'software resolution', (the ratio between scan size and number of pixels), the sensitivity of the piezo along the XY direction, and the nominal radius of the tip. While the software resolution and the piezo sensitivity are relatively 'easy' to control, the main limiting step for AFM imaging is the geometry and the size of the scanning tip. In an ideal case, the tip of the AFM would be single atom sharp. Since often the apical radius of the tip is comparable or bigger compared to the sample size, the so-called convolution effect takes place (Figure 1.2.5). The sample appears broader on the AFM image compared to its real dimensions. When imaging DNA, the tip must be nanometer sharp, in order to have reliable data.

### 1.3.6 Short review of AFM application in DNA imaging

AFM imaging has been successfully applied to numerous DNA studies (58). It was used to study the properties of DNA, influenced by the surface charge (59,60), its sequence(61-64), as well as the level of supercoiling (65-67). Several studies focused on the persistence length of DNA of various topologies (33,68,69). AFM was also used to assess the effects of UV radiation on the DNA structure (70,71) and its role in proteins binding (72).

DNA-protein interactions have also been widely investigated by AFM. Proteins such as RNA polymerase (73,74), Topo isomerase I (75), DNA gyrase (76) as well as numerous other DNA binding proteins (77-80) were imaged while in complexes with DNA molecules.

## Chapter 2: Physical properties of DNA

### 2.1 Towards an effective control of DNA's sub-molecular conformation on a surface

*This chapter is based on a paper submitted in ACS Macromolecules with the following authors:*

Aleksandre Japaridze<sup>1#</sup>, Dusan Vobornik<sup>1#</sup>, Ewelina Lipiec<sup>2</sup>, Andrea Cerreta<sup>1</sup>, Jacek Szczerbinski<sup>3</sup>, Renato Zenobi<sup>3</sup> and Giovanni Dietler<sup>1\*</sup>

#### *Affiliations:*

1 Laboratory of Physics of Living Matter, Ecole Polytechnique Fédérale de Lausanne, 1015 Lausanne, Switzerland

2 The Henryk Niewodniczanski Institute of Nuclear Physics, Polish Academy of Sciences, 31-342 Krakow, Poland

3 Laboratory of Organic Chemistry, Department of Chemistry and Applied Biosciences, ETH Zurich, 8093 Zurich, Switzerland

# These authors contributed equally to the manuscript and are co-first author

### **Abstract**

DNA is known to adopt different sub-molecular conformation based on its environment. Below we discuss conditions that either preserve the DNA's physiological B-conformation or lead to a partial B-form to A-form reorganization upon DNA's deposition on a surface and a consecutive dehydration. We used Atomic Force Microscopy to image and study DNA with a well-defined base pair number and composition on mica. To enable the DNA's adhesion we either added divalent cations such as  $Mg^{2+}$  or  $Mn^{2+}$  to the DNA solution, or functionalize the surface with a silane layer. The contour length of deposited DNA on the silane layer was always in perfect agreement with the B-form conformation, whereas the length of cation-deposited DNA was always shorter. For the DNA fragments whose length was below 300 base pairs this shortening was of the order of 20% with respect to the silane deposited ones – thus indicating a substantial conformational reorganization towards the much shorter A-conformation. To move forward we varied the DNA length and sequence composition, the equilibration time and compared nicked to non-nicked molecules, thus identifying several factors controlling the DNA transition. We performed Tip-enhanced Raman spectroscopy measurements confirming spectroscopically that cation-deposited DNA undergoes a partial B-to-A form conformational transition upon drying. Based on TERS data we could pinpoint the positions along the DNA where this transition was more probable to take place, namely the ends of linear DNA molecules. Finally, we proposed a simple thermodynamic model which enabled us to qualitatively as well as quantitatively describe the B-to-A DNA shortening, indicating the role of the surface binding strength in the final DNA sub-molecular conformation.

## 2.1.1 Introduction

It has been sixty years since the double helical structure of DNA was uncovered (2). This structure, which is now called the B-form DNA, was actually just one of many stable DNA sub-molecular conformations that were observed using X-Ray diffraction or NMR experiments (8). The sub-molecular conformation adopted by DNA molecules was shown to depend on many different conditions such as the base pair sequence, salt concentration in the solution, etc. Diffraction data (3,8) showed that DNA undergoes a conformational transition upon drying from the well-known B-form helix to a shorter A-form. DNA also undergoes B-to-A form transition when placed in ethanol (81) or when the surface onto which DNA is deposited is cooled down to 2°C (82). There are several AFM studies that reported a partial B- to A-form transition as a consequence of different environmental factors (81-84), but never as a function of the DNA deposition method and the subsequent difference in the DNA-surface bonding strength.

While both the B-form and the A-form DNA are right-handed helical structures, these two forms display significant differences. The contour length of A-DNA is approximately 30% shorter and its diameter 0.3 nm larger compared to the B-DNA (8,85).

DNA has been extensively studied by AFM since the late 1980s by visualizing the overall shape of the molecules without providing the sub-molecular structural information (86,87). These images were used to extract statistical data that allowed understanding the physical properties of DNA (24,60,69,88,89). These studies were assuming that the B-form was preserved and the influence of the deposition method on the DNA shortening and DNA sub-molecular conformation have therefore never been rigorously assessed. Later measurements on high resolution AFM have allowed direct visualization of the sub-molecular conformation of DNA in aqueous environment that agreed with the B-form (90,91), or appeared to show conformational heterogeneity within single molecules (92,93).

For AFM imaging on mica surface two main methods of DNA deposition have emerged: in one, the mica surface is silanized, creating a positively charged layer, which allows binding of the negatively charged DNA backbone (22). In the other method, divalent cations such as  $Mg^{2+}$ ,  $Ni^{2+}$ ,  $Mn^{2+}$  are used to bridge the negatively charged mica surface with the DNA. There are clear differences between these deposition methods: silanization leads to strong DNA binding, with DNA adopting a 2D projection of their 3D shape (24), while divalent cations result in much weaker absorption, with DNA relaxing in 2D (59). When using divalent cations, the final DNA shape is strongly depend also on the cation type and concentration used (94,95).

Most of the AFM studies use long DNA molecules, requiring several micrometers size images. This leads to a systematic error in the contour length determination: the pixel size in these images is relatively big (several nm) which causes an apparent decreased contour length due to the lack of resolution on DNA bends (59). To avoid above mentioned problem we used short DNA molecules containing 251, 500, or 845 base pairs (bp). Typically, in a 300 nm x 300 nm image we could measure contour lengths of ~10 molecules. This allowed increasing the number of pixels in order to get approximately 1 pixel/nm<sup>2</sup>, at the same time, reducing the acquisition time and minimizing the effects of thermal drift (96).

In order to strengthen the findings obtained by AFM, we used another efficient experimental procedure for DNA conformation determining, namely Tip-enhanced Raman scattering (TERS). The identification of



sub-molecular conformation of a single double stranded DNA is impossible by means of standard Raman spectroscopy due to several reasons; first, the Raman-scattering cross-section of DNA is very low, which makes the technique ineffective for single DNA molecules. Second, due to the diffraction limit the Raman laser beam cannot be focused onto a nanometer sized spot to collect spectra on separate locations along a single DNA strand. TERS combines the chemical sensitivity of Raman spectroscopy with the spatial resolution of scanning probe microscopy (STM/AFM). It allows collecting Raman spectra with a spatial resolution below 20 nm (97). By covering the apex of the AFM tip with a metallic nanoparticle that amplifies the electromagnetic field in the close vicinity of the tip, the tip acts as an optical nano-antenna, enhancing the Raman light scattered off a small volume of the sample located below the tip. Consequently, TERS delivers highly spatially resolved chemical information, and is an emerging tool for DNA studies (98-101).

Beyond its biological role, DNA's robustness and the ease of its self-assembly have led to the development of an intense research effort to develop DNA-based nanotechnology, with a particular focus on nano-structural (102) and nanotemplating (103) applications. Knowing and controlling DNA's sub-molecular conformation could prove essential for these applications.

## **2.1.2 Materials and methods**

### **251 base pairs DNA fragments preparation**

251 base pairs (bp) DNA was prepared using negative supercoiled pBR322 plasmid DNA (4361 bp) purchased from Fermentas (Switzerland). DNA fragments were amplified from pBR322 by PCR using 2 primers (5' CCGATTCACTCAAGAA 3' and 5' TTCACGTTGCTCGCGTAT 3'), subsequently separated on 1.5% agarose gel and purified using a Wizard SV Gel and PCR Clean-Up System extraction kit from Promega (Switzerland). DNA was then placed in the TE buffer composed of 10 mM Tris and 1 mM EDTA solution at pH 8, or in ultrapure Milli-Q water (at 18.2 M $\Omega$ .cm resistivity).

### **500 base pairs DNA fragments preparation**

500 base pairs DNA was prepared using the 100bp DNA Ladder marker purchased from Promega (Switzerland). The 500 bp band was extracted from 1.5% agarose gel and purified using extraction kit from Promega. DNA was then placed in the TE buffer.

### **845 base pairs DNA fragments and nicked DNA fragments preparation**

Double stranded DNA with 845 bp was prepared by digesting supercoiled Phix174 plasmid DNA (5386 bp) purchased from Fermentas with XhoI (162 bp) and SspI-HF (1007 bp) restriction enzymes (NEB). After digestion, the resulting 845 bp DNA fragment was separated on 1.5% agarose gel and purified using a Promega extraction kit. DNA was then placed in the TE buffer.

845 bp nicked fragment was obtained by further digesting the above mentioned 845bp DNA fragment with Nt.BstNBI nicking enzyme (NEB). As a result we obtain 3 nicked positions at 285 bp, 351 bp and 391 bp.

## DNA deposition protocols

All samples were prepared at room temperature and at constant humidity (20-22%).

The protocols to deposit DNA using  $Mg^{2+}$ ,  $Mn^{2+}$  or APTES were adjusted to obtain roughly the same DNA surface density while minimizing the surface roughness.

For  $Mg^{2+}$  and  $Mn^{2+}$  mediated deposition, the DNA solution was first diluted using ultrapure water to a final concentration of 0.5-1 ng/ $\mu$ L. Afterwards  $MgCl_2$  or  $MnCl_2$  was added to a final concentration of 2 mM for  $Mg^{2+}$  or 1 mM for  $Mn^{2+}$  deposition. A 20  $\mu$ L droplet of the solution was then deposited on the freshly cleaved mica (Ted Pella Inc) and incubated for 3 minutes unless stated otherwise. Finally, the sample was gently rinsed two times with 1 mL of ultrapure water, and gently dried using a compressed nitrogen flow and rapidly imaged.

For the APTES deposition, the mica surface was first functionalized with APTES ( $\geq 98\%$  purity, Sigma-Aldrich, Switzerland) in a separate step prior to DNA deposition. We diluted APTES in ultrapure water to a final concentration of 0.1 vol%. APTES molecules polymerize in contact with water, which can lead to a relatively rough substrate surface, instead of getting a flat monolayer of silane, a layer of silane chunks is produced (22,104). To minimize the silane layer roughness, the low concentration APTES solution was only used during the same day when it was prepared. A 10 to 15  $\mu$ L droplet of APTES solution was deposited on freshly cleaved mica for one minute and then rinsed once with 1 mL of ultrapure water. Finally the surface was dried using a gentle flow of compressed nitrogen. No  $MgCl_2$  or  $MnCl_2$  was added to the solution containing DNA this time. The initial DNA solution was diluted using ultrapure water to a concentration of 0.5 ng/ $\mu$ L. A 20  $\mu$ L droplet of the solution was deposited on the substrate for 3 minutes. The concentration of DNA was lowered with respect to  $Mg^{2+}$  or  $Mn^{2+}$  deposition because the stronger interaction of DNA with APTES otherwise results in the surface overcrowding. The sample was then rinsed two times with 1 mL of ultrapure water, and dried using a gentle nitrogen flow.

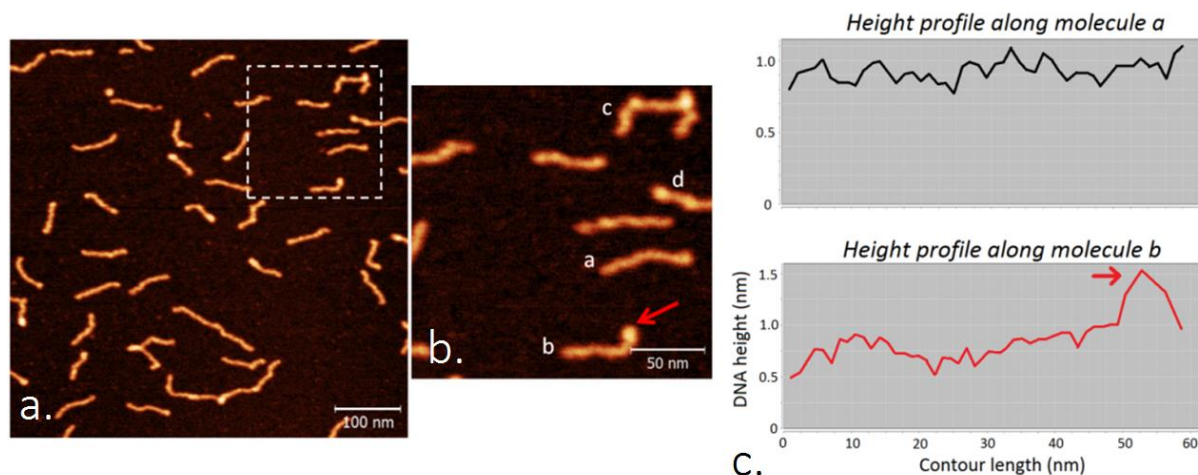


**Figure 2.1:** **a)** Typical AFM image showing 251bp DNA molecules deposited with  $Mg^{2+}$  **b)** Zoomed image of the initial large scale image, showing some of the DNA molecules that are not traced for the statistical analysis. Some molecules have a larger end (molecule **b**), or cross each other (molecules **c**) or partially fit in the scan frame (molecule **d**) **c)** the corresponding height profiles of molecule **a**, showing uniform height and molecule **b**, showing a larger end

When DNA is deposited using divalent cations it is possible for cations to “bridge” the same DNA molecule, creating a link between two parts of the negatively charged DNA’s backbone and strongly bending it. We

see some evidence of this in AFM images of cation deposited DNA as several molecules have their ends appearing higher and thicker (indicated by a red arrow on the molecule **b** on Figure 2.1). To avoid confusion between the B- to A- form conformational transition-induced shortening, and the shortening that could be due to cation bridging of the same strand, we systematically excluded from our analysis any DNA molecules that displayed ends that appeared higher or larger. We have also eliminated from the analysis all the molecules that were only partly in the scan-frame (molecule **d** on Figure 2.1), and all the molecules crossing each other (molecule **c** on Figure 2.1).

### **AFM instruments and probes**

AFM images were collected using NanoScope IIIa (Veeco Instruments, Santa Barbara, CA, USA) operating in tapping mode in air. All AFM images consist of 512 x 512 pixels with a scan frequency of  $\leq 1$  Hz. Measurements were done with Tap150 tips (Bruker, DE), with typical resonant frequencies between 120-160 kHz, spring constant 5 N/m and nominal radius of 10 nm.

### **Analysis software and procedures**

AFM images were flattened using the Gwyddion (105) software (Version 2.25) and no further image processing was carried out. DNA data were analyzed using “DNA Trace”, Java-based analysis software that has been described elsewhere (106).

### **TERS measurement of 500bp DNA**

TERS probes were prepared by coating silicon-based AFM cantilevers with silver. We chose the ATEC-NC probes (Nanosensors and OMCL-AC160BN, Olympus) since they enable seeing the tip from top. The tips were coated with 20 nm of silver (Aldrich 99.99 % pure) using a BAL-TEC MCS010 evaporation system, under a pressure of  $2.7 \times 10^{-6}$  Torr. AFM topography and phase images were acquired in air in semi-contact mode at scan rates of 0.2–0.3 Hz, scan sizes of 1000–3000 nm, and scan resolution of 512×512 or 256×256 pixels, with an NTEGRA Spectra Upright (NT-MDT) system.

Based on AFM topographies and phase images we selected our targets - 8 points along each investigated DNA strand. The contour length of 500bp DNA molecules deposited on mica with magnesium ions was approximately 146 nm. Eight spectra were collected along every molecule, with the distance between consecutive tip positions being equal to approximately  $146/7 \text{ nm} \approx 21 \text{ nm}$ . This value matched the estimated spatial resolution of TERS (98). We believe that we avoided under sampling, thanks to the chosen step size.

We believe, the reduction of the step size down to few nanometers would increase the exposure of the DNA to laser light, which eventually would lead to its photodamage, as described elsewhere by Domke et al. (322). TERS spectra were collected in the spectral range of  $2400 \text{ cm}^{-1} - 200 \text{ cm}^{-1}$  using a Solar T-II Raman spectrometer coupled to an Andor Newton 971 UVB CCD camera (cooled to  $-86^\circ\text{C}$ ). The green (532 nm) Nd:YAG laser power measured at the sample level was kept below 0.42 mW to avoid appearance of contaminations from amorphous carbon. The laser exposure time for a single spectrum acquisition was set to 5 seconds (98).

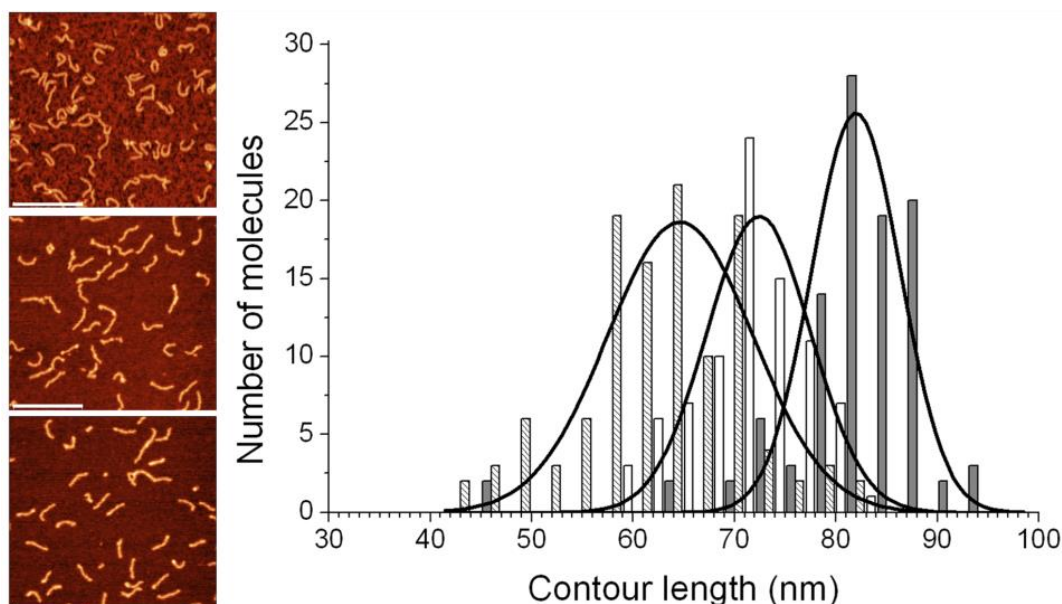


**Figure 2.2:** Typical AFM images of 251 bp DNA imaged in air with the corresponding histograms of contour length. Upper AFM image shows APTES deposited DNA, middle image shows the same molecules deposited with  $Mn^{2+}$ , while the lower image shows  $Mg^{2+}$  deposited DNA (200nm scale bars are shown in all 3 images). Histograms are based on lengths measured for 101 DNA molecules deposited on APTES (grey bars), 84 molecules deposited using  $Mn^{2+}$  (white bars), and 116 molecules deposited using  $Mg^{2+}$  (dashed bars). The graph also shows the corresponding Gauss fits.

## 2.1.3 Results

### 2.1.3.1 251 bp DNA : The Contour length measurements in air

Figure 2.2 shows typical AFM images of 251bp DNA deposited with different methods on mica surface. After tracing the APTES deposited DNA molecules, we observed that the contour length was centered at 82 nm, which was in perfect agreement with the B-DNA conformation (the expected contour length of B-conformation DNA for 251bp is ~83 nm, whereas that of A-form DNA is ~58 nm). The contour length of the same DNA but deposited with  $Mn^{2+}$  was shorter and the average value centered at 72 nm.  $Mg^{2+}$ -deposited DNA was shortest on average, centered at 65 nm. The full width half maximum (FWHM) values of the three Gauss fits were 10 nm, 12 nm and 17 nm for APTES,  $Mn^{2+}$  and  $Mg^{2+}$  respectively.

There is evidence showing that the strength of DNA attachment to the substrate is higher with larger divalent cations, and that  $Mn^{2+}$  binds DNA to the surface more firmly than  $Mg^{2+}$  (95). It is also known that DNA deposited on APTES is bound more strongly than when using divalent cations (24,59). Based on this we proposed that the observed reduction in DNA length was due to a partial B-to-A form conformational transition that was more probable to occur with weaker binding. It is known that DNA can undergo the B-to A-conformation change upon drying (3,8,81), but our data suggest that binding to a surface can completely or partly inhibit this transition depending on the surface binding strength. The stronger the DNA attachment to the surface, the less its conformation can undergo any modifications. APTES surface binds DNA strongly so that even after drying its contour length is comparable to its physiological B-form length. On the other hand, cations cause a weaker DNA binding, allowing a partial transition towards the A-form that is expected upon drying, evidenced by the contour length shortening.

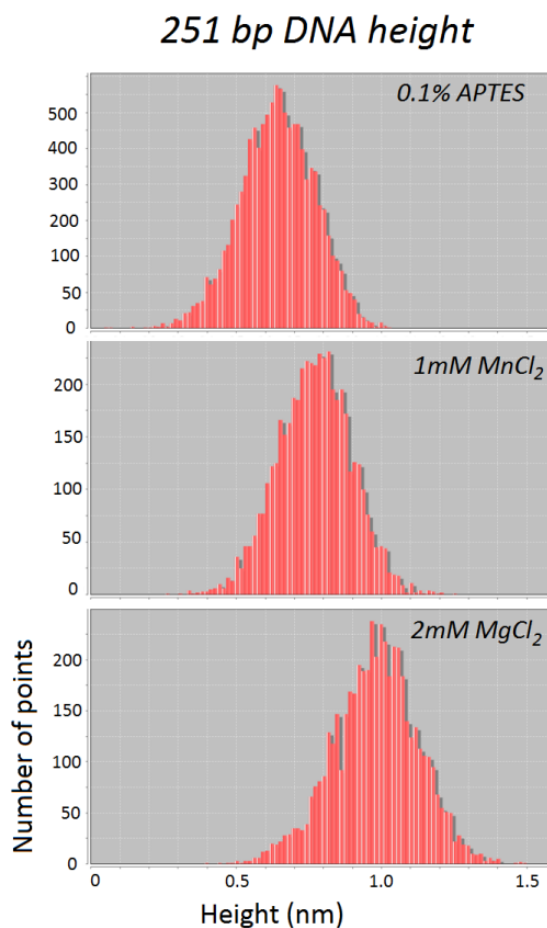


**Figure 2.3:** Height histograms for traced 251bp DNA molecules deposited with APTES, Mn<sup>+</sup> and Mg<sup>+</sup>

### 2.1.3.2 Calculating the amount of base pairs undergoing the B-to-A transition

AFM enabled us to measure not only the contour length of DNA molecules, but also the height of the DNA. The diameter of the A-form DNA obtained from X-ray diffraction and NMR experiments is 0.3nm larger than the one of B-form DNA (8,107). The diameter difference should be corresponding to the height difference of the DNA stands once deposited on the surface. Height histograms of traced molecules in Figure 2.3 show that Mg<sup>2+</sup> deposited DNA on average are higher than APTES deposited DNA. This data further supports that we observe a conformational transition from B- to A-form for the Mg<sup>2+</sup>-deposited DNA.

If we assume that the smaller length is due to the conformational change of a part of the total base pairs from B- to A-form, we can evaluate the fraction of base pairs which underwent this transition. If we define the number of base pairs being in the A-form part of DNA as  $N_A$ , and the number of base pairs being in the B-form part of the molecule as  $N_B$  for any given DNA of  $N_{bp}$  base pairs, we can write down a simple relation:

$$N_A \cdot l_A + N_B \cdot l_B = L_{cont} \quad (2.1)$$

$$N_A + N_B = N_{bp} \quad (2.2)$$

Where:  $l_A = 0.23$  nm and  $l_B = 0.332$  nm are the rise per base pair of A-form and B-form DNA (85),  $L_{\text{cont}}$  is the measured DNA contour length (for this calculation we took the center of corresponding Gauss fits as  $l$ ). Let's consider the case with 251bp DNA ( $N_{\text{bp}} = 251$  is the total number of base pairs of the molecule). It is easy to solve the two equations and verify that the fraction  $N_A/N_{\text{bp}}$  of base pairs that are in the part of the DNA that has switched its conformation to the A-form is  $\sim 44\%$  of the total number of base pairs for  $\text{Mn}^{2+}$ -deposited DNA and  $\sim 72\%$  for  $\text{Mg}^{2+}$ -deposited DNA.

### 2.1.3.3 500 bp DNA : The Contour length measurements in air

To verify if the number of base pairs and the nucleobase sequence had an impact on the DNA conformational transition, we performed the same experiment with a 500 bp DNA fragment having a different base pair composition. Figure 2.4 shows the corresponding contour length histograms obtained upon measuring the length of 123 APTES deposited molecules (dark grey bars), 132 molecules deposited with  $\text{Mn}^{2+}$ , and 123  $\text{Mg}^{2+}$  deposited molecules. The three distributions were again fitted with the Gauss equation, and the centers of the fits were at 163 nm for APTES deposition, 154 nm for  $\text{Mn}^{2+}$  deposition, and 146 nm for  $\text{Mg}^{2+}$  deposition. The respective FWHM values are 11 nm, 12 nm and 19 nm for APTES,  $\text{Mn}^{2+}$  and  $\text{Mg}^{2+}$  deposition respectively.

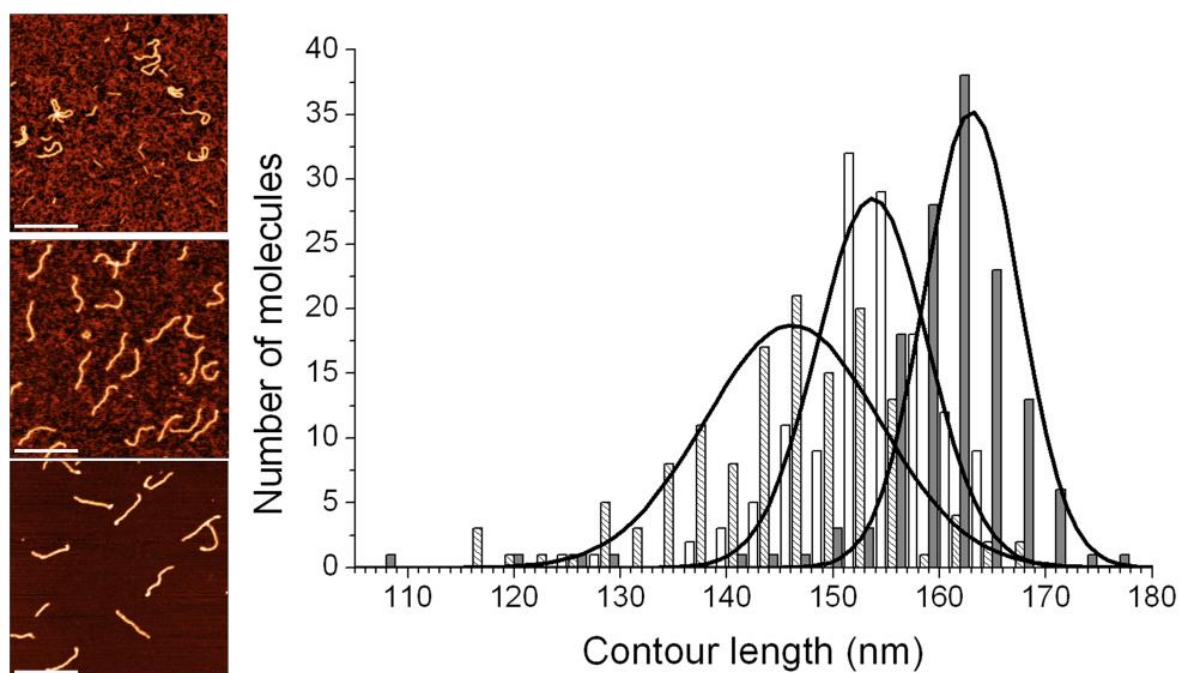


**Figure 2.4:** Typical AFM images of 500 bp DNA with the corresponding histograms of contour length. Upper image shows DNA deposited on APTES modified mica, middle image shows the same molecules deposited with  $\text{Mn}^{2+}$  and the lower image shows  $\text{Mg}^{2+}$  deposited DNA (200nm scale bars are shown in all three images). Histograms are based on lengths measured for 123 DNA molecules deposited on APTES (grey bars), 132 molecules deposited using  $\text{Mn}^{2+}$  (white bars), and 123 DNA molecules deposited using  $\text{Mg}^{2+}$  (dashed bars). The graph also shows best Gauss fits for the three distributions.

Upon changing the nucleobase sequence and nearly doubling the number of base pairs of the measured DNA, the data in figure 2.4 still agreed well with the previous data in Figure 2.2. At 163 nm, the length of DNA deposited on APTES was again in perfect agreement with the length expected for the B conformation DNA. DNA deposited with  $Mn^{2+}$  and with  $Mg^{2+}$  was again shorter and thus appeared to partially have switched its conformation towards the A-form DNA. However, percentually, with the longer DNA fragment the number of base pairs that were converted to the A-form appeared to be smaller. The contour length of 251 bp DNA deposited with  $Mg^{2+}$  was centered at 65 nm, and therefore we could have expect the 500 bp DNA to have its contour length distribution centered at two times that value, namely  $\sim 130$  nm. Instead the experimental value was 146 nm, a more modest shortening with respect to APTES deposited DNA. By using equations 2.1 and 2.2 above, we could calculate that for the 500bp DNA deposited with  $Mg^{2+}$   $\sim 40\%$  of base pairs had reorganized into the A conformation for the 500bp DNA. This value is significantly lower compared to the 251bp DNA, where we observed a  $\sim 70\%$  base pair rearrangement. Interestingly while the percentage value for  $Mg^{2+}$  deposited DNA was significantly different, the absolute value of length reduction was almost the same for both DNA  $\sim 20$  nm. The same goes for  $Mn^{2+}$  deposited DNA, where absolute length change values were almost identical for the 251 bp and the 500 bp DNA at respectively 10 and 9 nm shorter compared with the expected B-conformation length. One way to explain this finding was that the transition was more likely to start at the free ends of DNA molecules and propagate towards the center of the molecule. If this was true, given the same deposition time, the same absolute length equivalent DNA would undergo the change, which would result in longer molecules having a much smaller percentual change.

#### 2.1.3.4 500 bp DNA : Equilibration time vs. conformational transition

DNA is known to adopt a 2D relaxed conformation on mica surface when deposited with low concentrated cations (59). To verify if the number of DNA base pairs that undergo the transition is affected by the 2D-equilibration time, we conducted experiments with varying the equilibration times (Figure 2.5) Table 2.1 summarizes the contour length distributions for  $Mg^{2+}$  deposition where DNA was allowed to equilibrate on the mica surface in the presence of  $Mg^{2+}$  for 10, 17 and 32 minutes prior to rinsing and drying. As the control experiment we deposited the same 500 bp DNA on an APTES treated surface for 3 minutes. The distributions were once again fitted with the Gauss equation, the central value of the peak, its width, as well as the full width at half maximum were then extracted and are shown in Table 2.1 below.

**Table 2.1 Contour length dependency on DNA equilibration time**

Deposition type	Number of molecules	Average Length [nm]	$\Delta$ Length	Xc [nm]	FWHM [nm]
0.1% APTES 3min	123	163 $\pm$ 8	-	164	11
10min - $Mg^{2+}$	120	153 $\pm$ 14	- 6%	159	26
17min - $Mg^{2+}$	105	147 $\pm$ 10	- 10%	148	23
32min - $Mg^{2+}$	110	143 $\pm$ 11	-12%	143	23

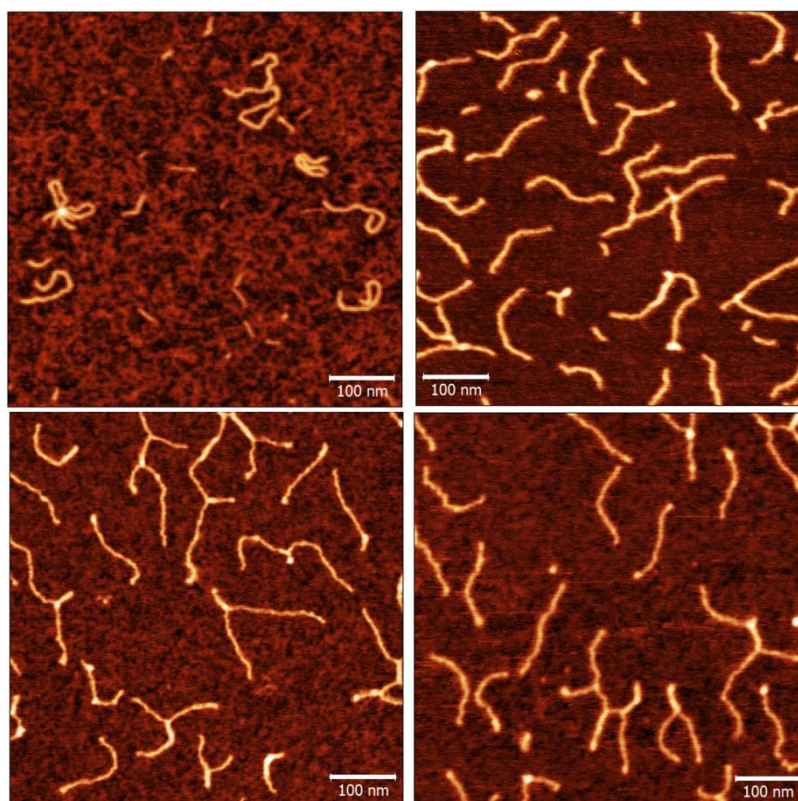


**Figure 2.5:** Typical AFM images of 500bp DNA imaged in air together with corresponding histograms of contour lengths as a function of relaxation time. (upper left AFM image represents DNA deposited on APTES modified mica; upper right image shows DNA deposited using Mg<sup>2+</sup> and rinsed and dried after 10 minutes on mica; lower left AFM image shows DNA deposited using Mg<sup>2+</sup> and rinsed and dried after 17 minutes; lower right image shows the same molecules deposited on Mg<sup>2+</sup> and rinsed and dried after 32 minutes). Scale bars 100nm.

These experiments showed that the deposition time strongly influenced the conformation of DNA. The longer the DNA was left on the surface hydrated and in the presence of cations to equilibrate, the shorter the final contour length was. The APTES deposited DNA resulted again in a contour length that was in excellent agreement with the physiological B-form DNA with a much narrower distribution. On the other side, Mg<sup>2+</sup> deposited DNA, which was left to equilibrate for 10 and 17 minutes on the surface had a significantly shorter average contour length. Finally, DNA equilibrated for 32 minutes had its average contour length slightly shorter than the 17 minutes one.



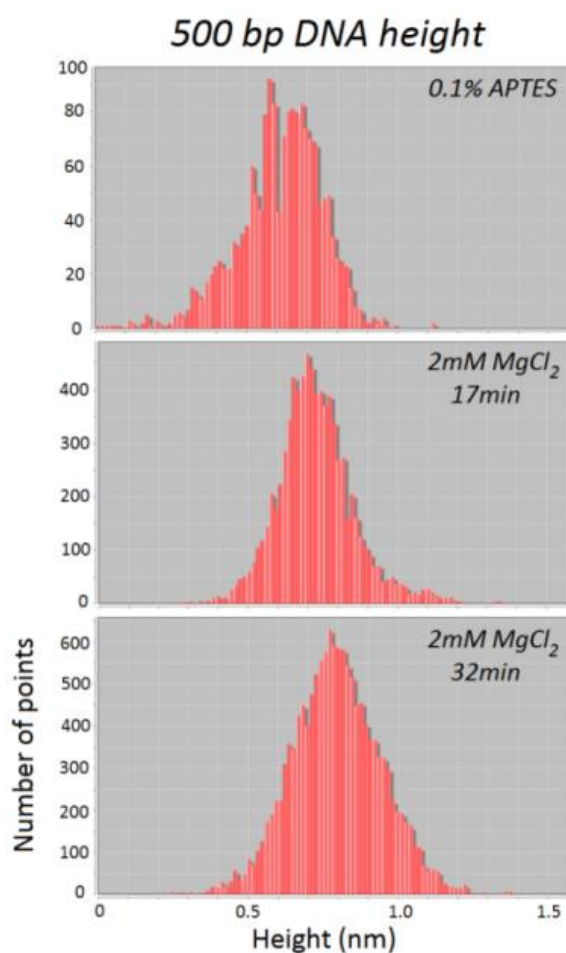


**Figure 2.6:** Height histograms for 500bp DNA molecules deposited with APTES and Mg<sup>+</sup> for 17min and 32min

Height histograms for traced 500bp molecules showed that 32min Mg<sup>+</sup> deposited DNA was higher than 17min Mg<sup>+</sup> deposited as well as APTES deposited DNA. The increase in the height of the DNA as the function of deposition time, we think is directly linked to the bigger fractions of DNA undergoing B-to A form transition with longer deposition times.

Interestingly the dependence of the contour length on the equilibration time did not appear to be linear, as the shortening effect of time appeared to be more significant in the beginning and reached a threshold toward longer deposition times ( $\Delta$ Length in Table 2.1). It is important to stress that just adding Mg<sup>2+</sup> or Mn<sup>2+</sup> to the DNA that was then deposited on APTES always resulted in the same B-form DNA contour length. In order to justify this statement we added 2mM MgCl<sub>2</sub> and 1mM MnCl<sub>2</sub> in the DNA solution before depositing them on 0.1% APTES treated mica. The average contour length of 500bp DNA stayed unaffected by the presence of salts in the solution and was the same as for the APTES deposited DNA (Table 2.2). Therefore, the observed effect of cations on the contour length shortening is only related to the DNA equilibration on the surface and not to their presence in the DNA solution.

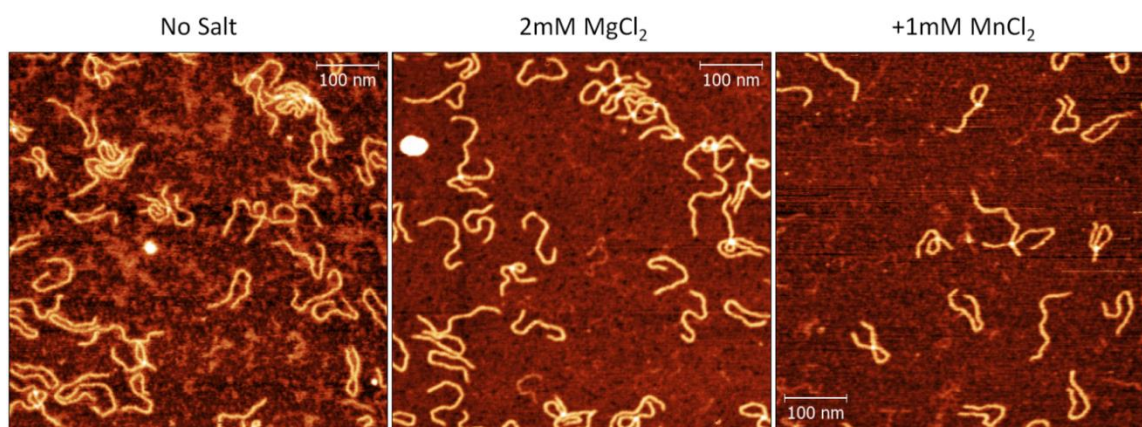


**Figure 2.7:** Typical AFM images of 500bp DNA deposited on 0.1% APTES for 3min with and without the presence of cations in solution.

It is known that allowing DNA to equilibrate on the mica surface with  $Mg^{2+}$  (2D relaxation) leads to longer end-to-end distance and to the elimination or minimization of DNA-DNA crossings (34,36). Despite the existing data, no effects concerning DNA sub molecular conformation in relationship with the surface equilibration was previously reported in literature (22,59,60,83,88,89,94,95,108,109).

**Table 2.2 Contour length of APTES deposited 500bp DNA in the presence of salts**

500bp on 0.1% APTES	Number of molecules	Contour Length [nm]
Control	120	164 ± 8
+ 2mM $MgCl_2$	100	164 ± 5
+ 1mM $MnCl_2$	100	162 ± 5

### 2.1.3.5 845 bp DNA : Effect of nicked sites on conformational transition

When comparing the 251 bp and the 500 bp DNA experiments, we observed that the longer the DNA molecules were, the lesser the percentage of base pairs reorganized into the A-DNA conformation. One possible explanation for this was that it was more probable for the DNA to start changing its conformation at the two free ends of the molecule, where strands could easier reorganize from B-into the A-form helix. If this was the case, a DNA molecule with nicks – single stranded breaks in the DNA backbone – would similarly be able to start undergoing conformational transition at these nicked sites. Nicking would result in a shorter DNA length than the same molecules without any nicks when undergoing dehydration on a surface in the exact same conditions (cation concentration, equilibration time, drying rate, etc.). To verify this hypothesis we have used 845 bp DNA where we have induced nicks at three positions (see materials and methods) and compared its contour length to that of an intact 845 bp DNA. Table 2.3 summarizes the results of these experiments while the representative images and the corresponding histograms are shown in Figure 2.8. Both samples were deposited in the same way: 15 minutes of relaxation time with  $Mg^{2+}$  prior to rinsing and drying. The contour lengths were measured for 100 molecules for both the nicked and the control non nicked sample. As a second control, we deposited the non-nicked DNA on

APTES surface for 3 minutes. There was a clear difference in the contour length confirming our hypothesis: when deposited with  $Mg^{2+}$  the center of the Gauss fit for the non-nicked DNA was at  $269 \pm 9$  nm, and for the nicked distribution it was at  $256 \pm 11$  nm. This experiment, coupled with the 251 and 500 bp DNA experiments, strongly suggests that the B- to A-form transition, which occurs upon the drying, was much more probable, at either the free ends, or at nicked sites on DNA molecules.

**Table 2.3. Effect of nicked sites on DNA contour length**

845 bp DNA - deposition method	Number of molecules	Average Length [nm]	$\Delta$ Length	Xc [nm]	FWHM [nm]
Non-nicked-0.1% APTES	50	$281 \pm 10$	-	280	19
Non-nicked - $Mg^{2+}$	100	$269 \pm 9$	- 4%	269	23
Nicked - $Mg^{2+}$	100	$256 \pm 11$	- 9%	258	23

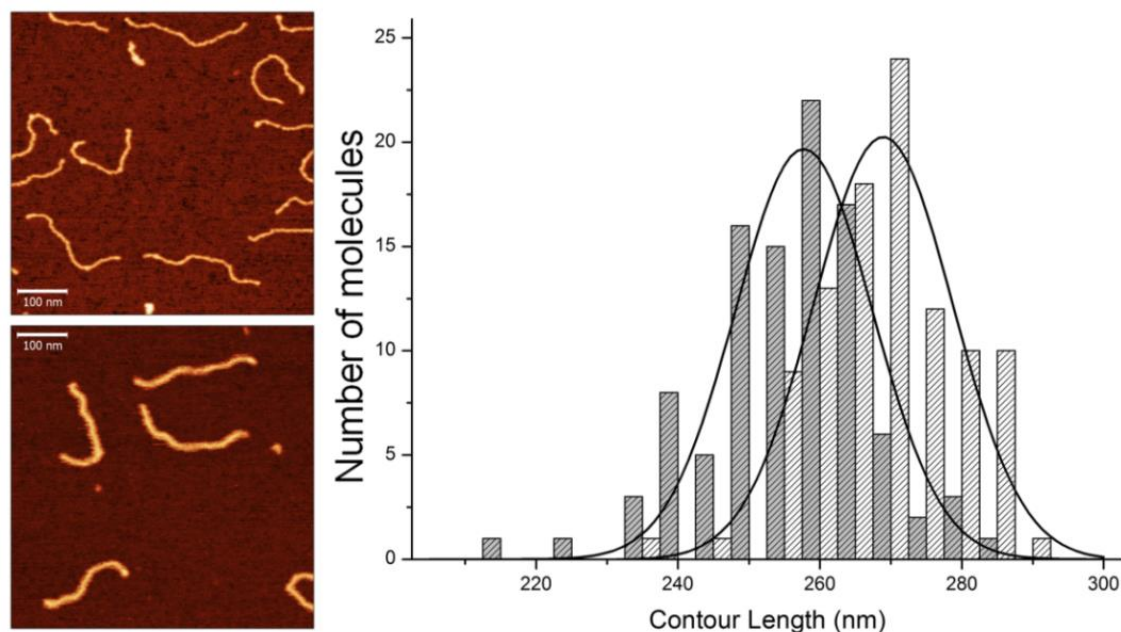


**Figure 2.8:** Typical AFM images of 845bp DNA deposited with  $Mg^{2+}$  together with the corresponding Histograms of contour length (upper left AFM image shows intact DNA molecules; lower left image shows nicked DNA). Scale bars 100nm.

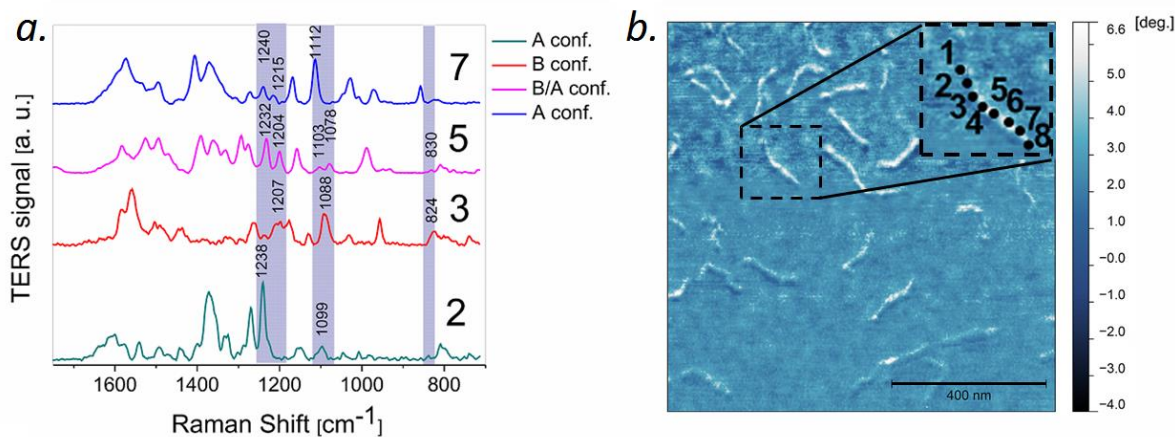


**Figure 2.9: TERS study of 500bp DNA: a)** spectra collected along 500bp DNA strand corresponding to tip positions 2, 3, 5, 7 marked on **b)** AFM phase image of the 500bp DNA (scale bar 400nm).

### 2.1.3.6 500bp DNA: Tip enhanced raman spectroscopy measurements

In order to confirm the AFM observation of partial B-to-A-form DNA transition upon deposition with cations, we used Tip-Enhanced Raman Spectroscopy (TERS) and looked for independent spectroscopic evidence. We applied TERS to identify the sub-molecular conformation along individual strands of 500bp DNA deposited with 2mM Mg<sup>2+</sup>. Figure 2.9 (a) shows a typical TERS spectra, showing A-DNA, B-DNA and a mix of A-DNA and B-DNA conformations collected along a single strand of 500bp DNA. Each DNA strand was measured at 8 different positions marked on the DNA phase image presented in Figure 2.9 B (the spectra were collected at DNA positions 2,3,5 and 7). The DNA conformation in each of eight positions along the DNA strand was recognized based on three criteria: i) The symmetric stretch of PO<sup>2-</sup> (>1095 cm<sup>-1</sup> – A conformation, <1095 cm<sup>-1</sup> – B conformation, doublet – B/A conformation); ii) The symmetric stretching vibration of -O-P-O- (an appearance of a peak at ~830 cm<sup>-1</sup> – B or B/A conformations); and iii) The shape of the peak related to asymmetric stretch of PO<sup>2-</sup> at ~1250 cm<sup>-1</sup>. Sharp and relatively intense peak indicates A conformation. Broad and diffuse peak is characteristic for B conformation. All three criteria were considered in assignment of the conformation. Sharp and relatively intense peak would indicate A-conformation, whereas broad and diffuse peak was characteristic for B conformation.

The relative percentage of A-DNA, B-DNA and mix of A/B-DNA spectra was manually calculated, based on those spectral features, in each measurement point and the results are shown in Figure 2.10.

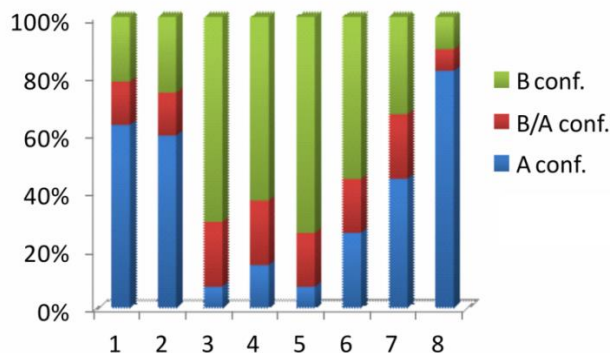


**Figure 2.10:** the percentage of A-DNA, B-DNA and mix of A-DNA and B-DNA conformations detected at each tip position 1-8 on Figure 2.9. Data was collected along 27 individual 500bp DNA molecules along 8 different positions

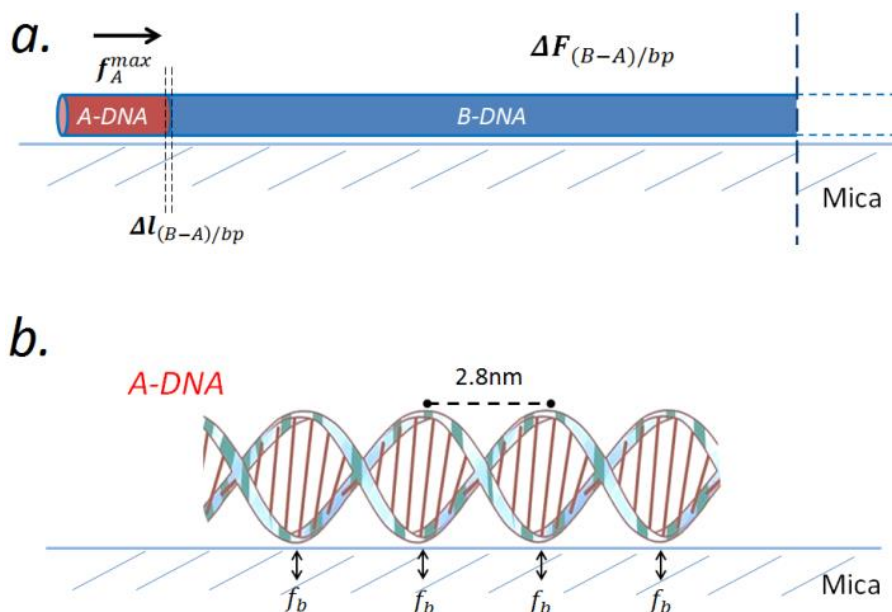


**Figure 2.11.** Schematic representation of: **a)** B-to-A DNA transition:  $f_A^{max}$  is the maximal force acting on the converted A-DNA part;  $\Delta l_{(B-A)/bp}$  is the length difference between one base pair of B- and A-DNA;  $\Delta F_{(B-A)/bp}$  is the free energy change per base pair between B and A form DNA. **b)** the forces acting on the DNA every helical pitch to keep the DNA attached to the surface.

TERS spectra were collected along 27 individual 500bp DNA molecules, at eight positions along each one: the positions along the molecule were approximately the same for each molecule in order to collect data that can be compared at each position. The acquisition of spectra along the molecule was repeated 2-4 times for the sake of data reproducibility. In total 461 TER spectra were acquired with 9 tips. The DNA conformation was determined for all obtained spectra. The distribution of the conformation at each of the eight probed locations along the DNA strands is presented in Figure 4D. The A-DNA conformation was predominantly detected at the free ends of linear DNA (in positions 1, 2, 7 and 8), while the central part of the DNA (positions 3, 4, 5, and 6) was predominantly in B-DNA conformation.

Raman and TERS spectra of the DNA contained also bands related to nucleobase content, mainly in the spectral range from  $1720\text{ cm}^{-1}$  to  $1300\text{ cm}^{-1}$ . In the collected TER spectra ring stretching modes were present at  $\sim 1550\text{ cm}^{-1}$ , C=N stretching at  $1450\text{ cm}^{-1}$  -  $1500\text{ cm}^{-1}$ , and C-N stretching at  $\sim 1370\text{ cm}^{-1}$  (29, 30). According to the spatial resolution of TERS in our particular measurements ( $\sim 20\text{ nm}$ ), each spectrum comprised the fingerprint of approximately 54 nucleobases (28). The ring breathing and stretching modes of different nucleobases had very similar wavenumbers, resulting in overlapping bands. Consequently, it was impossible to resolve the signal from single nucleobases

### 2.1.3.7 Thermodynamic Model describing the B-to-A transition

In order to explain our experimental findings, we proposed a thermodynamic model where for simplicity we considered one half of the DNA molecule whose B-form part was much longer than the A-form part, and then calculated the maximal length of the A-DNA part it could convert to (Fig. 2.11a).

The model was based on the following experimental findings:

1) DNA deposited on  $Mg^{2+}$  treated surface (weak interaction force  $f_b$  between DNA and the surface) showed a decrease in length corresponding to approximately  $\sim 10$  nm of A-DNA conformation on each side of the linear DNA, independently of the total length of the linear DNA.

2) On the contrary, DNA deposited on APTES treated mica (strong interaction force  $f_b$  between DNA and the surface) did not show any length decrease and its total length was compatible with the B-DNA conformation.

3) The fact that the two ends of a linear DNA changed into A-DNA conformation whereas the central part remained in the B-form was supported by TERS measurements.

According to the thermodynamic Model:

a) The driving mechanism for the B-to-A transition was the free energy change between the two DNA sub-molecular states. The exact value of the free energy change per base pair for B-to-A transition  $\Delta F_{(B-A)/bp}$  depends on many factors, such as DNA sequence, salt concentration, surface interaction, etc. For our calculations we decided to take an average value of the free energy change for B-to-A (or A-to-B) transition per base pair (110-112) and we assumed that this change was favourable for the B to A transition:  $\Delta F_{(B-A)/bp} \sim 10^{-20} J$ .

This free energy difference  $\Delta F_{(B-A)/bp}$  should be equal to the work performed on the DNA end to 'slide' towards the center upon B-to-A transition by the length  $\Delta l_{(B-A)/bp}$ , which was the length difference between the converted A form DNA and its previous B form per base pair (Fig. 2.11a). Based on the free energy change, the maximal force  $f_A^{max}$  that could act on the A-form part could be estimated:

$$f_A^{max} \cdot \Delta l_{(B-A)/bp} = \Delta F_{(B-A)/bp} \rightarrow f_A^{max} = \frac{\Delta F_{(B-A)/bp}}{\Delta l_{(B-A)/bp}} \quad (2.3)$$

Where :  $f_A^{max}$  was the maximal force acting on the A-Form part of the DNA molecule;  $\Delta l_{(B-A)/bp}$  was the difference in length between B and A form DNA per base pair, namely ( $\sim 0.05$ nm);  $\Delta F_{(B-A)/bp}$  was the free energy difference between B and A form DNA per base pair, ( $\sim 10^{-20} J$ ).

If we plug estimated values in the formula 2.3 above, the maximal force acting on the A-form part of the DNA molecule becomes:  $f_A^{max} \sim 0.2nN$

b) As the next step we estimated the 'frictional' force arising between a DNA strand and the mica surface by using the existing data based on DNA pulling experiments (113-115). The first assumption that we made was that the force needed to detach DNA from the surface, while pulling on it, was the same as the force acting on DNA when it slides along the surface. The second assumption that we make was that the binding force needed to detach DNA from the surface was acting between the surface and the part of each helical turn that was in 'direct' contact with the surface (Fig. 2.11b). We took into account these two assumptions discussed above and estimated the maximal length of the A-form DNA based on its surface interaction strength. The B-to-A transition would eventually stop when the difference in the free energy gain between A- and B-forms would be equal to the work done by the 'friction' force for the maximal A-form DNA length.

$$f_A^{max} = f_b \cdot \left( \frac{l_A^{max}}{\text{helical pitch}} \right) \rightarrow l_A^{max} = \frac{f_A^{max}}{f_b} \cdot \text{helical pitch} \quad (2.4)$$

Where :  $l_A^{max}$  was the maximal length of DNA converted into A form;  $f_A^{max}$  was the maximal force acting on the A-DNA part ( $\sim 0.2$ nN);  $f_b$  was the binding force between DNA and the surface.

Once again, in our calculations we took just an average value of the binding force  $f_b$  between a DNA and a specific surface. For DNA interaction with the mica surface ( $Mg^{2+}$  case) we took a typical value of  $f_b \sim 0.05$ nN and for the DNA-APTES interaction  $f_b \sim 1.3$ nN (113-115). We insert these values into Eq. 2.4 and

got the maximal length of A-DNA (from one end): APTES-mica :  $l_{APT}^{max} \sim 0.52$ nm and for  $Mg^{2+}$  mica:

$$l_{Mg}^{max} \sim 9.6\text{nm}.$$

According to the model, the maximal A-DNA length for DNA deposited on APTES treated mica should be  $\sim 1$  nm, which explains why we experimentally don't observe any measurable compaction. On the contrary, when the DNA is bound weakly on the mica surface ( $Mg^{2+}$  case), a linear DNA should shorten by a total amount of  $\sim 19.2$  nm ( $\sim 2 \times 9.6$  nm). This value is very close to our experimentally measured value, where  $Mg^{2+}$  deposited DNA (irrespective of its length) is typically  $\sim 20$ nm shorter than the B-form length. This simple model explained also why the DNA shortening was not dependent on the DNA contour length and why it tended to 'slow down' after long deposition times.

## 2.1.4 Conclusion

Here we present a study of the contour length shortening that DNA undergoes when deposited and dried on a surface using the most common DNA deposition methods. Using high resolution AFM measurements we have uncovered important length differences between DNA samples deposited using different methods, which are consistent with the DNA's conformation either remaining in the physiological B-form, or with parts of the molecule reorganizing into the A-form helix. TERS measurements confirmed the local sub-molecular conformation changes and showed that the changes were preferentially occurring at the ends of linear DNA molecules. We proposed a simple thermodynamic model which qualitatively as well as quantitatively described the B-to-A DNA transition, indicating the role of the surface binding strength in the final DNA sub-molecular conformation.

Our data showed that when DNA was deposited on silanized mica (using APTES) and dried subsequently, it remained in its physiological B-form conformation. However, when the same DNA molecules were deposited using divalent cations (using  $Mn^{2+}$  or  $Mg^{2+}$ ), we always observed DNA shortening molecules upon drying, which was consistent with a partial B- to A-form conformational transition.

The large variability of contour lengths within the same sample for DNA deposited using cations showed important systematic heterogeneity. Based on this, trying to measure the conformation or molecular substructure locally on just a couple of molecules would not yield a relevant conclusion concerning the overall conformation of all the DNA molecules within the sample. We also observed a significant difference between the conformation of DNA deposited using different cations:  $Mn^{2+}$ -deposited DNA had its contour length distribution closer to the silane deposited molecules than to the one of  $Mg^{2+}$ -bound DNA. We attribute this to the stronger DNA-surface binding with  $Mn^{2+}$  with respect to  $Mg^{2+}$  (95), which makes conformation changes more difficult.

We performed AFM experiments on three different DNA molecules, whose main difference was their number of base-pairs and different nucleobase content (DNA fragments used in the experiments had 251 bp, 500bp and 845 bp). Sequences of base pairs were different and randomly chosen. We observed that the longer the DNA molecule, the lesser the percentage of DNA's base pairs whose conformation changed upon drying. However, the total length of DNA that would change conformation remained approximately constant. For example, for  $Mn^{2+}$ -deposited DNA, both 500 bp and 251 bp samples were  $\sim 11$  nm shorter than the contour length that was expected for the B-conformation. In view of this finding we tested the hypothesis that the transition from B- to A-form was initiated at the two ends of the DNA molecule. By using TERS measurements, as well as by comparing the contour lengths of nicked DNA with its non-nicked counterpart, we found that the conformational transition was significantly higher at the free ends of DNA rather than in the center of it. These experiments indicated that the conformational changes originated at the loosely bound DNA ends or regions of nicked sites.

Finally, we observed that the time during which the DNA was left to equilibrate on the surface in cation-containing solution prior to drying was an important parameter. The longer the equilibration time prior to drying, the more pronounced was the B-to-A conformational transition. The effect of equilibration time on the contour length appeared more important at short times (less than 20 minutes), but tended towards a threshold after that.



In order to observe the effect of contour-length shortening in the experiments we used very short molecules (251 bp), much shorter ones than many previous studies on this subject, where the ratio of contour-length shortening to the total length was much more important. We also minimized the pixel-size errors by always using highly resolved images with approximately 1 nm<sup>2</sup> per pixel resolution. In some of the previous contour length studies the pixel size was up to 16 nm<sup>2</sup> (59), easily making it impossible to make the same observations as ours. Finally, we compared the same samples deposited in three different ways, but measured in the exact same manner, thus eliminating any measurement or sample preparation differences that might have occurred when different studies by different authors are compared.

Our evidence of a partial B- to-A form DNA conformational transition was initially based on DNA length changes measured by AFM. We wanted to confirm these measurements by using an independent technique, namely Tip-Enhanced Raman Spectroscopy (TERS). Not only did TERS experiments confirm conformational changes, but they also allowed us to see that the B-to-A conformation change was more probable at the ends of the linear molecules, while their central parts remained in the B-DNA conformation. This further explained the differences observed on DNA molecules of different lengths where the same sample preparation resulted in different percentages of nucleobases that were re-organized from physiological B- to dehydrated A-conformation. For example, short 251 bp DNA molecules on average had over 70% of their base pairs re-organized into the A-form helix, and this percentage fell to 40% for the longer 500 bp DNA for Mg<sup>2+</sup> deposited DNA.

In conclusion, our study offers a detailed insight into various factors to be taken into account when DNA sub-molecular conformation and structure are important. This work is relevant for the use of DNA in nanotechnology, for example for DNA-based nano-templating (103) where DNA is deposited on a surface and often dried for its final application. The nanometer precision that is sought in such templating would be entirely compromised if DNA changes its conformation upon drying. This study might also shed light on the large contradictory data concerning the electrical properties of DNA, where the B-conformation was generally assumed, but rarely properly assessed (116-118)

For the first time we have combined high resolution AFM and TERS experiments to show that a DNA undergoes partial conformational transition upon cation mediated deposition and drying on a surface, which results in the substantial shortening of DNA and is more pronounced for short (hundreds of base pairs) molecules with respect to longer ones (thousands of base pairs). We also show that the physiological B-form DNA's structure is preserved upon drying when DNA is strongly bound to a silanized surface.

## 2.2 Conformational properties of DNA inside narrow slits

*This chapter is based on a paper in preparation with the following authors:*

Aleksandre Japaridze<sup>1</sup>, Cristian Micheletti<sup>2</sup>, Enzo Orlandini<sup>3</sup>, Kathleen Smith<sup>1</sup>, Francesco Valle<sup>4</sup> and Giovanni Dietler<sup>1</sup>

1 - Laboratory of Physics of Living Matter, EPFL, 1015 Lausanne, Switzerland

2 - SISSA - Scuola Internazionale Superiore di Studi Avanzati and CNR-IOM Democritos, Trieste, Italy

3 - Dipartimento di Fisica e Astronomia and Sezione INFN, Università di Padova, Padova, Italy

4 - Consiglio Nazionale delle Ricerche (CNR), Istituto per lo Studio dei Materiali Nanostrutturati (ISMN), Bologna 40129, Italy

### **Abstract**

We have used well characterized slits of different sizes to collect high resolution atomic force microscopy images of confined linear and circular DNA with the aim to assess the impact of the spatial confinement on their statistical equilibrium properties.

Our findings, supported by numerical simulations, indicate that confinement imposes a large stress on the DNA evidenced by a pronounced anisotropy and tangent-tangent correlation function in respect to non-constrained DNA. For the strongest confinement we observed hairpins associated with the nicked sites. Based on these findings, we propose that spatial DNA confinement in vivo can promote the formation of localized defects at mechanically weak sites that could be co-opted for biological regulatory functions.

## 2.2.1 Introduction

Characterizing the properties of DNA in spatial confinement is one of the open challenges for both, theory and experiments (34,119-129). The increasing interest for such problem arises because of its relevance for all living organisms, whose genetic material is always subject to a high degree of compaction. It is also important because of several of its practical implications in nano-manipulation contexts, based on nanoslits (130-132) and nanochannels (122,124,128,129,133,). These confinement devices open new perspectives for harnessing the physical behaviour of confined DNA in various setups (e.g. microfluidics) for sorting molecules according to their length and topology (134) and even for barcoding profiling (135). One standing challenge is how to measure in detail the effect of spatial confinement on DNA conformational properties. Almost all available probing techniques are based on optical measurements (119-124), where the lack of direct interaction with the molecule implies that one can access only overall and low resolution shape properties (such as the molecular extension or the presence of defects).

Here we present a novel experimental method for studying DNA under quasi-two-dimensional confinement. We combine the capability of atomic force microscopy (AFM) to provide high-resolution images with a microfluidics device of a very well defined geometry and dimension. We studied  $\mu\text{m}$ -long linear and circular DNA (0.5kb up to 5.4 kb) translocated inside our system - an array of rectangular channels, of tuneable height and width, resting on a mica surface. After the confined, DNA adhered to the mica and hence experienced the effects of quasi-two-dimensional slit-like confinement, the slits were then removed and the surface imaged by AFM (schematically represented on Figure 2.2.3). The approach was complementary to the ones previously used (69,139), in that the AFM probes offered an unprecedented resolution of individual DNA conformations. The main disadvantage of the technique though, was the fact that AFM measurements could only be taken after the confining matrix was removed (277).

There were clear differences between our experimental procedure and previously used ones. There was no need for using either an external electrical field (124,132,133), or a pressurized flow cell to “pull” the DNA inside the slits. DNA translocation was fully based on the Laplace pressure and the DNA diffusion inside the hydrophilic PDMS slits. The most important difference though was the possibility to study non-stained DNA in the experiments. DNA properties such as the contour length and the persistence length can be significantly changed upon binding of various fluorescent Dyes (136-138). Therefore using non-stained DNA for experimental purposes was vital to understand the properties of real DNA in confinement.

In order to characterize the conformational properties of DNA under confinement, various metric observables were profiled, including the complete tangent-tangent correlation function, and the chain asphericity. The measurements for DNA inside large slits closely followed the behaviour expected theoretically for equivalent model chains in equilibrium on an attractive surface in the presence of mild lateral confinement. This clarified that the considered experimental setup offered a practical means of realizing quasi-two-dimensional confinement in equilibrium and could be exploited for practical purposes.

For narrower slits, however, the accord with theoretical expectations was systematically degraded by the fact that the chains had a larger anisotropy than expected. The detailed analysis of the conformations revealed that these deviations were due to the occurrence of relatively extended defects in the form of hairpins and extended regions of interwound segments, which could involve up to 10% of the chain length. These differences were not observed for giant slits where the same experimental protocol was used. We therefore speculate that these defects reflect genuine properties of confined DNA, possibly due to nicked sites, that have not been reported so far.

## 2.2.2 Materials and Methods

### Linear 0.5 kb DNA

500 base pairs DNA was prepared using the 100bp DNA Ladder marker purchased from Promega (Switzerland). The 500 bp band was extracted from 1.5% agarose gel and purified using extraction kit from Promega. DNA was then placed in the TE buffer.

### Circular DNA

2.7kb (pUC19 2686 bp); 4.4kb (pBR322 4361 bp); 5.4kb (F<sub>x</sub>174 5386 bp) supercoiled plasmid DNA were purchased from Fermentas (Switzerland) and nicked using Nt.BstNBI nicking enzyme (NEB). Nicked plasmids were further extracted from 1.5% agarose gel and purified using extraction kit from Promega. DNA was then placed in TE buffer composed of 10 mM Tris and 1 mM EDTA solution.

### Master Fabrication

The masters used in the present work were fabricated following two different procedures according to the lateral size of the features. The large slits master was fabricated by contact photolithography with a Mask Aligner Karl Suss MJB40 ( $\lambda=365$  nm). High contrast masks were obtained by engraving a thin aluminium layer using an IR-laser printer (ScribaR, Scriba Nanotecnologie srl.). The exposure interval was adjusted to match the contrast of the mask. Negative photoresist SU8 (All Resist, CITY, COUNTRY), was spin coated at 2000 RPM on flat polycarbonate substrate (surface roughness < 10 nm), resulting in a film of 5  $\mu$ m thickness. After alignment and exposure, the master was dipped in the resist developer for 1 min to develop it and postbaked at 150° C for 30 minutes to enhance crosslinking of photoresist. During postbaking, the section of the channel becomes round shaped. This curvature improves the peel-off of the mold in replica molding. The patterned areas were always in the range of 5 mm x 5 mm.

The small slits master, consisting of an array of parallel slits whose width and height are 1  $\mu$ m and 230 $\pm$ 15 nm, respectively, and a 1.4  $\mu$ m pitch, was obtained from the polycarbonate portion of a commercially

available CD-Rom. The metallic part was peeled off using scotch tape and the underlying polycarbonate was rinsed with ethanol to remove the chemicals present on its surface.

## Replica Molding

The microfluidics devices used to laterally confine the DNA molecules during the deposition process were fabricated by replica molding of the suitably realized masters. Polydimethylsiloxane (Sylgard 184) and its curing agent were mixed in ratio 10:1, degassed and poured on top of the polycarbonate/SU8 master. Curing was performed at 80° C for 8 hours, in a standard thermostatic oven. After peel-off, the PDMS replicas were rinsed and stored in deionised water.

## PDMS slits

PDMS slits used in the experiments had a rectangular shape (Figure 2.2.1). In order to clean the PDMS slits and make the surface hydrophilic, before every experiment the slits were treated with a plasma stream (a low intensity plasma stream at 500m Tor.) which decreased the height with time. One minute plasma treatment was resulting in slits with  $\sim 140 \pm 10\text{nm}$  height. Increasing the plasma exposure up to 7min would result in slits of  $\sim 55 \pm 10\text{nm}$  in height (Figure 2.2.2). The width of the slits was not affected by the plasma treatment. Straight after plasma treatment the slits were placed and gently pressed with a Teflon clamp on a freshly cleaved mica surface.

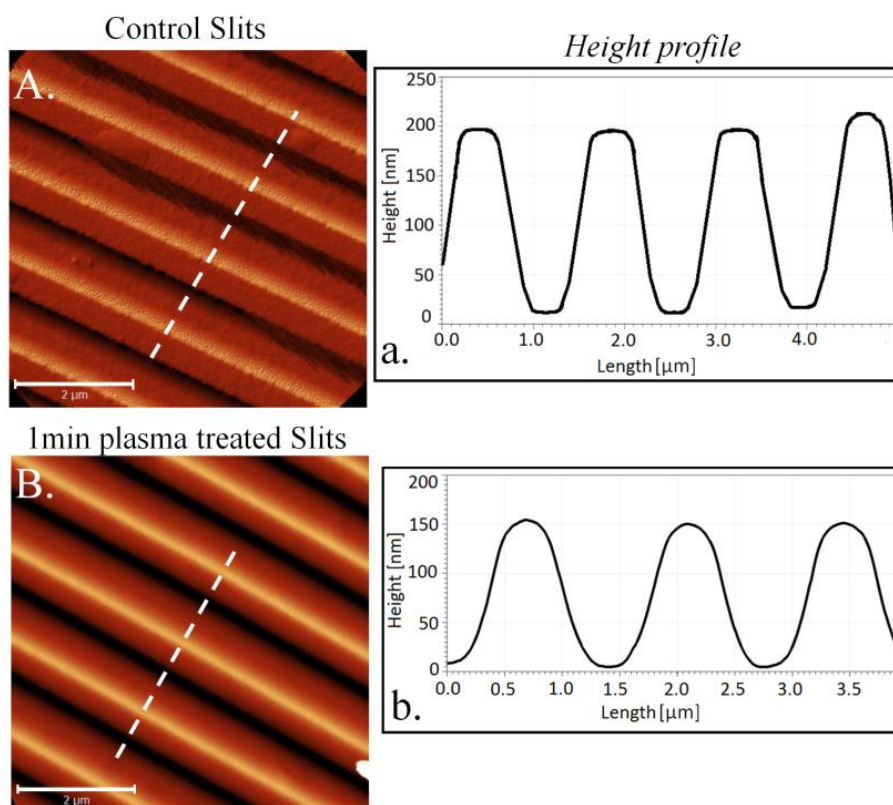


**Figure 2.2.1:** AFM images of **A)** Untreated small slits and **B)** One minute plasma treated small slits. **a) b)** Corresponding height cross-section along the white dotted line on **A)** and **B)**. Scale bars 2 μm

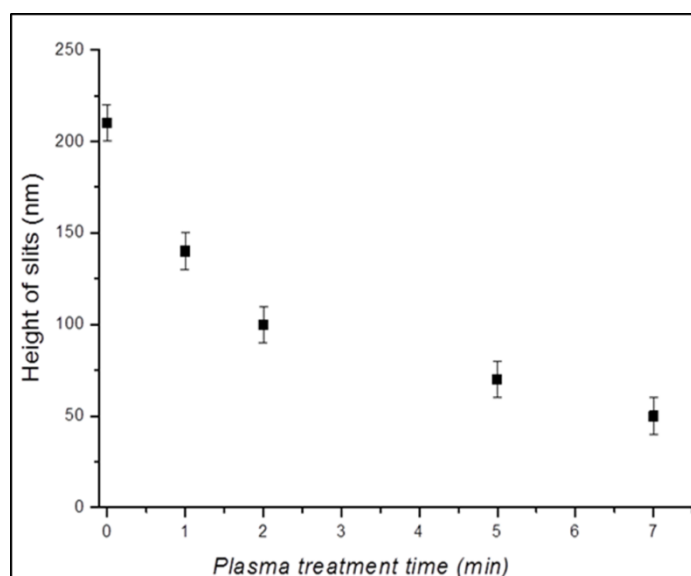


**Figure 2.2.2:** The slit height decrease as the function of plasma treatment time

PDMS slits used in our experiments had the following dimensions:

**Table 2.2.1:** Slit dimensions

Slits after 1min Plasma treatment		
	Small Slits	Giant Slits
<b>Height</b>	140 nm	1,5 $\mu\text{m}$
<b>Width</b>	600 nm	10 $\mu\text{m}$
<b>Separation</b>	600 nm	15 $\mu\text{m}$

### Sample preparation

A 10 $\mu\text{L}$  aliquot containing DNA (typical concentration 0.5–1.5 ng/ $\mu\text{l}$ ) and 1.5mM MgCl<sub>2</sub> final concentration was deposited on one side of the slits on a freshly cleaved mica surface. The sample was then incubated in a warm moist environment for 30 minutes, letting the DNA diffuse into the slits. Afterwards the slits were gently removed, the surface gently rinsed twice with 1ml Milli-Q water (18.2 M $\Omega$ .cm resistivity) and then blow-dried.

### AFM

AFM images were collected using a MultiMode SPM with a Nanoscope III controller (Veeco Instruments, Santa Barbara, CA, USA) operated in tapping-mode in air. The AFM cantilevers used in air had a spring constant of 5 N m<sup>-1</sup> (Veeco cantilevers, TAP150A) with resonance frequencies ranging between 120 and 160 kHz. All the recorded AFM images consist of 512 x 512 pixels with scan frequency  $\leq 1$  Hz. Images were simply flattened using the Gwyddion software (Version 2.25) and no further image processing was carried out (105).

## Statistical Analysis

**Persistence length:** We measured the persistence length  $l_p$  of DNA using the bond correlation function for polymers in 2D (since the DNA adsorbed on the mica surface adopts a 2D conformation):

$$\langle \cos(\theta) \rangle = e^{(-s/2 \cdot l_p)} \quad (2.2.1)$$

where  $\theta$  is the angle between the tangent vectors to the chain at two points separated by the distance  $s$  and  $l_p$  the persistence length (36).

## Anisotropy and Asphericity

Typical shape measurements for circular DNA included the anisotropy  $\Sigma$  and the asphericity  $A_2$ , which are defined as the combinations of the small ( $R_{g1}$ ) and large ( $R_{g2}$ ) principal axes of the radius of gyration tensor  $R_g$  (278).

$$\Sigma = \langle R_{g1}^2 / R_{g2}^2 \rangle \quad (2.2.2)$$

$$A_2 = \langle (R_{g1}^2 - R_{g2}^2)^2 / (R_{g1}^2 + R_{g2}^2)^2 \rangle \quad (2.2.3)$$

## DNA Analysis software and procedures

DNA molecules (typically 40 to 50 individual molecules) were analyzed using “DNA Trace”, Java-based analysis software that has been described elsewhere (106).

## Computational methods: The model

Circular DNA molecules confined within slits, described by two walls placed respectively at  $z = 0$  (bottom) and  $z = H$  (top), are modelled as semiflexible self-avoiding rings of  $N$  spherical beads of diameter  $\sigma$ . To take into account the connectivity, self-avoidance and bending energy of the chain we consider respectively the three potential energies  $U_{FENE}$ ,  $U_L$ ,  $U_{bend}$  whose explicit parametrization are given by:

$$U_{FENE} = - \sum_i^{N-1} 15\epsilon \left( \frac{R_0}{\sigma} \right)^2 \ln \left[ 1 - \left( \frac{d_{i,i+1}}{R_0} \right)^2 \right]$$

$$U_{bend} = \sum_{i=2}^{N-1} \epsilon \left( \frac{l_p}{\sigma} \right) \cdot \left( 1 - \frac{\vec{b}_{i-1} \cdot \vec{b}_i}{|\vec{b}_{i-1}| |\vec{b}_i|} \right)$$

$$U_L = \sum_{i,j>i}^N 4\epsilon \left[ \left( \frac{\sigma}{d_{i,j}} \right)^{12} - \left( \frac{\sigma}{d_{i,j}} \right)^6 + \frac{1}{4} \right] \cdot \theta(2^{1/6} \sigma - d_{i,j})$$

where  $\vec{b}_i \equiv \vec{r}_{i+1} - \vec{r}_i$  is the  $i$ th chain bond,  $d_{i,j} = |\vec{r}_i - \vec{r}_j|$  is the distance of the bead centers  $i$  and  $j$ ,  $R_0 = 1.5\sigma$  is the maximum bond length and  $\epsilon$ , the characteristic unit of energy of the system is set equal to the thermal energy,  $k_B T$ . Finally,  $\theta$  is the Heaviside function. In order to enforce the steric hindrance with the

top wall of the slit placed at height  $H$ , we add the shifted Lennard-Jones (hence purely repulsive) potential energy

$$U_{wall}^{top} = \sum_i^N 4\epsilon \left[ \left( \frac{\sigma}{\delta_i} \right)^{12} - \left( \frac{\sigma}{\delta_i} \right)^6 + \frac{1}{4} \right] \cdot \theta(2^{1/6}\sigma - \delta_i)$$

where  $\delta_i \equiv \frac{D}{2} - \Delta_i$  and  $\Delta_i$  is the distance of the  $i$ th bead from the top wall. Finally, to mimic attraction on the bottom wall we add a full Lennard-Jones potential (i.e. repulsive at very short distance and attractive at long distances)

$$U_{wall}^{bottom} = \sum_i^N 4\epsilon_a \left[ \left( \frac{\sigma}{r_i} \right)^{12} - \left( \frac{\sigma}{r_i} \right)^6 \right] \cdot \theta(1.5\sigma - r_i)$$

where  $r_i$  is the distance of the  $i$ -esim bead from the bottom wall.

The system is parametrised after DNA (assuming complete screening of its electrostatic charge as appropriate for solutions with sufficiently high ionic strength and neglecting hydrodynamic interactions) and hence set  $\sigma = 5.0\text{nm}$ , with either  $lp = 50\text{nm}$  or  $lp = 60\text{nm}$ .

The system dynamics is described within a Langevin scheme:

$$m\ddot{\vec{r}}_i = -\gamma\dot{\vec{r}}_i - \nabla U + \vec{\eta}$$

where  $\gamma$  is the friction coefficient and  $\eta$  is the stochastic delta-correlated noise. The variance of each Cartesian component of the noise,  $\sigma_\eta^2$  satisfies the usual fluctuation dissipation relationship  $\sigma_\eta^2 = 2\gamma k_B T$

As customary, we set  $m/\gamma = 2\tau_{LJ}$ , with  $\tau_{LJ} = \sigma\sqrt{m/\epsilon} = \sigma\sqrt{m/k_B T}$  being the characteristic simulation time. From the Stokes friction coefficient of spherical beads of diameters  $\sigma$  we have:  $\gamma = 3\pi\eta_{sol}\sigma$  where  $\eta$  is the solution viscosity. By using the nominal water viscosity,  $\eta_{sol} = 1\text{cP}$  at all channels widths and setting  $T=300\text{K}$  and  $\sigma = 5.0\text{nm}$ , one has  $\tau_{LJ} = 6\pi\eta_{sol}\sigma^3 / \epsilon \sim 600\text{ns}$ .

The Langevin equation is integrated numerically with the LAMMPS simulation package with an integration time step of  $0.01\tau_{LJ} \sim 0.8\text{ns}$ . The starting point of the various simulations is a perfect circular configuration lying on the bottom wall. To allow the equilibration of the system from this initial state, the first  $2 \cdot 10^6$  integration time steps are disregarded from the analysis of any observables. All relevant observables are calculated on snapshots of the systems taken every  $10^5$  integration time steps.



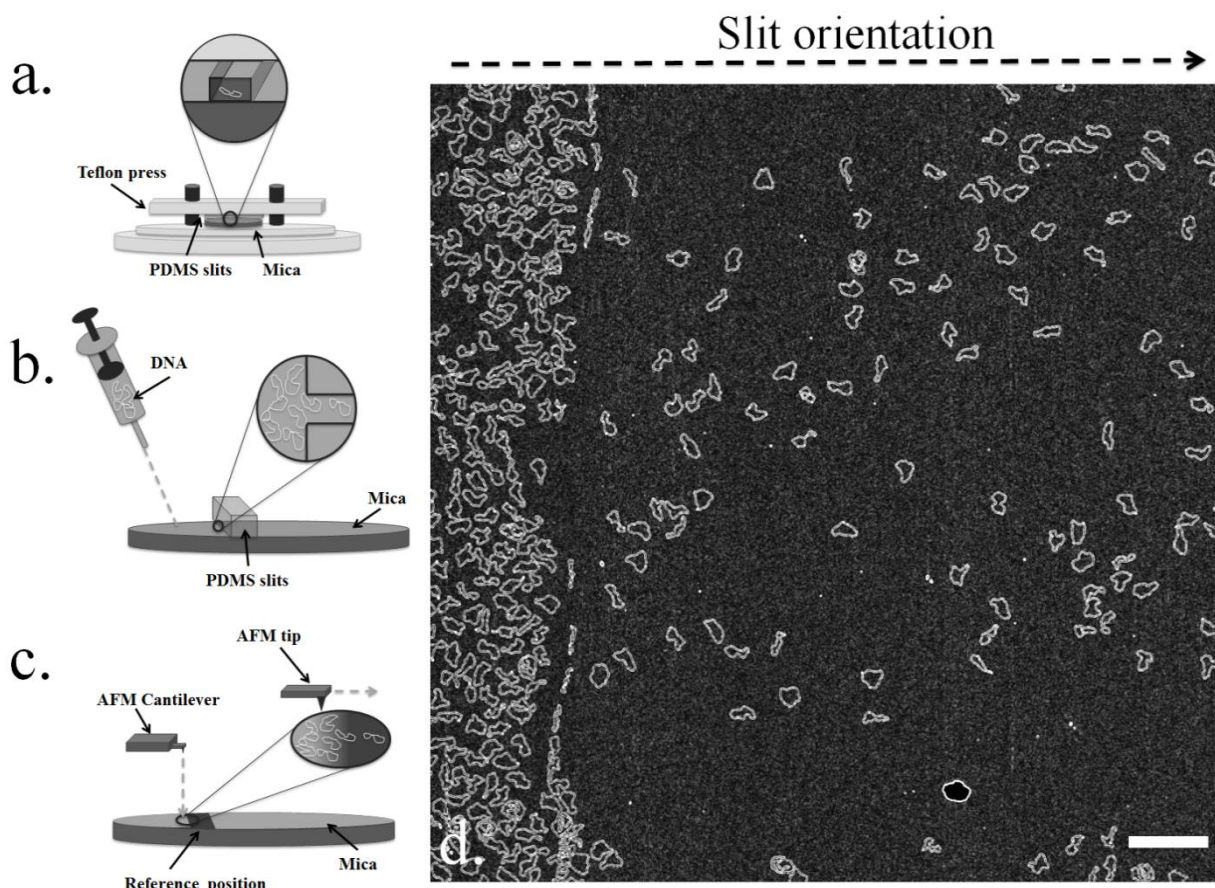


**Figure 2.2.3:** Different steps of sample preparation. Schematic representation of: **a)** the Teflon clamp where the plasma treated slits are gently pressed on the surface of the mica **b)** the sample deposition and the zoomed image showing the translocation of circular DNA inside the slits **c)** an AFM tip scanning the mica surface **d)** a typical AFM image showing circular 2.7kb DNA migrating into giant slits. The orientation of the slit is indicated by the dashed arrow. Scale bar 1 $\mu$ m

## 2.2.3 Results

In this work we present a novel experimental method for studying DNA under mild quasi-two dimensional confinement. The whole experimental procedure consists of several steps: treatment of PDMS slits with plasma stream (to make them hydrophilic), their deposition on a mica surface, DNA diffusion inside them, DNA adsorption on mica surface and finally AFM imaging (Figure 2.2.3).

We used two kinds of slits, with very different dimensions. The small slits had width of  $\sim 600$ nm (Figure 2.2.1) and the giant slits of 10  $\mu$ m (see Materials and Methods section). In order for the slits to exert confinement on the molecules, the free radius of gyration should be of the same order of size as the confinement dimensions of the slits ( $\text{max}R_g \sim \text{confinement dimension}$ ). Therefore the giant slits (width of 10  $\mu$ m) should not have exerted any confinement on even the biggest DNA used in our experiments (5.4kb circular DNA). The experiments performed with giant slits served as control measurements, making sure no artefacts were arising from experimental steps influencing the shape parameters of DNA molecules (experimental steps such as capillary drag, removing of slits, rinsing and drying the surface). First we

performed experiments with circular DNA of various sizes, in order to study metric properties in the confinement. The circularity of objects was chosen on purpose since all forms of prokaryotic organisms contain circular DNA, rather than its linear form (140,141). In the second part of the experiments we studied dynamical properties of DNA with various topologies, by comparing the migration of linear and circular DNA inside the slits.

### 2.2.3.1 Metric properties of circular DNA in confinement

#### 2.7kb DNA

Our first experiments were performed on 2.7kb nicked circular DNA, trapped inside giant and small slits. We measured different shape parameters, such as the persistence length, a parameter describing flexibility of polymers (34) and the Anisotropy of molecules. We calculated the DNA persistence length directly from the bond correlation function and checked if the confinement had any influence on it.

As expected for the smallest 2.7kb DNA, the statistical parameters outside and inside the slits did not differ (in order for the 2.7kb DNA to experience any confinement, the free radius of gyration had to be of the same order of length, as the confinement width) (Figure 2.2.4). The 2D measured radius of gyration for 2.7kb DNA was  $R_{g2.7kb}=110 \pm 10\text{nm}$ , whereas all dimensions of slits were much larger. These results showed that the molecules could diffuse and relax freely inside the slits, feeling no confinement. Even the smallest slits with nominal width of 600nm were too large for DNA to experience any confinement (Figure 2.2.5). The persistence length for 2.7kb circular DNA outside the slits was  $\sim 50\text{nm}$  (Table 2.2.2), perfectly agreeing with the expected value (69,139). These results suggested that, there was no confinement effect of 600 nm as well as 10  $\mu\text{m}$  slits on 2.7kb DNA. Circular DNA could freely diffuse inside slits and adopt a relaxed 2D conformation (Figure 2.2.4).

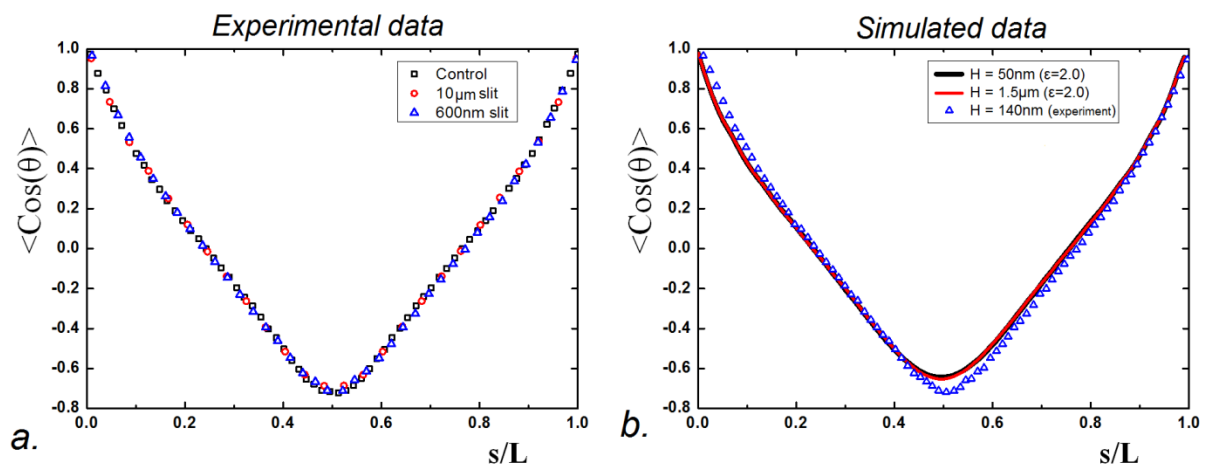


**Figure 2.2.4:** Correlation functions for 2.7kb circular DNA: experimental data (left) and simulations data (right). Simulations data confirmed that both 50nm and 1.5 $\mu\text{m}$  height slits would not influence the shape of the 2.7kb rings. Once DNA is bound to the surface, only the width of the slits influences its morphology.

## 5.4kb DNA

The results changed once we used longer 5.4kb circular DNA in our experiments with  $R_{g,4.4kb}=190 \pm 10\text{nm}$ . We observed a change in the global shape of the molecules as well as a higher value for the persistence length of translocated DNA molecules. The morphology of the DNA, based on AFM images, was clearly influenced as well (Figure 2.2.5 and Figure 2.2.6). The molecules inside small slits adopted much more elongated shapes compared to the ones experiencing no confinement (control DNA and inside giant slits) indicating spatial confinement by the slits. We measured the asphericity ( $A_2$ ) for circular DNA. The closer the value of Asphericity to 0 the more circular the object is, whereas  $A_2=1$  means the object is linear. For 5.4kb circular DNA, the value changed from  $A_{\text{cont}}=0.27\pm 0.03$  to  $A_{600\text{nm}}=0.34\pm 0.03$ , where  $A_{\text{cont}}$  is the Anisotropy for control 5.4kb DNA and  $A_{600\text{nm}}$  Anisotropy for 5.4kb DNA confined inside 600nm slits.

The shape of the correlation function for molecules inside small slits (Figure 2.2.7a) changed too. Once the DNA migrated inside the slits, the initial part of the correlation function, decayed much slower, indicating longer correlated DNA segments, leading to higher persistence length. The minima of the correlation function was also much lower, compared to the correlation function of non-confined DNA (Figure 2.2.7a), all indicating a change in the global shape of the confined DNA.

The value of the apparent persistence length of DNA was strongly affected by the confinement. The initial value of  $\sim 60\text{nm}$  increased by as much as  $\sim 16\%$ , reaching the value  $\sim 70\text{nm}$  (Table 2.2.2). Our measurements suggest that 5.4kb circular DNA experienced mild lateral confinement once translocated inside small 600nm slits but not inside giant  $10\ \mu\text{m}$  slits.

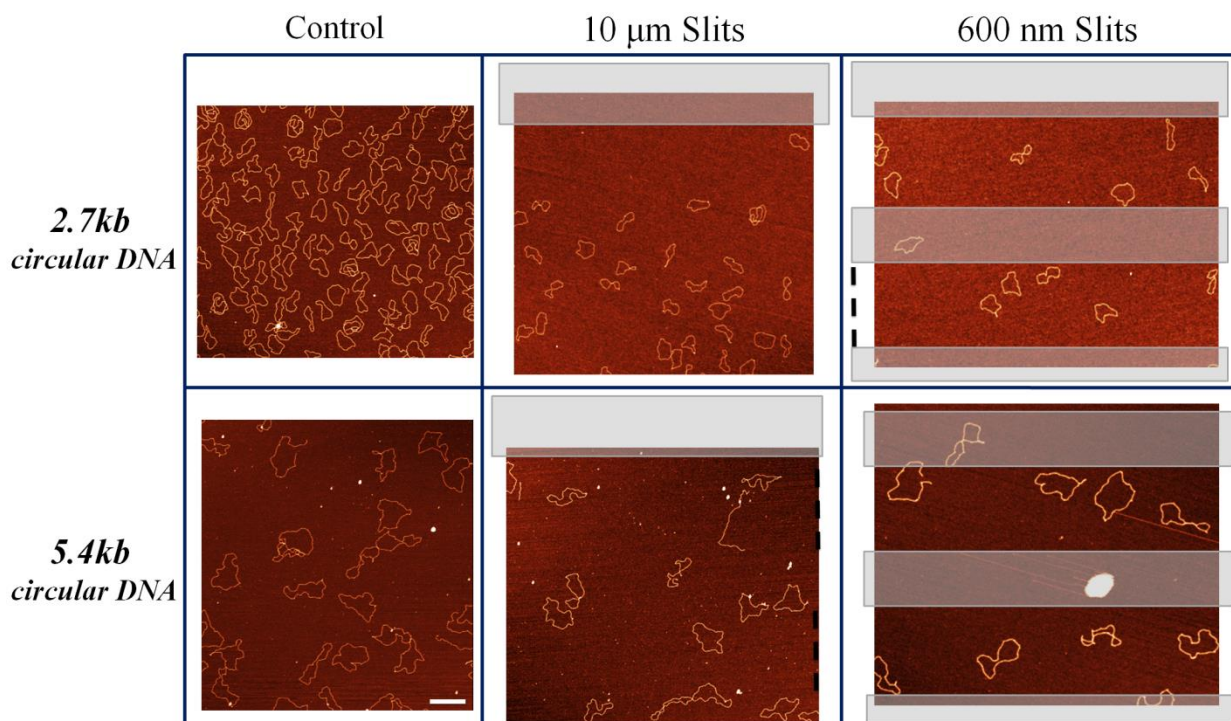


**Figure 2.2.5:** Large scale AFM images of 2 types of circular DNA (2.7kb and 5.4kb) versus slit size. Left column shows control measurements; middle column shows DNA inside  $10\ \mu\text{m}$  giant slits; right column shows DNA inside 600nm small slits. Transparent rectangles represent hypothetical places where the slits were placed. DNA molecules that are under the theoretical slits are not included in the statistics. Scale bars 500nm.

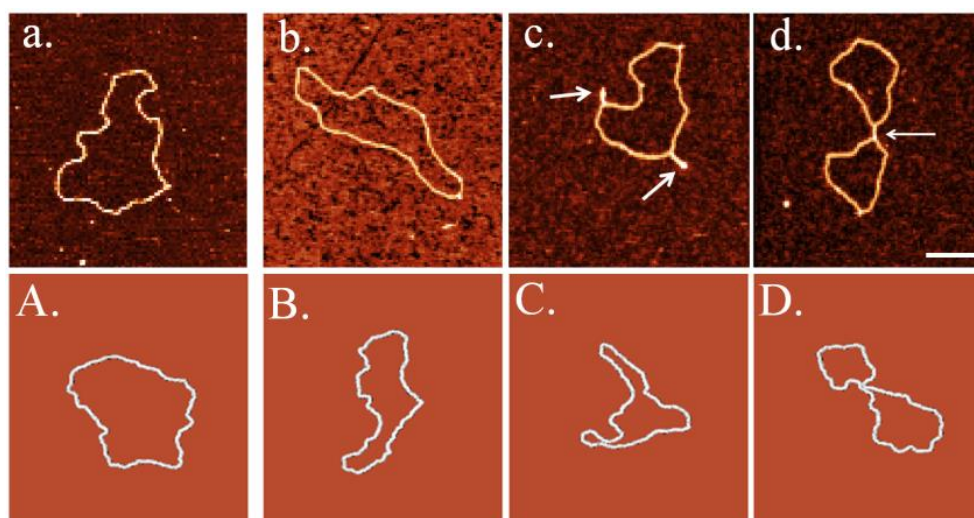


**Figure 2.2.6:** Snapshots of 5.4kb DNA in experiment and simulations: **a) A)** Control **b) B)** Elongated **c) C)** Hairpins (indicated by white arrows) **d) D)** Interwound (indicated by white arrow). Scale bars 100nm.

### 2.2.3.2 Computer simulations

To better understand the experimental results we have performed computer simulations on DNA rings of 2.7kb and 5.4kb sizes inside slits of various dimensions. Computer simulations helped us to investigate the role of the slit width and height on DNA morphology.

Simulations performed on 2.7kb rings showed that the adsorption process of DNA in our experiments could be well described by an equilibrium process deep in the adsorbed phase (Figure 2.2.4). Once DNA was bound to the surface, it was perfectly relaxing in two dimensions reaching equilibrium, with the height of the DNA not affecting the DNA configurations. The only parameter that affected the DNA shape parameters was the width of the channels. If the dimensions of the DNA were comparable to the width of the slits, than we could observe the effects of confinement on single molecules.

In Figure 2.2.7b we compared the experimental data of the bond-bond correlation function obtained for 5.4kb DNA rings confined in giant (black circles) and small ( $w = 600\text{nm}$  red squares) slits with the corresponding (i.e. green curve and blue curve) numerical simulation (chains of persistence length  $l_p = 60\text{nm}$  have been simulated). The good agreement between simulations and experimental data was clear. Interestingly, in order to have the best agreement between the experimental and simulated curves for molecules confined inside small slits, we had to select those conformations of rings which had a higher anisotropy. In particular the set of DNA configurations with anisotropy  $A_2 \geq 0.5$ , gave the best agreement with the experimental data (Figure 2.2.7b blue curve).

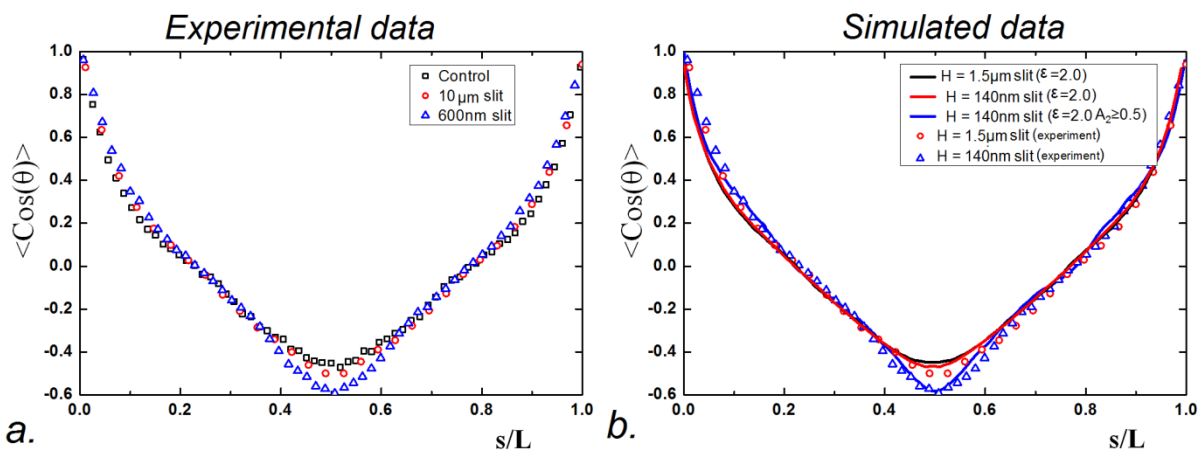


**Figure 2.2.7: a)** Experimentally measured bond correlation function of 5.4 kb circular DNA for control (black squares), Inside giant slits (red spheres) and inside small slits (blue triangles). **b)** Experimental vs calculated bond correlation function for 5.4 kb circular DNA. Here we show the effect of  $A_2$  on the bond-bond correlation function for chains in small slits. As the bond-bond correlation function is computed for more and more anisotropic configurations the minimum becomes more pronounced. In particular if we take the set of configurations with  $A_2 \geq 0.5$ , the agreement with the experimental data is much better.

**Table 2.2.2:** Shape parameters of circular DNA of various sizes

Sample	$N$	$L_{\text{contour}}$ (nm)	$l_p$ (nm)	Anisotropy $\Sigma$	Asphericity $A_2$	Max $R_{g2}$ (nm)	Min $R_{g1}$ (nm)	$\langle R_{g2} \rangle$	$\langle R_{g1} \rangle$	Max $R_g$
<b>2.7 kb circular (<math>R_g = 110 \pm 10 \text{ nm}</math>)</b>										
Control	70	830 $\pm$ 30	52 $\pm$ 2	0.28 $\pm$ 0.02	0.36 $\pm$ 0.02	310	81	278	141	123
Giant Slits (10 $\mu\text{m}$ )	100	840 $\pm$ 30	54 $\pm$ 2	0.33 $\pm$ 0.03	0.30 $\pm$ 0.02	321	98	273	150	124
Small slits (600 nm)	50	820 $\pm$ 20	51 $\pm$ 2	0.33 $\pm$ 0.03	0.32 $\pm$ 0.03	317	84	271	147	121
<b>5.4 kb circular (<math>R_g = 190 \pm 15 \text{ nm}</math>)</b>										
Control	60	1560 $\pm$ 50	63 $\pm$ 2	0.38 $\pm$ 0.03	0.27 $\pm$ 0.03	567	139	449	258	216
Giant Slits (10 $\mu\text{m}$ )	45	1520 $\pm$ 100	64 $\pm$ 2	0.39 $\pm$ 0.03	0.27 $\pm$ 0.03	564	150	434	254	229
Small slits (600 nm)	50	1490 $\pm$ 120	72 $\pm$ 2	0.32 $\pm$ 0.03	0.34 $\pm$ 0.03	595	93	450	235	219

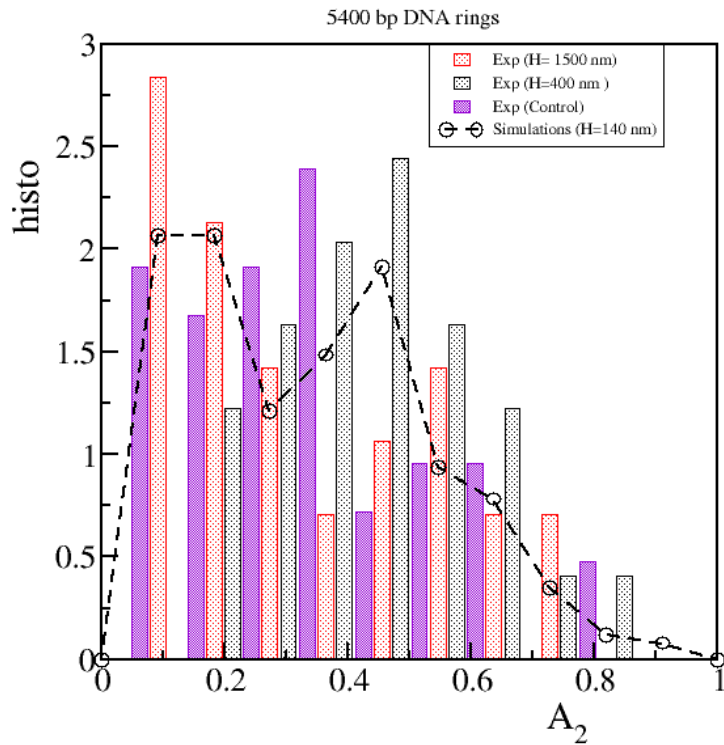


**Figure 2.2.10:** Comparison between anisotropy for 5.4 kb circular DNA inside and outside slit for experiment and simulations.

### 2.2.3.3 Using AFM resolution to investigate DNA structure: DNA hairpins

To understand why according to our experimental results 5.4kb DNA configurations inside small slits were more anisotropic than expected from simulations, we looked closely at the conformations of individual rings. The extremely high resolution of AFM enabled us to observe nanometre length defects in the form of hairpins (Figure 2.2.6c) and interwound structures (Figure 2.2.6d). These structures were clearly influencing the average value of the Anisotropy, resulting in more ‘linear’ conformations (Figure 2.2.10).

First we defined the hairpin ratio: the ratio between the minimal (white dotted line on figure 2.2.11) and the maximal (blue dotted line on figure 2.2.11) arm length between two hairpins along the DNA contour:

$$\text{Hairpin arm ratio} = \frac{l_{\min}}{l_{\max}} \quad (2.2.4)$$

We measured the frequency and the relative position of these hairpins along the circular DNA. Interestingly the position of the hairpins was coinciding with the position of the nicked sites in the 5.4 kb DNA. Nicking of the 5.4kb DNA was resulting nicking at 5 positions. Four of them would be in close proximity (positions 61bp, 294bp, 360bp and 400bp) whereas the fifth nick would be further downstream (at position 3551bp). The smallest arm ratio would be 0.51 while the biggest 0.84.

To make sure, the hairpin position was coinciding with the nicked sites, we took a smaller 4.4kb DNA which had nicked sites at different positions compared to 5.4kb DNA. Nicking in the 4.4kb DNA was resulting in two nicked positions at 640bp and 2853bp with the theoretical arm ratio 0.96.

The position of the hairpins was clearly dependent on the construct used, agreeing well with the theoretically predicted position of the nicked sites (Figure 2.2.12). We also measured the frequency, the length and the height of the hairpins (Figure 2.2.13 and Table 2.2.3). Although, the average length of the hairpins was different for the two constructs ( $45 \pm 20\text{nm}$  for 4.4kb,  $65 \pm 40\text{nm}$  for 5.4kb DNA), the relative DNA length stored in the structures was up to 10% of the DNA contour length (Table 2.2.2). For the smallest 2.7kb DNA, we didn't observe any hairpins, once again indicating no lateral confinement. Based on these findings we propose that spatial DNA confinement can expose localized defects in the DNA (nicked sites in our case), which can play an important biological role (142,143)

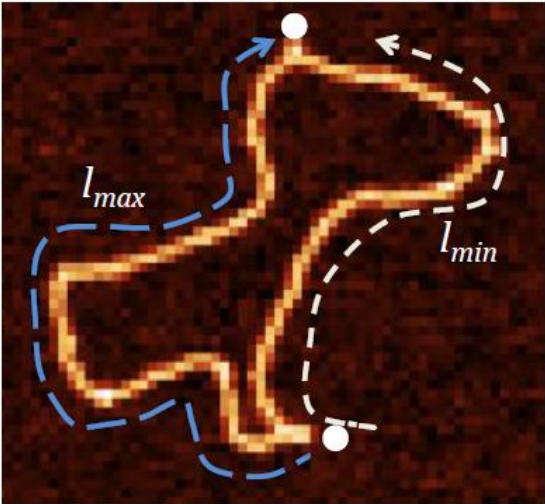


**Figure 2.2.11:** The hairpin arm ratio is calculated by measuring the ratio between the minimal and maximal arm length between the hairpins

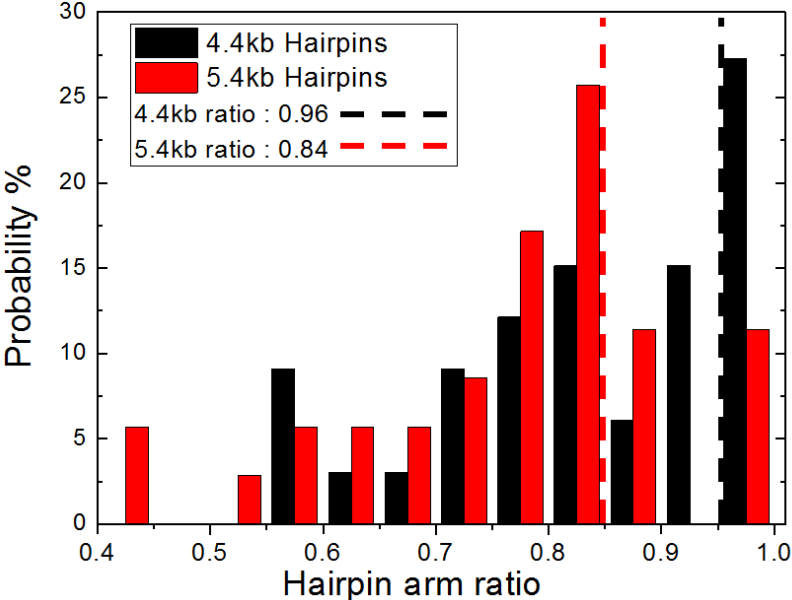


**Figure 2.2.12:** The hairpin arm ratio distribution for 4.4kb (black bars) and 5.5kb (red bars) nicked DNA. Red and black dotted lines represent the theoretical positions of the

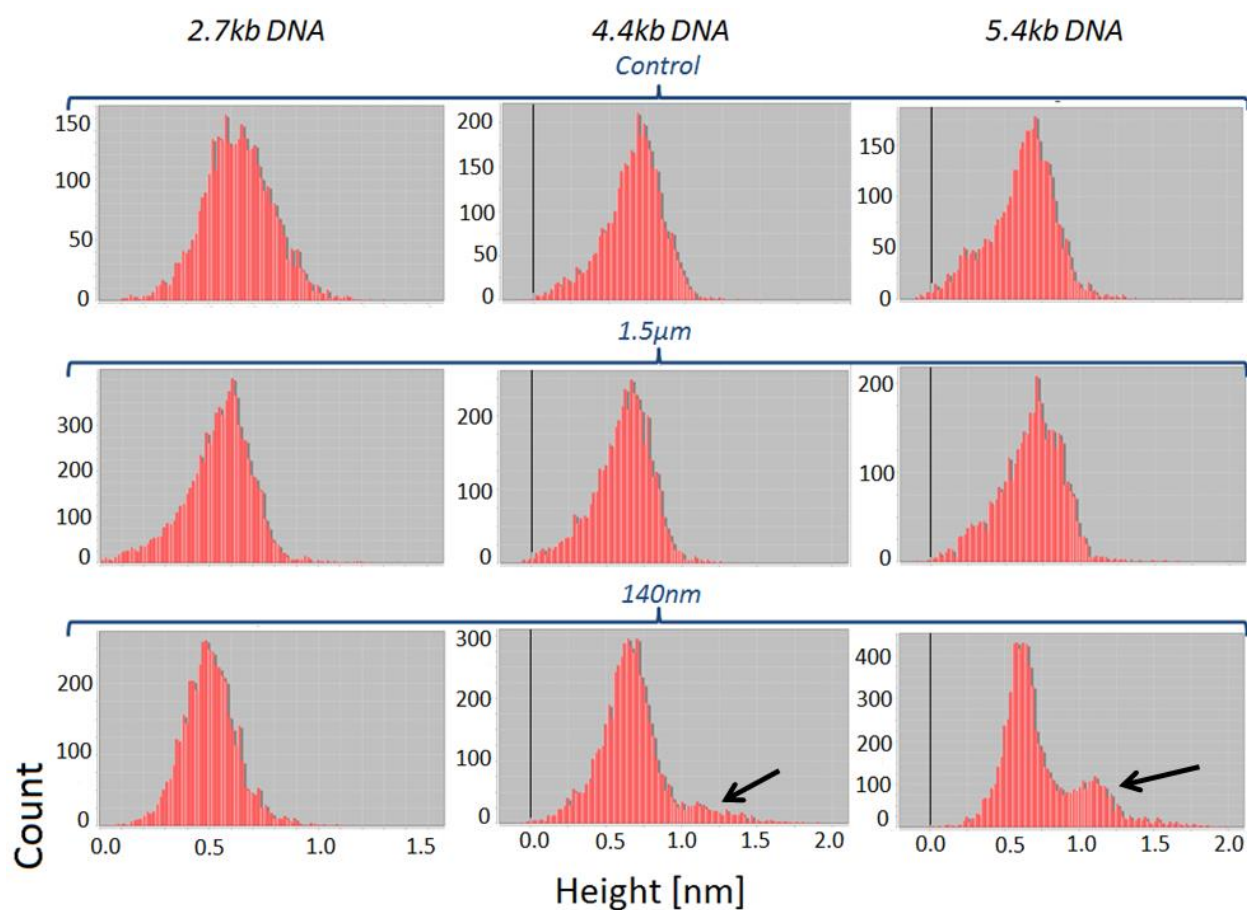


**Figure 2.2.13:** Height distributions along DNA molecules of various sizes inside 600nm and 10µm slits together with the control samples. Black arrows indicate the appearance of a peak at ~1.2nm, corresponding to the height of hairpins present for 4.4kb and 5.4kb DNA trapped inside 600nm slits. This indicates that only for the 4.4kb and 5.4kb DNA trapped inside 600nm, hairpins and intertwined regions of higher height are formed.

**Table 2.2.3:** Characteristics of DNA hairpins formed in 600nm slits

<b>DNA</b>	<b>Hairpin length <math>L_h</math> (nm)</b>	<b>Total DNA stored</b>	<b>Highest theoretical hairpin arm ratio</b>	<b>&lt;Experimental arm ratio&gt;</b>	<b>Hairpin probability</b>
<b>4.4kb</b>	$50 \pm 20$	8%	0.96	0.85	75 %
<b>5.4kb</b>	$65 \pm 40$	9%	0.84	0.77	95 %



### 2.2.3.4 Dynamic properties of DNA in confinement

After studying metric properties of circular DNA, we asked ourselves, whether we could obtain DNA dynamics data with our techniques. To answer this question, we studied the migration of DNA mixes of various sizes and topologies inside the small slits.

When equimolar amounts of 0.5kb linear and 4kb circular DNA were mixed and translocated through the slits, the linear DNA migrated without feeling any confinement (Figure 2.2.14). This was resulting in much quicker diffusion through the slits. Therefore if we would start AFM imaging outside the slits and gradually go towards the place where the slits were, by counting the ratio of the DNA ( $r_{l/c}$  = 0.5kb linear/4kb circular) we should have seen a change. Indeed the initial ratio of linear to circular DNA was  $r_{l/c} \sim 0.9$ , which increased and reached 1.8, once DNA migrated in the slits. This meant that due to difference in the diffusion coefficients, small linear DNA was migrating quicker in the slits, than larger circular ones.

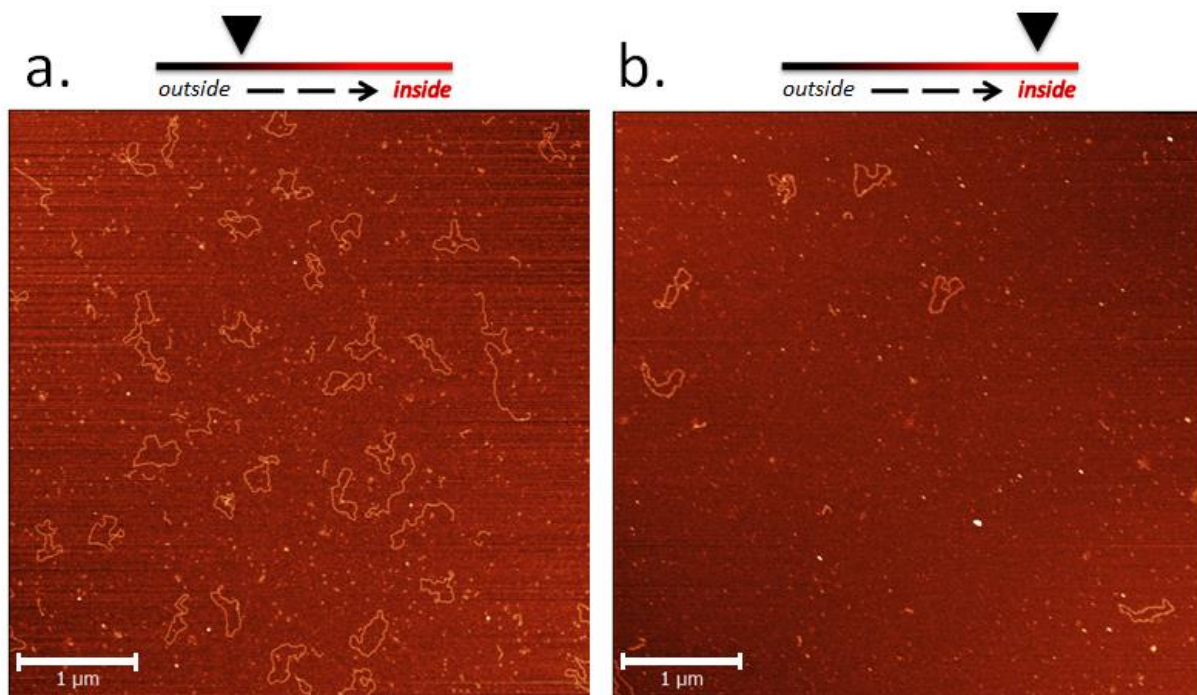


**Figure 2.2.14:** 500bp linear and 4.0 plasmid DNA mix migration inside the slits. **a)** Control and **b)** Inside small slits; with the schematic representation of the position of the image, outside and deep inside the slits. Scale bars 1μm

To further test migration properties of DNA, we imaged a mix of same sized linear and circular DNA of 4.4kb (Figure 2.2.15). The initial ratio of  $r_{l/c} = 2.1$  decreased almost 10 fold and reached  $r_{l/c} = 0.2$  once translocated inside the slits (this ratio was not changing inside large slits).

The slits acted as topological sieves, separating DNA based on its size and also its topology.

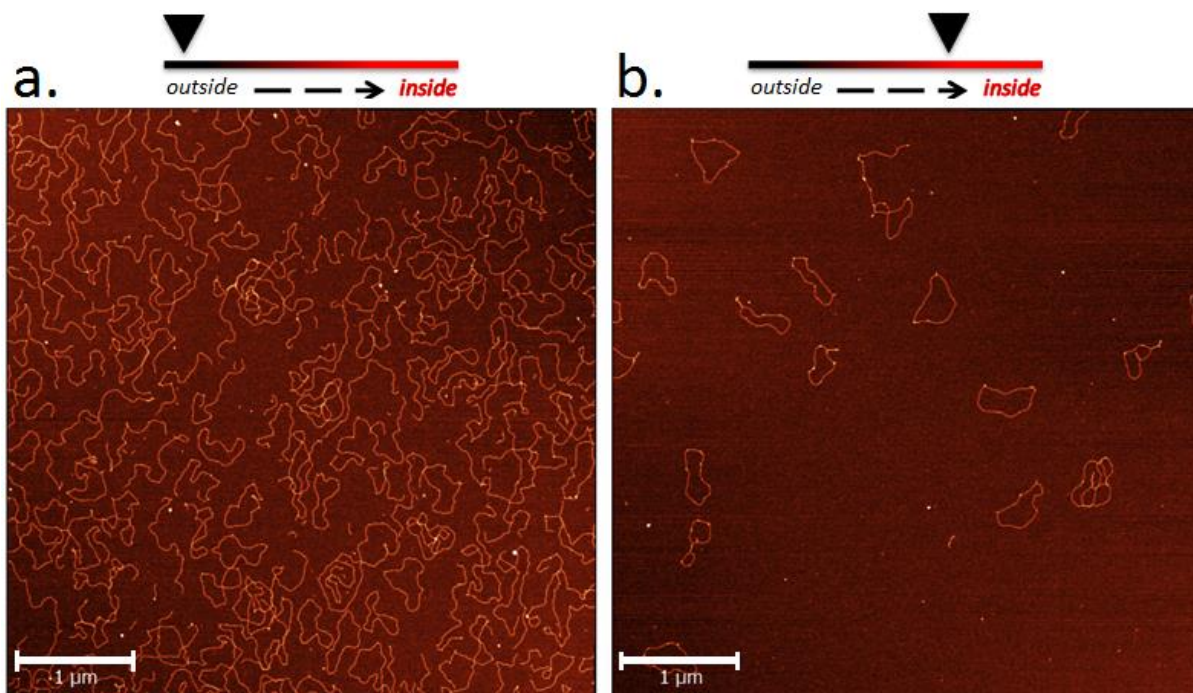


**Figure 2.2.15:** 4.4kb linear and circular DNA mix migration inside the slits. **a)** Control and **b)** Inside small slits; with the schematic representation of the position of the image, outside and deep inside the slits. Scale bars 1 $\mu$ m

## 2.2.4 Conclusions

In this work we described a new experimental method for studying the effects of spatial confinement on statistical properties of DNA. We demonstrated by combining Atomic Force Microscopy with conventional nanofabrication tools, that it is possible to study the properties of confined DNA molecules with nanometre resolution without using any staining dyes. We performed experiments with various sized circular DNA and observed quasi-two dimensional confinement for the 5.4kb DNA rings when translocated inside 600nm slits. The significantly improved resolution enabled us to study statistical parameters such as persistence length and anisotropy of individual circular DNA. Our experimental findings were supported by molecular dynamics simulations, capturing well the change in the bond-bond correlation function and the tendency for DNA rings to have higher Asphericity. Computer simulations revealed that the molecules could be well described by an equivalent model of DNA in equilibrium on an attractive surface in the presence of mild lateral confinement.

The method was also useful to investigate the diffusion properties of DNA molecules of various size and topology. When different sized or different topology DNA mixes were translocated inside the small slits, the molecules which had the highest diffusion coefficient migrated furthest inside the slits. The confinement acted as topological sieve, separating molecules based on their size and topology.

Most importantly, we discovered nanometer sized local defects in the DNA rings overlapping with the nicked regions in the molecule. We think confinement helps expose these thermodynamically weak

positions by forming hairpins and interwound regions, which themselves can act as structural markers (142) for different biological processes (143,144).

Although this method is limited by AFM resolution, it needs a very small quantity of sample; it gives a possibility to study DNA molecules of various sizes, topology and shape, by directly visualizing them and assessing their statistical shape parameters. We believe that the possibility of easily fabricable confinement of tuneable dimensions opens new possibilities for experimental studies, which will shed new insights of polymer behaviour under confinement.

## Chapter 3: DNA-protein complexes

### 3.1 Influence of DNA Binding Dyes on Bare DNA Structure Studied with Atomic Force Microscopy

*This chapter is based on a paper published in ACS Macromolecules with the following authors:*

Aleksandre Japaridze<sup>1</sup>, Alexander Benke<sup>2</sup>, Sylvain Renevey<sup>1</sup>, Carine Benadiba<sup>1</sup>, and Giovanni Dietler<sup>1</sup>

*Affiliations:*

1 - Laboratory of Physics of Living Matter, EPFL, 1015 Lausanne, Switzerland

2 - Laboratory of Experimental Biophysics, EPFL, 1015 Lausanne, Switzerland

#### **Abstract**

Fluorescent dyes are widely used for staining and visualization of DNA in optical microscopy based methods. Although the binding mechanism for the dyes is known, how this binding affects DNA remains poorly understood. Here we present an Atomic Force Microscopy study of the influence of staining dyes on bare DNA properties. We studied the influence of dyes on the persistence length, the total contour length and the morphology of single DNA molecules. We tested PicoGreen, Dapi and DRAQ5, three widely used staining dyes. Based on our measurements, when imaged at typical concentrations PicoGreen dye showed little effect, Dapi dye decreased the DNA persistence length and DRAQ5 decreased the persistence length and elongated the DNA at the same time. When used at high concentrations, all of the dyes induced drastic changes in the DNA morphology. Our study clearly shows that DNA-binding dyes, irrespective of their DNA binding mechanisms, strongly influence the physical properties of DNA. These changes are strongly dose and dye type dependent, therefore should be taken into consideration when conducting experiments.

### 3.1.1 Introduction

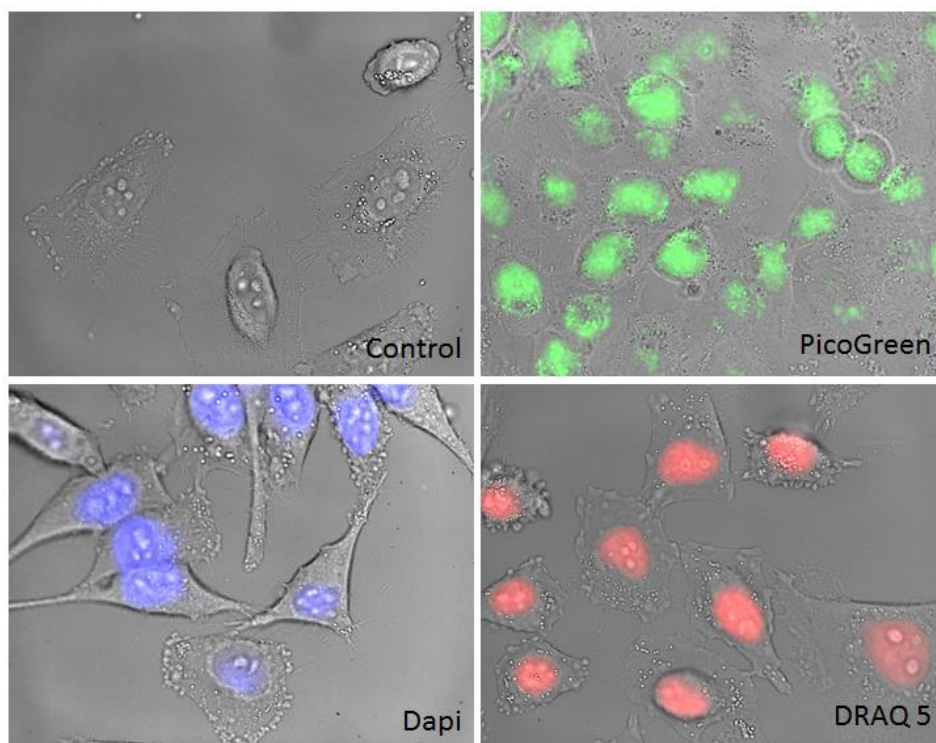


**Figure 3.1.1:** Composed optical and fluorescent images of HeLa cells stained with Dapi, DRAQ5 and PicoGreen dyes.  
(PicoGreen : 100x; Dapi : 5000x; DRAQ5 : 10000x)

Fluorescence microscopy is a widely used technique in cell biology, biochemistry and medicine among other fields of scientific research. The need to label and visualize DNA and chromatin has gained importance in different fields of biological research (Figure 3.1.1), with experiment ranging from measurements done on isolated DNA (122,132,145-148) to experiments in fixed and living cells (149-153). To perform all of these experiments, there is a large variety of DNA labelling dyes available. Some bind to the minor/major grooves of double-stranded DNA, while others intercalate into DNA and some do both (122,138,150-161). The influence of DNA labelling dyes on the DNA structure and its properties is still a topic of debate, since no clear data exist on how strongly they influence physical properties (138, 153-160). Nevertheless, several works revealed that parameters such as the contour length and the persistence length of bare DNA can be significantly changed by fluorescent dyes upon binding (137,138,153-161).

On the example of intercalating YOYO-1 dye, Günther et al. showed that mechanical and structural properties of dsDNA were changing (138). Wojcik et al. showed that DRAQ5 dye detached H1 and H2B histones in a concentration dependent manner in living cells (153). Higher concentrations of the dye even caused aggregation and partial loss of chromatin organization. In optical tweezer experiments Sischka et al. compared different DNA binding agents with different binding modes, showing changes in the mechanical response of DNA pulling as the function of the dye binding mechanisms (157). Despite observing significant changes in the DNA morphology, detailed molecular mechanism behind those phenomena has been poorly understood (137,138,153-162).

In our study we tested how DNA binding dyes affected DNA nanoscale organization and its structure. We used Atomic Force Microscopy (AFM), a widely used technique in bio-nano sciences with nanometer spatial resolution (163-165). AFM enabled us to visualize and measure physical properties of single DNA molecules. We performed experiments with three widely used dyes in cell biology and biophysics which have different emission spectra and differently bind DNA, namely PicoGreen, Dapi and DRAQ5.

### 3.1.2 Materials and methods

#### Linear DNA

The basis of the linear 1.4kb DNA (UPPU) were Fis (U) and H-NS (P) protein binding sites amplified from the tyrT uas sequence. Linear 1.4kb fragments were extracted from 1.5% agarose gel and purified using extraction kit from Promega. DNA was then placed in TE buffer composed of 10 mM Tris and 1 mM EDTA solution.

#### AFM

AFM images were collected using a MultiMode SPM with a Nanoscope III controller (Veeco Instruments, Santa Barbara, CA, USA) operated in tapping-mode in air. The AFM cantilevers used in air had a spring constant of  $5 \text{ N m}^{-1}$  (Veeco cantilevers, TAP150A) with resonance frequencies ranging between 120 and 160 kHz. All the recorded AFM images consist of  $512 \times 512$  pixels with scan frequency  $\leq 1$  Hz recorded at  $1.5 \times 1.5 \mu\text{m}$  scale. Images were simply flattened using the Gwyddion software (Version 2.25) (105) and no further image processing was carried out.

#### DNA persistence length

The persistence length is a basic mechanical property of polymers that quantitatively describes its conformational flexibility. A typical value of  $L_p$  for double stranded DNA is estimated to be  $\sim 50\text{nm}$  (34,35,69,139,166,167).

We measured the persistence length  $L_p$  of DNA by directly fitting the bond correlation function for polymers in 2D:

$$\langle \cos(\theta) \rangle = e^{(-s/2 \cdot l_p)} \quad (3.1)$$

where  $\theta$  is the angle between the tangent vectors to the chain at two points separated by the distance  $s$  and  $l_p$  the persistence length (34,35,69,139,166,167).

Knowing the final shape of a DNA (whether it's a 2D relaxed conformation or a 2D projection of a 3D conformation) is very important in order to correctly calculate the DNA persistence length, because using the equivalent of equation 3.1. in 3D leads to an overestimation of persistence length by a factor of 2.

$$3D \langle \cos(\theta) \rangle = e^{(-s/l_p)} \quad (3.2)$$

In our experiments we used  $\text{Mg}^{2+}$  to bridge DNA with mica surface, resulting in complete 2D relaxation. The 2D relaxed conformation was confirmed by calculating the critical exponent for DNA. First we

measured the end-to-end distance  $\langle \xi(s) \rangle$  for our DNA, then we used the power law dependency between the end-to-end distance and the DNA contour length given by:

$$\langle \xi(s) \rangle \sim s^\nu \quad (3.3)$$

where  $s$  is the contour length;  $L$  the total length of DNA and  $\nu$  the critical exponent.

The value of the exponent  $\nu$  depends on the dimension of the object, and it takes the value: 1, 0.75 or 0.58 for  $d=1$ ; 2; or  $d=3$  respectively (35,69,139).

**Table 3.1.1: Critical exponent of DNA as the function of Dye concentration**

Dye Concentration	Number	Critical exponent $\nu$	Conformation
Control	80	$0.80 \pm 0.05$	2D
<b>PicoGreen:bp</b>			
0.2:1	80	$0.78 \pm 0.05$	2D
0.67:1	80	$0.75 \pm 0.05$	2D
6.7:1	80	$0.79 \pm 0.05$	2D
<b>100:1</b>	<b>70</b>	<b><math>0.58 \pm 0.05</math></b>	<b>3D</b>
<b>Dapi:bp</b>			
0.33:1	80	$0.74 \pm 0.05$	2D
0.67:1	80	$0.72 \pm 0.05$	2D
6.7:1	100	$0.75 \pm 0.05$	2D
<b>50:1</b>	<b>50</b>	<b><math>0.56 \pm 0.05</math></b>	<b>3D</b>
<b>DRAQ5:bp</b>			
0.29:1	130	$0.72 \pm 0.05$	2D
0.67:1	100	$0.75 \pm 0.05$	2D
<b>6.7:1</b>	<b>130</b>	<b><math>0.52 \pm 0.05</math></b>	<b>3D</b>
<b>20:1</b>	<b>100</b>	<b><math>0.55 \pm 0.05</math></b>	<b>3D</b>

By directly measuring the critical exponent, we could distinguish the 2D relaxed conformations of a given DNA-dye complex from a 3D projected one (Table 3.1.1).

It turned out that for high dye concentrations, irrespective from dye type, DNA was adopting a 3D projected conformation on mica surface and not anymore a relaxed 2D one. Considering this we corrected the fitting function for the persistence length and used the 3D equation 3.2.

### **DNA tracing**

AFM images were analyzed using “DNA Trace” software previously described in reference (106). Based on the statistics of 50-100 individual molecules the contour length, the End-to-End distance distribution as well as the bond correlation function were calculated by the software.

### **DNA binding dyes**

Three different dyes have been used for our study: PicoGreen, DAPI, DRAQ5.

PicoGreen dye (552.5 g/mol) (Quant-iT PicoGreen dsDNA Assay Kit purchased from Invitrogen, stock solution 0.2mM) was used in the following dye:base pair (bp) ratios: 0.2:1; 0.67:1; 6.7:1; 100:1. The absolute concentration of PicoGreen was determined by measuring the optical density of the solution using extinction coefficient of  $E_{500} = 70,000 \text{ M}^{-1} \text{ cm}^{-1}$  at room temperature similarly as described elsewhere (154,168).

Dapi dye (457.5 g/mol) (purchased from Sigma-Aldrich, stock solution 11mM) was used in the following dye:bp ratios : 0.33:1; 0.67:1; 6.7:1; 50:1.

DRAQ5 dye (412.5 g/mol) (purchased from Biostatus, stock solution 5mM) was used in the following dye:bp ratios : 0.29:1; 0.67:1; 6.7:1; 20:1.

Typical concentrations used in staining are different for each dye and manufacturers suggest an optimal dilution factor of the stock solution, rather than the absolute concentration. In our work we qualitatively call these concentrations, typically used for staining in optical microscopy “low concentrations” (dye:bp – 0.2:1-0.67:1). The concentrations which are above this normally suggested range we qualitatively call “high concentrations” (dye:bp – 6.7:1-100:1).

### **AFM Buffer**

All AFM samples were prepared in the AFM Buffer consisting of 1mM Tris and 4mM MgCl<sub>2</sub> (pH = 7.0).

### **Sample preparation**

A control DNA sample was first prepared by mixing the 1.4kb DNA (typical concentration of 0.5–1 ng/μl) and the AFM Buffer in 20 μl volume and deposited on a freshly cleaved mica. After 5 minutes of deposition the mica was rinsed with 1 ml of double distilled water and dried under a gentle nitrogen flow.

For the samples containing dyes, the dyes were first diluted in the AFM Buffer accordingly to the desired dye:DNA ratio (final DNA concentration of 0.5–1 ng/μl). The DNA was then added in the solution and left for 15 min for incubation at room temperature (22°C). Afterwards, the whole mix was deposited on freshly cleaved mica for 5 minutes before being rinsed with 1 ml of double distilled water and dried with a gentle flow of nitrogen.



### **Gel Electrophoresis**

The gel electrophoresis experiment was performed in 1% agarose gel prepared in 1x TAE buffer. During electrophoresis the gels were submerged in 1x TAE buffer and the sample run at 50 V for 4 h. Afterwards the gel was stained using GelRed (purchased from Biotium) bath for 1hour.

### **Cell imaging protocol**

HeLa cells were grown in a humidified incubator at 37°C in 5% CO<sub>2</sub> in complete growth medium composed of Dulbecco's Modified Eagle Medium (Life Technologies) containing 10% of inactivated FBS south american (Life Technologies) and 1% of Penicillin/Streptomycin solution (Life Technologies). Before Dye incubation, cells were three times rinsed with 37°C prewarmed Leibovitz L-15 (Life Technologies) medium supplemented by 10% FBS and 1% Penicillin/Streptomycin solution. Dyes were added directly into Leibovitz media and incubated with Hela cells for 15 min, after incubation cells were washed three times with prewarmed Leibovitz. Concerning the DRAQ5 dye, we added 1uL of stock solution (from Abcam at 5mM) into 1mL of medium ; the PicoGreen dye was tested at 1000x (1uL into 1mL of medium) and the Dapi (Life Technologies) was tested at 1ug/mL corresponding to an addition of 20ul (50ug/mL of stock solution resuspended into PBS) at 1mL of medium. Imaging was performed on an inverted Zeiss Axiovert Z1 system with a 100×/1.46 α-Plan APOCHROMAT DIC oil objective (Carl Zeiss AG) using a sCmos camera and Visiview software (Visitron system GmbH).

## 3.1.3 Results

### 3.1.3.1 PicoGreen

The first dye used in our experiments was PicoGreen. It binds DNA by two processes: the quinolinium group intercalates into DNA while the two dimethylaminopropyl groups lie deep in the minor groove (149,154,161,168). The excitation maximum and the emission fluorescence spectra of PicoGreen are  $\sim 485$  nm and  $\sim 530$  nm respectively. The unbound dye has almost no fluorescence, it is very stable to photo-bleaching, allowing longer exposure times and assay flexibility, therefore it is very widely used in microscopy (149,152,154,161,168).

As the first step, we imaged 1.4kb linear DNA without PicoGreen dye. Figure 3.1.2 shows a typical AFM image of control DNA. The DNA was relaxed on the mica surface and showed no crossovers. As the next step we started adding PicoGreen to the DNA sample. At low PicoGreen concentration we did not observe any significant difference between the physical properties of bare and stained DNA. The results changed significantly once we added high dye concentrations. We directly noticed a difference in DNA shape and morphology (Figure 3.1.3). DNA stained with high PicoGreen concentration appeared longer and much more bend. On the molecules stained with high dye concentrations, we observed loops and crossings that were previously absent.

After visual comparison, the DNA fragments were traced and the histograms of contour length plotted. Figure 3.1.4 reflects a tight relation between PicoGreen concentration and DNA contour length. With increasing dye concentration DNA length distribution increased progressively. Notably, the average contour length of bare DNA  $L \sim 410 \pm 25$  nm increased by  $\sim 45\%$  with the highest dye concentration, reaching a value of  $L \sim 600 \pm 55$  nm (Table 3.1.2). To confirm this DNA length extension, upon PicoGreen binding, we checked the behaviour of stained DNA fragments on gel electrophoresis experiment (Figure 3.1.5). As expected, DNA bands migrated much slower than control DNA indicated on the gel electrophoresis results. Interestingly, calculating the persistence length by the bond correlation function given in equation (3.1). did not reveal any dependence on the staining concentration. The value stayed almost unaffected  $L_p \sim 60 \pm 3$  nm.

From our measurements, we could conclude that high concentrations of PicoGreen dye strongly increased the contour length of the DNA and changed the overall shape of the DNA without affecting its persistence length (Table 3.1.2).

**Table 3.1.2: Shape parameters of PicoGreen bound DNA**

PicoGreen : bp	Number of molecules	Average Length L [nm]	Elongation %	$L_p$ [nm]
Control	80	$410 \pm 25$	-	$61 \pm 3$
0.2:1	80	$410 \pm 20$	-	$63 \pm 3$
0.67:1	80	$430 \pm 45$	5%	$59 \pm 3$
6.7:1	80	$480 \pm 40$	16%	$64 \pm 3$
100:1	70	$600 \pm 55$	46%	$61 \pm 3$

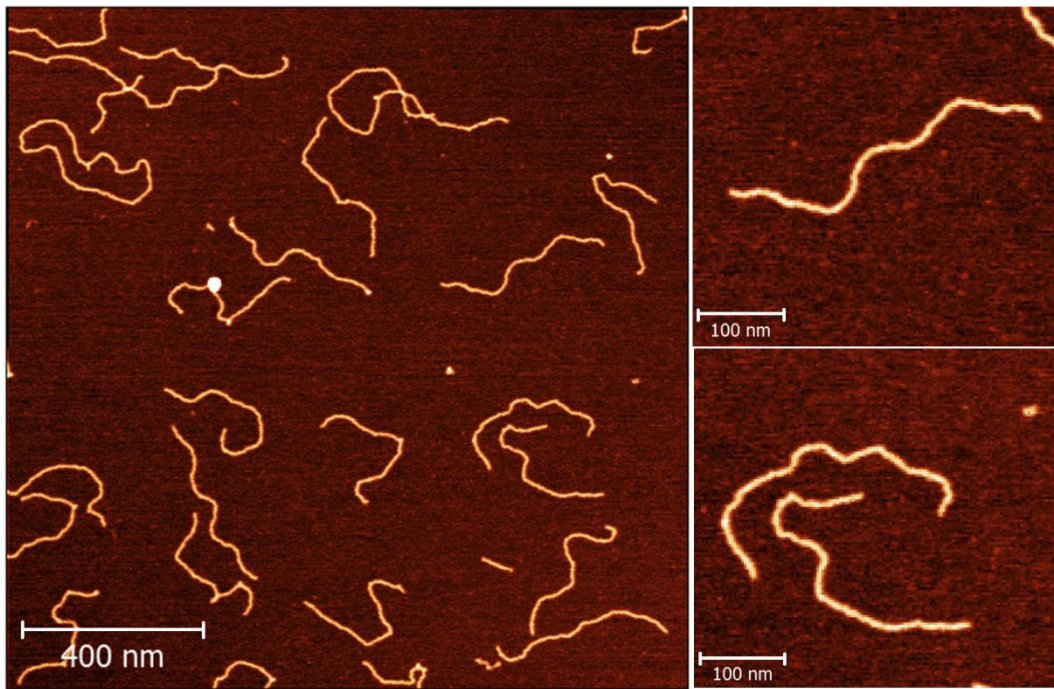


**Figure 3.1.2:** AFM images of control 1.4kb DNA. Right side represents zoomed images of single DNA molecules. Scale bars for large and zoomed AFM images are 400nm and 100nm respectively.

### PicoGreen

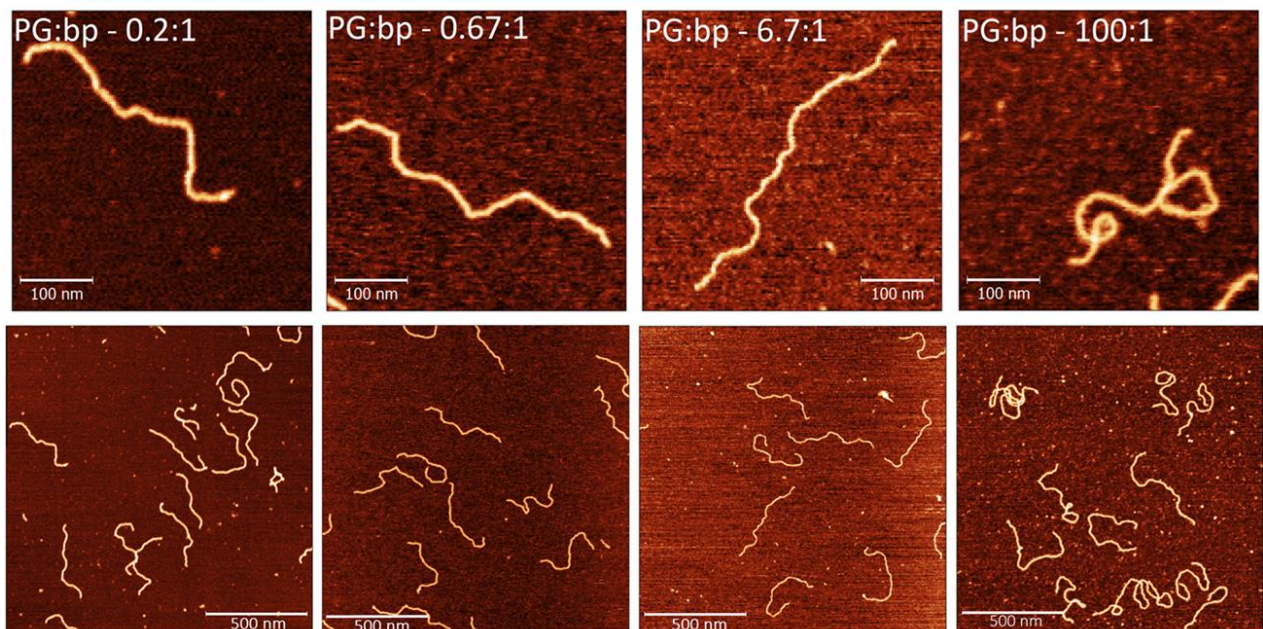


**Figure 3.1.3:** AFM images of 1.4kb DNA stained with PicoGreen. High concentration of PicoGreen leads to elongated DNA structures with crossovers and more compact structures. Scale bars for upper and lower AFM images are 100nm and 500nm respectively.

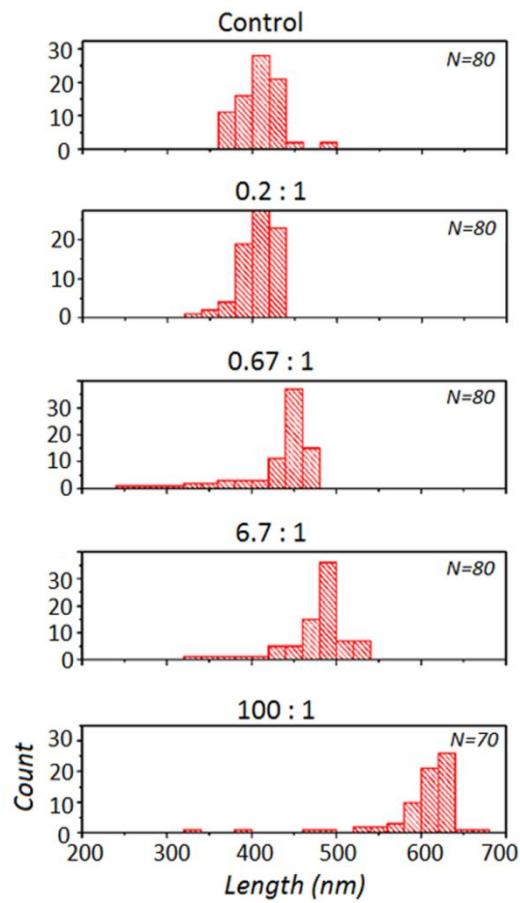


**Figure 3.1.4:** The contour length distribution for DNA-PicoGreen complexes as the function of PicoGreen concentration

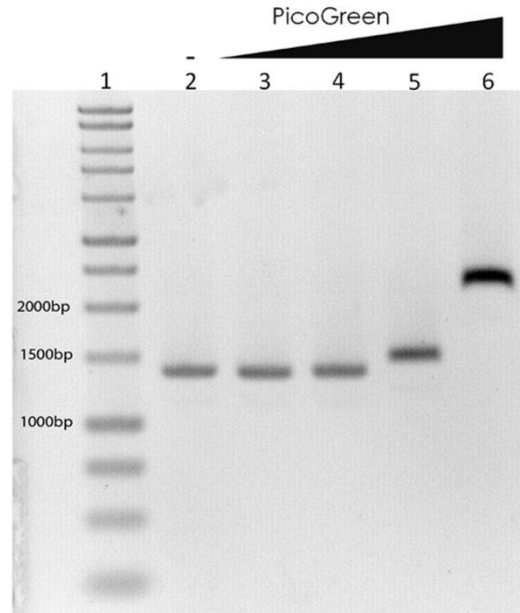


**Figure 3.1.5:** The DNA gel electrophoresis image. Lanes 1. : the marker DNA; 2 : control 1.4kb DNA; 3-6 : DNA stained with growing PicoGreen concentration (PicoGreen:bp – 0.2:1; 0.67:1; 6.7:1; 100:1)

### 3.1.3.2 Dapi

The second dye used in the study was Dapi. Dapi binds to the minor groove in AT basepair rich regions and was shown that it needs a run of 2 to 4 A'T basepairs to bind (154,169-173). The emission maximum of Dapi when bound to DNA is at 460 nm and with the excitation maximum at 358 nm.

Similarly to the experiments with PicoGreen described above, in the case of Dapi, we imaged 1.4kb linear DNA with increasing concentration of the dye and studied its physical properties. Figure 3.1.6 shows typical images of DNA stained with increasing Dapi concentration. Images show that DNA morphology changes upon labelling with Dapi. In the extreme case for the highest Dapi concentration, the DNA fragments formed loops and had a much more compact structure than the relaxed bare DNA (Figure 3.1.6). Compared to PicoGreen dye, Dapi did not change the average length of the DNA fragments as seen from the contour length distribution on Figure 3.1.7 as well as the gel electrophoresis image on Figure 3.1.8. On the contrary to PicoGreen the persistence length changed, strongly decreasing with the increasing dye concentration (Table 3.1.3). The initial persistence length of a bare DNA fragment of  $L_p \sim 60 \pm 3$  nm decreased and reached  $L_p \sim 35 \pm 3$  nm for the sample with the highest Dapi concentration, which is a  $\sim 40\%$  decrease.

Based on our measurements, Dapi dye did not change the total length of the DNA but strongly influenced the morphology of it, making the structures more compact and condensed. In extreme case, the apparent persistence length of the DNA decreased by 40% compared to non-stained DNA.

**Table 3.1.3: Shape parameters of Dapi bound DNA**

Dapi : bp	Number of molecules	Average Length L [nm]	$L_p$ [nm]	$\Delta L_p$
Control	80	$410 \pm 25$	$61 \pm 3$	-
0.33:1	80	$405 \pm 25$	$52 \pm 3$	- 15%
0.67:1	80	$400 \pm 30$	$47 \pm 3$	- 23%
6.7:1	100	$425 \pm 40$	$42 \pm 3$	- 31%
50:1	50	$420 \pm 30$	$35 \pm 3$	- 42%

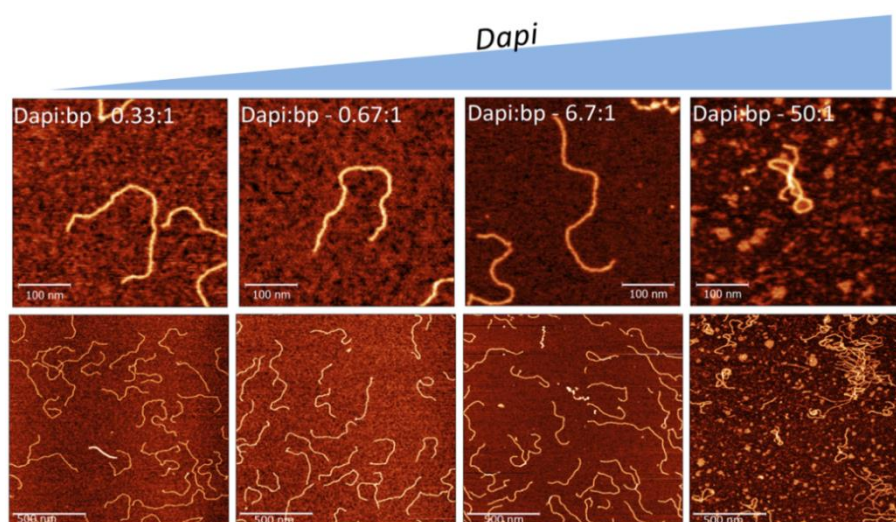


**Figure 3.1.6:** AFM images of 1.4kb DNA stained with Dapi. High concentrations of Dapi lead to flexible and collapsed DNA structures with many crossovers. Scale bars for upper and lower AFM images are 100nm and 500nm respectively.

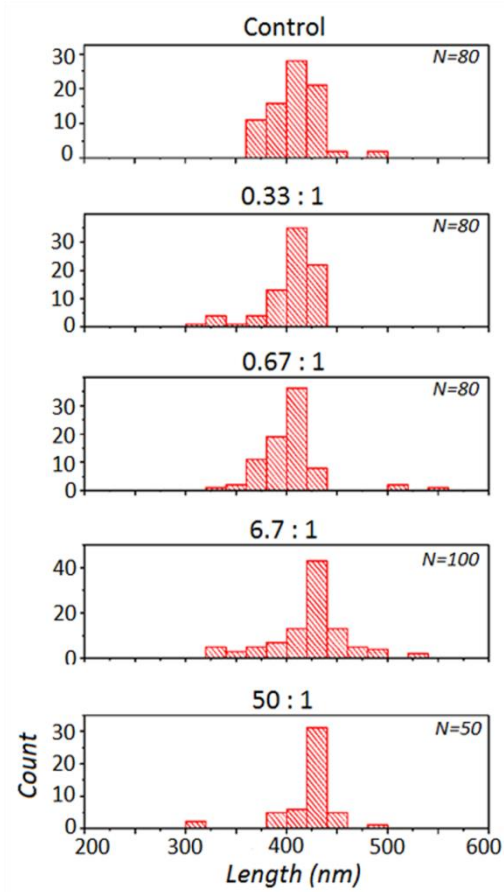


**Figure 3.1.7:** The contour length distribution for DNA-Dapi complexes as the function of Dapi concentration

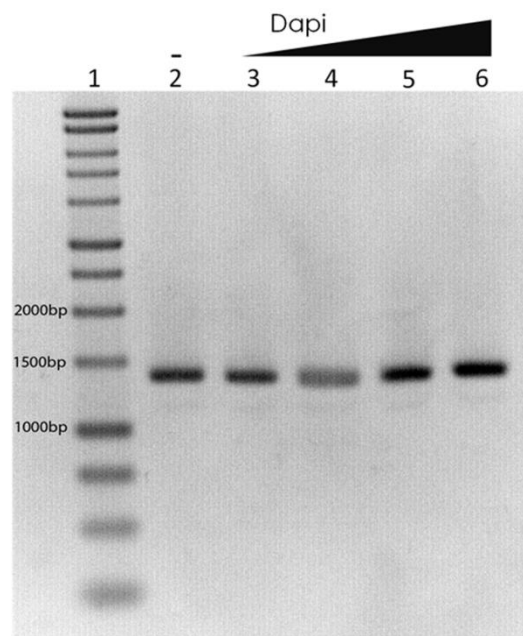


**Figure 3.1.8:** The DNA gel electrophoresis image. Lanes 1 : the marker DNA; 2 : control 1.4kb DNA; 3-6 : DNA stained with growing Dapi concentration (Dapi:bp - 0.33:1; 0.67:1; 6.7:1; 50:1)

### 3.1.3.3 DRAQ5

The last dye tested was DRAQ5. Its excitation maximum is at 646 nm and emission spectra at 697. It is an intercalator dye, which can bind to the minor groove in AT basepair rich regions as well. Interestingly, this dye is often used for live cell imaging (150,151,153,174).

DRAQ5 stained samples showed even stronger changes in the DNA properties compared to PicoGreen and Dapi. Figure 3.1.9 shows typical AFM images of the samples with different concentrations of the dye. The morphology as well as the total length of the DNA was drastically affected by the dye binding. The DNA fragments became longer (Figure 3.1.10) and migrated slower in the gel electrophoresis experiment with increasing concentration of the DRAQ5 (Figure 3.1.11). Even at the lowest DRAQ5:bp ratio of 0.29:1 used in the experiment, DNA was ~15% longer than in the control sample. The persistence length of the DNA was also strongly modified, with the initial value decreasing by ~45% and reached a value of  $L_p \sim 33 \pm 3$  nm (Table 3.1.4).

Based on our data, we could conclude that DRAQ5 dye strongly interacted with DNA and changed the physical properties of DNA. It increased the total length of DNA fragments by ~30% and decreased simultaneously the persistence length by ~45%.

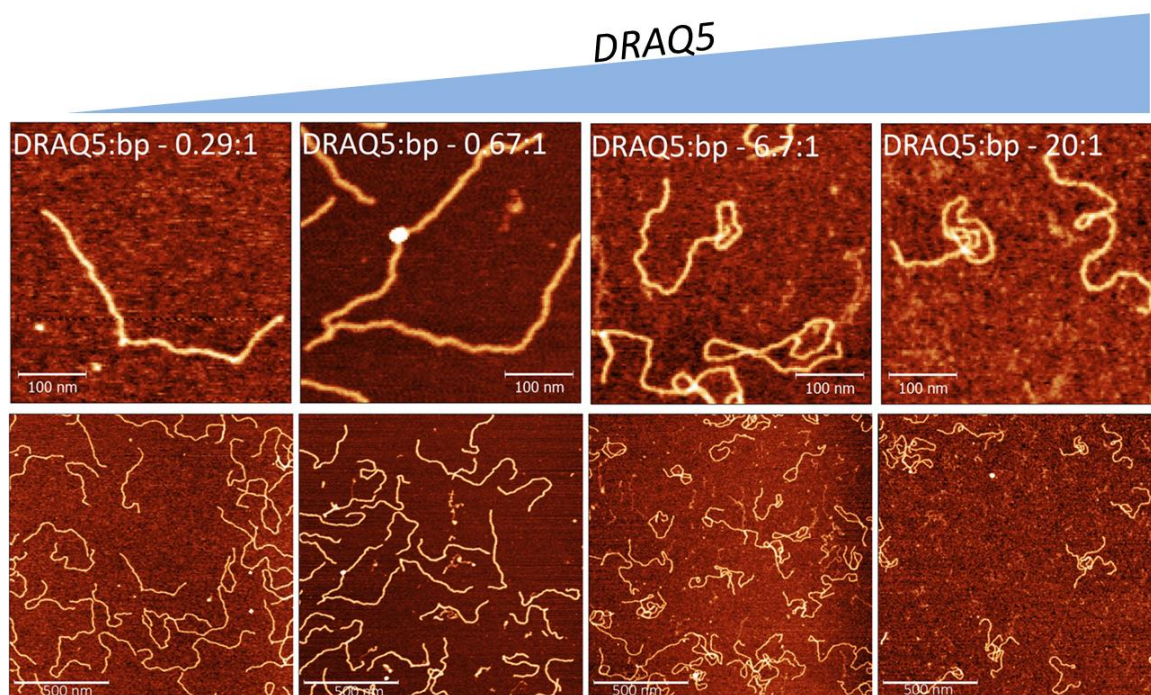


**Figure 3.1.9:** AFM images of DRAQ5 stained DNA. High concentration of DRAQ5 leads to longer and more flexible DNA structures. Scale bars for upper and lower AFM images are 100nm and 500nm respectively.

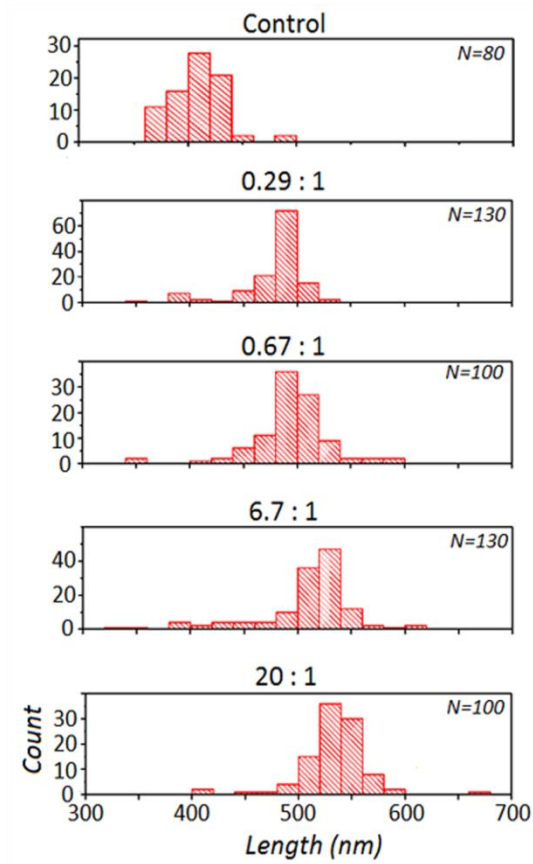


**Figure 3.1.10:** The contour length distribution for DNA-DRAQ5 complexes as the function of DRAQ5 concentration

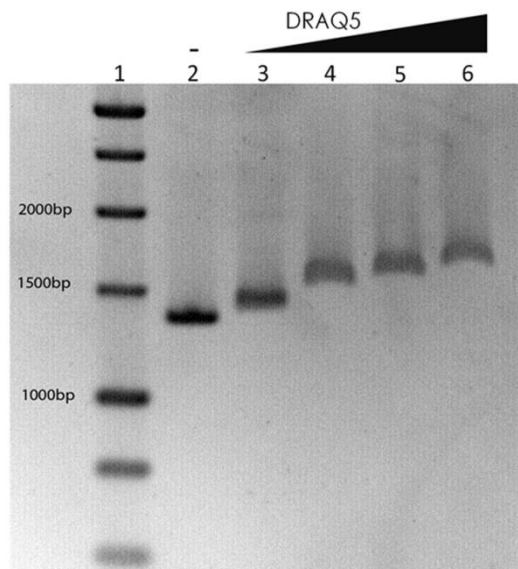


**Figure 3.1.11:** The DNA gel electrophoresis image. Lanes 1. : the marker DNA; 2 : control 1.4kb DNA; 3-6 : DNA stained with growing DRAQ5 concentration (DRAQ5:bp - 0.29:1; 0.67:1; 6.7:1; 20:1)



**Table 3.1.4: Shape parameters of DRAQ5 bound DNA**

DRAQ5 : bp	Number of molecules	Average Length [nm]	Elongation %	L <sub>p</sub> [nm]	ΔL <sub>p</sub>
Control	80	410 ± 25	-	61 ± 3	-
0.29:1	130	480 ± 30	16%	53 ± 3	- 13%
0.67:1	100	495 ± 35	20%	55 ± 3	- 10%
6.7:1	130	510 ± 45	24%	44 ± 3	- 28%
20:1	100	535 ± 30	30%	33 ± 3	- 46%

### 3.1.4 Conclusion

In this study we tested how DNA binding dyes affect nanoscale organization and structure of bare DNA molecules. Three different dyes with different binding modes, namely PicoGreen, Dapi and DRAQ5, were studied.

We compared the critical concentration at which significant structural changes in the DNA-dye complexes were appearing. Surprisingly even at low concentration (dye:bp – 0.2:1-0.67:1), both Dapi and DRAQ5 influenced the morphology of the DNA. DRAQ5 changed both the DNA contour length and the persistence length, while Dapi affected the persistence length only. PicoGreen dye showed no detectable effects when used at low concentrations. The structural and topological changes in the dye bound DNA were extremely clear when used in concentration above dye:bp > 6.7:1; with PicoGreen dye the contour length of DNA increased up to 45%, without affecting the persistence length; Dapi dye decreased the persistence length by 40% without changing the contour length of DNA fragments. Interestingly for the same concentration DRAQ5 affected both shape parameters, decreasing the persistence length and at the same time increasing the contour length.

PicoGreen dye is known to bind to the minor groove of the dsDNA as well as intercalate (154), though the binding mode is still not well understood. Generally screening the negative charges from the DNA backbone leads to the decrease of the persistence length (162,163). PicoGreen carries a single positive charge, therefore once bound to DNA, it should decrease the DNA persistence length. In our experiments the DNA persistence length was independent from the PicoGreen concentration. It can be hypothesized, that the increase in the DNA flexibility due to screening of one DNA charge per bound PicoGreen molecule is somehow counteracted by the local stiffening of PicoGreen-DNA complex (154). We measured an increase in the contour length of DNA for high PicoGreen concentrations. Intercalation leads to local unwinding and stretching of DNA in contrast to minor groove binding. Based on these data we can suggest a concentration dependent PicoGreen binding. At low concentrations (PicoGreen:bp < 0.67:1) PicoGreen presumably binds to DNA minor groove and at higher concentrations (PicoGreen:bp > 6.7:1) it starts to intercalate into DNA.

DAPI dye, a minor groove binding dye, has been shown to have a preferred mode of binding to AT rich sequences at low dye concentrations. Dapi carries a divalent positive charge, therefore when bound to DNA minor groove it screens the negative DNA backbone charge, making it more flexible. In agreement with this model, we saw a concentration dependent decrease in DNA persistence length. As mentioned above minor groove binding should retain the helicity and the pitch of the dsDNA. AFM as well as the gel electrophoresis experiments confirm this notion. At low concentrations the contour length of DNA doesn't change (Dapi:bp < 0.67:1). Interestingly at higher concentrations it was suggested that it might change its minor groove binding mechanism and intercalate into GC rich sequences as well (169-173). At high concentrations (Dapi:bp > 6.7:1) we observe only a slight increase of the average contour length. This suggests that in our case Dapi mostly acts as a minor groove binder, even at high concentrations.

DRAQ5 is an intercalating DNA dye, that has some preference to bind the minor groove in AT basepair rich sequences (149,150,153,174). When bound to DNA, in contrast to PicoGreen, we observed a continuous increase in the contour length, starting from the lowest dye concentration (DRAQ5:bp – 0.29:1). These results support that DRAQ5 acts as a strong intercalator, since intercalation leads to DNA base unwinding and elongation. Surprisingly, even though the net charge of DRAQ5 is zero and it should not screen any charges from the DNA, we measured a concentration dependent decrease in the persistence length. This behaviour could be linked to the minor groove binding mode of DRAQ5 that locally decreases the DNA stiffness (174). At low DRAQ5 concentrations we saw mostly DNA elongation (~20%) and a partial decrease in persistence length ( $\Delta L_p \sim 10\%$ ). At high DRAQ5 concentrations (DRAQ5:bp > 6.7:1) the decrease in DNA persistence length become more dominant ( $\Delta L_p \sim 45\%$ ) compared to contour length elongation (elongation~30%). Based on this we could conclude that DRAQ5 binding to DNA leads to a complex interplay of two phenomena, local unwinding due to intercalation and long range effect of increased flexibility.

In living cells DNA exist in a form of chromatin: complex of DNA and DNA binding proteins (histones and transcription factors). The effect the dyes have on a DNA organization in living cells quantitatively can be different from naked DNA data due to the interaction between DNA and these proteins. However, there are parts of cellular DNA which are not covered by histones, particularly in active euchromatin regions. Moreover, even in chromatinized DNA there are gaps between histones where dyes can bind. In addition, minor groove binders theoretically can bind even DNA on histones. Therefore, we think that qualitatively the effect should be similar as DNA binding dyes still bind DNA.

In general, our results show that DNA binding dyes affect DNA structure depending on the binding mechanism and in a clear concentration dependent manner. It means that when DNA is stained possible changes in the DNA properties has to be considered.

## 3.2 Functional Dissection of Intersubunit Interactions in the EspR Virulence Regulator of *Mycobacterium tuberculosis*

*This chapter is based on a paper published in Journal of Bacteriology with the following authors:*

Benjamin Blasco<sup>1</sup>, Aleksandre Japaridze<sup>2</sup>, Marco Stenta<sup>3</sup>, Basile I. M. Wicky<sup>3</sup>, Giovanni Dietler<sup>2</sup>, Matteo Dal Peraro<sup>3,4</sup>, Florence Pojer<sup>1</sup>, Stewart T. Cole<sup>1</sup>

*Affiliations:*

1 - Global Health Institute, Ecole Polytechnique Fédérale de Lausanne (EPFL), Lausanne, Switzerland

2 - Laboratory of the Physics of Living Matter, EPFL, Lausanne, Switzerland

3 - Laboratory for Biomolecular Modeling, Institute of Bioengineering, School of Life Sciences, EPFL, Lausanne, Switzerland

4 - Swiss Institute of Bioinformatics (SIB), Lausanne, Switzerland

### **Abstract**

The nucleoid-associated protein EspR regulates expression of genes associated with cell wall function and pathogenesis in *Mycobacterium tuberculosis*. EspR binds to several upstream sites of the *espACD* locus to promote its expression, regulating the function of the ESX-1 secretion system, a major virulence determinant. While direct binding to DNA appears to be mediated by an EspR dimer-of-dimers, the mechanism of EspR higher-order organization and its impact on chromosome structure and gene expression are poorly understood.

By using conventional and high resolution atomic force microscopy we studied the higher order organisation of EspR with the *espACD* promoter region. By substituting several key residues with Alanine we probed interactions at either the dimer or the dimer-of-dimers interfaces and directly assessed their role in the protein-DNA binding. Single point mutations at Arg70, Lys72, or Arg101 affected the overall binding of the protein to the DNA as well as, in certain cases, the possibility to form higher order structures in complex with the DNA.

Our results pinpoint key residues required for EspR function and higher-order oligomerization when bound to the DNA at the dimer (Arg70) and the dimer-of-dimers (Lys72) interface.

### 3.2.1 Introduction

EspR is an abundant 14.7kDa DNA-binding protein which is widely conserved among mycobacteria and other related actinomycetes. EspR is a key activator of the virulence-associated ESX-1 secretion system, by directly upregulating the *espACD* operon, which is known to encode three proteins required for proper ESX-1 activity, namely EspA, EspC, and EspD (175–177). *In vivo* studies showed that EspR binds hundreds of loci throughout the *Mycobacterium tuberculosis* chromosome and multiple frequently clustered binding sites (178). EspR binds variety of genes, sometimes topologically distant ones, but mainly serving a common biological function related to *M. tuberculosis* cell wall function and pathogenesis (178). Moreover, it is capable of influencing target gene expression in either a positive or negative manner. Most importantly, it appears that EspR negatively regulates its own expression (175,178). Since it often binds intragenic regions or sites far upstream of the transcriptional start site, it somehow acts differently compared to a classical transcriptional regulator. Regulation thus occurs over long distances by joining sites linearly distant from each other into a nucleoprotein complex. In a previous study, atomic force microscopy (AFM) was used to directly visualize nucleoprotein complexes formed by EspR with the full-length upstream region of *espACD* (1,357 bp) (179). Measurements showed that EspR was forming DNA loops and hairpins stabilized by EspR oligomers (179).

Proteins having a dual role in chromosome organization and gene expression, such as EspR, are the so called nucleoid-associated proteins (NAPs) (180). NAPs are small and abundant DNA-binding proteins that control bacterial gene expression by several possible mechanisms: blockage of RNA polymerase's accessibility to promoter regions; assembly of transcriptionally active promoter conformations, or displacement of other regulatory proteins. Upon binding, NAPs can strongly change DNA architecture, by bending, wrapping, and bridging the DNA (180).. Most of the previous studies of EspR have focused on its interaction with the *espACD* locus (175,178,179,181,182), which is subject to complex regulation by three NAP-like proteins. These regulators include: EspR, CRP, and Lsr2 (178,183,184), two members of two-component systems, PhoP and MprA (185–187), and long-range interactions along the *espACD* upstream region (181,188). Despite the fact that EspR can dimerize and form higher order oligomers along several binding sites within the promoter region (178,179,182), the exact mechanism by which EspR upregulates *espACD* expression is still unknown.

EspR consists of two domains, the DNA-binding domain in the N-terminal, which contains a typical helix-turn-helix motif, and the C-terminal dimerization domain, which is involved in the formation of the EspR dimers by providing hydrophobic and polar interactions that stabilize the assembly of the two EspR subunits (179,182). In live bacteria, the removal of the last 10 residues from the C-terminal of EspR (EspR $\Delta$ 10 mutant) resulted in the loss of its transcriptional activity (175), due to decreased capacity to homodimerize (179). EspR $\Delta$ 10 was also unable to shift the same DNA fragment at the concentration tested, consistent with stable EspR dimerization being necessary for cooperative, high-affinity binding (179).

In a previous study, a model for cooperative binding was proposed in which EspR binds DNA as a dimer-of-dimers, inserting one of the two dimer subunits into two consecutive major grooves while at the same time forming a stable interface between the two EspR dimers (179). This conformation is proposed to leave one subunit from each EspR dimer free for further protein-protein or protein-DNA interactions, promoting protein assembly into higher-order oligomers capable of bridging interactions between distant binding sites. Accordingly, protein binding would proceed in a cooperative manner, with EspR dimer-of-dimers initiating at high-affinity sites and further polymerizing along the DNA.

In order to gain a more complete understanding of EspR's mode of DNA binding, namely how it structures large DNA regions, we used AFM. We studied the higher order organisation of EspR and several of its mutated forms with the *espACD* promoter region. We studied to role of single point mutations affecting the overall DNA binding as well as proteins capacity to form higher order oligomeric structures.

### 3.2.2 Materials and methods

#### DNA

Linear fragments were generated by PCR, resulting in a 1.36 kb fragment covering the complete intergenic region between *espA* and *ephA* (PespA).

#### AFM sample preparation

EspR–DNA binding reaction was performed by incubating 6 nM DNA with varying concentration of EspR wildtype or mutant protein in 10 µl reaction volume for 10 min at room temperature (final concentration 10 mM Tris pH 7.5, 50 mM KCl, 1 mM DTT, 5% glycerol and 1 mM EDTA). The mixture was then diluted 5 times in H2O containing MgCl2 (2 mM final) and deposited onto freshly cleaved mica. After 5 min of incubation, the mica surface was gently rinsed with 1ml of Milli-Q water and subsequently gently blow-dried with filtered compressed air.

#### Protein Mutations

We tested the impact of four mutations on the EspR-DNA binding and their capacity to form higher order structures. Three mutations were point mutations at positions Arg70, Lys72, and Arg101, obtained by substituting the residues with Alanine. The fourth mutant was a truncated form of EspR, having last 10 amino acids deleted (Table 3.2.1).

**Table 3.2.1:** EspR Protein mutations

Name	Mutation position	Mutation ( <i>residue charge</i> )
<b><i>K72A</i></b>	72	Substitution of Lysine (+) with Alanine (0)
<b><i>R70A</i></b>	70	Substitution of Arginine (+) with Alanine (0)
<b><i>R101A</i></b>	101	Substitution of Arginine (+) with Alanine (0)
<b><i>EspR Δ10</i></b>	Last 10 amino acids	Deleting last 10 amino acids

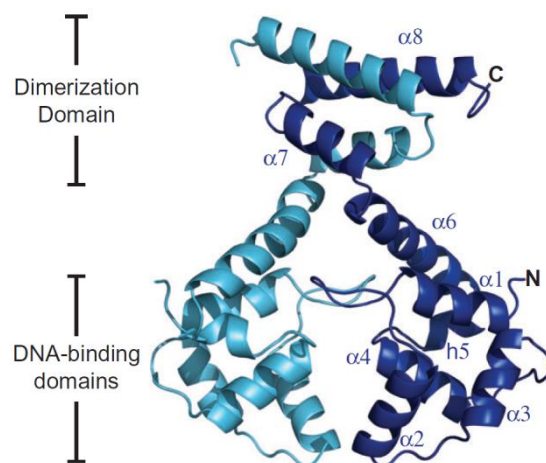


**Figure 3.2.1:** Structure of *EspR* dimer taken from (179)

### Measurements in air

AFM images in air were collected using a MultiMode SPM with a Nanoscope III controller (Veeco Instruments, Santa Barbara, CA, USA) operated in tapping-mode in air. The AFM cantilevers had a spring constant of 5 N/m (Veeco cantilevers, TAP150A) with resonance frequencies ranging between 120 and 160 kHz. All the recorded AFM images consist of 512 x 512 pixels with scan frequency  $\leq 1$  Hz, AFM images were obtained at separate locations across the mica surfaces to ensure a high degree of reproducibility of the recorded DNA fragments. Height of protein-DNA complexes was measured with NanoScope Analysis software (Version 1.20, Bruker, 2010) Images were simply flattened and magnified using Gwyddion software (version 2.22) (105), and no further image processing was carried out.

To calibrate the system, *EspR* protein variants and the linear *espACD* promoter fragment (*P<sub>espACD</sub>*) were separately imaged by AFM, and the corresponding heights were measured using the NanoScope Analysis software program (Version 1.20; Bruker, 2010). In protein-DNA binding experiments, proteins were considered DNA bound when the height measured at any point of the DNA molecule was at least 0.5 nm higher than the average height measured for the free DNA (Figure 3.2.2).

Each protein-DNA binding experiment was performed at least in duplicate. AFM images were obtained at several separate locations across the mica surface to ensure a high degree of reproducibility and were used for statistical analysis of protein-DNA complexes. Only protein-DNA complexes that were completely visible in the AFM image were considered for statistical analysis.

### Measurements in UHV

#### AFM tips

Diamond-like carbon (DLC) whiskers ultra-sharp AFM tips (NT-MDT, Russia) were used to image samples in UHV. Whiskers were grown on the silicon tips of Mikromasch company 15 Series cantilevers. The typical resonant frequency of these cantilevers is 325 kHz and their spring constant is 40 N/m. The nominal radius of these tips is below 3 nm.

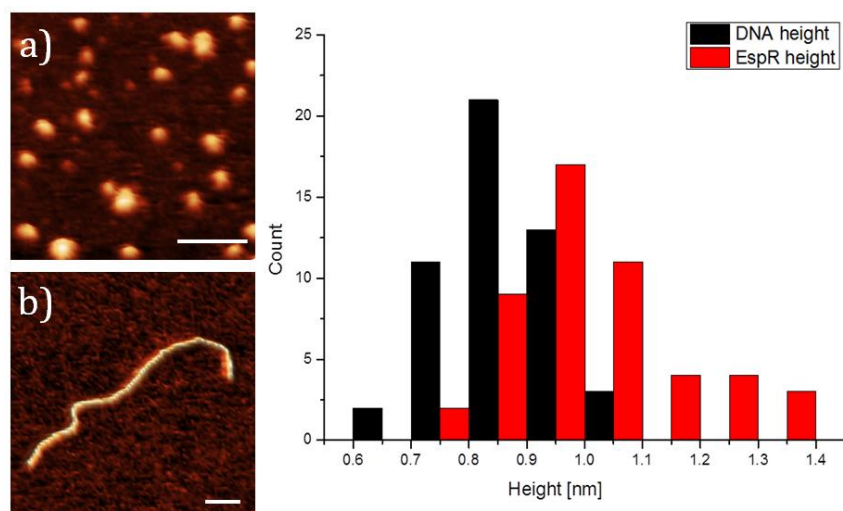


**Figure 3.2.2:** Zoomed 3D reconstructions of a) EspR and b) bare DNA deposited on Mica with the corresponding height histograms. We defined DNA bound by EspR if the height at any point along the DNA molecule was at least 0.5 nm higher than the height measured for the free DNA. Scale bars 50nm.

### UHV AFM instrument, settings and procedures

All UHV AFM images shown in this chapter were acquired using a home built AFM previously described (93,96). Imaging was performed at room temperature and in UHV at a pressure of approximately  $10^{-9}$  mbar. Samples were imaged using frequency modulation AFM where small and negative frequency shift values were used as z-position feedback set point (typically  $\Delta f$  was set to -2 Hz). At the same time the oscillation amplitude of the tip was always kept constant and equal to 10 nm using a separate feedback loop. Any eventual electrostatic tip-sample contact potential difference was systematically compensated before all measurements by applying an appropriate bias voltage that was determined using the “CPD compensation” module of Nanonis SPM control software ([www.specs-zurich.com](http://www.specs-zurich.com)). The software was also used to control the overall operation of the AFM.

## 3.2.3 Results

### 3.2.3.1 Wild type EspR binding to *PespACD*

In a previous study, Blasco et al (179) showed that EspR could form hairpins when bound to the *PespACD* DNA region. To get deeper insight into the molecular mechanisms of EspR action, we used AFM to systematically compare protein-DNA complexes formed at different concentrations by the EspR variants when bound to the full 1.36 kb *PespACD* upstream region. As first step, we bound EspR wild type protein at the lowest concentration (EspR:DNA 280:1). In this way the proteins would predominantly bind the strongest binding sites along the DNA and not form any higher order complexes. Figure 3.2.3 shows typical large scale AFM images of control and EspR bound DNA. We defined DNA bound by EspR if the height measured at any point along the DNA molecule was at least 0.5 nm higher than the average height measured for the free DNA (Table 3.2.2 and Figure 3.2.2).

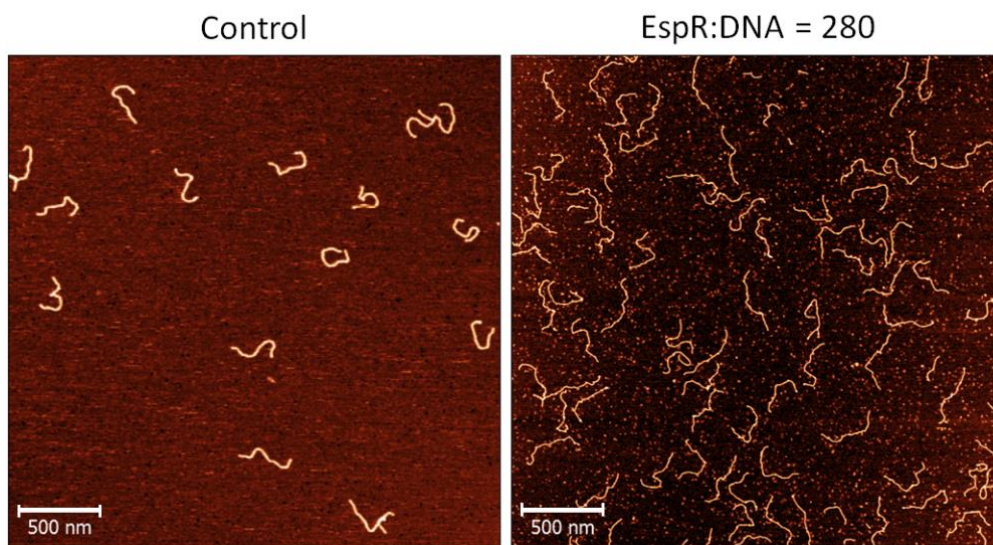


**Figure 3.2.3:** Typical AFM image of *PespACD* DNA control(left) and EspR- *PespACD* complexes. Scale bars 500nm.

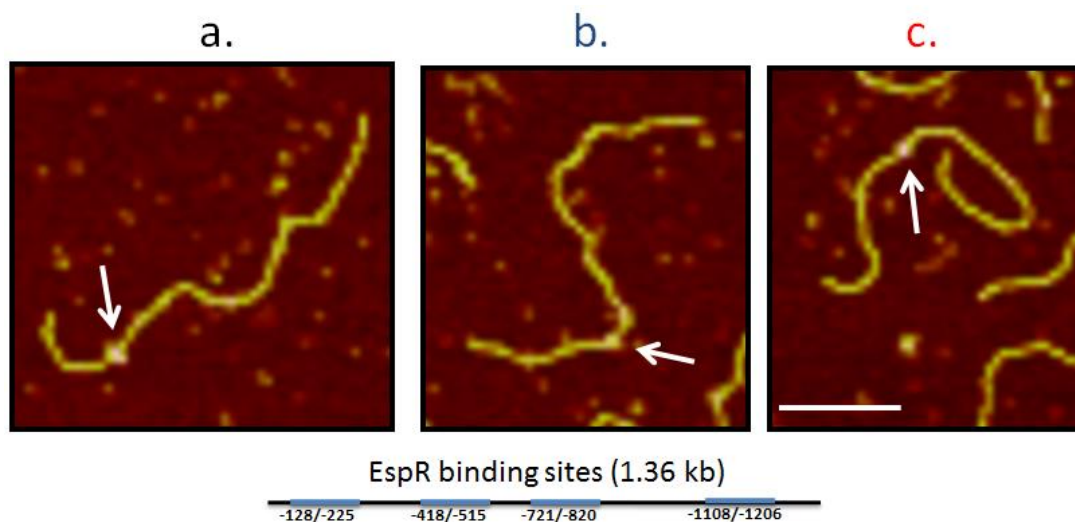


**Figure 3.2.4:** AFM images with the corresponding schematic representation of three strong binding sites for EspR. White arrows indicate the positions of bound EspR relative to the linear ends at positions: **a)**  $100 \pm 10$  nm &  $310 \pm 30$  nm **b)**  $140 \pm 15$  nm &  $280 \pm 15$  nm **c)**  $180 \pm 15$  nm &  $240 \pm 15$  nm. Scale bar 100 nm.



We selected those single bound DNA complexes and measured the relative positions where the proteins were bound. Since the DNA fragment was linear, we could measure the distance between the bond and the DNA ends. In this way we discovered that, at low concentration, EspR was predominantly binding at three positions on the *PespACD* fragment (Figure 3.2.4). These binding sites were positioned in respect to the linear ends of the DNA at:

Linear distance (min and max distance) to the DNA ends:

- a)  $100 \pm 10 \text{ nm}$  &  $310 \pm 30 \text{ nm}$
- b)  $140 \pm 15 \text{ nm}$  &  $280 \pm 15 \text{ nm}$
- c)  $180 \pm 15 \text{ nm}$  &  $240 \pm 15 \text{ nm}$

These sites were nicely overlapping with the theoretical positions of the strong binding sites in the *PespACD* fragment (178). Our results showed that at low concentration, EspR was indeed first occupying strong binding sites on the promoter sequence.

**Table 3.2.2:** Sample heights

Sample	Height
<i>Bare PespACD DNA</i>	$0.9 \pm 0.2 \text{ nm}$
<i>wildtype EspR</i>	$0.5 \pm 0.2 \text{ nm}$ & $1.0 \pm 0.2 \text{ nm}$
<i>K72A</i>	$0.5 \pm 0.2 \text{ nm}$ & $1.1 \pm 0.2 \text{ nm}$
<i>R70A</i>	$0.6 \pm 0.2 \text{ nm}$ & $1.3 \pm 0.2 \text{ nm}$
<i>R101A</i>	$0.6 \pm 0.2 \text{ nm}$ & $1.2 \pm 0.2 \text{ nm}$
<i>EspR <math>\Delta 10</math></i>	$0.5 \pm 0.2 \text{ nm}$ & $1.0 \pm 0.2 \text{ nm}$

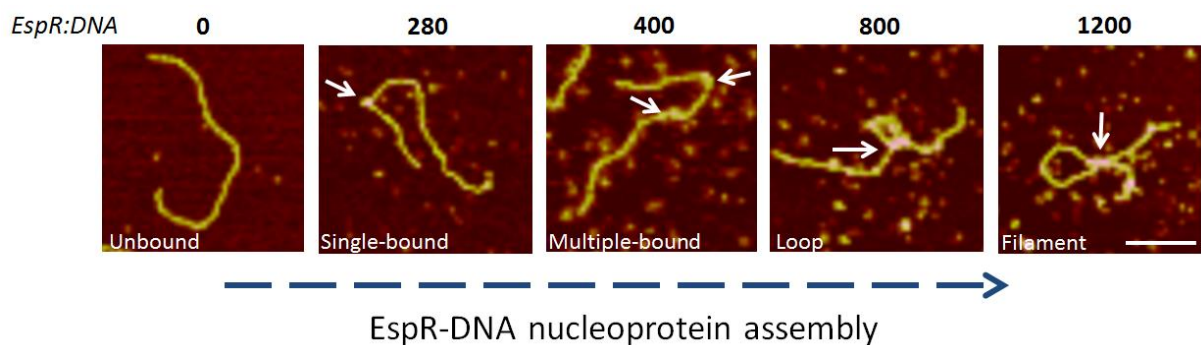


**Figure 3.2.5:** The proposed model of concentration dependent *EspR*- *PespACD* nucleoprotein complex formation. At low concentrations ( $EspR:DNA \leq 400$ ) initially strong binding sites are occupied by the *EspR*. Increasing the protein concentration leads to stabilisation of looped structures, which than further polymerase and form hairpin structures. Scale bar 100 nm.

### 3.2.3.2 Wild type EspR concentration dependent binding

As the next step, we studied the effect of the increasing EspR concentration on the resulting nucleoprotein complex formation. We gradually increased the concentration of the protein and investigated the specific structures formed (we used 280; 400; 800 and 1200 protein to DNA ratios). As discussed above, at low protein concentration (EspR:DNA  $\leq 400$ ), only strong binding sites were occupied. For the lowest ratio used (EspR:DNA =280) only ~45% of all structures were bound by the protein. 90% of all bound structures were either bound at single or multiple positions and only the remaining 10% were complex looped structures. The number of total bound structures increased dramatically and reached ~95% when the protein:DNA ratio was increased up to 1200 (Table 3.2.3). This meant that increasing amounts of the protein led to higher number of bound DNA. Interestingly, when used at the highest ratio, EspR proteins started forming higher order nucleoprotein complexes (Figure 3.2.5, 3.2.6 and 3.2.7). Up to ~30% of all bound structures were looped or filamentous nucleoprotein structures (Table 3.2.2 and Figure 3.2.7). As a control, we used EspR bound with the non-specific DNA fragment (1.3kb), not containing strong EspR binding sites (Protein:DNA control=400). Based on these data, we could propose a concentration dependent model of EspR-DNA nucleoprotein formation (Figure 3.2.5). At low EspR concentrations only strong DNA binding sites are occupied. Increasing the amount of the protein leads to further polymerisation of the DNA-protein complexes and formation of the looped structures, which than further forms filamentous hairpin structures (Figure 3.2.6).

**Table 3.2.3:** Concentration dependent EspR-DNA nucleoprotein complexes:

Protein :DNA	N	Relaxed	Bound	Single-bound	Multi-bound	Looped	Filament
<b>EspR :PespACD : 280</b>	175	57%	43%	33%	6%	3%	1%
<b>400</b>	195	32%	68%	37%	21%	8%	2%
<b>1200</b>	190	6%	94%	21%	46%	20%	7%
<b>Control</b>	190	59%	41%	33%	4%	3%	1%

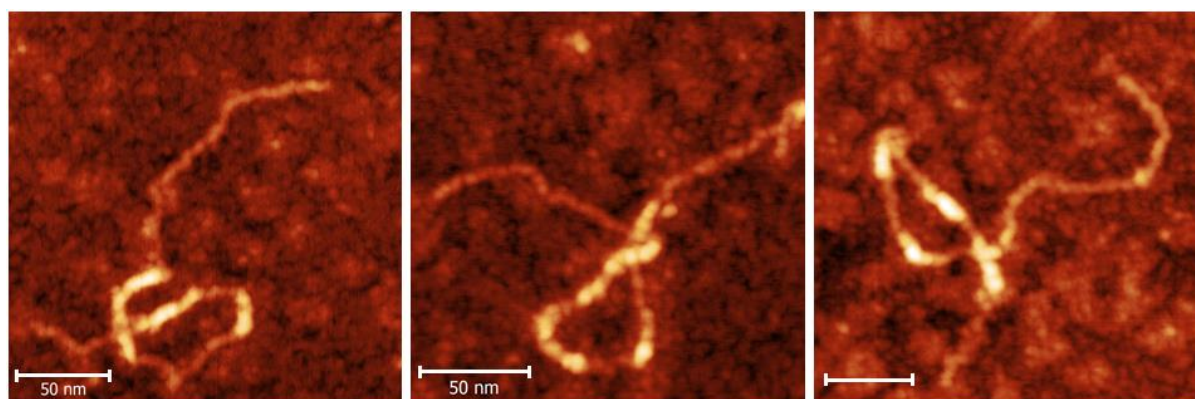


**Figure 3.2.6** High resolution AFM images of wild type EspR-PespACD DNA complexes. Scale bars 50 nm.

### 3.2.3.3 EspR mutants binding to *PespACD*

After studying how the wildtype protein was binding to the *PespACD* fragment, we investigated if certain mutations in the protein structure would influence its ability to bind DNA. To understand this, we incubated *PespACD* DNA with varying concentration of EspR variants (Protein:DNA ratio=280-1200). We studied the role of four mutations on the EspR-DNA binding and their capacity to form higher order structures. Three of the mutations were point mutations at positions Arg70, Lys72, and Arg101, obtained by substituting the residues with Alanine. The fourth mutant was a truncated form of EspR, having last 10 amino acids deleted. With the help of these mutations we could probe interactions at either the dimer, or the dimer-of-dimers interfaces. Incubating DNA fragment with increasing concentrations of EspR mutants, enabled us to directly compare wildtype proteins with the mutated ones in terms of their overall DNA binding affinity and capacity to form higher order complexes. Once again as a control experiment we incubated mutant EspR proteins with a 1.3kb DNA fragment, that did not contain the specific binding sites with the ratio Protein:DNA control=400 (Figure 3.2.7 and Figure 3.2.9).

As expected, gradual increase of the mutated protein concentration resulted in growing number of bound DNA molecules, similarly as in the case with the wild type EspR (Figure 3.2.7). Interestingly, for the same highest protein to DNA ratio of 1200, with the mutated forms of the protein, the total amount of bound DNA molecules was significantly lower compared to the wild type (between 50-85%). The lowest binding affinity was observed in the EspR $\Delta$ 10 mutant, where only half of the observed molecules were in bound state. These results indicate that Arg70, Lys72, and Arg101 as well as the last ten residues were very important for protein stability and optimal DNA-binding.

Based on our AFM data we could also estimate the capacity of EspR mutants to form higher order structures. Once again, the number of observed looped structures and filaments strongly varied between different mutants and were always fewer, compared to the wild type protein (Figure 3.2.9). As discussed above, for the highest wild type EspR to DNA ratio of 1200 tested, almost 30% of all observed bound structures were either looped or filamentous. In contrast, the R70A and K72A EspR-DNA complexes were incapable of forming DNA loops. Most of the DNA-bound proteins were gathering at isolated regions across the DNA fragments, while the overall DNA architecture appeared relaxed (Figure 3.2.7). Similarly, the truncated form EspR $\Delta$ 10 also caused globular DNA aggregation with little structuring effects on *PespACD*. Interestingly the R101A mutant, although showing overall lower DNA-binding affinity (~75%), still retained the ability to form some nucleoprotein loops (~22%).

Finally, we could conclude that the higher-order protein organization leading to DNA looping and filament stabilization was sequence-specific. We tested the binding affinity of wild type EspR and its variants for the control DNA fragment that did not contain any strong binding sites. We observed a decreased binding affinity (<40%) as well as almost complete disappearance of specific looped structures (<7%) (Figure 3.2.8 and figure 3.2.9).

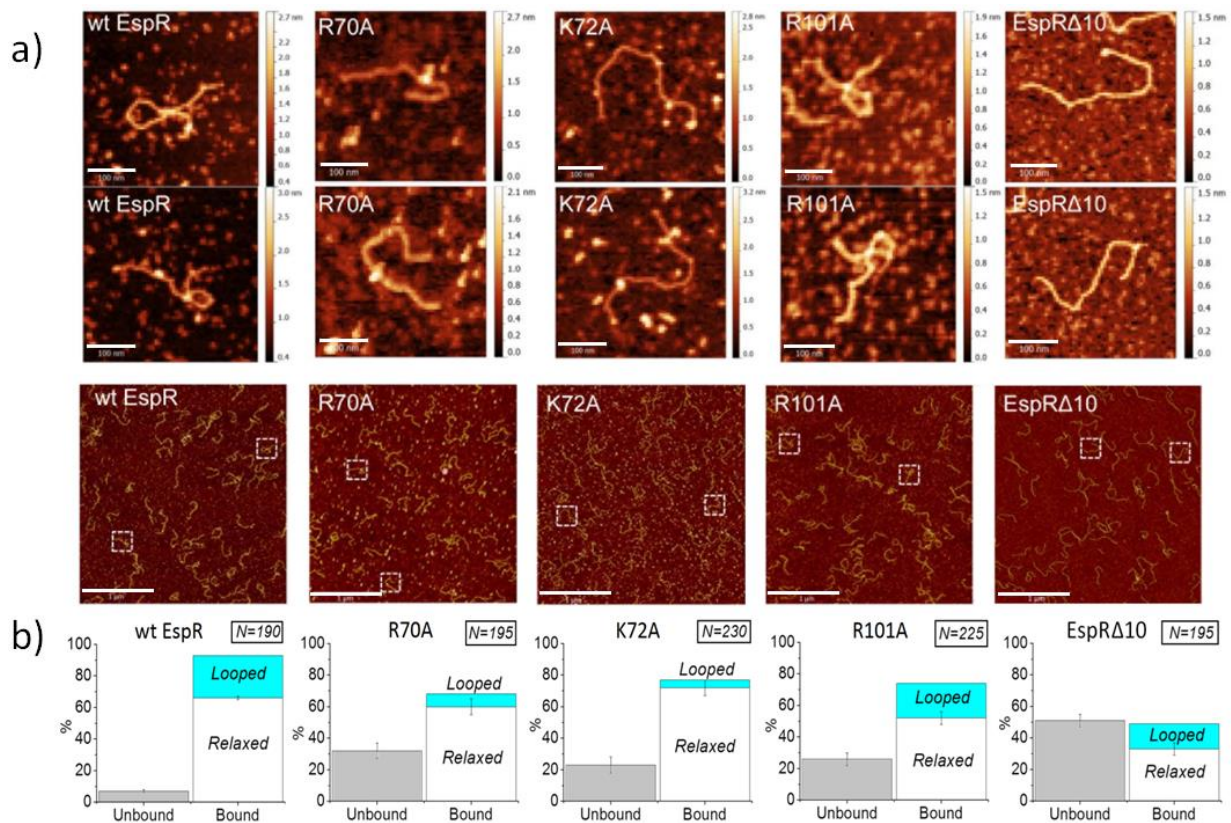


**Figure 3.2.7** AFM images of *EspR* wild-type and mutant-DNA complexes (a) wild type *EspR* (7.2 μM) incubated with *PespACD* (6 nM) showed large amounts of DNA-protein complexes with frequent DNA looping. The R70A, K72A, and *EspR*Δ10 mutants showed significantly lower DNA binding affinity compared with wild type *EspR*. These mutants also showed almost no DNA loop formation under identical conditions. Only the R101A mutant, despite lower DNA affinity still formed some DNA loops that were similar to those formed by wild type *EspR*. The first two rows show zoomed images (305 x 305 nm) of selected DNA molecules from the corresponding (same column) representative large-field AFM images (3 x 3 μm) in the third row. (b) Quantification of *PespACD* binding and DNA loop formation mediated by *EspR* variants. The number of DNA molecules analysed for each protein-DNA binding reaction is indicated in the square panels. The standard error bars indicate the variation in the number of “bound” versus “unbound” DNA molecules observed in the different AFM images for a given protein-DNA binding reaction. Scale bars for zoomed and large scale images are 100nm and 1μm respectively

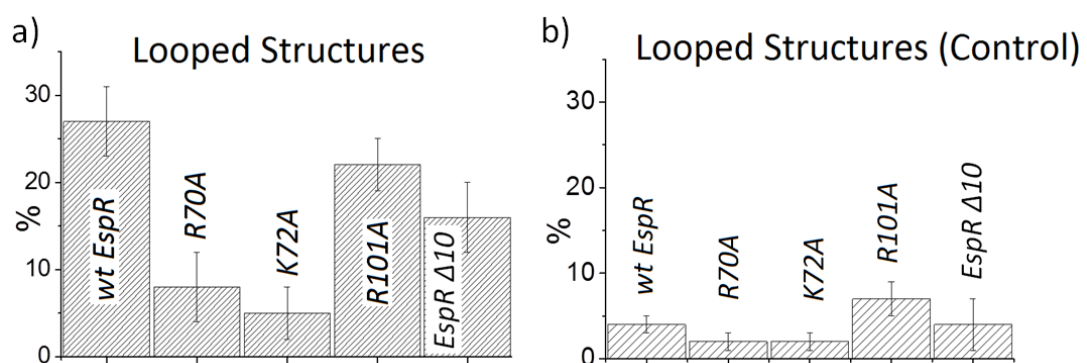


**Figure 3.2.8** Comparison of the percentages of looped DNA structures ( $\pm$  standard errors) induced by the different *EspR* variants tested on (a) *espACD* and (b) control DNA fragments.

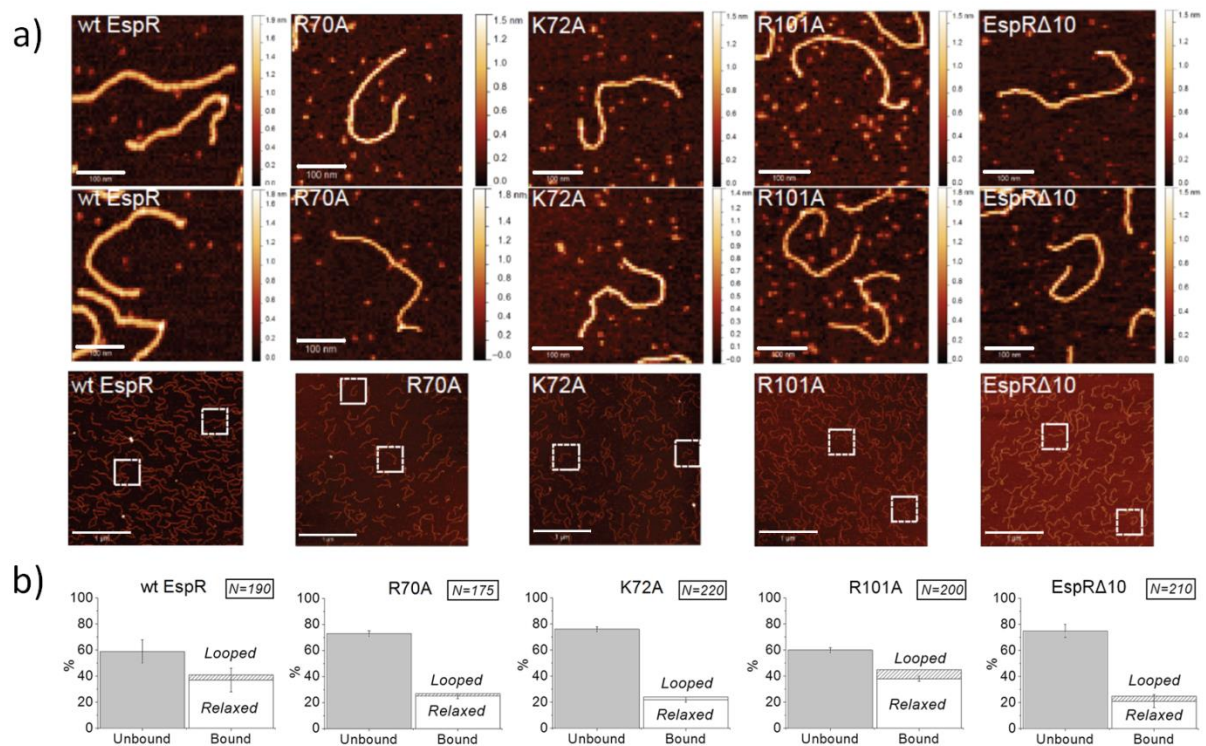


**Figure 3.2.9** Control AFM images of EspR variants ( $7.2 \mu\text{M}$ ) incubated with the non-specific DNA fragment ( $1.3 \text{ kb}$ ,  $6\text{nM}$ ). (a) The two first rows show selected zoomed images ( $305 \times 305 \text{ nm}$ ) of DNA molecules from the corresponding (same column) representative large field AFM images ( $3 \times 3 \mu\text{m}$ ) in the third row. (b) Statistics on free and protein-bound DNA molecules are shown. The number of DNA molecules analysed for each protein-DNA binding reaction is indicated. The standard error bars indicate the variation in the number of “bound” versus “unbound” DNA molecules observed in the different AFM images for a given protein-DNA binding reaction. Scale bars for zoomed and large scale images are  $100\text{nm}$  and  $1\mu\text{m}$  respectively.

### 3.2.4. Conclusions

EspR is a global regulator involved in pathogenesis of the *Mycobacterium tuberculosis*. It is an activator of the major virulence determinant, the ESX-1 secretion system, and thereby represents a possible drug target for tuberculosis disease treatment (189). Previous studies showed a direct link between transcriptional activity of EspR and conserved residues of the DNA-binding as well as residues involved in the dimerization domain (175,179,182). While the link between the DNA-binding domain and EspR transcriptional activity appears obvious, the relationship between EspR-EspR intersubunit interactions and transcriptional activity is much more complex to investigate.

In this study, we used atomic force microscopy to study the binding and the formation of higher order structures between EspR and its native *espACD* promoter. From our results, a concentration dependent model of EspR-mediated promoter organization could be drawn. As the first step, EspR dimer would nucleate at one or more high-affinity binding sites on the *espACD* promoter. Afterwards, cooperative polymerization would lead to linking of more distant DNA sequences and formation of transcriptionally active looped nucleoprotein complex.

We addressed also the question regarding the role of several charged residues in DNA binding stability of EspR. Replacing charged residues of Arg70, Lys72, and Arg101 with alanine, resulted in proteins with altered DNA-binding capacity. DNA binding efficiency was reduced almost twofold in the C-terminal mutant (EspR $\Delta$ 10), which had the last 10 residues deleted. These mutations also strongly affected the protein ability to form looped structures with *espACD* promoter. Only Arg101 mutant, despite lower DNA-binding affinity compared to wild type EspR, retained the capacity to form some higher order nucleoprotein loops.

Blockage of any of the steps required for EspR-*pespACD* loop formation would result in EspR dysfunction. Although AFM resolution is insufficient to determine the specific oligomeric state of the protein and understand how EspR mediates the interaction between the adjacent DNA duplexes, it still helps us understand the process of EspR-promotor interaction.

### 3.3 DNA sequence directs the assembly of H-NS filament

*This chapter is based on a paper submitted in the Journal of Biological Chemistry with the following authors: Aleksandre Japaridze<sup>1</sup>, Sylvain Renevey<sup>1</sup>, Patrick Sobetzko<sup>4</sup>, Liubov Stoliar<sup>2</sup>, Giovanni Dietler<sup>1</sup>, Georgi Muskhelishvili<sup>2,3</sup>*

Affiliations:

1 - Laboratory of Physics of Living Matter, EPFL Lausanne, Switzerland;

2 - Jacobs University D-28759 Bremen, Germany;

3 - UMR5240 CNRS/INSA/UCB, Université de Lyon, F-69003; INSA Lyon, Villeurbanne, F-69621, France

4 - Current address: Philipps-Universität Marburg, LOEWE-Center for Synthetic Microbiology, Marburg, Germany

#### **Abstract**

The cooperative binding of abundant nucleoid-associated proteins (NAP's) with numerous sites in the bacterial genome leads to stabilisation of distinct three-dimensional nucleoprotein structures. H-NS is a DNA architectural protein that preferentially binds AT-rich sequences and compacts DNA by bridging two duplexes. H-NS is involved in regulating both the gene expression as well as the shape of the chromosome. Growing evidence indicates that the nucleoprotein structures formed upon H-NS cooperative binding depend on environmental conditions. However, it is still unknown whether the variation in spatial organisation of H-NS binding sites on the genome can influence H-NS binding to the DNA and direct an assembly of distinct higher-order structures. In this study we used Atomic Force microscopy to visualize the formation of H-NS nucleoprotein complexes with different arrangements of H-NS binding sites on a circular DNA. We show that the binding site organisation is determinative for the final higher-order nucleoprotein structure. We thus provide the first experimental evidence that spatial organisation of binding sites for a nucleoid-associated protein can lead to structural differentiation of the bacterial chromatin.

### 3.3.1 Introduction

Bacterial chromosome is a highly dynamic entity undergoing structural changes during the whole bacterial growth cycle (190,191). These structural changes are thought to involve the binding effects of highly abundant nucleoid-associated proteins (NAPs), which themselves are produced in growth phase-dependent manner and when bound to DNA stabilize distinct three-dimensional structures (192-194). The histone-like nucleoid-structuring protein (H-NS) is one of the major NAPs (195) present continuously during the entire bacterial growth cycle. H-NS is regarded as a universal gene silencer (196), regulating the expression of horizontally acquired genes, the pathogenicity islands and virulence gene clusters in a wide range of bacterial pathogens (197-204). The binding sites for H-NS are non-randomly distributed in the genome (192,205), and it is assumed that H-NS is involved in the structural organisation of the nucleoid as well (206,207). H-NS has binding preference for curved DNA (208-210) and AT-rich sequence motifs (211). Importantly, H-NS belongs to a family of "DNA-bridging" proteins, repressing transcription by joining two DNA helices within a rigid nucleoprotein filament (212,213). The bridged DNA-H-NS filament can adopt an interwound configuration, presumably forming a right-handed plectoneme (194,213).

It is known that the superhelical density of the chromatin changes significantly during the bacterial growth cycle and adaptation to altered environment (214). H-NS plays an important role in this adaptation as one of the abundant NAPs involved in homeostatic regulation of DNA supercoiling (215). H-NS binding is known to constrain negative supercoiling in the DNA (216), also the binding of H-NS was shown to depend on supercoiling level of the DNA itself (217-219). It was proposed that binding of H-NS starts nucleating at high-affinity binding sites and then spreads along the DNA forming interwound filament (194,211). In keeping with this notion, during the bacterial growth cycle the H-NS nucleoprotein filament appears to expand from the initial binding loci in both directions along the DNA, whereby this spreading mechanism has been implicated in gene silencing (205,220). Interestingly, H-NS can also polymerise on a single DNA duplex leading to its apparent stiffening (221), yet the bridging of DNA has been specifically implicated in both "caging" and stalling the transcription machinery (222-224).

Despite the increasing evidence that environmental conditions can determine the DNA binding mode of H-NS, the role of the spatial arrangement of H-NS binding sites for the 3D nucleoprotein structure remains unknown. To answer this question we used circular DNA constructs carrying H-NS binding sites with different spatial arrangements and imaged their nucleoprotein complexes with H-NS using Atomic force microscopy. We demonstrate that distinct spatial arrangements of H-NS sites not only result in distinct structures having different flexibility and periodicity on the filament but also compact the DNA to different extent. We thus provide the first evidence that spatial pattern of binding sites for an abundant NAP (H-NS in our case) is determinative for the resulting 3D organisation of DNA-protein complexes.



### 3.3.2 Materials and Methods

#### Constructs

The basis of the UPUP, UPPU and PUUP construction were factor for inversion stimulation (FIS) and H-NS binding sites amplified using *E. coli* genomic DNA from the *tyrT* UAS sequence (U) and the *proV* gene (P) respectively. In the first amplification step, chromosomal DNA was used to produce linear P fragments flanked by HindIII and XbaI restriction sites on the one side and BamHI site on the other, as well as P fragments flanked BamHI site on the one, and NheI and EcoRI sites on the other. The U fragments with flanking restriction sites were produced in similar way.

UP and PU intermediate constructs were generated by joining U and P sequences cleaved at the BamHI linker end, ligation and cloning in pUC18 using the HindIII and EcoRI restriction sites.

In a second cloning step UP and PU were amplified from the intermediate UP and PU plasmids and joined via XbaI and NheI compatible sticky end ligation removing XbaI and NheI restriction sites, and cloned in pUC18 using HindIII and EcoRI sites. In the final constructs all U and P sequences are arranged as direct repeats. The annotated plasmid maps with the exact position of the FIS and H-NS binding sites are shown on Figure 3.3.1.

#### AFM Sample preparation

At first for every DNA construct a control sample without H-NS was prepared. The constructs were nicked using the Nt.BstNBI nuclease (NEB) and further purified from 1% agarose gel. DNA was diluted in the P1 buffer (1 mM TRIS-HCl, 4 mM MgCl<sub>2</sub>, 0.003% Tween 20, 2.5% Glycerol, pH 7.9) to a final concentration of 0.5ng/μl, than a 20 μl aliquot of the mix was deposited on a freshly cleaved mica for 7 minutes. The mica was then rinsed with 1ml of ultrapure (18.2 MΩ·cm resistivity) water and dried under a gentle flow of compressed filtered air.

Several samples at different H-NS:DNA ratios were then prepared for each DNA construct. Similarly to the control, in this case HNS was first diluted in the P1 buffer to the desired concentration. Then the DNA was added to a final concentration of 0.5ng/μl and 20 μl solution of the whole mix was left for incubation at 37°C for 5 minutes. Afterwards the mix was deposited on freshly cleaved mica for 7 minutes. The sample was then rinsed with 1ml of ultrapure (18.2 MΩ·cm resistivity) water and dried with a gentle flow of compressed filtered air.

#### DNA deposition on APTES modified mica surface

For the APTES deposition the mica surface was functionalized with APTES in a separate step prior to DNA deposition. Pure APTES (≥98% purity) was purchased from Sigma-Aldrich (Switzerland) and diluted in ultrapure water to a final concentration of 0.1vol%. A 15 μL droplet of diluted APTES solution was deposited on freshly cleaved mica for one minute, and then rinsed with 1 mL of ultrapure water. Finally the sample surface was dried using a gentle flow of compressed nitrogen.

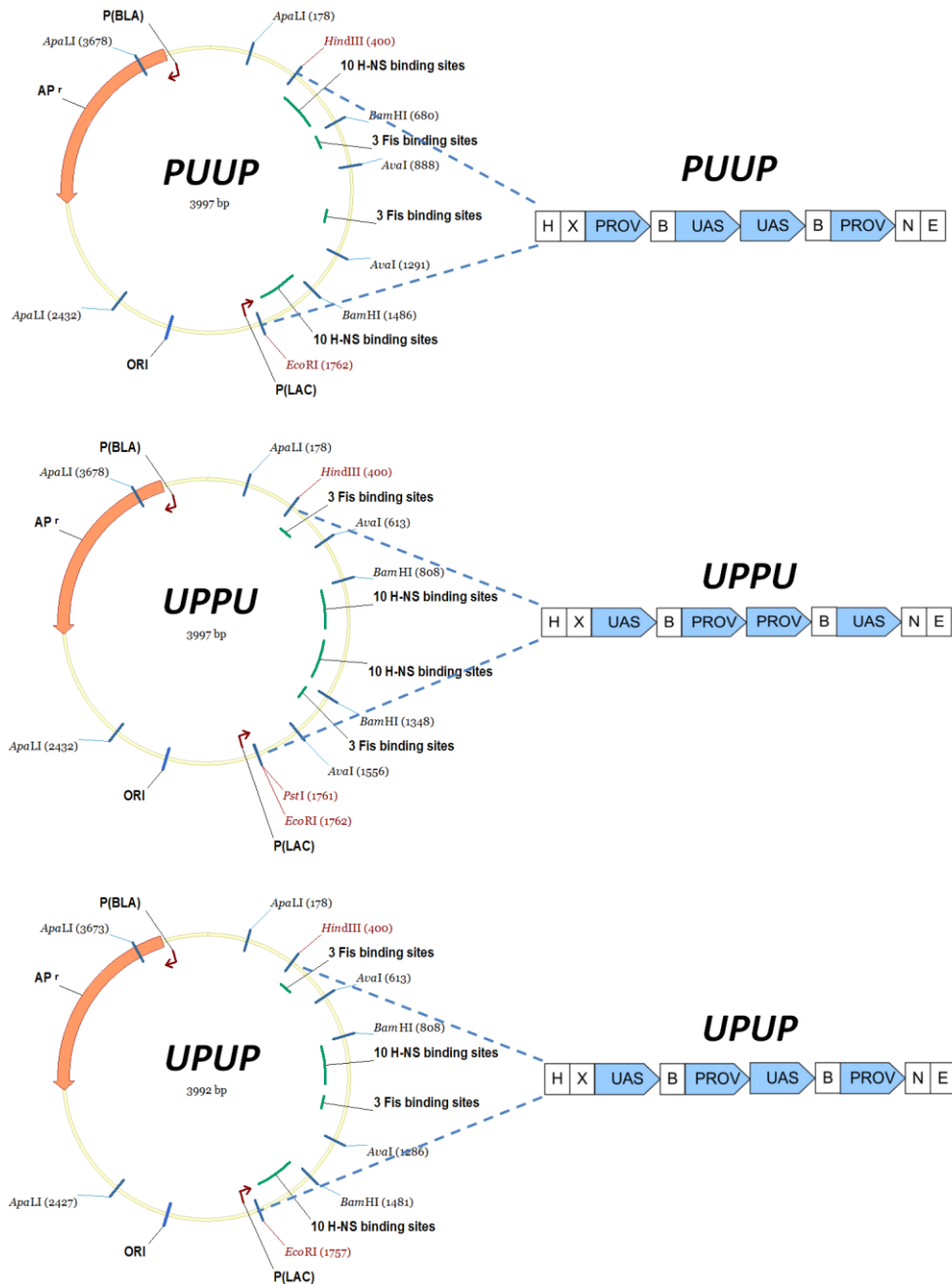


**Figure 3.3.1:** DNA maps of all three circular DNA used in the experiments. Linear dotted lines indicate the region of the inserted construct.

### AFM in air

AFM images were collected using a MultiMode SPM with a Nanoscope III controller (Veeco Instruments, Santa Barbara, CA, USA) operated in tapping-mode in air. The AFM cantilevers used in air had a spring constant of 5 N/m (Bruker cantilevers, TAP150A) with resonance frequencies ranging between 120 and 160 kHz. All recorded AFM images consist of 512 x 512 pixels with scan frequency  $\leq 1$  Hz. Each H-NS-DNA binding experiment was performed at least in duplicate. AFM images were obtained at several separate locations across the mica surface to ensure a high degree of reproducibility and were used for statistical analysis of H-NS-DNA complexes. Only H-NS-DNA complexes that were completely visible in AFM image

were considered for statistical analysis. The images were simply flattened using the Gwyddion software (Version 2.25) without further image processing (105).

### **Ultra High Vacuum AFM**

Images were collected using a home built AFM operating at room temperature and in UHV, as described elsewhere (93,96). Ultrasharp tips (<http://www.ntmdt-tips.com/products/group/dlc>) with nominal radius below 3nm were driven at resonant oscillation frequencies (~190-255 kHz) at 10 nm constant amplitude. All images were acquired at scan frequencies between 0.5-1 Hz. Images were collected using non-contact frequency modulation AFM operating mode, where a small negative frequency shift, typically of -2Hz, was used as a feedback setpoint. This means that at all times during imaging no compressive force was applied to the sample, and only small attractive forces of typically ~30pN were exerted by the AFM tip on the sample. All images were flattened and their height range adjusted using Gwyddion software without any further image processing.

### **Analysis software**

DNA molecules (typically 70 to-80 individual molecules) were analyzed using “DNA Trace”, Java-based analysis software that has been described elsewhere (106).

### **Persistence length determination**

We measured the persistence length  $l_p$  of DNA using the bond correlation function for polymers in 2D:

$$\langle \cos(\theta) \rangle = e^{(-s/2 \cdot l_p)} \quad (3.3.1)$$

where  $\theta$  is the angle between the tangent vectors to the chain at two points separated by the distance  $s$  and  $l_p$  the persistence length (36).

### **Analyses of topoisomer distributions.**

H-NS was purified as described previously (194). The PUUP, UPPU and UPUP plasmid DNA (250 ng) was incubated with increasing H-NS concentrations in a buffer containing 12.5 mM Tris-HCl pH 8.0, 50 mM NaCl, 2.5 mM MgCl<sub>2</sub>, 0.5 mM EDTA and 100µg/ml gelatin in a 20 µl volume for 30 min at 37°C. Afterwards TopoI of *E. coli* (kind gift of M. Glinkowska) was added for another 30 min. The reaction was stopped by addition of EDTA and phenol extraction. Purified plasmids were subjected high resolution gel electrophoresis for analyses of topoisomer distributions of plasmids using 1xTBE 1% agarose gels in the presence of different chloroquine concentrations as described previously (225).

### 3.3.3 Results

In order to study the role of spatial organisation of H-NS binding sites in nucleoprotein filament formation we generated three DNA constructs containing strong H-NS binding sites with different spatial organisation (see Materials and Methods).

DNA fragments were composed of the regulatory DNA sequences from the *E. coli proV* and *tyrT* gene promoters cloned into pUC18 backbone. *ProV* is the first gene of an operon encoding a transport system involved in sensing elevated osmolarity (226). The negative regulatory element (NRE) of this operon partially overlaps with the 5'-end of *proV* gene and contains several H-NS binding sites ( $K_D$  values between <15 nM and 25 nM). H-NS binding starts cooperatively at two high affinity sites in NRE silencing the operon (218). The upstream activating sequence (UAS) of the *tyrT* (tyrosyl tRNA) gene promoter contains strong binding sites for another abundant NAP, namely FIS (227). Interestingly, binding of H-NS at UAS antagonizes the activation of the *rrnB* promoter by FIS (222) but the *tyrT* UAS does not contain characterised high-affinity binding sites for H-NS. We thus constructed plasmids containing the *proV* NRE sequences (spanning about 230 bps and denoted as "P") and the *tyrT* UAS sequences (spanning about 80 bps and denoted as "U") in three different tandem arrangements (UPUP, PUUP and UPPU; see Fig.3.3.1) in which each repetitive element (either P or U) was separated by about 40bps of the intervening DNA. These three plasmid constructs were visualized by atomic force microscopy (AFM) after incubation with increasing concentrations of H-NS. To avoid complications of visualising distinct structures due to intertwining of the supercoiled DNA, the constructs were relaxed by nicking with Nt.BstNBI nuclease (see Materials and methods).

#### 3.3.3.1 Global organisation of the DNA by H-NS

Once the constructs were incubated in the presence of H-NS, three broad classes of structures started to emerge (Figure 3.3.2). Two of these classes had very distinct architectures denoted as filament-loop (FL) (DNA structures having one tight filament and one opened DNA region) and loop-filament-loop (LFL) structures (two opened DNA regions connected with a filament). The third class consisted of more complex architectures (representative images are shown on Figure. 3.3.3). Most importantly, these three classes of structures formed with different efficiency depending both on the DNA construct used as well as H-NS concentration (Table 3.3.1a-c). For PUUP construct harbouring two *proV* regions (denoted as P) with high-affinity H-NS binding separated by two copies of the *tyrT* UAS sequences (denoted as U), the Loop-filament-Loop structures prevailed over Filament- Loop structures at the low and intermediate

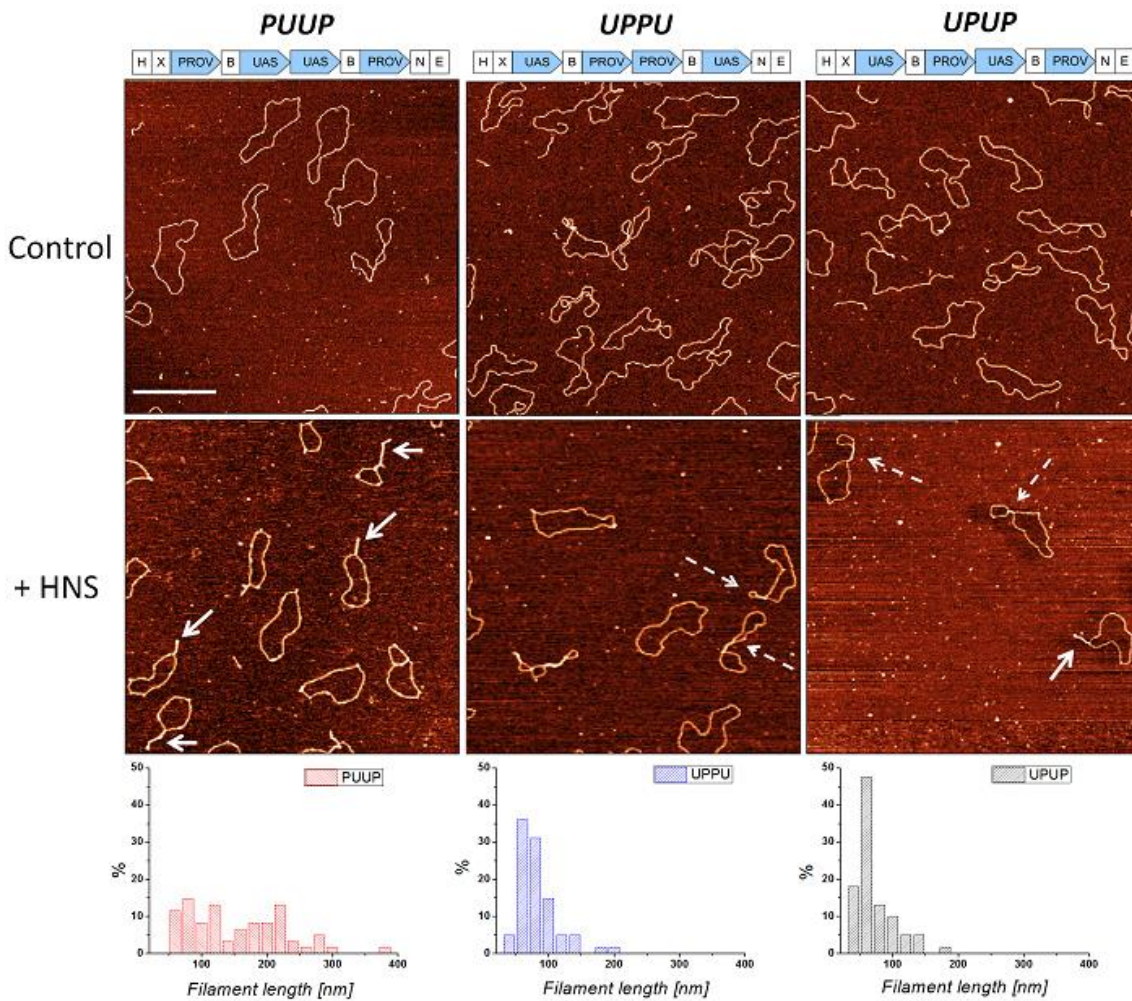


**Figure 3.3.2:** AFM images of control and H-NS bound circular DNA constructs plotted with the respective distributions of maximal filament length. White continuous arrows indicate Filament-Loop structures and dashed arrows indicate Loop-Filament-Loop structures. Scale bar 500nm

(H-NS:PUUP < 9:1 molar ratio) H-NS concentrations (Table 3.3.1a). However, at the highest H-NS concentrations (H-NS:DNA molar ratio of 13 : 1) mostly the FL structures ( $\approx 50\%$ ) were observed (Table 3.3.1a). For UPUP construct, similarly to PUUP, the LFL structures prevailed over FL structures at the low and intermediate H-NS concentrations. Yet in contrast to PUUP, at the highest H-NS concentrations the UPUP construct formed the FL and LFL structures with almost identical efficiency (Table 3.3.1b). Interestingly, the third construct UPPU, in which the high-affinity H-NS binding sites are flanked by *tyrT* UAS region, formed exclusively LFL structures attaining the maximum (17%) at the highest used H-NS concentrations (Table 3.3.1c). Notably, also the overall amount of structures bound by H-NS for these three constructs was different. The lowest was for UPPU ( $\sim 55\%$  bound), slightly higher for UPUP ( $\sim 65\%$  bound) and highest for PUUP ( $\sim 80\%$ ). These data suggested that, although H-NS could bridge distant sites in the DNA in all of the three constructs, the spatial organisation of the binding sites determined both the efficiency of H-NS binding as well as the ensuing DNA structures.

**Table 3.3.1a:** Shape parameters of PUUP-H-NS complexes

<i>H-NS : PUUP</i>	<i>Relaxed</i>	<i>1/2 crossing</i>	<i>Filament -Loop</i>	<i>Loop-Fil-Loop</i>	<i>Other</i>	<i>Total</i>	<i>Unbound</i>	<i>Bound</i>
Control	58%	15%	4%	3%	20%	144	73%	27%
6 : 1	46%	24%	3%	8%	18%	157	71%	29%
9 : 1	42%	9%	7%	20%	23%	158	51%	49%
13 : 1	21%	1%	49%	6%	22%	156	22%	78%

**Table 3.3.1b:** Shape parameters of UPUP-H-NS complexes

<i>H-NS : PUUP</i>	<i>Relaxed</i>	<i>1/2 crossing</i>	<i>Filament -Loop</i>	<i>Loop-Fil-Loop</i>	<i>Other</i>	<i>Total</i>	<i>Unbound</i>	<i>Bound</i>
Control	58%	21%	3%	3%	15%	134	79%	21%
6 : 1	42%	7%	8%	17%	26%	133	49%	51%
9 : 1	40%	4%	9%	17%	30%	116	44%	56%
13 : 1	25%	11%	23%	22%	19%	96	36%	64%

**Table 3.3.1c:** Shape parameters of UPPU-H-NS complexes

<i>H-NS : PUUP</i>	<i>Relaxed</i>	<i>1/2 crossing</i>	<i>Loop-Fil-Loop</i>	<i>Other</i>	<i>Total</i>	<i>Unbound</i>	<i>Bound</i>
Control	48%	25%	6%	21%	142	73%	27%
6 : 1	55%	11%	11%	24%	170	65%	35%
9 : 1	47%	13%	15%	25%	152	60%	40%
13 : 1	31%	13%	17%	39%	151	44%	56%

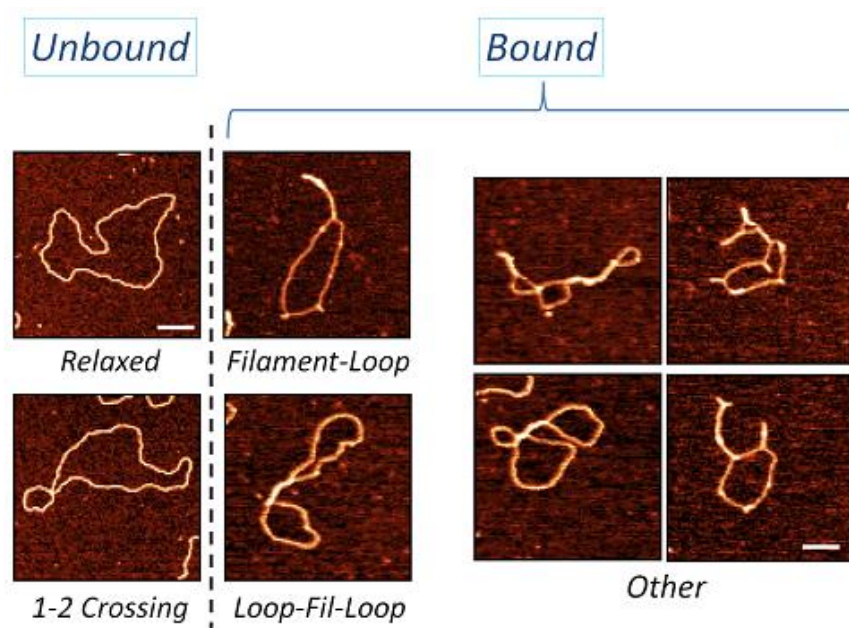


**Figure 3.3.3:** AFM images of specific structures formed by H-NS DNA complexes. Scale bar 100 nm.

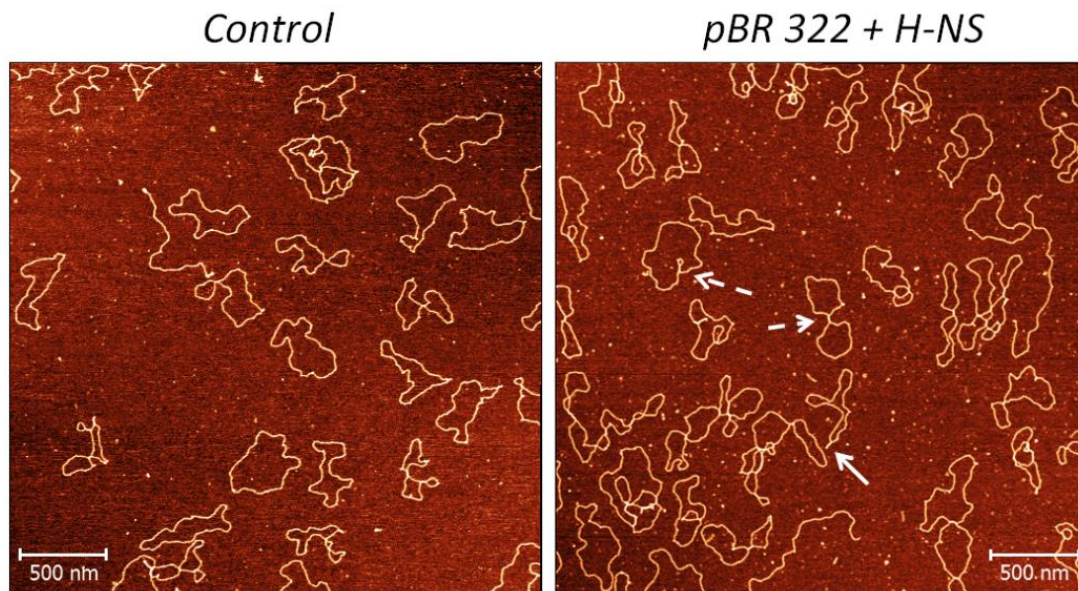


**Figure 3.3.4:** AFM images of pBR322 (4.4kb) control DNA with and without H-NS. Scale bars 500 nm.

To make sure the observed structures were directly linked with the arrangement of strong H-NS binding sites, we measured the binding of H-NS to a circular DNA which did not have any strong H-NS binding sites. For this reason we used 4.4kb circular relaxed pBR322 DNA (Figure. 3.3.4). When bound with H-NS (H-NS:pBR322 13:1) we observed a mixture of both FL ~7% (white continuous arrows) and LFL ~14% (white dashed arrows) structures, both structures lower compared to constructs containing strong binding sites. The total number of bound structures (~58%) was lower compared to PUUP and UPUP constructs for the same H-NS : DNA ratio (13:1 molar ratio), but comparable to UPPU construct.

### 3.3.3.2 Properties of the H-NS filaments

To get more insight into the specific organisation of H-NS filaments formed on different constructs we decided to measure the persistence lengths of the nucleoprotein complexes. The plasmid constructs, in the absence of H-NS showed fairly similar persistence lengths of about ~60 nm (Figure. 3.3.5 and Table 3.3.2). Addition of H-NS significantly affected the persistence lengths for all three constructs (Figure. 3.3.5 and Table 3.3.2). At the highest H-NS concentration, the decrease of persistence length was more significant for UPPU (44±2 nm) compared to both UPUP (54±2 nm) and PUUP (64±2 nm).

This difference in persistence length can be directly correlated to the formation of H-NS filaments that locally stiffen the DNA. Presumably the binding of H-NS screens negative charges from the DNA, locally decreasing the persistence length, though bridging the DNA and forming the filament stiffens the structure on a larger scale.

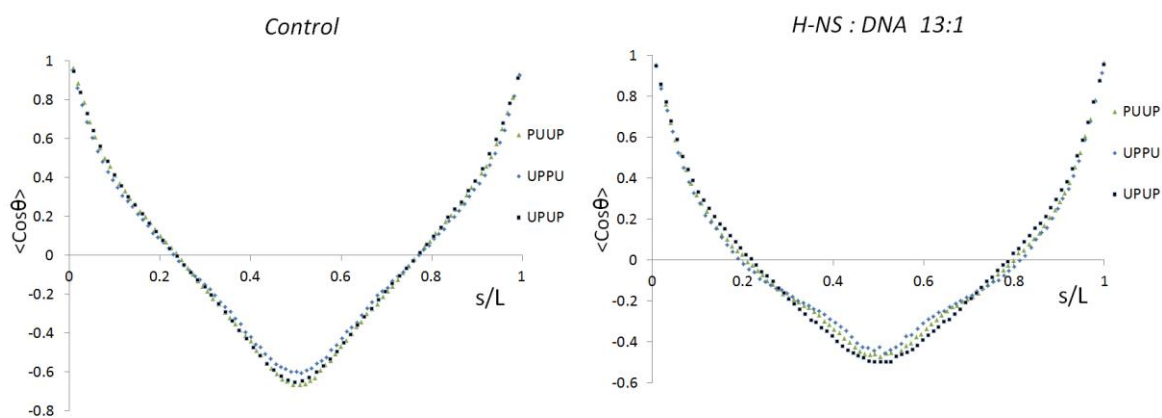


**Figure 3.3.5:** The persistence length is calculated by fitting the slope of the correlation function. The steeper the decay, the lower the persistence length of the construct. We see that the shape of the correlation function is identical for all three constructs without adding H-NS. The decay rate as well as the shape of the correlation function changes significantly when we add H-NS. The initial part of the correlation function of H-NS-PUUP construct decays slowest indicating high persistence length, whereas the one of UPPU decays fastest, leading to the lowest persistence length.

As the next step, we measurements the filament lengths for different constructs. The filaments formed at UPUP showed a slightly higher average length compared to UPPU, whereas filaments formed at PUUP had the largest average length (Figure 3.3.2 and Table 3.3.2). These observations reflect well the difference in the persistence length. PUUP construct with the longest filament on average, had the highest persistence length. To make sure these differences in filament length were not due to the experimental deposition method, we imaged the nucleoprotein complexes on APTEs modified mica surface (Figure 3.3.6a).

**Table 3.3.2:** Shape parameters of DNA constructs bound with HNS deposited with  $MgCl_2$  on Mica surface (HNS:DNA molar ratio 13:1)

DNA on 4mM $MgCl_2$		Number of Molecules	DNA Contour length $L$ [nm]	DNA persistence length $l_p$ [nm]	Average Filament length $l$ [nm]
Control	PUUP	75	$1170 \pm 35$	$62 \pm 2$	-
	UPUP	75	$1180 \pm 60$	$61 \pm 2$	-
	UPPU	70	$1210 \pm 50$	$59 \pm 2$	-
H-NS : DNA = 13:1	PUUP + HNS	75	$1190 \pm 55$	$64 \pm 2$	$155 \pm 70$ nm
	UPUP + HNS	70	$1150 \pm 50$	$54 \pm 2$	$75 \pm 30$ nm
	UPPU + HNS	70	$1170 \pm 50$	$44 \pm 2$	$65 \pm 30$ nm



APTES treated surface, due to strong charge-charge interactions, kinetically traps the complexes and thus better preserves 3D configuration of the DNA (22,33,59). DNA constructs deposited on APTES, without the presence of H-NS, showed compact structures with multiple DNA crossovers, indicating a strong DNA-surface interaction. DNA did not show any branching or filamentous structures characteristic features of H-NS binding. Interestingly when bound with H-NS, DNA showed multiple DNA-DNA contacts, with the whole construct adopting an elongated filamentous structure.

Furthermore we could compare the nucleoprotein complexes by the propensity of branching when deposited on APTES (Figure 3.3.6b). For our constructs, PUUP had the most frequent branching of all plasmids (Table 3.3.3). Results obtained for APTES-deposited H-NS-DNA complexes indicated that the differences observed between the constructs were independent of the specific deposition method used.

We infer that the PUUP and UPPU constructs, which differentially bind H-NS and preferentially form FL and LFL structures respectively, significantly differ also in terms of the stabilized filament length (Figure 3.3.6; Table 3.3.2 and Table 3.3.3). Importantly, plotting of the filament lengths at the maximal H-NS concentration (H-NS:DNA=20:1) against the plasmid contour length revealed an inversely linear dependency for PUUP but not for UPPU and UPUP (Figure 3.3.7), indicating a difference in DNA packing by H-NS.

**Table 3.3.3:** Shape parameters of H-NS-DNA complexes deposited on APTES modification mica surface (HNS : DNA molar ratio 20:1)

<b>APTES</b> <i>H-NS: DNA ratio 20:1</i>	<b>Number of</b> <b>Molecules</b>	<b>DNA Contour</b> <b>length L [nm]</b>	<b>DNA Branching</b> <b>[%]</b>	<b>Average max Filament</b> <b>length l [nm]</b>
<i>PUUP</i>	35	1305 ± 35	22 %	45 ± 15 nm
<i>UPUP</i>	35	1300 ± 50	14 %	35 ± 10 nm
<i>UPPU</i>	33	1315 ± 25	14 %	30 ± 10 nm

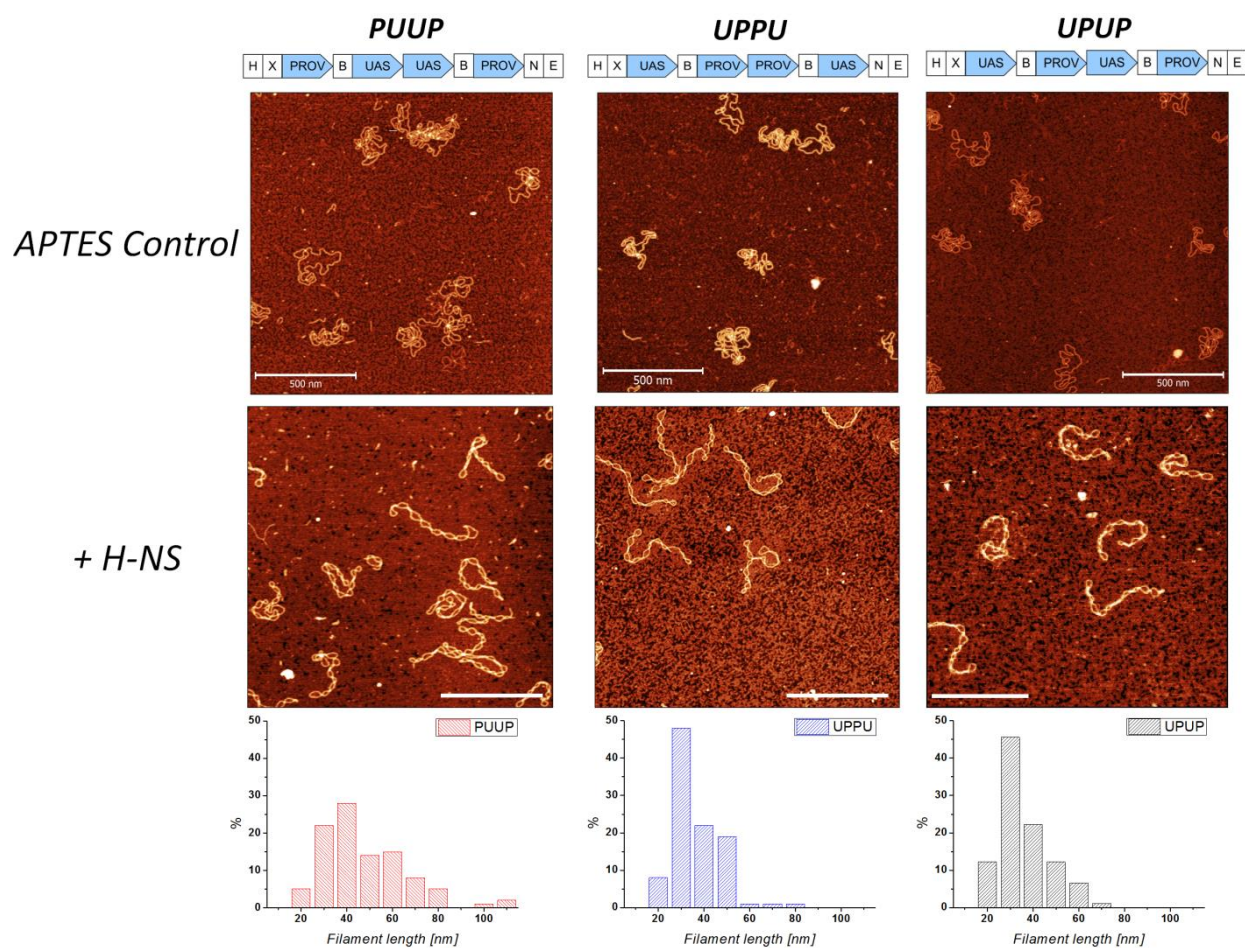


**Figure 3.3.6a:** AFM images of different constructs with and without H-NS (H-NS:DNA molar ratio 20:1) plotted with the respective distributions of maximal filament length. Upper AFM image show control DNA deposited on APTES treated mica imaged in air; lower images represent DNA constructs bound with H-NS deposited on APTES. Scale bars 500 nm.

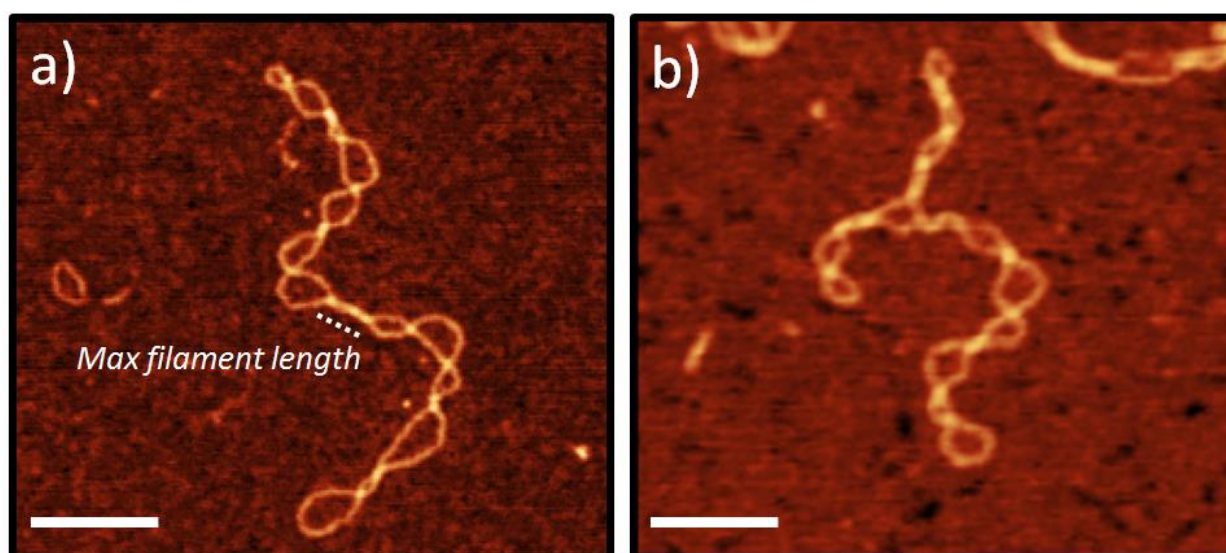


**Figure 3.3.6b:** Close up AFM images of different constructs bound with H-NS deposited on APTES. a) The dashed line shows the maximal filament length for structures on APTES b) Typical branched structure on APTES. Scale bars 100 nm.

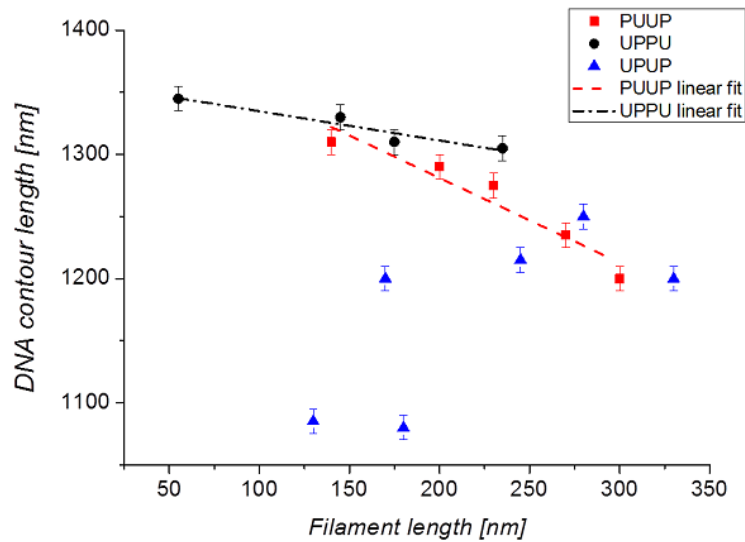


**Figure 3.3.7:** DNA contour length dependency on H-NS filament length. PUUP construct shows a negative linear dependency on filament length, indicating a linear shortening of the contour length as the function of H-NS filament length (red line shows a linear fit). UPPU construct shows no clear dependency of the DNA contour length as the function of H-NS filament.

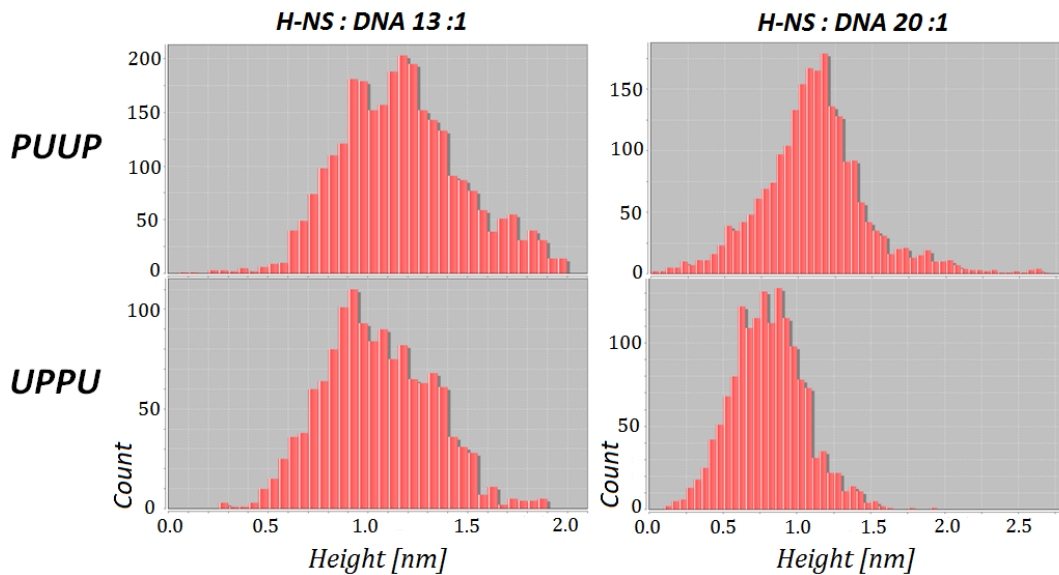


**Figure 3.3.8:** Height distribution along H-NS filaments for PUUP and UPPU constructs at different H-NS : DNA concentration. For both H-NS : DNA concentration the average height along the PUUP filament is higher than the height of UPPU filament indicating different packing

### 3.3.3.3 H-NS filament height

Based on the data in Figure 3.3.7, UPPU and PUUP fragments had clearly different packing of the H-NS filament. PUUP filament was resulting in DNA compaction, whereas the UPPU filament was not. These differences in packing must had to result in different heights of the packed filament, with higher filament indicating more compaction. In order to characterize the different types of filaments formed by PUUP and UPPU constructs, we measured the height distribution along these filaments for different H-NS concentration. As predicted, for both 13:1 and 20:1 H-NS to DNA ratios, the average height along the PUUP filament was higher than the one for UPPU construct (Figure 3.3.8).

### 3.3.3.4 H-NS binding distinctly constrains the DNA on different constructs.

AFM is a surface imaging technique. The sample needs to be deposited and attached to the necessary surface to be imaged. Therefore to check, how reliable our AFM measurements were, we asked ourselves whether the differences in DNA packing measured by AFM could be observed also in solution. Binding of H-NS was shown to constrain DNA supercoils *in vitro* (216). This constraint can be analysed by first forming H-NS- supercoiled DNA complexes, than relaxing the available free supercoils by DNA topoisomerase treatment and finally monitoring the distribution of plasmid topoisomers after removal of the bound protein.

We monitored the distribution of topoisomers of supercoiled PUUP, UPPU and UPUP constructs in complex with increasing concentration of H-NS after treatment with *E.coli* topoisomerase I (topoisomerase I exclusively removes negative supercoils).

The plasmids were analyzed in the presence of different chloroquine (an intercalator) concentrations. We found that that UPPU constrains DNA more efficiently than PUUP or UPUP (Figure 3.3.9; the effect is clearly seen at highest H-NS concentrations indicated by white arrows, lanes 3, 10 and 17). Even at the highest chloroquine concentration used, the UPPU DNA remained negatively supercoiled, whereas both the PUUP and UPUP DNA's migrated as positively supercoiled species.

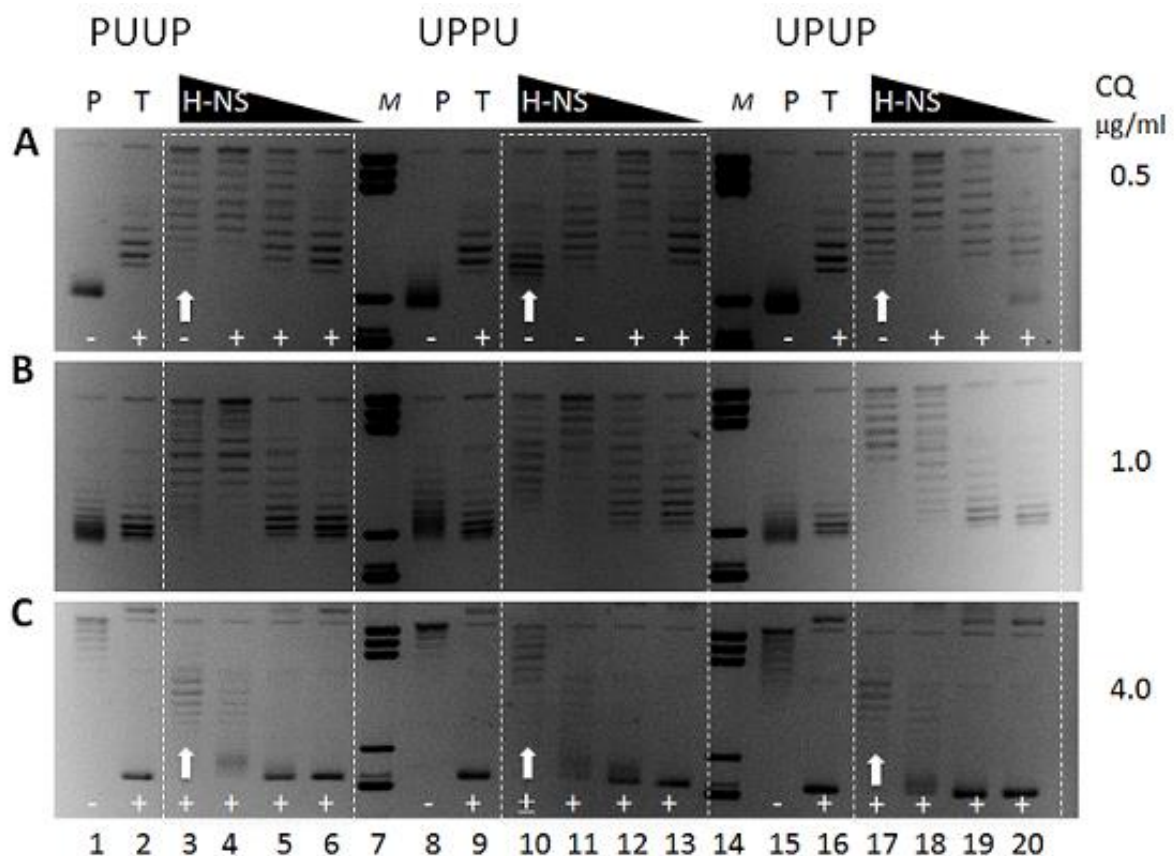


**Figure 3.3.9:** High-resolution agarose gel-electrophoresis of PUUP, UPPU and UPUP constructs. The plasmids were incubated with different H-NS concentrations and relaxed by *E. coli* TopoI. P- untreated plasmid; T - TopoI treatment; M- DNA size marker. **A.** Gel-electrophoresis at 0.5 µg/ml chloroquine concentration. Note that under these conditions the plasmids relaxed by TopoI treatment (line T) migrate as moderately positively supercoiled species in the gel. Addition of H-NS has negligible effect at lowest concentrations (lanes 6, 13 and 20) but with increasing concentrations (lanes 5, 12

and 19) the migration of plasmids is retarded because they are less positively supercoiled due to protection of negative supercoils by H-NS binding. This effect becomes more conspicuous at higher H-NS concentration for PUUP and UPUP (lanes 4 and 18) but not for UPPU (lane 11). This is because at this concentration the constraint of DNA by H-NS is enough to preserve negative supercoils and so, the population in lane 11 migrates as negatively supercoiled species. This difference in the efficiency of constraint between UPPU and the other constructs is clearly evident at the highest H-NS concentration (lanes 3, 10 and 17, indicated by white arrows).

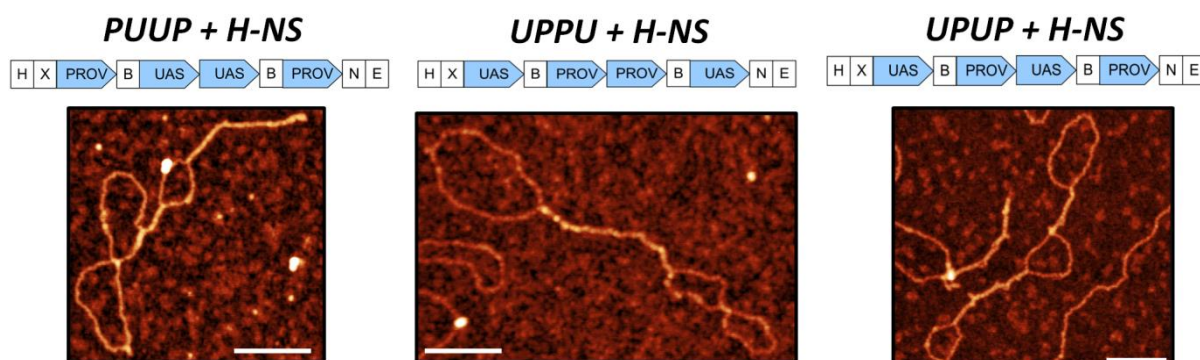


**Figure 3.3.10:** AFM images of different constructs bound with H-NS (H-NS : DNA molar ratio 20:1) imaged in ultra high vacuum. Scale bars 100 nm.

### 3.3.3.5 Periodic structure of H-NS filaments

After making sure, the observed filament differences were reproducible in solution, to gain more insight into the packing differences of the H-NS filaments between the UPPU and PUUP constructs we used Ultra High Vacuum AFM. Imaging the sample in ultra high vacuum gave us the opportunity to acquire extremely high-resolution data on the filaments (Figure 3.3.10).

In both, PUUP and UPPU constructs, the filaments demonstrated a clear periodicity, but the periodicity was being different (Figure 3.3.11). PUUP filament periodicity was  $\sim 5$ -10nm, whereas for UPPU filament it was  $\sim 10$ -20nm (Table 3.3.4). The latter periodicity is in agreement with the values obtained previously for interwound H-NS nucleoprotein filament formed on the linear lambda phage DNA (194). Taken together our data indicate that not only the overall shape of the DNA but also the packing, stiffness and extension of the H-NS nucleoprotein filament depend on the spatial organisation of the H-NS binding sites in the substrate DNA.

**Table 3.3.4:** Shape parameters of H-NS-DNA complexes in UHV

<b>UHV</b> <i>H-NS: DNA ratio 20:1</i>	<b>Number of Molecules</b>	<b>DNA Contour length <math>L</math> [nm]</b>	<b>Filament periodicity [nm]</b>	<b>Average Filament length <math>l</math> [nm]</b>
<i>PUUP</i>	60	$1270 \pm 80$	5-10	$220 \pm 70$
<i>UPUP</i>	60	$1240 \pm 110$	5-10	$205 \pm 60$
<i>UPPU</i>	60	$1310 \pm 55$	10-20	$150 \pm 95$

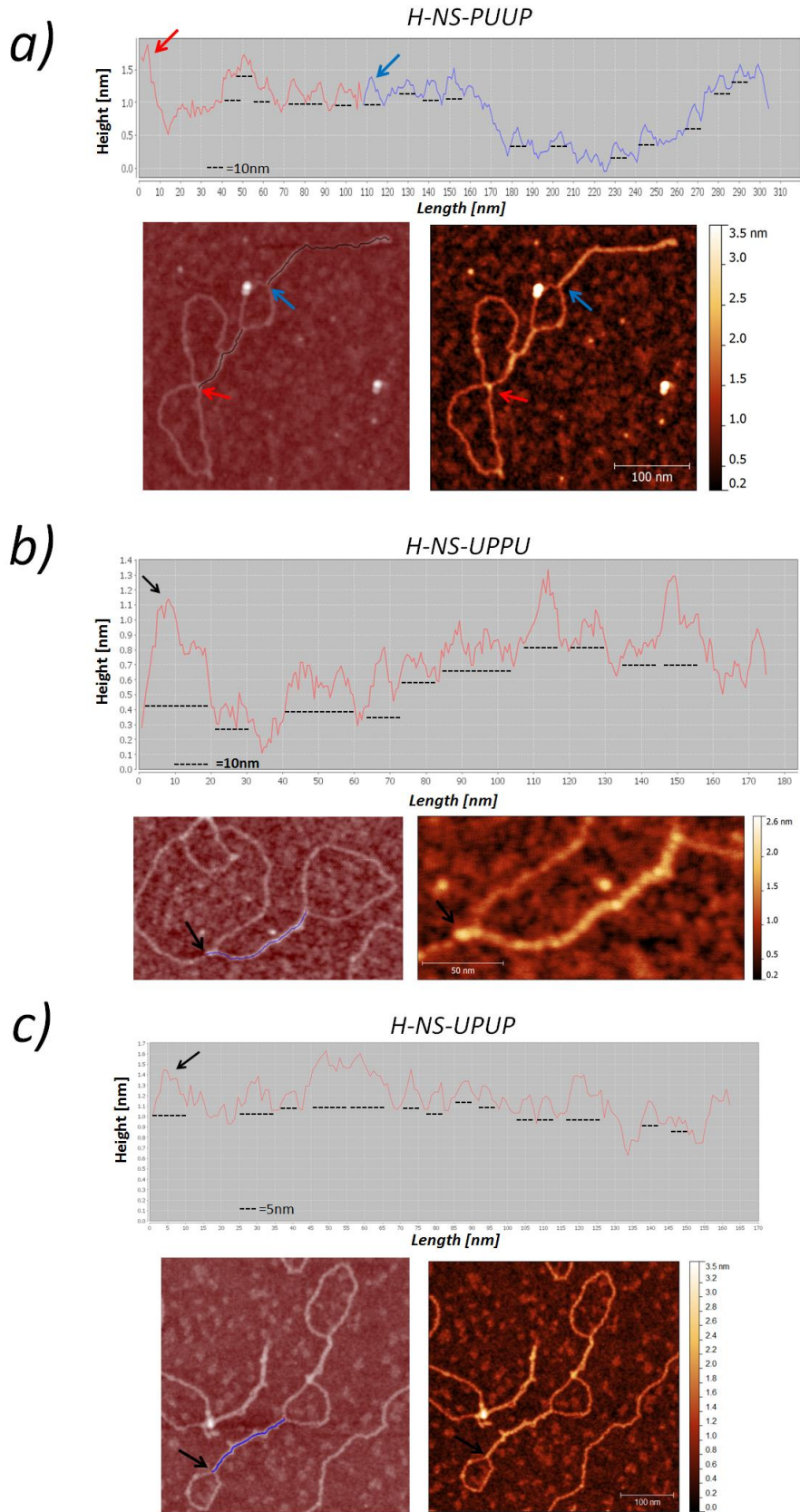


**Figure 3.3.11:** Measurement of the filament periodicity in ultra high vacuum. Height measurements along individual filaments. a) PUUP filament (100nm scale bar); b) UPPU filament (50nm scale bar); c) UPUP filament (100 nm scale bar). The arrows indicates the start of the height profiles

### 3.3.4 Conclusions

In this study we investigated how different spatial arrangements of DNA sequences containing strong binding sites for an abundant DNA architectural protein determine the final 3D structure of the assembled nucleoprotein complex. For this reason we used H-NS, an abundant DNA-bridging NAP involved in many cellular processes, such as bacterial motility, stress response and virulence (196,228). For our experiments we constructed various combinations of DNA sequences harbouring high-affinity H-NS binding sites from the *proV* promoter, linked with UAS regions of a stable RNA (*tyrT*) promoter characterized by bending anisotropy (Figure 3.3.1). The sequences were arranged in three different configurations : in one construct two *proV* regions were “sandwiched” between two flanking UAS regions (UPPU), in the second construct two UAS regions were “sandwiched” between two flanking *proV* (PUUP), whereas in the control construct individual *tyrTUAS* and *proV* regions were arranged in an alternating manner (UPUP).

When bound with H-NS protein, we started observing huge differences between the nucleoprotein complexes formed on individual constructs:

First: depending on the DNA sequence, different types of nucleoprotein complex were stabilised by H-NS. PUUP arrangement predominantly formed Filament-loop structures; UPPU formed Loop-filament-loop structures and UPUP formed both structures with almost identical efficiency.

Second: we found that the binding affinity of H-NS and the resulting length of the H-NS filament varied significantly. The filament length and accordingly the persistence length were largest for H-NS-PUUP complex, being higher compared to both H-NS-UPPU and H-NS-UPUP complexes.

Third: we observed an inversely linear dependency of PUUP contour length on the H-NS filament length. For UPPU and UPUP construct no such dependency was observed.

Fourth: H-NS constrained supercoils more efficiently when bound to UPPU, rather than PUUP or UPUP.

Fifth: PUUP construct had a higher branching probability than any other construct when bound with H-NS and deposited on APTES treated surface.

Finally: UPPU formed an H-NS filament of distinct periodicity, different from both PUUP and UPUP.

To sum up, PUUP and UPPU construct differed across all the measured parameters, irrespective of measurement details (Table 3.3.5). Interestingly, for the “mixed” construct UPUP all the measured parameters lied in-between, with some of them being more similar either to PUUP or UPPU. The H-NS-UPUP structures were more similar to UPPU with filament length and propensity of branching, and to PUUP in terms of exhibited constraint of DNA superhelicity and filament periodicity. The overall H-NS binding affinity and the persistence length showed average values (Table 3.3.5). Our data indicates that the spatial organization of H-NS binding sites on the DNA can direct the assembly of distinct 3D nucleoprotein structures.

To understand why PUUP form more extended H-NS filaments compared to the other constructs, we looked at the spatial arrangement of the H-NS binding sites? The main difference between PUUP and the other constructs was the large separation of the *proV* regions (regions harbouring high-affinity binding sites). Assuming that nucleation of the H-NS filament requires H-NS bounding at high-affinity sites with another DNA duplex (211), the probability of independent engagement of distant secondary DNA sites

would be higher for PUUP construct (due to the largest linear distance between the H-NS binding regions separated by UAS sequences). This assumption is strengthened with the measurement where highest percentage of bound versus unbound plasmids are observed for PUUP (~80%) compared to UPPU (~55%) or UPUP (~65%). We propose that simultaneous nucleation of H-NS at the remote *proV* regions bridges and subsequently produces extended filaments as observed with PUUP (Figure 3.3.2). Importantly, PUUP showed also a linear decrease of the plasmid contour length as the function of the increasing H-NS filament length, which was not the case with filaments formed on UPPU or UPUP (Figure 3.3.7). The very opposite behaviour was observed for UPPU construct, which showed shorter filaments and binding of H-NS constrained higher levels of negative superhelicity (Figure 3.3.9). All of these observations strongly suggest that the H-NS filaments formed with UPPU and PUUP constructs, characterized respectively by shortest and largest linear distance between the *proV* regions, represent distinct nucleoprotein structures. This notion was fully consistent with the different specific structures formed on these constructs (filament-loop and loop-filament-loop for PUUP and UPPU, respectively), with the different average height of the filaments (Figure 3.3.8) and most importantly with the distinct periodicity of the corresponding H-NS filaments (10-20 nm and 5-10 nm for UPPU and PUUP, respectively).

We infer that the spatial organisation of strong H-NS binding sites is directing the formation of nucleoprotein structure. Since the filament formation on UPPU leads to an efficient constraint of superhelicity, we can assume that the binding of H-NS is likely to stabilize a tightly interwound plectoneme as suggested earlier (194,211). In the case of PUUP with the longest filaments, without substantial constraint of superhelicity (Table 3.3.5) the duplexes are most likely bridged without tight intertwining. A question arises, how can H-NS binding regions in UPPU nucleate plectoneme formation and in PUUP not? To answer this question, we have to look at the sequences of structures constructs. At high protein concentrations UPPU forms exclusively LFL structures in which a filament is connecting two spatially separated loops (Table 3.3.1c). We propose, that the close proximity of adjacent *proV* regions during the polymerisation of the filament initiates cooperative interactions between high-affinity H-NS binding sites. These sites represent thermodynamically unstable and easily deformable regions characterized by low average negative melting energy (218). We can imagine UPPU filament as two contiguous *proV* regions intertwined with partner duplex in a tight plectonemic configuration. The strong H-NS binding sites located at +25 and +131 in the *proV* NRE are separated by ~ten helical turns. In UPPU construct it would lead to each of the two high affinity H-NS binding sites located in close spatial vicinity. The nucleation of H-NS at the consecutive high-affinity sites would lead to formation of a high-pitch plectoneme with high intrinsic twist, which would explain the experimental finding on higher superhelicity constrained by H-NS, as well as distinct periodicity, persistence length and average height of the filament for UPPU (Figure 3.3.12).



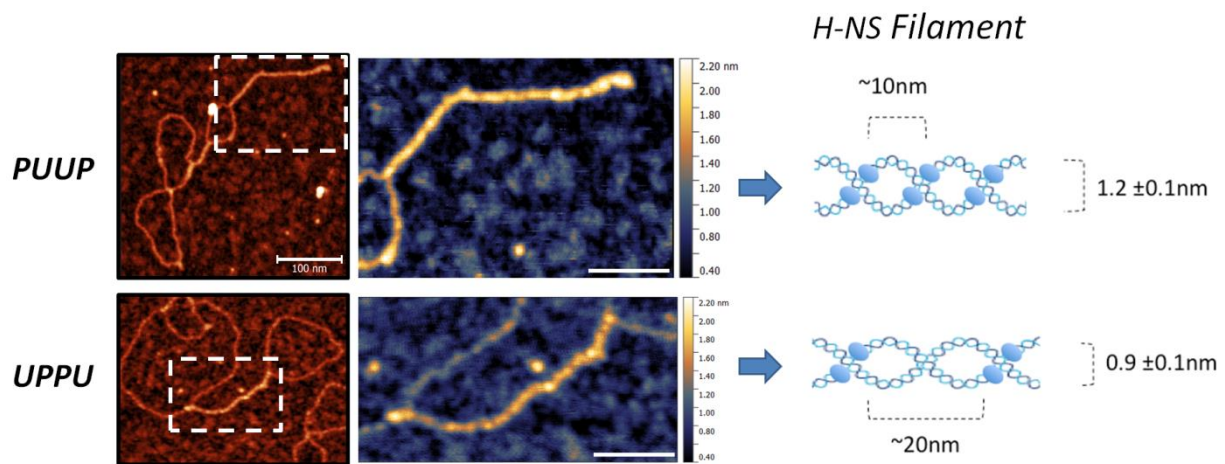


**Figure 3.3.12:** MAFM images with a schematic representation of low and high pitch H-NS plectonemes formed by PUUP and UPPU constructs. Scale bars for large and zoomed AFM images 100nm and 50nm respectively.

We emphasize that whereas various modes of H-NS binding have been previously observed under the variation of H-NS oligomeric structure, DNA supercoiling, ionic strength and temperature (199,200,209, 227-219,221), it is the first time the role of the DNA sequence arrangement in H-NS binding has been studied. We would like to stress out that not only changes in the composition of abundant NAPs characterized by distinct modes of DNA binding (191,228), but also distinct spatial organisation of NAP binding sites can lead to variability of chromosomal structures and topological differentiation in the bacterial genome. We think that the discovered principle is by far more general and is not limited to just H-NS protein. We believe this behaviour can be readily exploited in future for DNA sequence-directed assembly of distinct 3D nucleoprotein structures.

**Table 3.3.5:** Comparison of every shape parameter measured for H-NS-DNA complexes at different H-NS concentration and in different measurement conditions discussed in the results.

<b>In Air</b> ( <i>H-NS : DNA 13:1</i> )			
<b>Constructs</b>	<b>PUUP</b>	<b>UPUP</b>	<b>UPPU</b>
<b>Structures</b>	Fil-loop 50%	Fil-Loop 23% Loop-Fil-Loop 22%	Loop-Fil-Loop 17%
<b>Bound</b>	~ 80%	~ 65 %	~ 55 %
<b>Lp</b>	64 ± 2	54 ± 2	44 ± 2
<b>&lt;Filament length&gt;</b>	155 ± 70 nm	75 ± 30 nm	65 ± 30 nm
<b>Ultra High Vacuum</b> ( <i>H-NS:DNA 20:1</i> )			
<b>&lt;Filament length&gt;</b>	220 ± 70 nm	205 ± 60 nm	150 ± 95 nm
<b>Periodicity</b>	5-10 nm	5-10 nm	10-20 nm
<b>Compaction</b>	Yes	No	No
<b>APTES</b> ( <i>H-NS:DNA 20:1</i> )			
<b>&lt;Filament length&gt;</b>	45 ± 15 nm	35 ± 10 nm	30 ± 10 nm
<b>Branching probability</b>	22%	14%	14%

## 3.4 Upstream Binding of Idling RNA Polymerase Modulates Transcription Initiation from a Nearby Promoter

*This chapter is based on a paper published in the Journal of Biological Chemistry with the following authors: Veneta Gerganova<sup>1</sup>, Sebastian Maurer<sup>1,6</sup>, Liubov Stoliar<sup>1</sup>, Aleksandre Japaridze<sup>2</sup>, Giovanni Dietler<sup>2</sup> William Nasser<sup>3</sup>, Tamara Kutateladze<sup>4</sup>, Andrew Travers<sup>5</sup> and Georgi Muskhelishvili<sup>1</sup>*

Affiliations:

1 - School of Engineering and Science, Jacobs University Bremen, Germany,

2 - Laboratory of Physics of Living Matter, EPFL Lausanne, Switzerland;

3 - UMR5240 CNRS/INSA/UCB, Universite' de Lyon, INSA-Lyon, France,

4 - Ivane Beritashvili Centre of Experimental Biomedicine, Tbilisi, Georgia,

5 - MRC Laboratory of Molecular Biology, Cambridge, United Kingdom

6 - Present address: Center for Genomic Regulation (CRG) Barcelona, Spain

### Abstract

The bacterial gene regulatory regions are often distinctly organized in arrays of RNA polymerase binding sites of ill-defined function. It has been previously observed that upstream of the canonical promoter of *Escherichia coli* *fis* operon contains closely spaced polymerase binding sites.

Here we studied by means of atomic force microscopy the binding of RNA polymerase to the *fis* promoter. We showed that simultaneous binding of the polymerase at the promoter and at an upstream transcriptionally inactive site stabilizes a RNAP oligomeric complex *in vitro*, suggesting that a specific DNA geometry is stabilized upon binding. This notion is strengthened by our data that shows that only the insertions of half a helical turn (insertion of 5A/T or 5G/C base pairs) but not the full turn (insertion of 10A/T base pairs) of DNA decreases the RNAP binding affinity to *fis* promoter.

### 3.4.1 Introduction

It is well known that changes of the holoenzyme composition of *Escherichia coli* RNA polymerase (RNAP)<sup>3</sup> plays important role in gene regulation during the bacterial growth cycle (229, 230). On the other hand, the role of RNAP binding site arrays in the promoter region is less studied. However, there is growing evidence that the flexibility of genetic regulation can be increased by organizing promoter arrays in tandem and/or divergent orientation, often recognized by distinct holoenzymes (231-237). The promoter arrays not only enable the utilization of different RNAP holoenzymes for transcription, but facilitate the transformation of physiological signals under the changing growth conditions.

Several studies in prokaryotes implicated the role of closely spaced RNAP binding sites in the regulation of both the strength and the pattern of gene transcription (238-242). These studies suggested that particular arrangements of the RNAP binding sites may have had a regulatory function. For example, in the phage  $\lambda$  control region, the RNAP molecules were binding closely spaced divergent promoters, and were interfering with each other (243). This interference was shown to provide an effective way to regulate divergent genes by means of a single transcription factor (244). Promoters arranged in tandem can also show strong transcriptional interference due to the pausing of the upstream initiating polymerase over the downstream promoter (245). In many cases the divergently oriented promoters can cooperate, with the diffusion of DNA negative supercoils induced by the translocating RNAPs (246) coupling the operons leading to their coherent expression (247). During the last decade, the role of closely spaced and overlapping promoters has become increasingly evident in gene regulation, both in prokaryotes and eukaryotes (248-253). In addition to this regulatory complexity of individual promoter regions, recent genome-wide studies using chromatin immunoprecipitation (ChIP) experiments revealed a significant number of DNA-bound RNAP molecules that could not be associated with ongoing transcription (254-256). Numerous unusual promoter-like sites, or promoter regions of unspecified biological function (257) were discovered, indicating that the genomic transcriptional landscape is much more complex than previously anticipated (258). Interestingly, over 90% of the identified *E. coli* gene promoters were found to be surrounded by other promoter-like signals (259). It is highly possible that these signals serve the purpose of enhancing the local concentration of RNAP near the promoter. It is also possible that closely spaced RNAP binding sites provide a mechanism for engaging RNAP molecules into higher-order nucleoprotein complexes, analogous to recombination complexes involving multiple recombinase molecules binding adjacent DNA sites and acting both as regulatory and catalytic components of the complex (260-262).

The so-called "stringently" controlled promoter of the *fis* operon, encodes the abundant nucleoid-associated protein FIS (263). It is characterized by sensitivity to DNA supercoiling (264), which is not surprising, since FIS is a global regulator involved in the homeostatic control of DNA supercoiling (215). The expression pattern of *fis* is closely reflected in the variation of the FIS protein concentration, which is accumulated in very large amounts (>50,000 copies) during cell growth in rich medium and afterwards sharply drops to about 1% of its maximal concentration (265).

Previously, an array of closely spaced polymerase binding sites were identified in the *fis* promoter. These binding sites included tandem (*fisP1*, *fisP2* and *fisP3*) as well as divergently (*div*) orientated sites upstream of the promoter (Figure 3.4.1). Although potentially all of these upstream sites could drive transcription when cloned in episomal reporter constructs, in the native chromosomal context they do not function as *bona fide* promoters (266), therefore the array of RNAP binding sites was proposed to represent a regulatory unit (241).

In this study we investigate the influence of the upstream binding of RNAP on *fis* operon by means of atomic force microscopy (AFM). We show that RNAP forms a higher-order complex on simultaneous binding of the upstream and *fisP1* sites *in vitro*. Our AFM data suggests that mutations by disrupting the helical periodicity between the RNAP binding sites outside the promoter region strongly decreases the binding affinity of RNA polymerase to the promoter.

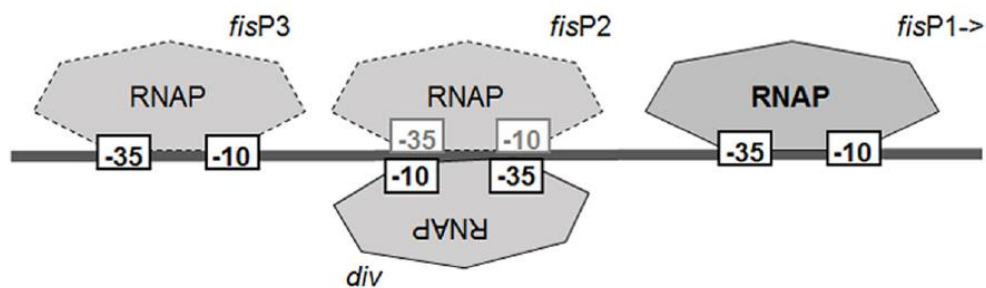


**Figure 3.4.1:** Schematic representation of the spatial arrangement of RNAP binding sites in the regulatory region of the *fis* operon. The orientation of binding sites is indicated by the order of the RNAP binding -10 and -35 elements. The binding elements of the *fisP2* site and *div* partially overlap. *Div* is a stronger binding site and stronger promoter when isolated on an episome compared with *fisP2* (241), therefore we consider in the text only binding of *div*. Only *fisP1* is considered to be engaged in active transcription *in vivo*.

## 3.4.2 Materials and methods

### pVG-*fis4* Circular DNA construct

The *rrnB* terminator was PCR amplified from pBAD24 (primers 5' CCCAAGCTTATAAAAACGAAAGGCTCAGT CG- 3' and 5' CGCGGATCCTCGAGCGGCCGCTAGCCCGGGATGCATCGCGAAAAAGGCCATCCGTCAGGATG-3'). The PCR product was digested by HindIII and BamHI and cloned into a HindIII/BamHI-digested pUC18 backbone. The *E. coli* CSH50 strain carrying a chromosomal *fisP-yfp* fusion was kindly provided by Dr. Berger and Alissa Respet. The *fisP-dusB-yfp-cat* fragments were amplified with Phusion DNA Polymerase (Finnzymes) (primers 5'-GGTGGTCGCTAACATCCTTG-3' and 5'-AGGAAACAGCTATGACC ATG-3'), and subsequently KpnI digested and cloned into a SmaI/KpnI-digested pUCTER backbone. The resulting plasmid was subsequently sequenced and named pVG-*fis4* (Figure 3.4.1). All mutations were introduced with the Phusion Sitedirected Mutagenesis kit (ThermoScientific) according to the manufacturer's recommendations. All mutated plasmids derived in this way were sequenced by Eurofins MWG Operon.

### APTES modified mica surface

For the APTES deposition, the mica surface was functionalized with APTES in a separate step prior to DNA deposition. Pure APTES ( $\geq 98\%$  purity) was purchased from Sigma-Aldrich (Switzerland) and diluted in ultrapure water to a final concentration of 0.1vol%. A 15  $\mu\text{l}$  droplet of diluted APTES solution was deposited on freshly cleaved mica for one minute, and then rinsed with 1 ml of ultrapure water, and finally dried using a gentle flow of compressed nitrogen.

### AFM – pVG-fis4 Circular DNA-RNAP complexes on APTES

RNAP-DNA complexes were formed by incubating TopoII relaxed plasmid DNA molecules (final concentration  $\sim 0.5\text{ng}/\mu\text{l}$ ) and RNAP (purchased from NEB, final volume dilution of 1:2000) in 20 $\mu\text{l}$  P-Buffer (1mM Tris-HCl pH8.0, 10mM KCl, 0.003% Tween, 2.5% Glycerol, 4mM  $\text{MgCl}_2$ ) at 37°C for 2 minutes. After depositing the RNAP-DNA mix on mica surface for 5 minutes the mica was rinsed with 1 mL of ultrapure water and finally dried using a gentle flow of compressed nitrogen. DNA relaxation with TopoII

### DNA relaxation by TopoII

2 $\mu\text{l}$  Circular DNA ( $\sim 100\text{ng}/\mu\text{l}$  initial concentration) was incubated in 20  $\mu\text{l}$  volume using Topo Buffer and 1 $\mu\text{l}$  TOPO II (Affymetrix)I for 30min at 37°C, followed by heat inactivation of Topo II for 20min at 65°C.

### AFM setup

AFM images were collected using a MultiMode SPM with a Nanoscope III controller (Veeco Instruments, Santa Barbara, CA, USA) operated in tapping-mode in air. The AFM cantilevers used in air had a spring constant of 5 N m<sup>-1</sup> (Bruker cantilevers, TAP150A) with resonance frequencies ranging between 120 and 160 kHz. All the recorded AFM images consist of 512 x 512 pixels with scan frequency  $\leq 1$  Hz. Images were simply flattened using the Gwyddion software (Version 2.22) and no further image processing was carried out (105).

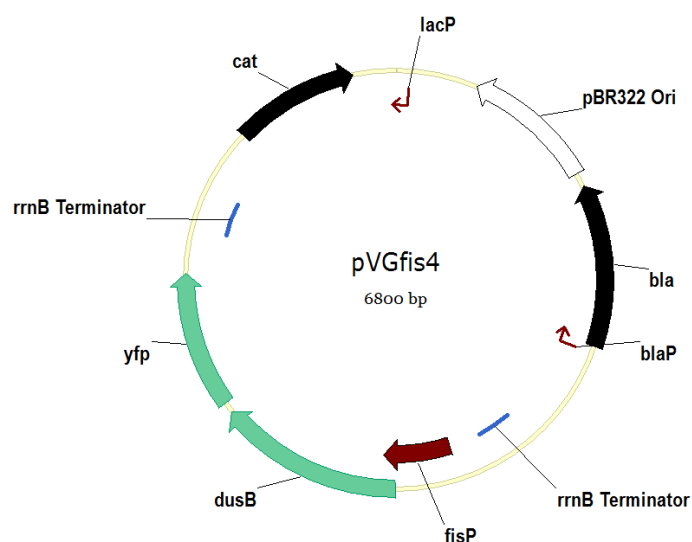


**Figure 3.4.2:** The map of the pVG-fis4 circular construct

### 3.4.3 Results

#### 3.4.3.1 RNAP-linear *fis* promoter complexes

The first question we asked was, how would RNA polymerase bind the specific arrangement of binding sites in the *fis* promoter region and would it induce the formation of higher-order RNAP complexes or not. For this purpose, we imaged the RNAP nucleoprotein structures using a 816-bp DNA fragment comprising the *fis* promoter sequence from -108 to +106 with respect to *fis*P1 initiation start site at +1 flanked by vector sequences. On this fragment, the upstream *div* site was located near the fragment centre and *fis*P1 was closer to one end (as shown schematically on Figure 3.4.1 and Figure 3.4.3). We defined the DNA as RNAP bound, when the height measured at any point along the DNA molecule was at least 3 nm higher than the average height measured for the free DNA (Figure 3.4.4).

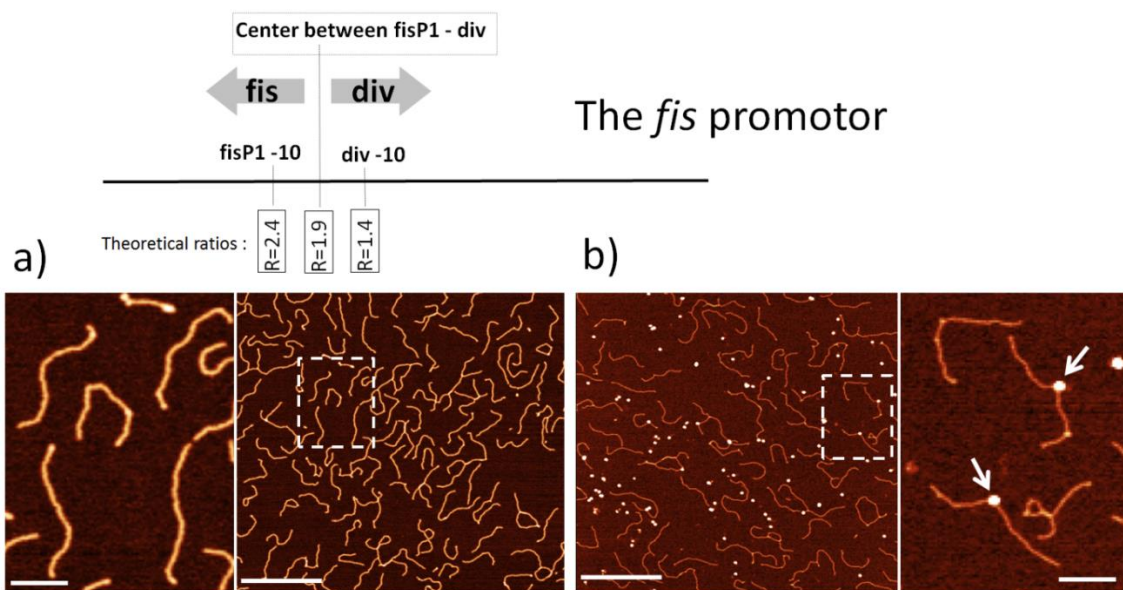


**Figure 3.4.3:** Schematic representation of the *fis* promoter sequence with *fis*P1 and *div* RNAP binding regions. Large scale and zoomed atomic force microscopy images of **a)** Control and **b)** RNA bound DNA complexes. White arrow indicates the position of RNAP binding. Scale bars for zoomed and large scale images 100nm and 500nm respectively

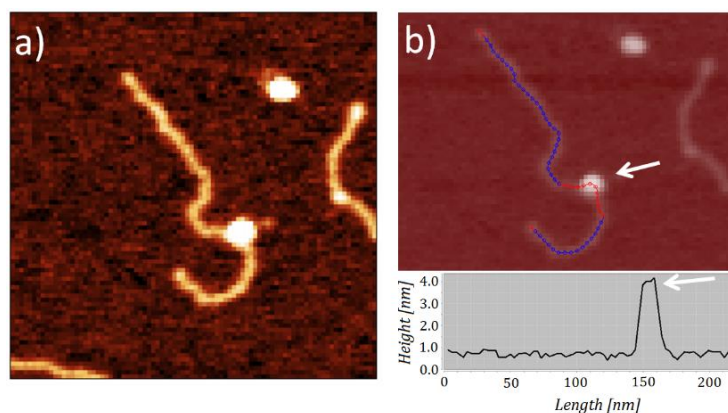


**Figure 3.4.4:** Defining DNA as RNA polymerase bound. We defined the DNA as bound, when the height measured along the DNA at any position was at least 3 nm higher than the average height measured for the control DNA. 3nm

corresponds to the mean height of RNAP measured by AFM. Traced molecule bound with RNAP (position of RNAP is indicated by the white arrow) with the corresponding height cross-section below.

As clearly seen by Figure 3.4.3, RNA polymerase appeared as a large spherical object overlapping with the DNA strand, with the typical height of  $3.0 \pm 0.5$  nm. By counting the total number of bound and free DNA molecules, we could define the relative binding of the RNAP to the DNA fragment as:

$$\text{Total bound \%} = \frac{N_{\text{bound}}}{N_{\text{total}}} \quad (3.4.1)$$

where  $N_{\text{bound}}$  was the number of bound and  $N_{\text{total}}$  the total number of DNA molecules observed in our AFM images. Analysis of 270 individual structures revealed that  $\sim 30 \pm 5\%$  of all DNA were bound with RNA polymerase. By tracing the distance between the centre of the bound RNA to the free ends of the linear fragment, we could distinguish which binding position was occupied on the promoter (Figure 3.4.5 and Table 3.4.1). As expected, the *fisP1* sequence ( $\sim 30\%$ ) was more probable to be occupied than the *div* site ( $\sim 10\%$ ). The *div* site was overlapping with the *fisP2* RNAP binding site (see Figure 3.4.1), therefore it would be impossible to distinguish which one was bound by AFM resolution. However, because *div* is a stronger binding site for RNAP compared to *fisP2* (267), we assumed that RNAP predominantly binds at the *div* site. Interestingly, aside from single and double bound nucleoprotein complexes, we found that roughly  $\sim 10\%$  of all bound RNAP had larger height and diameter compared to single RNAP (Figure 3.4.5). Taken together, these data are consistent with previous findings showing that RNAP can simultaneously bind at the *fisP1* and *div* sites *in vitro* (267). Most importantly we could demonstrate the formation of a higher-order complex on simultaneous binding of RNAP at the *fis* promoter region.

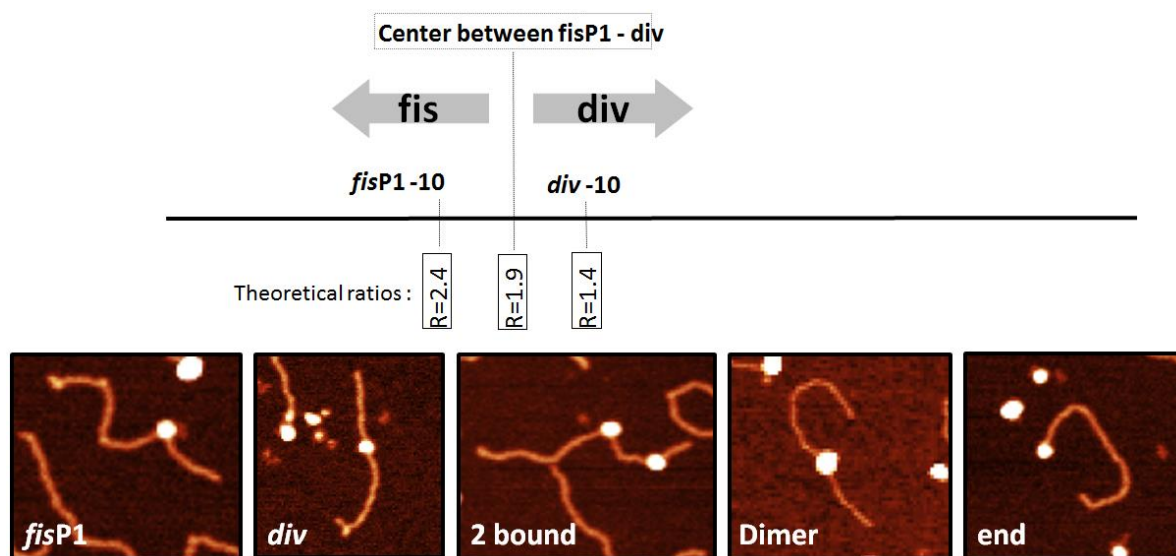


**Figure 3.4.5:** Schematic representation of the *fis* promoter sequence and the corresponding Atomic force microscopy of specific DNA complexes formed by RNAP on linear *fis* DNA fragments. Representative images show the complexes formed on the linear DNA after incubation with RNAP.



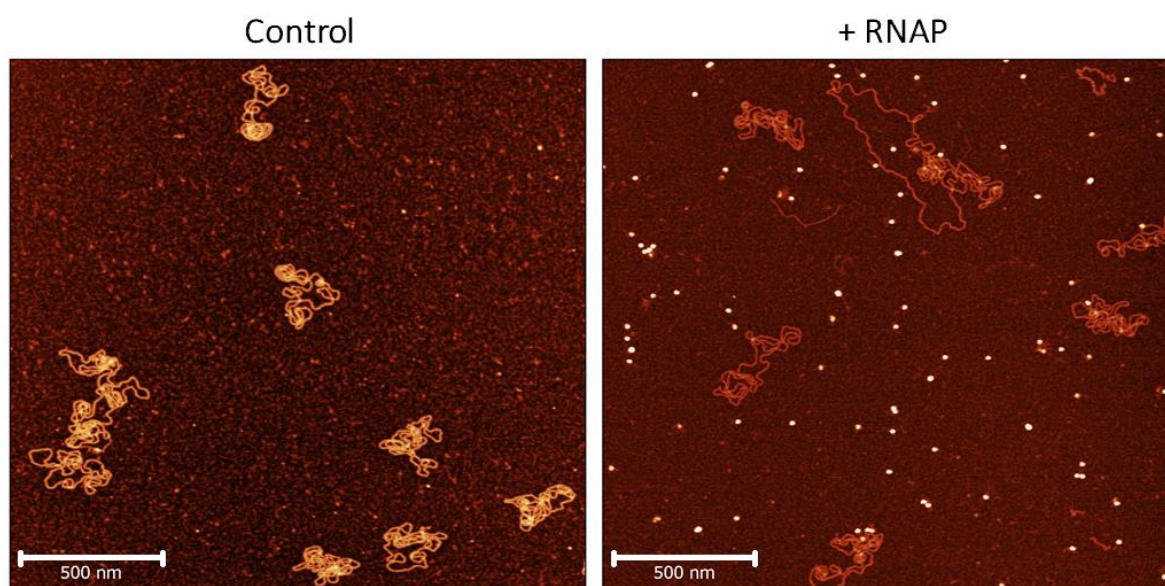
**Table 3.4.1:** Relative binding positions of RNAP on the linear *fis* promoter

Construct	N	<i>fis</i> P1	<i>div</i>	Double bound	end
RNAP-Linear DNA	115	31±5%	11±5%	9±5%	49±5%

### 3.4.3.2 RNAP-circular *fis* promoter complexes

Above mentioned data showed that, roughly in half of all bound structures, the RNA was positioned at one of the ends of the linear DNA fragment (Table 3.4.1). To avoid nonspecific RNAP binding, we studied the binding of the RNA polymerase to a much larger circular DNA containing the *fis* promoter (6.8kb pVG-*fis*4 plasmid DNA). To simplify the visualization of the RNAP-circular DNA complexes, the plasmids were relaxed by Topo II before the experiment and imaged on the APTES surface (Figure 3.4.6). The role of APTES, due to its strong charge interactions with the DNA, is to kinetically trap the complexes. As a result, it allows obtaining a better preservation of their 3D solution shape (33,59).

By using the equation (3.4.1) we estimated the overall binding of the RNAP to the circular DNA. This time, the overall binding was much more specific, with 54±6% of all imaged circular DNA being bound with RNAP (Table 3.4.2). Once again, we observed structures bound at single position, at two closely spaced positions and bound by RNAP oligomers (Figure 3.4.7). Interestingly almost two thirds (65 ± 5%) of all bound DNA, were bound to two RNAP and only 20% to a single RNAP, indicating higher specificity of RNAP binding compared to linear DNA fragment.

**Figure 3.4.6:** Atomic force microscopy of RNAP-circular wildtype DNA complexes. Scale bar 500 nm.**Table 3.4.2:** Relative binding affinity of RNAP to circular DNA

Construct	N	Total bound	Double bound	Single bound	Dimers
RNAP-Circular DNA	100	54 ± 6%	65 ± 5%	20 ± 5%	15 ± 5%

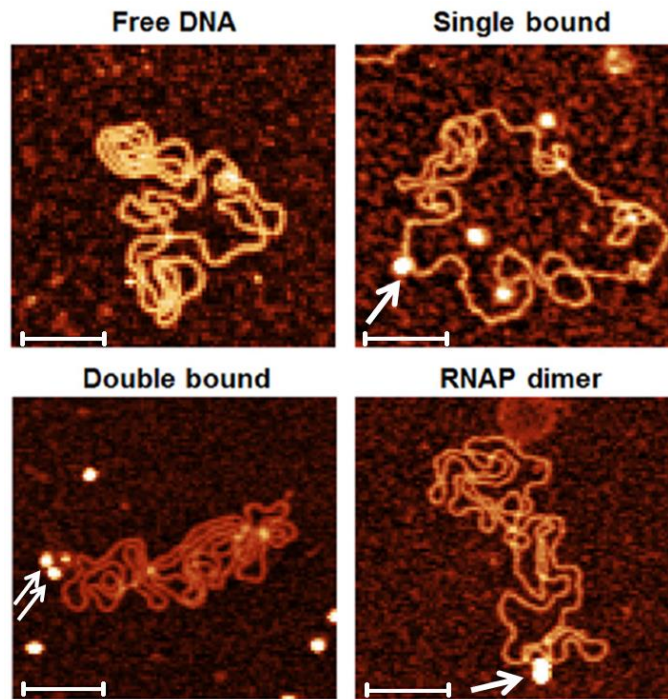


**Figure 3.4.7:** Specific DNA complexes formed by RNAP with circular DNA on the APTES modified surface. Representative images show the free plasmid DNA and the complexes formed on the same DNA after incubation with RNAP. In the representative images only the complexes indicated by the white arrows are assumed to be bound. Scale bar 500 nm.

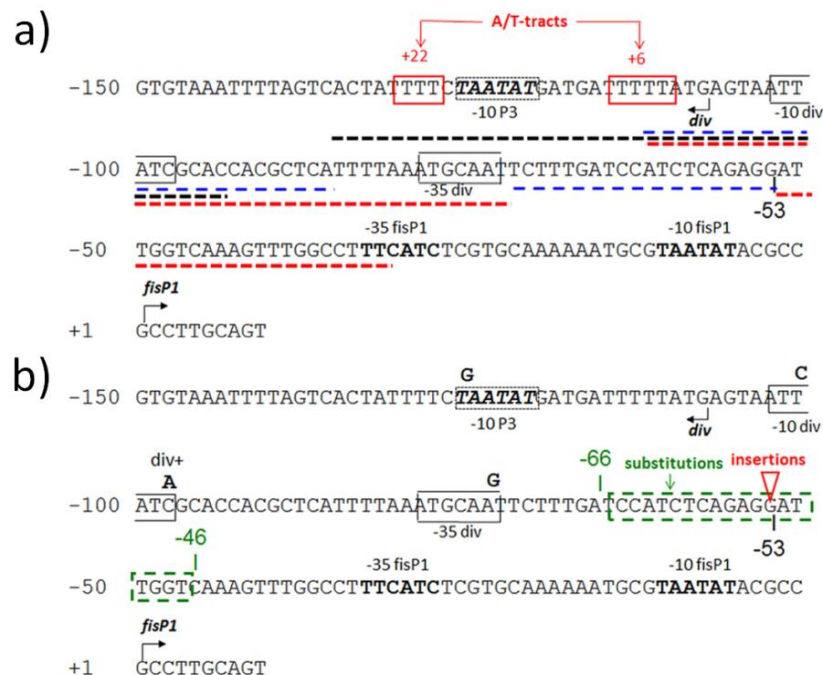


**Figure 3.4.8:** a) sequence of the *fis* promoter region. The div -10 and -35 elements are boxed, and *fisP1* -10 and -35 elements are in bold. The IHF binding site is underlined (black dashed line). The CRP binding sites are underlined (blue dashed lines). The FIS binding regions are underlined (red dashed lines). The A/T tracts downstream of div are boxed (red boxes); b) Summary of the modifications in the *fis* promoter region. Substitutions in the -10 and -35 elements of div and -10 element of *fisP3* site (italics, dashed box) are indicated in bold; substitutions in the spacer between *fisP1* and div are boxed (green dashed box). The position of the 5G/C, 5A/T, and 10A/T insertions are indicated by the red triangle.

### 3.4.3.3 Modified linker DNA-RNAP complexes

To understand the role of special organisation of RNAP binding sites in the *fis* promoter, we decided to alter the geometry of RNAP binding sites and see if this would have an effect on the RNAP-DNA nucleoprotein complex formation. The *fis* promoter region contains binding sites for several NAP proteins including FIS itself. The *fisP3* -10 element overlaps with the IHF binding site; the *div* -10 element overlaps with the IHF binding site, CRP binding site II, and FIS binding site III, whereas the *div* -35 element overlaps with FIS binding site IV (267, 268). To minimize the possible interference with regulatory protein binding in the *fisP1* upstream region, we introduced mutations in the region between *fisP1* and the upstream RNAP sites. These insertions did not alter the sequence of any of the FIS, CRP, or IHF binding sites (Figure 3.4.8a). We introduced A/T-stretches corresponding to half a helical turn (5A/T) or a full turn (10A/T) of the DNA between positions -53 and -54 with respect to the start point of the *fisP1* transcription (initiation site at +1). The insertion point was located between the adjacent CRPI and FISII binding sites (267) in the centre of the 40-bp sequence which separates the -35 RNAP hexamers of the *fisP1* and *div* (Figure 3.4.8). To make sure the sequence of the insert (A/T stretches) would not be utilized by RNAP as fortuitous A + T-rich UP elements (269), we also inserted a stretch of five guanines (5G/Cs) in the same position. It is important to stress that both the 5A/T and 5G/C insertions would alter the helical phasing between the bound polymerase molecules, whereas 10A/T would not. The last construct we designed was obtained by substituting guanines (G) for all thymines (T), and cysteines (C) for all alanines (A) within a 19-bp region (positions -46 to -66 with respect to the start point of *fisP1* transcription) between the *fisP1* and *div* sites. We called this construct the “GC-rich spacer”, in which the thermodynamic stability of the DNA in the linker region between the divergent RNAP binding sites could be increased without altering their helical register (Figure 3.4.8).

To understand the impact of the insertions on the RNAP nucleoprotein complex formation at the *fis* promoter we repeated the AFM experiments for the mutated circular as well as linear DNA. We quantified the RNAP binding to the plasmid constructs carrying the 5G/C, 5A/T, and 10A/T insertions, as well as the GC-rich spacer construct and compared the values to the wildtype construct (Figure 3.4.9). At the used RNAP concentrations about 60–75% of plasmids were bound by a single RNAP molecule, 15–20% were bound by two RNAP molecules and the remaining 10-20% bound with RNAP dimer molecules (Table 3.4.3). The results for the distinct structures formed by the mutated constructs were comparable to the RNAP-wildtype complexes (Table 3.4.2). The measurements of the arm ratios of complexes formed on linear fragments at the same RNAP concentrations (Table 3.4.4) supported our hypothesis that, in complexes formed on plasmid constructs, the RNAP was indeed binding either at *div*, or *fisP1*, or both *div* and *fisP1* sites. Interestingly, when we compared the relative binding of RNAP to the DNA construct, we found that both the 5A/T (54%) and 5G/C (57%) plasmid constructs were significantly impaired in RNAP binding, whereas the 10A/T (94%) and GC-rich spacer (92%) constructs showed almost no difference compared to the wild type (Figure 3.4.10). This significant difference in binding of the constructs that differ only by modifications in the *fis* regulatory region, indicates that we indeed observed the variation in occupation of the *div* and *fisP1* sites and not of any plasmid borne promoters. We thus infer that alteration

of the spatial organisation of RNAP binding sites by insertion of half a helical turn of the DNA between *div* and *fisP1* strongly interferes with RNAP binding.

**Table 3.4.3:** Specific DNA complexes formed by RNAP with circular mutated DNA

Construct	N	Double bound	Single bound	Dimers
5A/T	100	15 ± 5%	75 ± 5%	10 ± 5%
5G/C	100	15 ± 5%	70 ± 5%	15 ± 5%
10A/T	100	20 ± 5%	60 ± 5%	20 ± 5%
GC-rich spacer	100	20 ± 5%	60 ± 5%	20 ± 5%

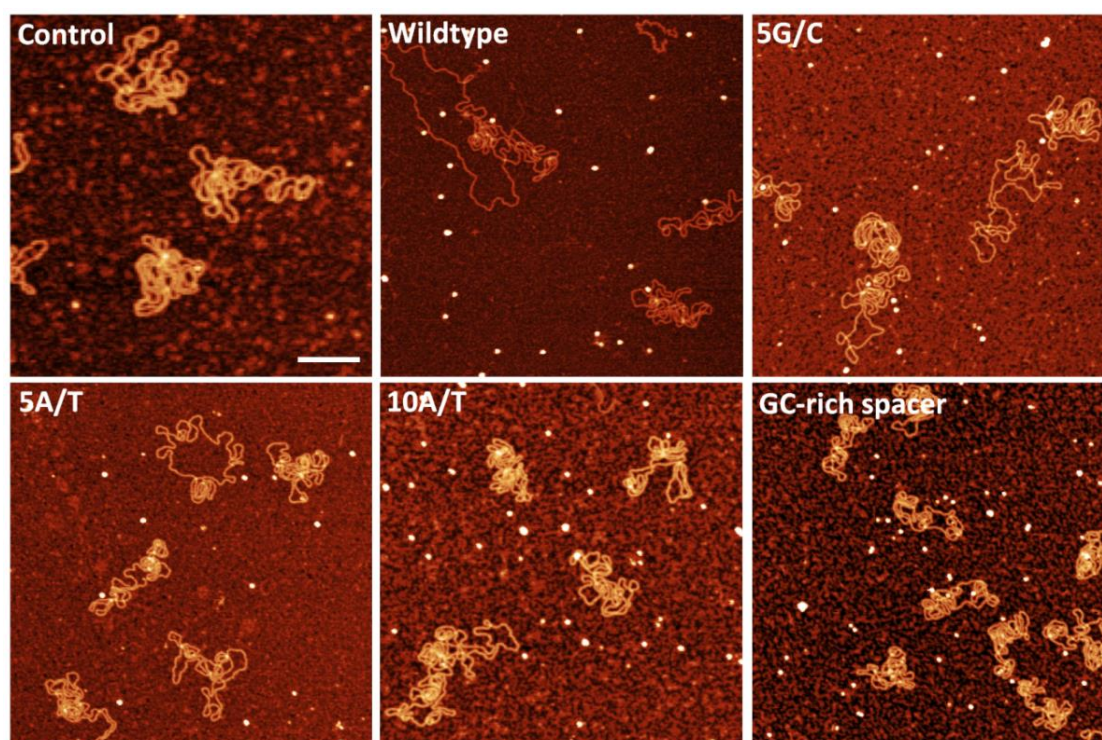


**Figure 3.4.9:** AFM images of variants of RNAP-circular DNA complexes on the APTES surface. Scale bar 200 nm.

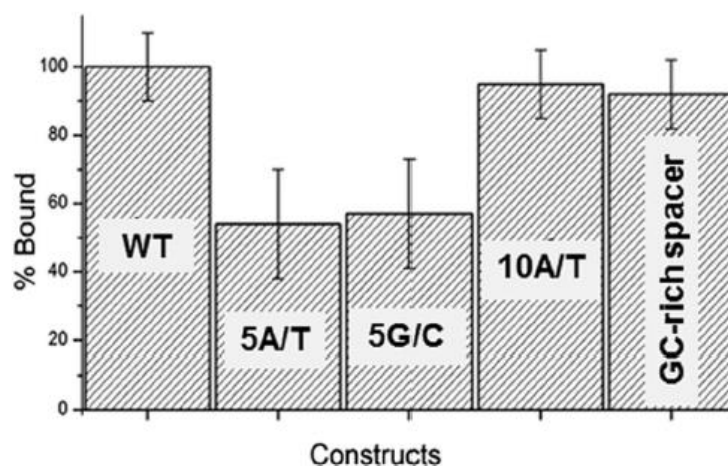


**Figure 3.4.10:** Quantification of RNAP binding to plasmid DNA. The columns are based on analyses of 100 DNA-RNAP complexes for each modified promoter construct. The standard error bars indicate the variation in the number of “bound” versus “unbound” DNA molecules based on the individual AFM images for a given DNA-RNAP complex.

**Table 3.4.4:** Relative binding of RNAP to linear mutated *fis* promoter

RNAP-Linear DNA	N	<i>fisP1</i>	<i>div</i>	Double bound	end
5A/T	105	33%	15%	6%	46%
5G/C	110	32%	19%	12%	37%
10A/T	110	17%	12%	16%	55%
GC-rich spacer	90	25%	19%	9%	47%

### 3.4.4 Conclusions

In this study we described the binding of RNAP to the native *fis* operon encoding the pleiotropic regulator FIS (270,271). We revealed a higher-order assembly consistent with a RNAP oligomer, presumably a dimer, as well as RNAP binding to the divergently oriented *fisP1* and *div* sites. The centres of the -10 RNAP binding elements of these divergent sites were separated by approximately nine helical turns, suggesting a particular local geometry of the complex with RNAP molecules binding nearly on the same face of the DNA helix. Although the propensity of the RNAP holoenzyme to dimerize is long known (272-275), the physiological relevance of this observation remains obscure.

We also studied the role of the spatial arrangement of the RNAP binding sites on the *fis* promoter. The multitude of regulators and the overlap of their binding sequences with those of RNAP required the use of insertion mutations, which did not affect any of the known regulator binding sites. We observed that the insertions of half a helical turn (5A/T and 5G/C) but not the full turn (10A/T) of DNA decreasing the RNAP binding affinity to *fis* promoter. Even substituting bases within a 19-bp sequence in the linker DNA between the divergent *fisP1* and *div* sites, but keeping their helical arrangement (GC-rich spacer construct) did not affect the RNAP binding.

We believe that exploration of the interactions of closely spaced RNAP binding sites in other model systems, including eukaryotes (253,276), will provide important insights into the complexity of the transcriptional regulatory mechanisms.

## Chapter 4: Hyperplectonemems

*This chapter is based on a paper in preparation with the following authors:*

Aleksandre Japaridze<sup>1</sup>, Fabrizio Benedetti<sup>2</sup>, Andrzej Stasiak<sup>2</sup>, Florence Pojer<sup>3</sup>, Stewart Cole<sup>3</sup>, Paolo De Los Rios<sup>4</sup>, Georgi Muskhelishvili<sup>5</sup>, Giovanni Longo<sup>1</sup>, Giovanni Dietler<sup>1</sup>

Affiliations:

1 - Laboratory of Physics of Living Matter, EPFL Lausanne, Switzerland;

2 - Center for Integrative Genomics, University of Lausanne, Switzerland

3 - Global Health Institute, EPFL, Lausanne, Switzerland

4 - Laboratoire de Biophysique Statistique, EPFL, Lausanne, Switzerland

5 - UMR5240 CNRS/INSA/UCB, Université de Lyon, F-69003; INSA Lyon, Villeurbanne, F-69621, France

### Abstract

Bacterial chromatin has a compact structure, which dynamically changes its overall shape in response to changes in the bacterial growth rate and growth phase. Despite its compactness, this folded organisation must not impair its function. Determining how large chromatin domains are packed in very compact structures, but still stay accessible for proteins and transcription machinery is of great importance to understanding how genetic regulation is linked to DNA and chromatin structure.

In order to address these questions, we used Atomic Force Microscopy (AFM) to study large supercoiled double stranded DNA of various contour lengths (2.7kb up to 45kb). These analyses allowed us to describe a completely new type of DNA organisation, which we called hyperplectonemes. Hyperplectonemes are highly ordered, dynamic structures, formed by large supercoiled molecules, in the presence of attractive DNA-DNA potential. First, we studied in detail their structural dependence on various environmental factors. Next, we investigated their binding to nucleoid associated proteins, FIS, H-NS and HU. In conclusion, we propose that this emerging DNA organisation is a basic structure of bacterial chromatin, which is, *in vivo*, further modulated by numerous DNA binding proteins and condensing agents.

## 4.1 Introduction

Bacterial DNA is folded into a compact nucleoid body, which is a dynamic entity that alters its overall structure in response to changes in the bacterial growth rate and growth phase. The nucleoid consists of hundreds of DNA loops, which must be compacted at least 1000-fold to fit inside the bacterial cell. Yet, this folded organisation must not impair its function (279,280). The ordered DNA packing, as well as the dynamics in the evolution of its structure, are achieved through different mechanisms and are correlated with changes in the distribution and utilization of DNA supercoiling. Furthermore, the chromatin structure is regulated by a complex interplay of nucleoid-associated proteins (NAPs) and condensing agents (207,279-283). Despite the clear link between DNA supercoiling and genetic regulation (284-287), the global role of supercoiling in chromatin organisation remains poorly understood.

Previous studies have evidenced the segregation of supercoils into topologically independent domains inside bacterial chromatin (288-290). Typically, the size of the domains ranges from 10kb (kilo base-pairs) up to 100kb (288-290). Unfortunately, the size and the borders of these domains have been ill-defined and appeared to be strongly dependent on the experimental method used. Furthermore, due to simplicity of handling, most of previous experimental and computational studies have focused on smaller DNA, with typical sizes between 1-5kb (69,126,291-294,320-321). Only few studies focused on the molecules of sizes above 10kb (295,296), which is comparable to some domains in bacterial chromatin. Based on computer simulations for small DNA molecules, several groups showed that the plectonemic structure of the DNA is the minimum energy conformation for a highly supercoiled DNA (20,296,297). These results, confirmed by electron microscopy (EM) and atomic force microscopy (AFM) (21,22,65), led to a more complete understanding of the behaviour of few kb-sized DNA and of the physics governing them at the short length scales. On the other hand, there is still no experimental data for circular DNA at the larger scales, which are comparable to those found in viruses or bacterial domain sizes (tens of kilo base pairs). Determining how large chromatin domains can be packed in very compact structures in cells and bacteria and yet be accessible and active for NAPs is of paramount importance in understanding how genetic regulation is linked to DNA structure. Unravelling this problem would be a leap towards understanding the nature of chromosomal organization, how is it imposed and how the NAPs function to package DNA and dynamically constrain superhelicity.

In order to address these questions, we imaged with AFM large supercoiled double stranded DNA (dsDNA) of various contour lengths, ranging from 2.7kb up to 45kb. We were interested in the different structures DNA molecules formed and in their dependence on the various preparation parameters. We measured the overall morphology of the DNA and characterized the resulting conformations, correlating them to the contour length, the presence of salts and supercoiling levels. We focused particularly on the comparison of the organisation of the large circular supercoiled molecules (contour length up to  $\sim 15\mu\text{m}$ ) with the smaller and better-studied DNA (contour length  $\sim 1-3\mu\text{m}$ ).

By enlarging our study to a wide range of DNA sizes, we were able to observe a structural phase transition, an emergence of highly ordered structures never characterized before. Supercoiled DNA larger than 22kb appeared to compact several simple plectonemes, to form higher order structures, which we called hyperplectonemes. The ratio of compaction of the hyperplectoneme (number of simple plectonemes per



filament) was strongly dependent on the supercoiling level, the presence of divalent salts, as well as on the contour length of the DNA. In some cases, up to 10 individual plectonemes were packed into a single hyperplectoneme filament.

We also performed AFM measurements on hyperplectonemes bound with various concentrations of NAPs. We tested 3 different NAPs: FIS, H-NS and HU, separately as well as pairwise combinations of FIS and H-NS. All three proteins strongly altered the structure of the DNA molecules. Importantly, when used pairwise, FIS and H-NS, formed distinct regions on the DNA, where either FIS or H-NS was predominantly bound. This led to creation of 'topological' domains with very different local sub-structure.

We propose that hyperplectonemes, this completely new DNA structure and organisation, arise when the length of the DNA molecules approaches the values typically found in live biological systems and is linked to the non-specific, environmentally mediated, attractive type of DNA-DNA interactions and globally supercoiled nature of the molecule. We believe that this organisation is the core structure of the bacterial chromatin which is further modified and organised by numerous NAPs in the bacteria. In conclusion, hyperplectonemes show how the nucleoid can be effectively compacted and organized, and at the same time be dynamic in nature and accessible to DNA binding proteins and enzymes.

## 4.2 Materials and methods

### DNA

2.7kb (pUC19 2686 bp) and 4.4kb (pBR322 4361 bp) supercoiled plasmid DNA were purchased from Fermentas (Switzerland). 8.4kb DNA (pET-28a His6/mTet3 8381 bp) was extracted from 1.5% agarose gel and purified using extraction kit from Promega. DNA was then placed in TE buffer composed of 10 mM Tris and 1 mM EDTA solution.

### Cosmid DNA

Chromatin, as well as plasmid DNA found inside bacteria, is in supercoiled form, and its supercoiling level is directly linked to the bacterial growth state. The high negative supercoiling density ( $\sigma$ ) is observed in exponential phase of bacterial growth, while only relaxed DNA can be found in the stationary phase. Supercoiling regulates many processes inside bacteria, such as replication and gene transcription (298). It is also a regulator of the global shape of the DNA. In our experiments, in order to minimize the differences in supercoiling levels between different DNA preparations, all DNA preparations were extracted from *E.coli* bacteria incubated and collected in the very same conditions.

Cosmid DNA of 22,6kb (IE241: 3879-3893 kb region); 30.6kb (IE8: 1825-1847 kb region), 42,6kb (I95: 4292-4326 kb region) and 45,6kb (I74: 1464-1501 kb region) consist of genomic DNA of *Mycobacterium tuberculosis* cloned into pYUB412 vector (8562 bp). The cosmids were amplified in *E.coli* (DH5 $\alpha$ ) grown in LB media. To ensure all molecules have comparable supercoiling levels, all DNA were extracted from mid exponential growth phase. DNA was extracted using Midi Prep extraction kit from Promega. DNA was then

placed in TE buffer (10mM Tris and 1 mM EDTA solution). More information about the DNA cosmids can be found at: <http://www.pasteur.fr/recherche/unites/Pmi/BAC-page.html>

## **NAPs**

**FIS** is a small protein (11.2kDa), expressed during the early exponential growth phase (max ~ 50,000 molecules/cell) of the bacteria (192). It acts as a global chromatin organiser, as well as acting as a gene activator in *E.coli* (225) (305). It was demonstrated that FIS stabilizes left-handed toroidal coils upon binding to strong binding sites in the upstream activating sequence of the *tyrT* promoter (306).

**H-NS** is a dimeric DNA-binding protein (15.4-kDa) that was discovered due to its effect on transcription *in vitro* (307). It is expressed during the whole growth cycle of the cell, reaching the highest cellular concentrations (~ 20,000 molecules/cell) in exponential growth phase and decreasing towards late stationary phase (192). H-NS acts as a global repressor (308), whereby its effect on transcription depends on the superhelical density of the DNA (215,309). H-NS binds preferentially to curved DNA sequences (209), bridges distant DNA sites (212,213) and constrains negative supercoils *in vitro* (210,216). High concentrations of H-NS strongly compaction the nucleoid and the overexpression is lethal for the cell (206).

**HU** is a small dimeric heat stable protein (composed of two subunits, HU $\alpha$  and HU $\beta$ , each ~9kDa in *E.coli*) (310). It is involved in chromosome structuring as well as regulating DNA transcription in *E. coli* (311,312). HU binds DNA non-specifically and is strongly influenced by the superhelical density of DNA (313). When bound, it bends the DNA (314), as well as introduces negative writhe into the molecule (194,315).

## **DNA relaxation by nicking enzyme**

42.6kb DNA was nicked using Nt.BsQI nicking enzyme (NEB). 50 $\mu$ l of DNA solution (130ng/ $\mu$ l) was incubated with 5 $\mu$ l of Nt.BsQI nicking enzyme + 10 $\mu$ l of Buffer 3 (NEB) and + 35 $\mu$ l ultrapure water for 2 hours at 37°C. The nicked DNA was afterwards extracted with phenol chloroform extraction and placed in TE buffer.

## **APTES modified mica surface**

Pure APTES ( $\geq$ 98% purity, purchased from Sigma-Aldrich, Switzerland) was diluted in ultrapure water to a final concentration of 0.1vol%. A 15  $\mu$ l droplet of diluted APTES was deposited on freshly cleaved mica for one minute, and then rinsed with 2 ml of ultrapure water, and finally dried using a gentle flow of compressed nitrogen.

## **AFM sample preparation**

The control DNA preparation was mixed with ultrapure water to achieve a final concentration of 1ng/ $\mu$ l in 20 $\mu$ l volume. The solution was then deposited on the treated surfaces and left to incubate for 5 minutes.

Afterwards, the sample was rinsed with 1 ml of double distilled water and dried under a gentle nitrogen flow.

Hyperplectoneme-NAP complexes were formed by preliminarily incubating the designated protein with the DNA (final DNA concentration 1ng/μl, final NAP concentrations 0.75-4ng/μl) in ultrapure water at 37°C for 5 minutes. The whole mix was then deposited on APTES treated mica surface for 5 minutes and consecutively rinsed and dried under a gentle nitrogen flow.

### **AFM in air**

AFM images were collected using a MultiMode SPM with a Nanoscope III controller (Veeco Instruments, Santa Barbara, CA, USA) operated in tapping-mode in air. The AFM cantilevers had a spring constant of 5 N/m (Bruker cantilevers, TAP150A) with resonance frequencies ranging between 120 and 160 kHz. All recorded AFM images consist of 512 x 512 pixels with scan frequency ≤1 Hz. Each experiment was performed at least in triplicates and AFM images were obtained at several separate locations across the mica surface to ensure a high degree of reproducibility. For the statistical analyses we considered only the DNA complexes that were completely visible in an AFM image.

Images were simply flattened using the Gwyddion software (Version 2.22) and no further image processing was carried out (105).

### **DNA tracing**

DNA molecules were traced using “DNA Trace” software previously described (106). Based on the statistics of tens of individual molecules, the software calculated the contour length, the radius of gyration and the bond correlation function.

### **DNA persistence length**

The persistence length is a basic mechanical property of polymers that quantitatively describes its conformational flexibility. A typical value of  $L_p$  for double stranded DNA is estimated to be ~50nm (69,167).

We measured the persistence length  $L_p$  of DNA by directly fitting the bond correlation function for polymers in 3D:

$$\langle \cos(\theta) \rangle = e^{(-s/2 \cdot l_p)} \quad (4.1)$$

where  $\theta$  is the angle between the tangent vectors to the chain at two points separated by the distance  $s$  and  $l_p$  the persistence length (36).

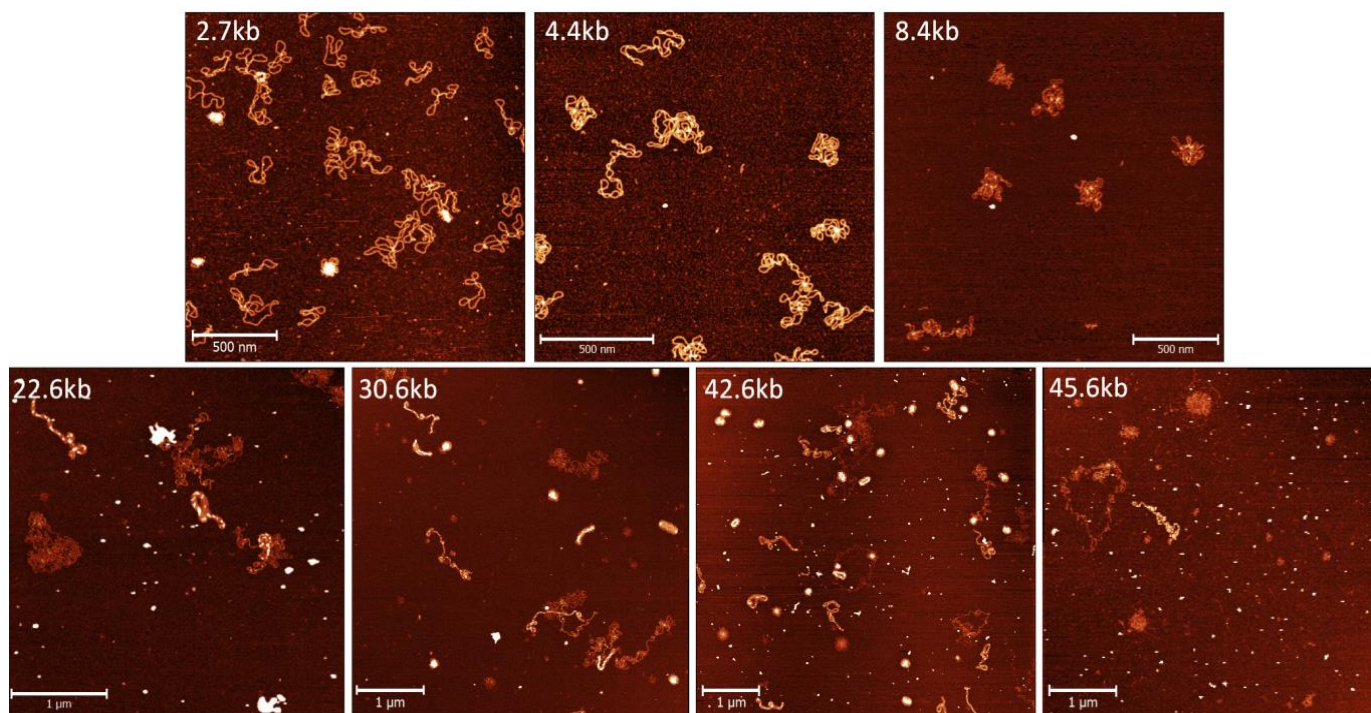


**Figure 4.1:** Typical large scale AFM images of supercoiled DNA of various sizes. Scale bars for upper and lower images 500nm and 1 $\mu$ m respectively.

## 4.3 Results

### 4.3.1 The formation of hyperplectonemes

To understand in which structures the DNA can be packed inside living systems, we studied and compared by AFM the physical properties of small (less than 10kb) and large (22.6kb to 45.6kb) supercoiled DNA deposited on APTES treated mica. We chose this chemical surface functionalization because of the strong interaction between the DNA and the APTES molecules, which produces kinetic trapping of the DNA structures and the so-called 3D-to-2D projected form of the molecule, rather than a 2D relaxation. Thus, this functionalization preserves the three-dimensional form of the DNA and yields a better understanding of the 3D shape of the molecules (22,33,299).

In Figure 4.1 and Figure 4.2 we present some typical large scale and close up AFM images of supercoiled DNA collected at the different sizes from 2.7kb to 45.6 kb. These images revealed two length scales at which supercoiled DNA structures strongly differed. Below 10kb, all supercoiled DNA showed plectonemically wound dsDNA (Figure 4.2a-c). The structures strongly resemble previously observed structures of supercoiled DNA (20-22). On the other hand, for DNA sizes above 20kb (Figure 4.2 d-g), we observed an emergence of new types of structures, showing large heterogeneity of complexity and organisation. Aside of relaxed DNA (probably nicked molecules), we highlighted compact toroidal and highly ordered plectonemically wound structures (Figure 4.3).

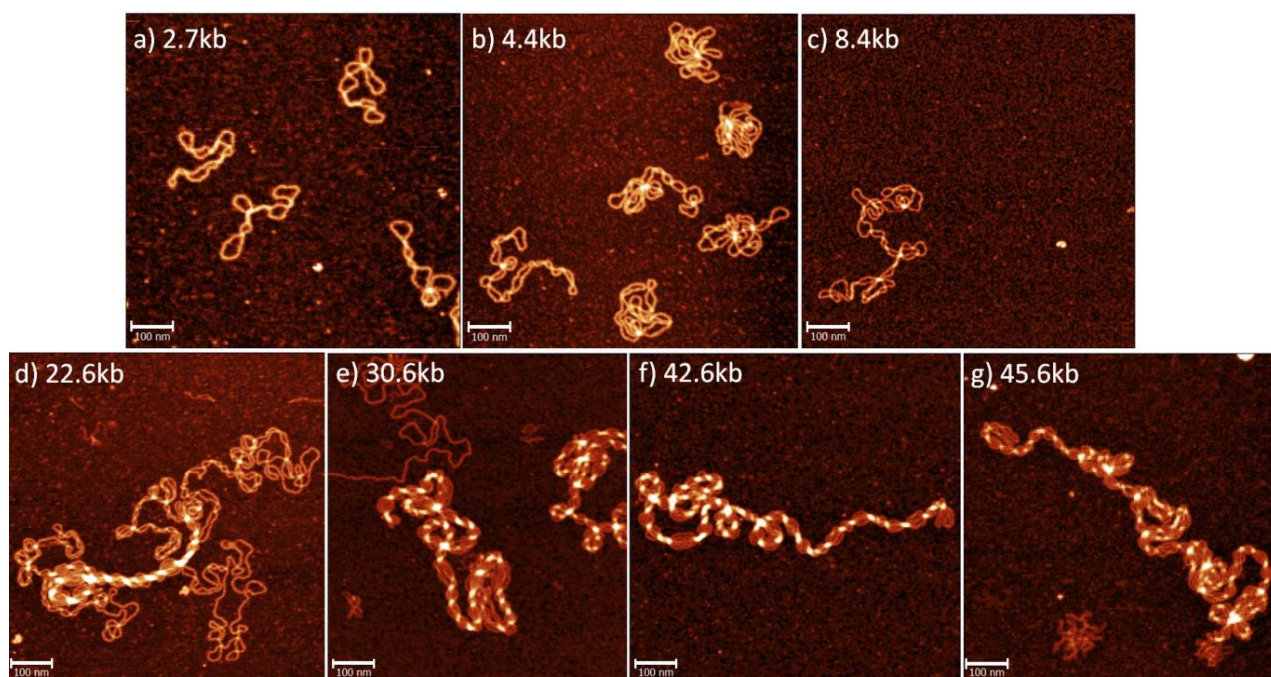


**Figure 4.2:** Typical structures of supercoiled DNA of various sizes. For DNA sizes below 10kb, simple plectonemes are observed. For DNA of ~20kb, partially formed hyperplectonemes, structures showing simple plectonemes joining into more complex higher order filaments emerge. Starting from ~30kb fully formed hyperplectonemes are seen. Scale bars 100nm.

The DNA toroidal structures (4.3b) have been previously observed when DNA was incubated in the presence of large concentrations of condensing agents, such as multivalent cations (300,301), polyamines (302,303) and silanes (108). Their existence in our samples suggests the presence of non-specific attractive forces between DNA strands, probably due to small amounts of unknown condensing agents.

Most importantly, we observed a so far uncharacterized class of highly ordered DNA structures. These tightly packed filamentous molecules were comprised of multiple individual plectonemically coiled DNA strands. These new type of higher order filaments, namely hyperplectonemes, were only partially formed for sizes 20-30kb and were fully formed for DNA larger than ~30kb (Figure 4.2e-g). In particular, the 22.6kb sample showed regions where simple plectonemes intertwined into a more complex filament.

This completely new type of DNA organisation appeared to be an emerging property of large supercoiled DNA. To understand which could be the factors governing the appearance of hyperplectonemes, we have screened several parameters of our deposition protocol. In particular, we focused on the analysis of the effect of salt concentration, substrate functionalization and supercoiling level. This extensive analysis highlighted how intra-molecular, non-specific, weak attractive potentials could be a driving force for stabilizing these peculiar structures.

The first parameter we tested was the role of salts in mediating DNA-DNA interactions. Monovalent salt are known to screen DNA charges, while divalent salts also can bridge DNA strands. The role of salts was clear in our experiments, since, by changing the salt concentration, we could significantly modify the overall morphology of the DNA.

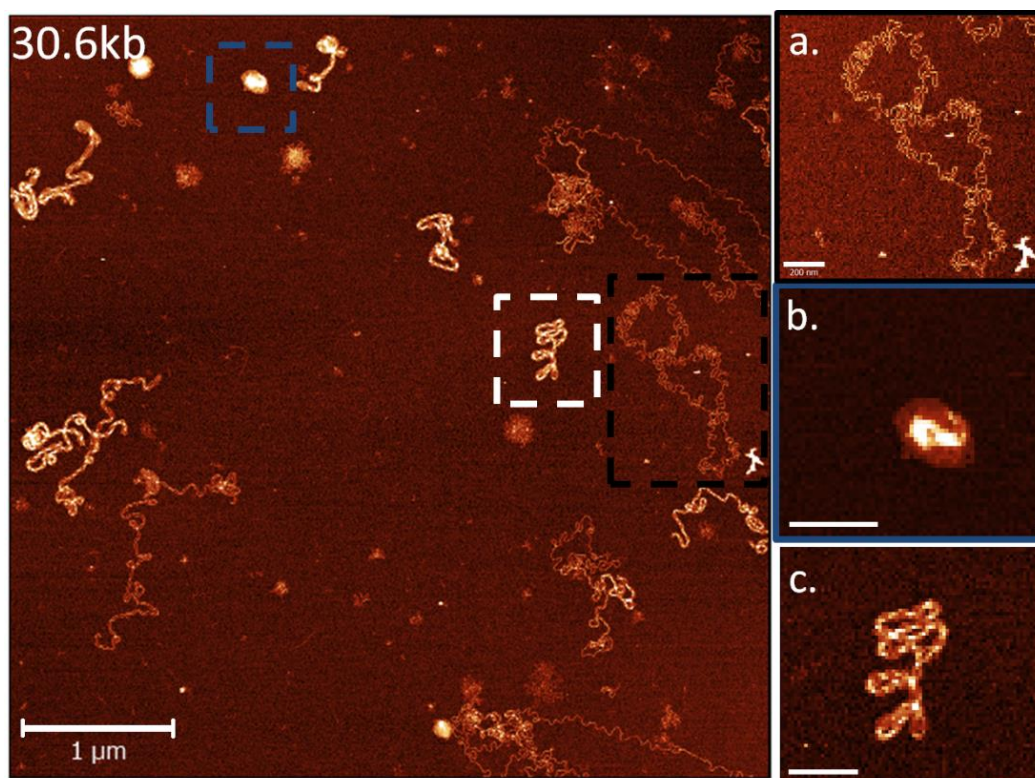


**Figure 4.3:** Large scale and zoomed AFM images showing: **a.** Relaxed **b.** Compact toroidal and **c.** Highly ordered plectonemic structures. Scale bars for large and zoomed images are  $1\mu\text{m}$  and  $200\text{nm}$  respectively.

For instance, the presence of even low concentrations of divalent salts ( $<10\text{mM MgCl}_2$ ) modified the molecular interactions in such a way that the resulting hyperplectonemic organisation was completely lost. When divalent salts were substituted with monovalent ones, there was only a partial loss of the higher order structures (Figure 4.4).

On the other hand, the screening of the different surface functionalization for the substrate was fundamental to determine the ideal surface for the experiments and to understand the role of the molecule-surface interactions in the arising of the compact structures. Indeed, we compared three different functionalization processes; APTES, poly-l-lysine and magnesium deposition. Remarkably, at low concentrations (0.1% vol fraction for 1 minute on bare mica), the APTES and the poly-l-lysine coated mica substrates produced similar aggregation patterns (Figure 4.5). This is not surprising, since both chemicals strongly bind the DNA. In literature, several groups have demonstrated how APTES as well as poly-l-lysine can condense DNA (108,304), yet this was shown only when directly added to the DNA solution, at much higher concentrations and at longer deposition times compared to our experimental procedures. In our experiments, we have employed a much lower functionalizing concentration, followed by thorough surface washing (see materials and methods). It is though possible that low amounts of the chemicals still dissolve from the surface into the solution and act as mediators for DNA-DNA attraction.

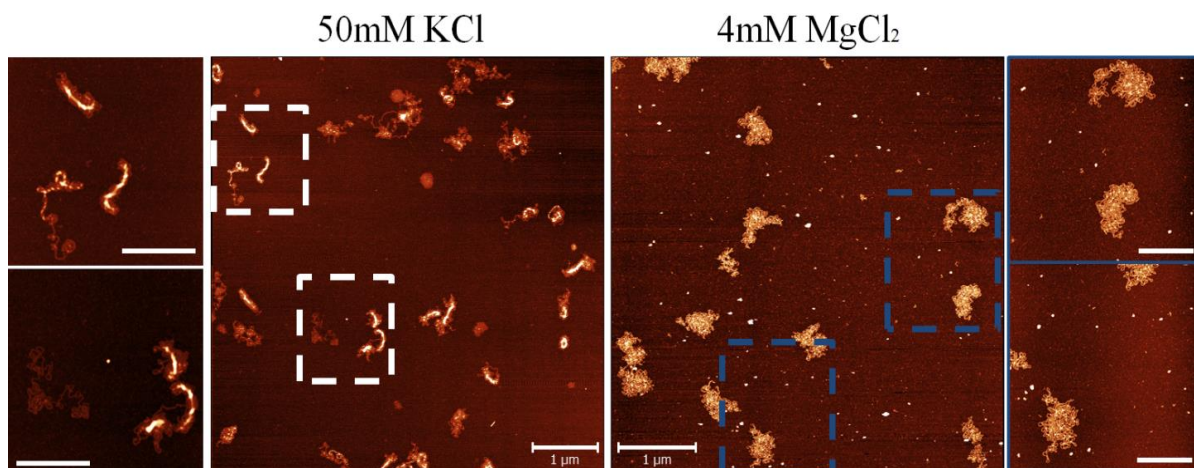


**Figure 4.4:** Influence of mono and divalent salts on hyperplectonemes deposited on APTES. Addition of monovalent KCl to the solution only partially impaired the formation of hyperplectonemes, whereas 4mM MgCl<sub>2</sub> was sufficient to completely disrupt plectonemic winding. Scale bars 1μm.

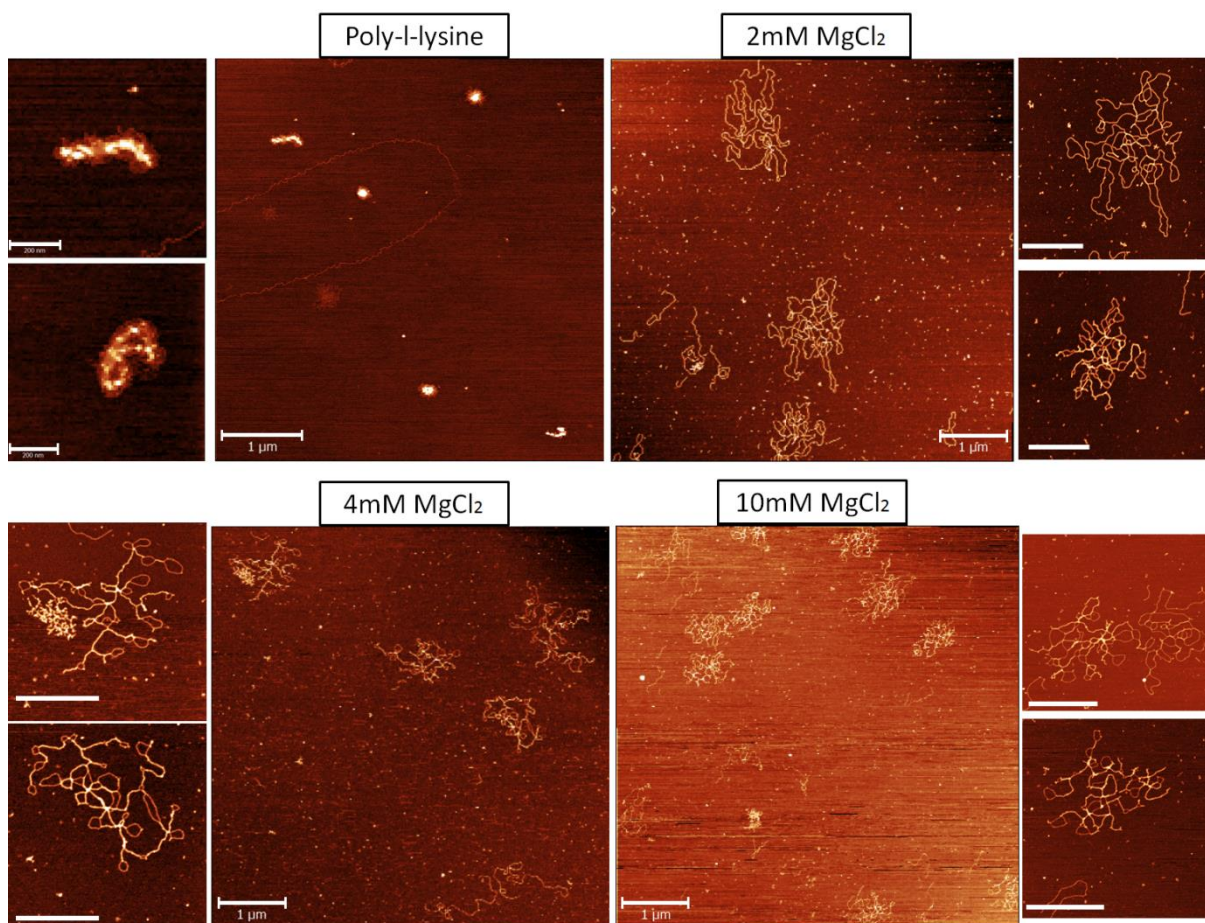


**Figure 4.5:** 42.6kb DNA deposited on poly-l-lysine treated surface and deposited with different concentrations of MgCl<sub>2</sub> (2mM, 4mM and 10mM). It can be seen, when deposited with MgCl<sub>2</sub> the hyperplectonemic structures are completely absent. Scale bars 1μm.

Once we had analysed the different steps of the deposition process, we studied the effects of the supercoiling levels. Specifically, we chose the largest DNA molecules (42.6 kb) and studied their morphology at different supercoiling levels. As seen in Figure 4.6, the topoisomers have different

organisations, and the level of supercoiling is governing the final degree of packing inside the hyperplectonemes. At the lowest supercoiling level, only simple plectonemes are formed with two dsDNA strands winding around each other (Figure 4.6a). These structures closely resemble small supercoiled DNA studied previously (<10kb) (20-22). In this case, probably the weak attractive potential was not sufficient to compact the structures. Once the supercoiling level was increased, the initially formed plectonemes started to fold further into the 1<sup>st</sup> order hyperplectoneme with one simple plectoneme folding on itself and stabilizing a complex looped structure (Figure 4.6b). The next step, further increasing the supercoiling, was the formation of a 2<sup>nd</sup> order hyperplectoneme of two simple plectonemes (Figure 4.6c). This packing process continues to form structures with up to 8-10 individual plectonemes packed into a tight filament as seen on Figure 4.6e.

In order to make sure that not only the attractive forces but also the supercoiling level was the key element in regulating the hyperplectoneme structure, we analysed DNA molecules, which we treated with a nicking enzyme. The nicking would produce single stranded breaks in the phosphate backbone and therefore result in the complete relaxation of the molecule. Figure 4.7 shows typical 42.6kb DNA molecules in supercoiled and nicked forms. Nicked DNA formed relaxed structures significantly larger in size, with lower height, clearly distinguishable dsDNA regions and almost no crossovers. The same 42.6kb DNA in supercoiled form stabilized a completely different type of organisation. Even previously observed compact toroidal forms completely disappeared. Therefore, we concluded that supercoiling was one of the key regulators in stabilizing hyperplectonemes.

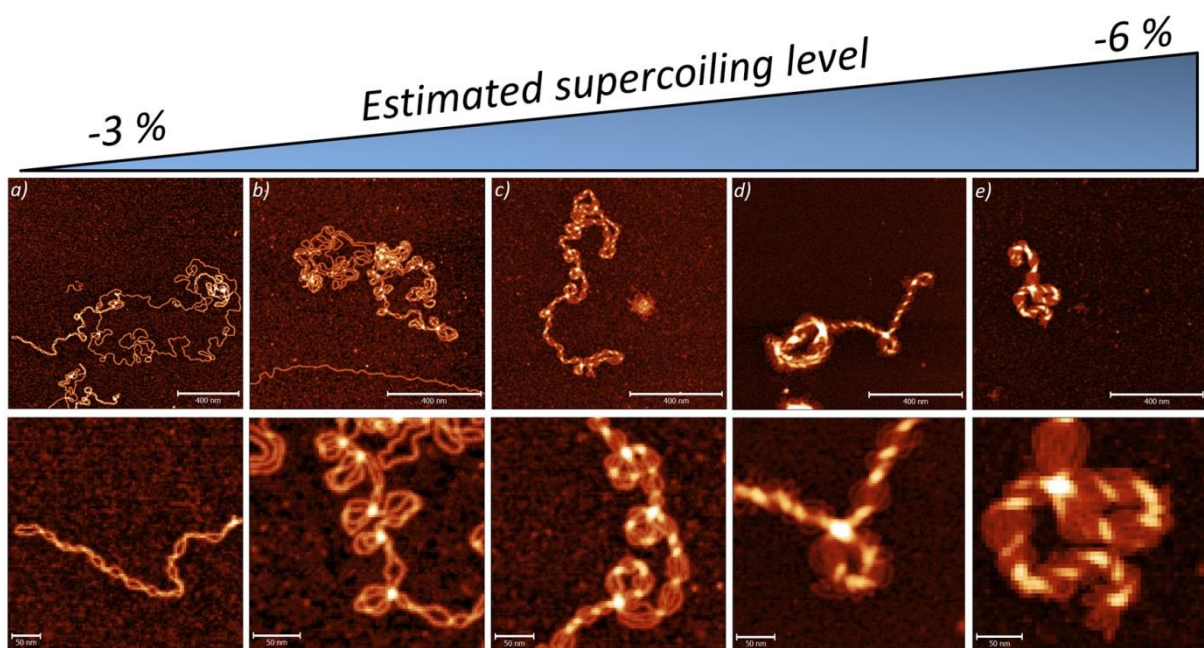


**Figure 4.6:** Formation of different order hyperplectonemes for 42.6kb DNA. Lower images represent the zoomed AFM images of Hyperplectonemes. a) Simple plectoneme b) 1<sup>st</sup> order hyperplectoneme c) 2<sup>nd</sup> order plectoneme d)-e) higher order hyperplectonemes formed with 6 and 8 individual plectonemes. Highly supercoiled DNA molecules in Figure 4.6e (supercoiling~ -6%) were treated with nicking enzyme for few minutes (2-5min) and than with ligase enzyme in order to partially relax them (decreasing their supercoiling to ~ -3%, fugre 4.6a). Scale bars for upper and lower AFM images are 400nm and 50 nm respectively.



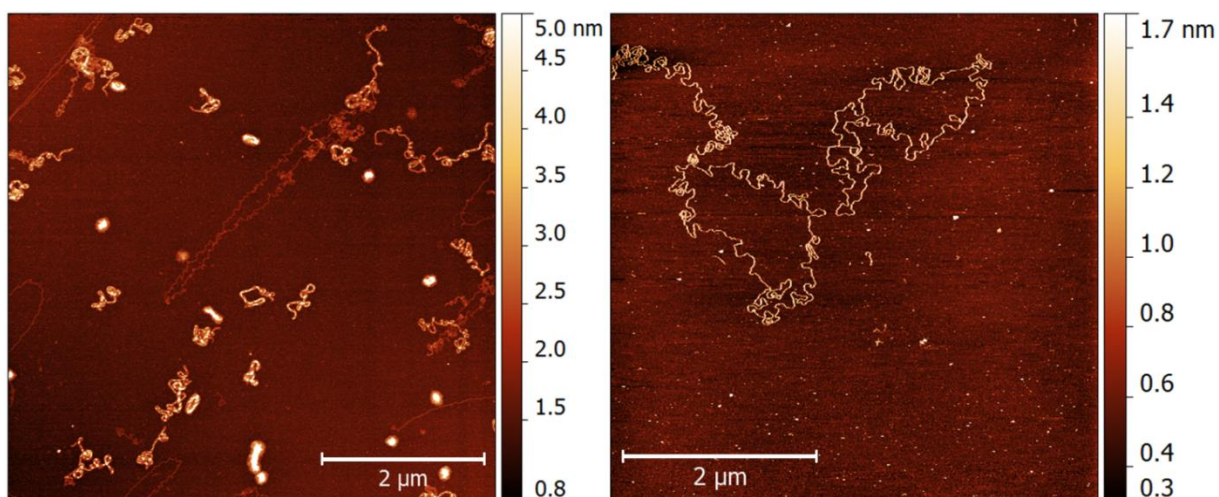


**Figure 4.7:** AFM image of supercoiled (left) and circular relaxed cosmid 42.6kb DNA on APTES treated mica. Nicking of the supercoiled DNA results in significantly larger DNA radius of gyration and complete disappearance of hyperplectonemes. Scale bars 2 $\mu$ m.

### 4.3.2 The persistence length of hyperplectonemes

The very high spatial resolution of AFM, allowed us in many cases to distinguish the number of individual DNA strands forming the higher order plectonemes. For cases where the DNA structures were too condensed to discriminate the single DNA strands inside a hyperplectoneme, we used the contour length as the reference to determine the order of plectonemes. At first, we characterized in detail the statistical parameters of the filaments, such as the contour length and the persistence length. Based on the theoretical contour length of the DNA (since we knew the number of base pairs), we traced the linear filament length of the structures and determined the number of single DNA strands in each hyperplectoneme.

As a control we used supercoiled 2.7kb and 4.4kb DNA, as well as the 42.6kb nicked relaxed DNA. These molecules were traced as circular objects, whereas the hyperplectonemes as linear structures. The only assumption we made was that the polymer physics models describing the persistence length of a single double stranded DNA (dsDNA) could be up-scaled and still be valid for a bundle of single dsDNA.

The typical persistence length value for a dsDNA is assumed to be 50nm (36,69,167). Based on our data, the persistence length for our control DNA (supercoiled 2.7kb and 4.4kb, and nicked 45.6kb DNA) was in the range between  $l_p = 45 - 55 \pm 5$  nm (Table 4.1). This extremely nice agreement with the predicted values, indicate that our experimental procedure was not influencing the mechanical properties of dsDNA. The persistence length of the hyperplectonemes was strongly dependent on compaction rate of the molecules. It was linearly proportional to the number of individual dsDNA, indicating a mechanistic model of filament compaction (Figure 4.8). For the highest hyperplectoneme order, comprised of 20 DNA strands, the low statistics resulted in the persistence length value that was less reliable.

**Table 4.1:** Statistical parameters of circular DNA

DNA Sample / Number of DNA strands	N <sub>molecules</sub>	Contour length <i>L</i> [nm]	R <sub>g</sub> [nm]	l <sub>p</sub> [nm]
2.7kb ( <i>Supercoiled</i> )	50	780 ± 80	55 ± 10	43 ± 2
4.4kb ( <i>Supercoiled</i> )	25	1280 ± 190	70 ± 20	44 ± 2
<b>42.6 kb DNA</b>				
1 ( <i>Nicked</i> )	10	12800 ± 580	420 ± 150	54 ± 2
4	7	2800 ± 130	250 ± 65	66 ± 5
6	7	1900 ± 100	170 ± 50	86 ± 5
8	10	1360 ± 90	140 ± 30	110 ± 10
10	5	1100 ± 30	130 ± 30	170 ± 10
12	10	910 ± 50	110 ± 30	185 ± 10
16	9	760 ± 50	120 ± 20	220 ± 10
20	8	540 ± 50	90 ± 20	290 ± 50

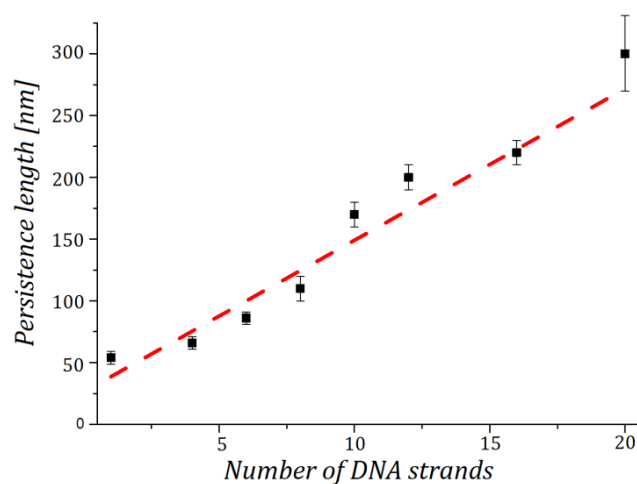


**Figure 4.8:** Hyperplectoneme persistence length as the function of number of DNA strands. Data taken from Table 4.1

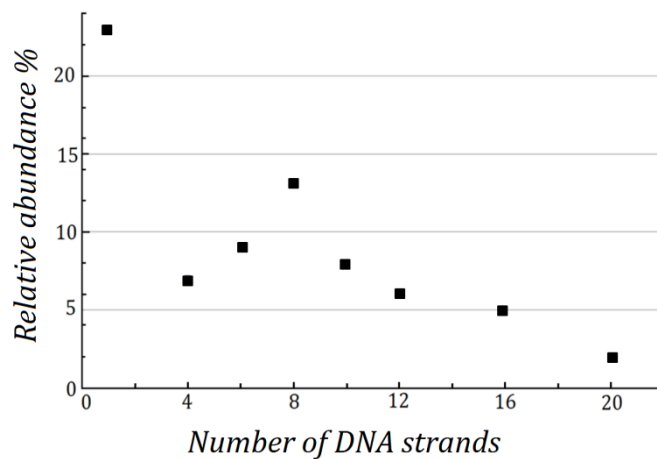


**Figure 4.9:** Relative abundance of nicked and hyperplectonemic structures of different order in 42.6kb DNA preparation extracted from exponentially growing *E.coli* cells.

### 4.3.3 The distribution of hyperplectonemes

To further characterize the hyperplectonemes we made statistics of different hyperplectonemic and nicked DNA populations (equation 4.2) within a DNA preparation (Figure 4.9). It is important to stress that every DNA extraction was unique in the way that the frequency of specific hyperplectonemic structures inside the population was similar but not constant.

$$Relative\ abundance\ \% = \frac{N_{Structure}}{N_{Nicked} + N_{Hyperplectoneme} + N_{Toroidal}} \quad (4.2)$$

Where  $N_{Structure}$  is the number of Nicked or specific hyperplectonemic population and  $N_{total}$  the total number of all DNA populations ( $N_{total} = N_{Nicked} + N_{Hyperplectoneme} + N_{Toroidal}$ ).

The distribution was primarily dependent on the growth state of the bacteria, from which the DNA was extracted (supercoiling levels of DNA inside the bacteria) (308). If the DNA was extracted from stationary phased *E.coli*, the molecules had significantly lower supercoiling levels and did not form hyperplectonemes (Figure 4.10). If the same DNA was extracted from bacteria in rich media, we could observe toroidal and hyperplectonemic DNA populations. These experiments confirmed that the structure of hyperplectonemes was directly linked to the metabolic state of the bacteria (Figure 4.10).

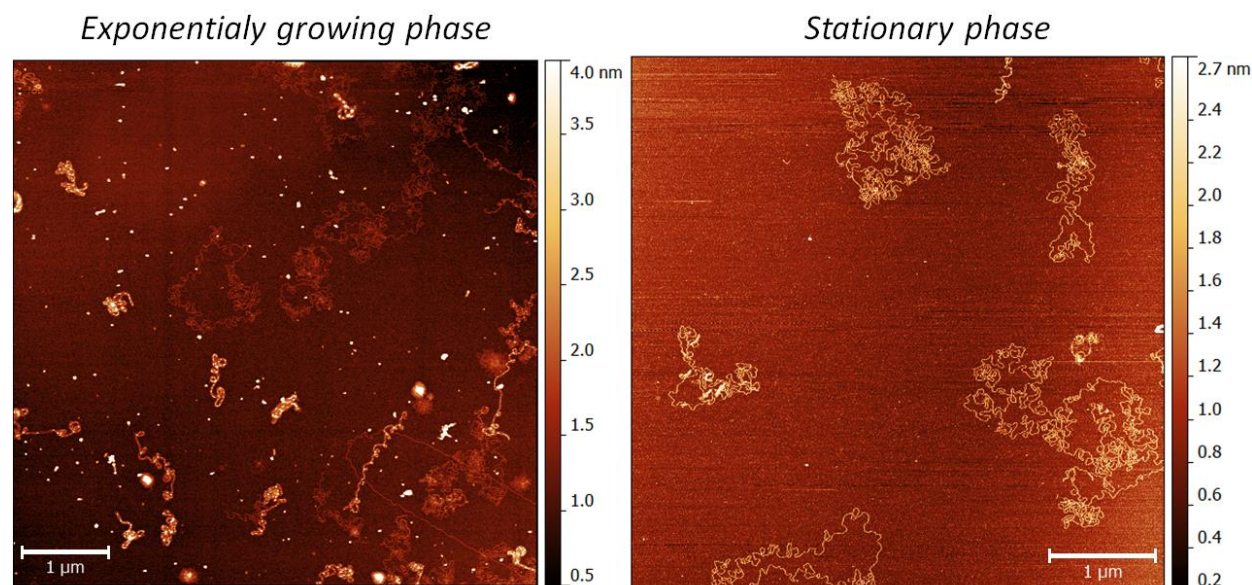


**Figure 4.10:** AFM images of 42.6kb DNA extracted from *E.coli* in rich medium (left) and *E.coli* deprived of nutrition (right). DNA from growing bacteria was highly supercoiled and formed hyperplectonemes, whereas when extracted from stationary culture, the DNA formed no hyperplectonemes. This indicates that the formation of hyperplectonemes is directly linked with the physiology of the cell. Scale bars 1  $\mu$ m.

## 4.4 Hyperplectoneme - NAP complexes

### 4.4.1 Nicked DNA - NAP complexes

The next step in our study was to investigate the structure of cosmid DNA when bound with various NAP proteins. For this purpose we used three most abundant DNA-binding proteins in exponentially growing *E.coli* cells (192), namely: factor for inversion stimulation (**FIS**), histone-like nucleoid structuring protein (**H-NS**) and histone-like protein (**HU**). Their structuring role has been previously studied on linear and small circular DNA molecules, but never on large supercoiled ones (210,212,213,306,314).

Since all of the three tested NAPs were supercoiling sensitive proteins, we decided to first study nucleoprotein complexes formed between nicked (relaxed) 42.6kb DNA and various proteins concentrations. In this way we would study their structuring effects on large DNA regions. We incubated cosmid DNA in the presence of increasing NAPs concentration and investigated the morphological changes the DNA underwent under the binding influence (Figure 4.11).

Figure 4.11 shows typical close up images of 42.6kb nicked DNA, bound with different FIS, H-NS and HU proteins. Interestingly, there was very little difference between the various NAPs used, when they were bound to relaxed DNA. At high concentrations, they all condensed the DNA at different degrees (Figure 4.11). This is a very interesting result, because it highlights the role of DNA supercoiling in nucleoprotein complex formation. When bacteria is in stationary phase and the overall supercoiling levels are low (298), various NAPs can have similar, condensing effects on the global DNA structure. We even propose, that the similar effects of DNA condensation by various NAPs, acts as a protective agent for DNA damage in stationary phase bacteria.

### 4.4.2 Hyperplectoneme - NAP complexes

As the next step, we repeated the same experiments as described above but with supercoiled DNA instead of the nicked ones. For the same NAP concentrations, the differences between nucleoprotein complexes formed by relaxed and supercoiled DNA were very large. All three proteins induced clear differences when bound to hyperplectonemes. We gradually increased the concentration of the proteins to study the structural changes hyperplectonemes would undergo when bound with the proteins.

#### **FIS**

Binding of FIS to hyperplectonemes at low concentrations ( $\sim 1\text{ng}/\mu\text{l}$ ) resulted in the partial loss of hyperplectonemic structures in the DNA. The molecules adopted a more opened structures, with simple plectonemes still visible (Figure 4.12a and Figure 4.13). In order to completely unwind the hyperplectonemes, higher FIS concentrations were needed ( $\sim 2.5\text{ng}/\mu\text{l}$ ). At highest FIS concentrations, DNA molecules appeared compact and condensed ('quasi-three dimensional' blob-like structures), similarly as for the nicked DNA molecules. Previously observed hyperplectonemes were completely absent for the highest FIS concentrations. Interestingly, depending on the order of hyperplectonemes, we could observe a gradual change in the morphology as FIS was binding. First the lower order

hyperplectonemes changed their shape, then was the turn of the more condensed hyperplectonemes and finally for the dense toroidal structures. This effect is probably linked to the difference in the surface area of the structures. Since toroids had the smallest surface area, a smaller amount of FIS proteins would bind and, to have a detectable change in shape, higher concentrations of proteins would be needed. The fact that FIS induced the formation of blob-like structures was not surprising, considering FIS is typically an activator protein. FIS mediated DNA-DNA contacts in space, increasing the local concentration of DNA binding sites, which than are utilized by transcription machinery.

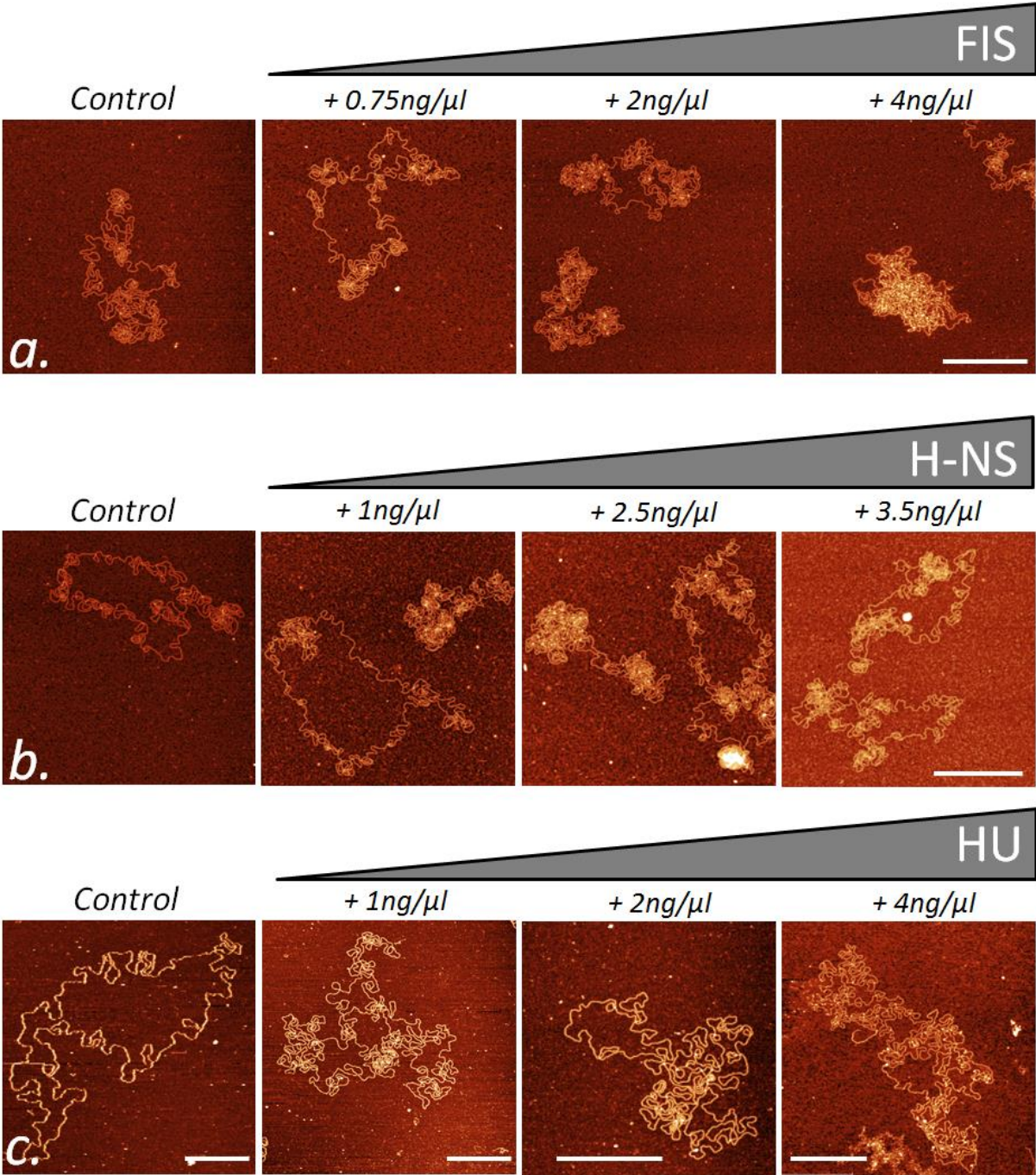


**Figure 4.11:** AFM images of relaxed 42.6kb DNA forming nucleoprotein complexes with **a)** FIS **b)** H-NS and **c)** HU. Increasing concentrations of all three proteins induced DNA condensation. Scale bars 500nm.

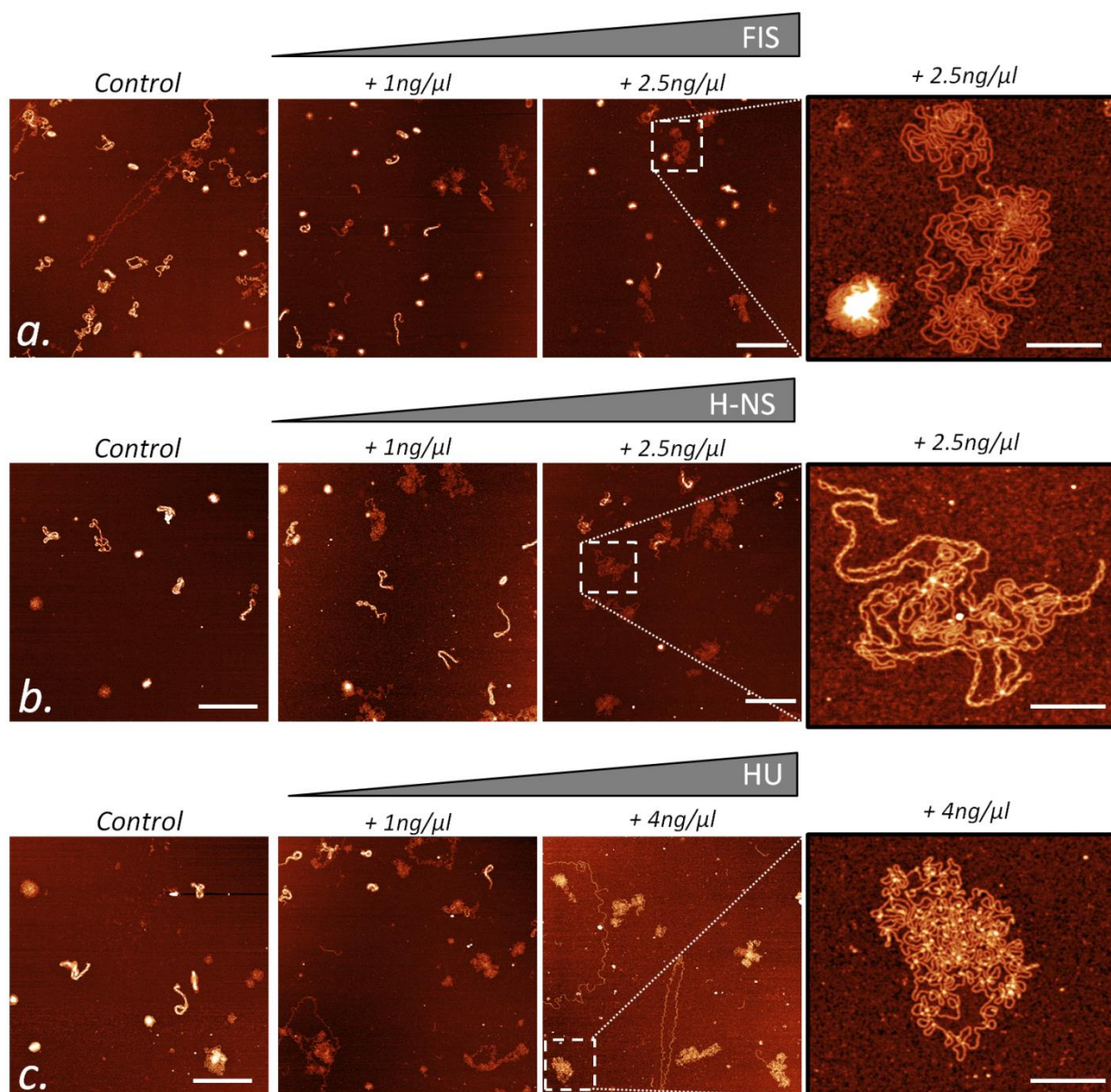


**Figure 4.12:** Large scale and zoomed AFM images of 42.6kb hyperplectonemic DNA forming nucleoprotein complexes with **a)** FIS **b)** H-NS and **c)** HU. High concentrations of FIS induced the loss of hyperplectonemes and condensed the DNA. High concentration of H-NS partially induced the loss of hyperplectonemes. H-NS bound DNA was forming large supercoiled regions with single plectonemes. With high concentrations of HU, DNA adopted a grid-like structure, with many DNA cross-overs and small loops. Scale bars for large and zoomed images are 1 $\mu$ m and 200nm respectively.

### H-NS

H-NS was previously shown to bridge DNA (212,213), as well as to constrain negative supercoils (210,216). In our experiments, H-NS stabilized extended filaments of plectonemically wound DNA (Figure 4.12b and Figure 4.13). The hyperplectonemes were partially opened and several simple plectonemes were visible (Figure 4.12b). In contrast to FIS, H-NS protein was not condensing the supercoiled DNA. It was stabilizing elongated filament structures. The structures were ‘quasi-one dimensional’. In contrast to FIS, the highest concentration of H-NS (~2.5ng/ $\mu$ l) was not sufficient to completely unwind the hyperplectonemes.

H-NS typically acts as a repressor protein. It forms filament-like structures, which are most likely thermodynamically very hard to open up to be accessible for transcription machinery. Therefore, whenever H-NS binds, it blocks DNA or makes it inaccessible for transcription.

## HU

When HU was bound to supercoiled DNA, it formed completely different structures than FIS or H-NS. At low concentrations ( $\sim 1\text{ng}/\mu\text{l}$ ), it unwound the hyperplectonemes resulting in with partially formed structures (Figure 4.12c). When used even at higher concentrations, the DNA structures appeared completely unwound and opened. In contrast to FIS, HU partially condensed the DNA, and the structures had much more uniform height and were quasi-two dimensional. Previously HU was shown to form toroidal coiling when bound to DNA (194). The HU-nucleoprotein complexes formed a grid-like structure (Figure 4.12c), with many DNA crossings and small, presumably toroidal loops.

HU binds DNA nonspecifically. It is interesting that the HU bound DNA were homogeneous in height and similar to each other (Figure 4.12c), in contrast to both FIS and H-NS, which showed larger diversity.

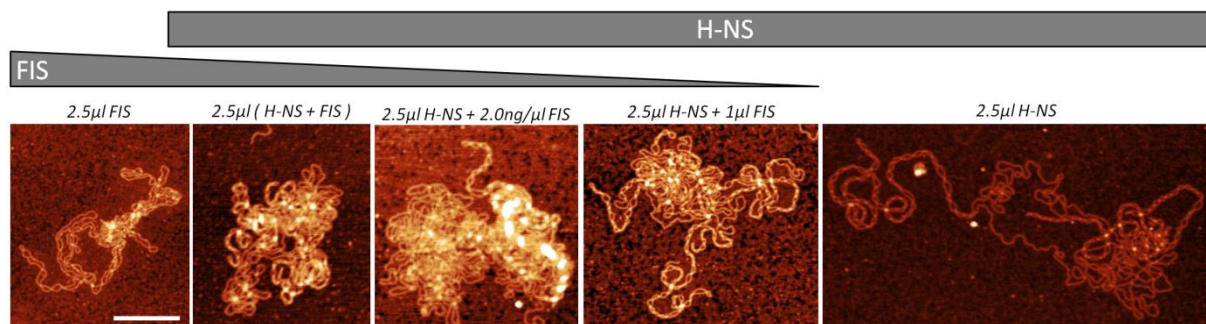


**Figure 4.13:** Zoomed images of 42.6kb hyperplectonemic DNA forming nucleoprotein complexes with FIS and H-NS separately or together at various FIS concentrations. FIS alone condenses the DNA, in contrast to H-NS protein, which upon binding elongates the DNA and forms long DNA filaments. When used in combination, depending on the ratio of the two proteins, either more filaments are formed, or larger DNA regions are condensed inside a blob-like configuration. Scale bar 200nm.

### 4.4.3 FIS + H-NS pairwise nucleoprotein complexes

Pairwise incubation of the H-NS and FIS protein with supercoiled revealed very interesting results. Separately, FIS was condensing DNA and H-NS forming long filaments. When both of proteins were used at the same time, depending on the ratio of the concentrations, we observed a combined effect of the two proteins (Figure 4.13). We kept the H-NS concentration fixed ( $2.5\text{ng}/\mu\text{l}$ ) and gradually increased the FIS concentration ( $1\text{ng}/\mu\text{l}$ ;  $2.0\text{ng}/\mu\text{l}$ ; and  $2.5\text{ng}/\mu\text{l}$ ).

The nucleoprotein complexes were showing two distinct configurations. When FIS was used at  $1\text{ng}/\mu\text{l}$  in the presence of H-NS ( $2.5\text{ng}/\mu\text{l}$ ), only a small part of the DNA was condensed into the blob-like structures.

Several plectonemes were visible, extending from the inner condensed core of the DNA to the outside. Gradual increase of the FIS concentration resulted in shortening of the plectonemes and increase of the condensed DNA region.

This meant that when both proteins were acting on supercoiled DNA, we observed a 'phase-like separation' between the regions, where the two proteins were binding. We observed the formation of domains of different local structure and order, depending on the proteins. We predict that these regions, where FIS and H-NS are separately bound, will have completely different dynamics and thermodynamic stability that will lead to different accessibility of transcription machinery.



## 4.5 Conclusions

In this final chapter, we studied a completely new type of DNA organisation, which we called hyperplectonemes, ordered DNA structures, which are formed by large supercoiled molecules in the presence of attractive DNA-DNA potential. These structures consisted of multiple simple plectonemes folding on itself, forming a higher order filament.

We first showed the size dependency of the hyperplectonemes, showing a lower size limit, under which DNA was not forming into hyperplectonemes. Afterwards, we studied the influence of various sample preparation factors on their structure. We showed that high concentrations of mono- and divalent salts resulted in partial or full the loss of structures. The sample deposition also played an important role in the formation of hyperplectonemes. When we deposited the DNA on APTES or poly-L-lysine treated surface, the hyperplectonemes were clearly visible. Both chemicals were shown to condense the DNA when used in the solution, therefore we cannot exclude that the chemicals play a role in mediating DNA-DNA attraction.

We also showed the importance of DNA supercoiling in the hyperplectoneme formation. Nicking the DNA resulted in complete relaxation of the DNA structures. Extracting DNA from stationary phase *E. coli* cells, where global DNA supercoiling is low, also resulted in relaxed DNA structures, showing a direct link between cell physiology and hyperplectonemes structures.

Finally we tested binding of hyperplectonemes to nucleoid associated proteins. The nucleoprotein complexes were strongly linked to the type of protein used and their function in the cell. FIS condensed DNA into various sized globular aggregates; H-NS unwound hyperplectonemes and formed linear filaments; HU induced small toroidal loops with a global mesh-like DNA structure. When used pairwise, FIS and H-NS, formed domain-like structures on DNA, with either extended filamentous or compact blob-like configurations. The ratio of the proteins was governing how much of the DNA was condensed or extended into the filament.

We think this new DNA organisation reflects bacterial physiology well and represents the basic structure of the bacterial chromatin, which is further modulated by numerous DNA binding and condensing proteins *in vivo*.

## Chapter 5: Conclusions and future perspectives

### Conclusions

DNA molecules are fundamental components of all living organisms. While sequencing techniques allow determining in detail the genetic sequence of hundreds of species, the correlation between sequence and function is still under intense scrutiny. The complexity of the DNA related machinery is such that many levels of organisation are found as well as multiple regulation mechanisms are involved in its function.

In this thesis we addressed some open questions by means of atomic force microscopy, specifically performing experiments to investigate the link between DNA topology and its function. We have presented several experiments, studying the physical and geometric properties of bare DNA (Chapter 2), and the interaction between DNA and bacterial transcription machinery (Chapter 3). We finalized our study by investigating large, bacterial domain sized supercoiled DNA molecules (sizes up to 45kb). We studied their structure with nanoscale resolution, and in presence of nucleoid associated proteins.

These studies led to new insights into the biophysical investigation of the link between DNA topology and function, which can be summarized in the following conclusions:

***a) Upon deposition, the sub-molecular conformation of the DNA either remains in the physiological B-form, or parts of the molecule reorganize into the A-form helix. This transition depends on the DNA-substrate binding strength.***

We determined length differences between DNA samples deposited on APTES treated mica (strong surface binding) and molecules deposited by using divalent  $Mn^{2+}$  or  $Mg^{2+}$  cations (weak surface binding). These differences were consistent with the length difference between DNA molecules in their physiological B-form, and with parts of the molecule reorganizing into the A-form. Subsequent TERS measurements confirmed the local sub-molecular conformation changes and showed that the A-form transition was predominantly occurring at the ends of linear DNA molecules (316). These results show the heterogeneity of the DNA sub-molecular structure, indicating the possibility of the DNA to undergo a transition from A-to-B form even in the presence of water. If indeed this transition takes place *in vivo*, this will lead to significant changes in the way proteins and gene regulatory machinery interacts with the DNA.

***b) The physical and shape properties, such as the persistence length, asphericity and anisotropy of DNA molecules change substantially under geometric confinement.***

By combining nanometer sized PDMS slits with AFM, we were able to visualize and study single DNA molecules under geometric confinement. We showed that, when DNA is weakly confined in space, the

molecules tend to elongate and adopt more anisotropic shapes. In this case, the persistence length increased and even the shape of the correlation function changed. Most importantly, when DNA is under stronger confinement, we were able to identify DNA defects in forms of hairpins and intertwined regions, superposed with nicked regions in the molecule. We propose that geometrical confinement *in vivo* can promote the formation of localized defects at thermodynamically weak sites in the DNA (317). This opens up new possible regulatory mechanism for DNA damage repair or gene expression regulation inside bacterial chromatin. If the hairpins are formed *in vivo*, they can act as markers for DNA damage sites, helping the DNA repair machinery to detect the weakspots in the genome or act as transcription blockage sites.

***c) DNA staining dyes strongly change the physical properties of the bare DNA molecules.***

We tested three different dyes (PicoGreen; Dapi and DRAQ5), which bind differently to the DNA (intercalating and minor groove binding modes). In all three cases, either the persistence length of the DNA decreased, or the contour length increased or both at the same time were modified. The overall morphology of the DNA, as well as its migration properties on agarose gel, was significantly affected in a dose and dye-type dependent manner. We conclude that stained DNA properties should not be considered as the same as the ones of a bare molecule (136). Accordingly, when performing experiments on stained cells or single DNA molecules, the possible effects of the dyes need to be taken into consideration.

***d) Single point mutations of a regulator protein can significantly impair its promoter binding affinity and disrupt the formation of higher order nucleoprotein complexes.***

By studying as a model system the EspR protein, a key regulator of virulence in *Mycobacterium tuberculosis* (MTB), we showed that single amino acid mutations, led to significantly lower DNA binding affinity. These key mutations also partially or completely disrupted the formation of higher order protein-DNA complexes, leading to silencing of the MTB virulence. This approach can be further generalised to other bacterial virulence regulators, opening up a possible drug targets for diseases (318).

***e) The binding site organisation for a nucleoid associated protein is determinative for the final higher-order nucleoprotein structure.***

We studied the H-NS protein and we showed that the spatial organisation on the DNA structure of strong binding sites for this protein led to the formation of very distinct 3D nucleoprotein filaments. The average length, persistence length, height and periodicity of the DNA filament were strongly linked to the protein binding site organisation (319). These results give a glimpse of the importance of the gene position in the bacterial genome, indicating a possible non-random organisation.

***f) The helical phasing between RNA polymerase binding sites upstream and within the *fis* promoter, lead to long-range cooperativity between distantly bound polymerase molecules.***

We showed that simultaneous binding of RNA polymerase withing the *fis* promoter and a helically phased upstream site stabilized a RNAP oligomeric complex. We demonstrated that the insertion of half a helical turn and not the full turn of DNA sequence, while not affecting directly the binding sites, decreased the RNAP binding affinity to *fis* promoter (74).

***g) In the presence of attractive potential, large supercoiled DNA molecules form very distinct, higher order plectonemic structures, that we call Hyperplectonemes. When bound with NAPs, these structures modulate their structure according to the function of the protein.***

We studied a completely new type of very ordered DNA organisation, which we called hyperplectonemes. These structures are formed by supercoiled molecules larger than 20kb, in the presence of non-specific attractive DNA-DNA potential. We investigated their structural properties and studied the role of the DNA-DNA interaction, of the deposition method and of the supercoiling level of the DNA in their appearance. We also investigated the binding of hyperplectonemes to three nucleoid associated proteins: FIS, H-NS and HU. The single NAPs induced very distinct structures when bound to supercoiled hyperplectonemes: FIS stabilized condensed blob-like structures; H-NS formed long and tight filamentous complexes; HU formed homogeneous grid-like structures. Interestingly, the pairwise combination of FIS and H-NS protein, lead to the formation of domain-like structures within single DNA molecules.

We believe, the hyperplectonemic organisation is the core structure of the bacterial chromatin which is further modified and organised by numerous NAP in the bacteria. In conclusion, the hyperplectonemes describes how the nucleoid can be effectively compacted and organized, but be dynamic in nature and accessible to DNA binding proteins and enzymes

A more detailed summary of every experiment is discussed in the corresponding chapter of the thesis.

## **Future perspectives**

The experimental results discussed in this thesis can be further extended in many directions:

**a)** We addressed the importance of surface binding strength in the sub-molecular conformation adopted by the DNA. The role of the DNA sequence in the extent of the B-to-A DNA transition can be further investigated. As a possible follow-up experiment, we could compare the structure of same sized DNA molecules with very different GC content.

**b)** For the experiments performed on DNA molecules in geometric confinement, we could extend our study to even larger molecules. We could test the Odijk confinement regime, where the DNA is under very strong confinement. We could test supercoiled as well as knotted DNA in our confinement set-up, assessing the role of topology on DNA.

**c)** The modifications induced by dyes on the DNA structure is of utmost importance, since numerous different dyes are commonly and routinely used in single molecule experiments. This means that we should expand our studies to include all of the most commonly used dyes, to understand their effect on the obtained results. Furthermore, in this thesis we tested linear DNA fragments and extending our study to circular relaxed and supercoiled DNA would give us extra information about DNA-dye interaction.

**d)** We could study the role of point mutations in numerous transcription factors interacting with promoter sequences. In general terms, the disruption of dimerization in a protein leads to lowered binding affinity and consequent silencing of the promoter, this opens new possibilities for future drug design.

**e)** Our results suggest that, as in the case of H-NS binding sites, the spatial arrangement of the binding sites of other major NAPs will lead to the formation of distinct 3D structures. Studying this will open up new perspectives in understanding the connection between DNA sequence and function.

**f)** Testing other promoter sequences containing several RNA polymerase binding sites, would be very interesting to understand the role of geometry in promoter transcription regulation.

**g)** There are numerous experiments that could be performed on the hyperplectonemes. We still don't know the origins of the attractive DNA-DNA potential. To test it, we could perform more fine-tuned experiments with various salt types and concentrations. It is important to perform Light Scattering and Cryo Electron Microscopy measurements to have more information about the bulk and 3D configurations of the structures. Taking cosmids with high AT content would give us more insight in the role of DNA sequence on forming hyperplectonemes.

It is also very important to test other major NAPs, as well as their combined effects on hyperplectonemes, to understand their role in structuring and regulating bacterial chromosome structures.

***“There is no end to education. It is not that you read a book, pass an examination, and finish with education. The whole of life, from the moment you are born to the moment you die, is a process of learning”- Jiddu Krishnamurti***

## Bibliography

- (1) Mischer, J. F. (1871) Über die chemische Zusammensetzung der Eiterzellen. *Medchem. Unters.*, 4, 441–460.
- (2) Watson, J. D. and Crick, F. H. C. (1953) Molecular structure of nucleic acids. *Nature*, 171, 737–738.
- (3) Franklin, R.E. and Goslings, R.G. (1953) The Structure of Sodium Thymonucleate Fibres. I. The Influence of Water Content. *Acta Cryst.*, 6, 673-677.
- (4) <http://www.atdbio.com/content/5/Nucleic-acid-structure>
- (5) Watson, J. D. and Crick, F. H. C. (1953) Genetical Implications of the structure of Deoxyribonucleic Acid, *Nature* 171 (1953), 964-967.
- (6) Franklin R. and Gosling R. G. (1953) Molecular Molecular Configuration in Sodium Thymonucleate, *Nature* 171, 740-741.
- (7) Franklin R. and Gosling, R. G. (1953) Evidence for 2-Chain Helix in Crystalline Structure of Sodium Deoxyribonucleate, *Nature* 172, 156-157.
- (8) Ghosh, A. and Bansal, M. (2003) A glossary of DNA structures from A to Z, *Acta Crystallographica D*, 59, 620-626.
- (9) Sinden, R. R. (1994) *DNA structure and function*, Academic Press, USA
- (10) Rich, A., Norheim, A. and Wang, A.H.J. (1984) The chemistry and biology of left-handed Z DNA, *Annual Review of Biochemistry* 53 (1): 791–846.
- (11) Rich, A. and Zhang, S. (2003) Z-DNA: the long road to biological function, *Nature Reviews Genetics* 4, 566-572.
- (12) [https://www.mun.ca/biology/scarr/iGen3\\_02-14.html](https://www.mun.ca/biology/scarr/iGen3_02-14.html)
- (13) Weil, R. (1963) The denaturation and the renaturation of the DNA of polyoma virus, *Proceedings of the National Academy of Sciences of the United States of America* 49, 480-7.
- (14) Weil, R. and Vinograd, J. (1963) The Cyclic Helix and Cyclic Coil Forms of Polyoma Viral DNA, *Proceedings of the National Academy of Sciences of the United States of America* 50, 730-8.
- (15) Vinograd J, Lebowitz J, Radloff R, Watson R, Laipis P. 1965. The twisted circular form of polyoma viral DNA. *Proc. Nat. Acad. Sci. USA* 53: 1104-II
- (16) Liu, L.F., Depew, R.E. and Wang, J.C. (1976) Knotted Single-Stranded-DNA Rings - Novel Topological Isomer of Circular Single-Stranded-DNA Formed by Treatment with Escherichia-Coli Omega Protein. *Journal of molecular biology* 106, 439-452.
- (17) Liu, L.F., Perkocha, L., Calendar, R. and Wang, J.C. (1981) Knotted DNA from bacteriophage capsids, *Proceedings of the National Academy of Sciences of the United States of America* 78, 5498-502.
- (18) Liu, L.F., Davis, J.L. and Calendar, R. (1981) Novel topologically knotted DNA from bacteriophage P4 capsids: studies with DNA topoisomerases, *Nucleic acids research* 9, 3979-89.
- (19) Shishido, K., Ishii, S. and Komiyama, N. (1989) The Presence of the Region on Pbr322 That Encodes Resistance to Tetracycline Is Responsible for High-Levels of Plasmid DNA Knotting in Escherichia-Coli DNA Topoisomerase-I Deletion Mutant. *Nucleic acids research* 17, 9749-9759
- (20) Adrian, M., ten Heggeler-Bordier, B., Wahli, W., Stasiak, A. Z., Stasiak, A. and Dubochet, J. (1990) Direct visualization of supercoiled DNA molecules in solution. *EMBO J.*, 9, 4551–4554.

- (21) Boles, T.C., White, J.H. and Cozzarelli N.R. (1990) Structure of plectonemically supercoiled DNA, *Journal of Molecular Biology*, 213,931- 51
- (22) Lyubchenko, Y., Shlyakhtenko, L., Harrington, R., Oden, P. and Lindsay, S. (1993) Atomic Force Microscopy of long DNA – imaging in air and under water. *Proceedings of the National Academy of Sciences of the United States of America* 90, 2137-2140.
- (23) Yamaguchi, H., Kubota, K. and Harada, A. (2000) Direct observation of DNA catenanes by atomic force microscopy. *Chemistry Letters*, 384-385.
- (24) Valle, F., Favre, M., Roca, J. and Dietler, G. (2005) Atomic force microscopy of complex DNA knots. *Physical and Numerical Models in Knot Theory* 36, 161-170.
- (25) Pavlicek, J.W., Oussatcheva, E.A., Sinden, R.R., Potaman, V.N., Sankey, O.F. and Lyubchenko, Y.L. (2004) Supercoiling-induced DNA bending. *Biochemistry* 43, 10664- 10668.
- (26) Lyubchenko, Y.L. (2004) DNA structure and dynamics - An atomic force microscopy study. *Cell Biochemistry and Biophysics* 41, 75-98.
- (27) Wyatt, P.J. (1993) *Light scattering and the absolute characterization of macromolecules*, Vol. 272, 1-40
- (28) Perkins, T. T., Smith, D. E., Larson, R. G., and Chu, S. (1995) Stretching of a single tethered polymer in a uniform flow. *Science*, 268(5207), 83–87.
- (29) Maier, B. and Radler, J. O. (2000) DNA on fluid membranes: A model polymer in two dimensions. *Macromolecules*, 33(19), 7185–7194.
- (30) Wang, M.D., Yin, H., Landick, R., Gelles, J., and Block, S.M. (1997) Stretching DNA with optical tweezers. *Biophys. J.*, 72(3), 1335–1346.
- (31) Williams, M. C., Wenner, J. R., Rouzina, I., and Bloomfield, V. A. (2001) Entropy and heat capacity of DNA melting from temperature dependence of single molecule stretching. *Biophys. J.*, 80(4), 1932–1939.
- (32) Rivetti, C., Walker, C., and Bustamante, C. (1998) Polymer chain statistics and conformational analysis of DNA molecules with bends or sections of different flexibility. *J. Mol. Biol.*, 280(1), 41–59.
- (33) Valle, F., Favre, M., De Los Rios, P., Rosa, A., and Dietler, G. (2006) Scaling exponents and probability distributions of DNA end-to-end distance. *Phys. Rev. Lett.*, 95, 158105.
- (34) De Gennes, P. G. (1979) *Scaling concepts in polymer physics*, Cornell Univ. Press, London.
- (35) Grosberg, A. Y. and Khokhlov, A. R. (1994) *Statistical physics of macromolecules*, AIP Press, New York.
- (36) Rubinstein, M. and H., C. R. (2003) *Polymer Physics*, Oxford University Press, Oxford.
- (37) Abbe, E. (1873) Beitrage zur Theorie des Mikroskops und der mikroskopischen Wahrnehmung. *Archiv für Mikroskopische Anatomie* 9: 413–420
- (38) Knoll, M. (1935) Aufladepotential und Sekundäremission elektronenbestrahlter Körper. *Zeitschrift für technische Physik* 16: 467–475.
- (39) Rust, M., Bates, M. and Zhuang X. (2006) Sub-diffraction-limit imaging by stochastic optical reconstruction microscopy (STORM), *Nature Methods* 3 (10): 793–796.
- (40) Hell, S. W. (2007) Far-Field Optical Nanoscopy, *Science* 316 (5828): 1153–1158.
- (41) Betzig, E., Patterson, G.H., Sougrat, R., Lindwasser, O. W., Olenych, S., Bonifacino, J. S., Davidson, M. W., Lippincott-Schwartz, J. and Hess, H.F. (2006) Imaging Intracellular Fluorescent Proteins at Nanometer Resolution, *Science* 313 (5793): 1642–1645

- (42) Binnig, G. and Rohrer, H. (1986) Scanning tunneling microscopy, *IBM Journal of research and development* 44, 279-293
- (43) Binnig, G., Quate, C. F. and Gerber C. (1986) Atomic Force Microscope, *Physical Review Letters* 56, 9, 930.
- (44) Martin, Y. and Wickramasinghe, H. K. (1987) Magnetic imaging by "force microscopy" with 1000 Å resolution. *App. Phys. Lett.*, 50(20), 1455–1457.
- (45) Roudit, C., Sekatski, S., Dietler, G., Catsicas, S., Lafont, F., and Kasas, S. (2009) Stiffness tomography by atomic force microscopy. *Biophys. J.*, 97(2), 674–7.
- (46) Zhong, Q., Innis, D., Kjoller, K. and Elings, V. B. (1993) Fractured polymer/silica fiber surface studied by tapping mode atomic force microscopy. *Surf. Sci. Lett.*, 290, L688– L692.
- (47) Eaton, P. and West, P. (2010) Atomic Force Microscopy, New York, NY, Oxford Univ. Press.
- (48) <http://pharm.virginia.edu>
- (49) <http://probe.olympus-global.com>
- (50) <http://www.parkafm.com>
- (51) <https://www.bruker.com>
- (52) <http://www.iupui.edu>
- (53) Zhong, Q., Innis, D., Kjoller, K., and Elings, V. B. (1993) Fractured polymer/silica fiber surface studied by tapping mode atomic force microscopy. *Surf. Sci. Lett.*, 290, L688– L692
- (54) <https://soils.ifas.ufl.edu>
- (55) Z. Liu, Z. Li, H. Zhou, G. Wei, Y. Song and L. Wang, *Immobilization and condensation of DNA with 3-aminopropyltriethoxysilane studied by atomic force microscopy*, *Journal of Microscopy* 218, 3 (2005), 233-239.
- (56) Garcia, R. and Perez, R. (2002) Dynamic atomic force microscopy methods. *Surf. Sci. Rep.* 47, 197-301
- (57) de Pablo, P. J. and Carrion-Vazquez, M. (2014) Imaging biological samples with atomic force microscopy. *Cold Spring Harbor protocols* 2014, 167-177
- (58) Hansma, H. G., Kim, K. J., Laney, D. E., Garcia, R. A., Argaman, M., Allen, M. J., and Parsons, S. M. (1997) Properties of biomolecules measured from atomic force microscope images: a review. *J. Struct. Biol.*, 119(2), 99–108.
- (59) Rivetti, C., Guthold, M., and Bustamante, C. (1996) Scanning force microscopy of DNA deposited onto mica: Equilibration versus kinetic trapping studied by statistical polymer chain analysis. *J. Mol. Biol.*, 264(5), 919–932.
- (60) Podestà, A., Indrieri, M., Brogioli, D., Manning, G. S., Milani, P., Guerra, R., Finzi, L., and Dunlap, D. (2005) Positively charged surfaces increase the flexibility of DNA. *Biophys. J.*, 89 (4), 2558–2563.
- (61) Moukhtar, J., Fontaine, E., Faivre-Moskalenko, C., and Arneodo, A. (2007) Probing persistence in DNA curvature properties with atomic force microscopy. *Phys. Rev. Lett.*, 98 (17), 178101.
- (62) Rivetti, C., Walker, C., and Bustamante, C. (1998) Polymer chain statistics and conformational analysis of DNA molecules with bends or sections of different flexibility. *J. Mol. Biol.*, 280(1), 41–59.
- (63) Zuccheri, G., Scipioni, A., Cavaliere, V., Gargiulo, G., De Santis, P., and Samorì, B. (2001) Mapping the intrinsic curvature and flexibility along the DNA chain. *PNAS*, 98(6), 3074–3079.



- (64) Scipioni, A., Anselmi, C., Zuccheri, G., Samori, B., and De Santis, P. (2002) Sequence dependent DNA curvature and flexibility from scanning force microscopy images. *Biophys. J.*, 83(5), 2408–2418.
- (65) Lyubchenko, Y. L. and Shlyakhtenko, L. S. (1997) Visualization of supercoiled DNA with atomic force microscopy in situ. *PNAS*, 94, 496–501.
- (66) Rippe, K., Mücke, N., and Langowski, J. (1997) Superhelix dimensions of a 1868 base pair plasmid determined by scanning force microscopy in air and in aqueous solution. *Nucleic Acids Res.*, 25(9), 1736–1744.
- (67) Shlyakhtenko, L. S., Potaman, V. N., Sinden, R. R., and Lyubchenko, Y. L. (1998) Structure and dynamics of supercoil-stabilized DNA cruciforms. *J. Mol. Biol.*, 280(1), 61–72.
- (68) Ercolini, E., Valle, F., Adamcik, J., Witz, G., Metzler, R., De Los Rios, P., Roca, J., and Dietler, G. (2007) Fractal dimension and localization of DNA knots. *Phys. Rev. Lett.*, 98(5), 058102.
- (69) Witz, G., Rechendorff, K., Adamcik, J., and Dietler, G. (2008) Conformation of circular DNA in two dimensions. *Phys. Rev. Lett.*, 101, 148103.
- (70) Jiang, Y., Ke, C. H., Mieczkowski, P. A., and Marszalek, P. E. (2007) Detecting ultraviolet damage in single DNA molecules by atomic force microscopy. *Biophys. J.*, 93(5), 1758–1767.
- (71) Ke, C., Jiang, Y., Mieczkowski, P. A., Muramoto, G. G., Chute, J. P., and Marszalek, P. E. (2008) Nanoscale detection of ionizing radiation damage to DNA by atomic force microscopy. *Small*, 4(2), 288–294.
- (72) Lysetska, M., Knoll, A., Boehringer, D., Hey, T., Krauss, G., and Krausch, G. (2002) UV light-damaged DNA and its interaction with human replication.
- (73) Kasas, S. et al. (1997). Escherichia coli RNA polymerase activity observed using atomic force microscopy. *Biochemistry* 36, 461-468.
- (74) Gerganova, V., Maurer, S., Stoliar, L., Japaridze, A., Dietler, G., Nasser, W., Kutateladze, T., Travers, A. and Muskhelishvili, G. (2015) Upstream Binding of Idling RNA Polymerase Modulates Transcription Initiation from a Nearby Promoter. *J. Biol. Chem.*, 290 (13), 8095-8109
- (75) Argaman, M., Bendetz-Nezer, S., Matlis, S., Segal, S. and Priel, E. (2003). Revealing the mode of action of DNA topoisomerase I and its inhibitors by atomic force microscopy. *Biochemical and Biophysical Research Communications* 301, 789-797.
- (76) Heddle, J.G., Mittelheiser, S., Maxwell, A. and Thomson, N.H. (2004). Nucleotide binding to DNA gyrase causes loss of DNA wrap. *Journal of Molecular Biology* 337, 597-610.
- (77) Sorel, I., Pietrement, O., Hamon, L., Bacconnais, S., Le Cam, E. and Pastre, D. (2006). The EcoRI-DNA complex as a model for investigating protein-DNA interactions by atomic force microscopy. *Biochemistry* 45, 14675-14682.
- (78) Sattin, B. D. and Goh, M. C. (2004) Direct observation of the assembly of RecA/DNA complexes by atomic force microscopy. *Biophys. J.*, 87(5), 3430–3436.
- (79) Bussiek, M., Tóth, K., Brun, N., and Langowski, J. (2005) DNA-loop formation on nucleosomes shown by in situ scanning force microscopy of supercoiled DNA. *J. Mol. Biol.*, 345(4), 695–706.
- (80) Hizume, K., Nakai, T., Araki, S., Prieto, E., Yoshikawa, K., and Takeyasu, K. (2009) Removal of histone tails from nucleosome dissects the physical mechanisms of salt-induced aggregation, linker histone H1-induced compaction, and 30-nm fiber formation of the nucleosome array. *Ultramicroscopy*, 109(8), 868–873.

- (81) Fang, Y., Spisz, T.S. and Hoh, J.H. (1999) Ethanol-induced structural transitions of DNA on mica. *Nucl. Acids Res.* 27, 1943-1949.
- (82) Feng, X.Z, Bash,R., Balagurumoorthy, P., Lohr, D., Harrington, R.E., and Lindsay, S.M. (2000) Conformational transition in DNA on a cold surface. *Nucleic Acids Research*, 28, 593-596.
- (83) Rivetti, C., and Codeluppi, S. (2001) Accurate length determination of DNA molecules visualized by atomic force microscopy: evidence for a partial B- to A-form transition on mica . *Ultramicroscopy*, 87, 55-66.
- (84) Sanchez-Sevilla, A., Thimonier, J., Marilley, M., Rocca-Serra, J. and Barbet, J. (2002) Accuracy of AFM measurements of the contour length of DNA fragments adsorbed on mica in air and in aqueous buffer. *Ultramicroscopy*, 92, 151-158.
- (85) Dickerson, R.E., Drew, H.R., Conner, B.N., Wing, R.M., Fratini, A.V. and Kopka, M.L. (1982) The Anatomy of A-, B-, and Z-DNA. *Science*, 216, 475-485.
- (86) Lindsay, S.M., Nagahara, L.A., Thundat, T., Knipping, U., Rill, R.L., Drake, B., Prater, C.B., Weisenhorn, A.L., Gould, S.A.C., and Hansma, P.K. (1989) STM and AFM images of nucleosome DNA under water. *Journal of Biomolecular Structure and Dynamics*, 7, 279-287.
- (87) Rothemund, P.W.K. (2006) Folding DNA to create nanoscale shapes and patterns. *Nature*, 440, 297-302.
- (88) Billingsley, D. J., Lee, A. J., Johansson, N. A. B., Walton, A, Stanger, L., Crampton, N., Bonass, W. A, and Thomson, N. H. (2014) Patchiness of ion-exchanged mica revealed by DNA binding dynamics at short length scales. *Nanotechnology*, 25, 025704.
- (89) Bussik, M., Mücke, N. and Langowski, J. (2003) Polylysine-coated mica can be used to observe systematic changes in the supercoiled DNA conformation by scanning force microscopy in solution. *Nucleic Acids Res.* 31, e137
- (90) Ido, S., Kimura, K., Oyabu, N., Kobayashi, K., Tsukada, M., Matsushige, K. and Yamada, H. (2013) Beyond the Helix Pitch: Direct Visualization of Native DNA in Aqueous Solution. *ACS Nano*, 7, 1817-1822.
- (91) Mou, J., Czajkowsky, D.M., Zhang, Y. and Shao, A. (1995) High-resolution atomic-force microscopy of DNA: the pitch of the double helix. *FEBS Lett.*, 371, 279-282.
- (92) Leung, C., Bestembayeva, A., Thorogate, R., Stinson, J., Pyne, A., Marcovich, C., Yang, J., Drechsler, U., Despont, M., Jankowski, T., Tschöpe, M., and Hoogenboom, B.W. (2012) Atomic Force Microscopy with Nanoscale Cantilevers Resolves Different Structural Conformations of the DNA Double Helix. *Nano Lett.* 12, 3846-3850.
- (93) Cerreta, A., Vobornik, D. and Dietler, G. (2013) Fine DNA structure revealed by constant height frequency modulation AFM imaging. *Eur. Polym. J.*, 49, 1916-1922.
- (94) Pastre, D., Pietrement, O., Fusil, S., Landousy, S., Jeusset, J., David, M-O., Hamon, L., Cam, E.L. and Zozime, A. (2003) Adsorption of DNA to Mica Mediated by Divalent Counterions: A Theoretical and Experimental Study. *Biophysical Journal*, 8, 2507–2518.
- (95) Alonso-Sarduy, L., Roduit, C., Kasas, S. and Dietler, G. (2011) Human topoisomerase II–DNA interaction study by using atomic force microscopy. *FEBS Letters*, 585, 3139–3145.

- (96) Cerreta, A., Vobornik, D., Di Santo, G., Tobenas, S., Alonso-Sarduy, L., Adamcik, J. and Dietler, G. (2012) FM-AFM constant height imaging and force curves: high resolution study of DNA-tip interactions. *J. Mol. Recognit.*, *25*, 486-493.
- (97) Stöckle, R., Suh, Y. D., Deckert, V. and Zenobi, R. (2000) Nanoscale chemical analysis by Tip-enhanced Raman Scattering. *Chem. Phys. Lett.* *318*, 131–136.
- (98) Lipiec, E., Sekine, R., Bielecki, J., Kwiatek, W. M. And Wood, B. R. (2014) Molecular Characterization of DNA Double Strand Breaks with Tip-Enhanced Raman Scattering. *Angew. Chemie Int. Ed.* *53*, 169–172.
- (99) Treffer, R., Lin, X., Bailo, E., Deckert-Gaudig, T. and Deckert, V. (2011) Distinction of nucleobases – a tip-enhanced Raman approach. *Beilstein J. Nanotechnol.* *2*, 628–637.
- (100) Treffer, R., Bohme, R., Deckert-Gaudig, T., Lau, K., Tiede, S. and Lin, X. (2012) Advances in TERS (tip-enhanced Raman scattering) for biochemical applications. *Biochem. Soc. Trans.* *40*, 609 – 614.
- (101) Najjar, S., Talaga, D., Schue, L., Coffinier, Y., Szunerits, S., Boukherroub, R., Servant, L., Rodriguez, V. and Bonhommeau, S. (2014) Tip-Enhanced Raman Spectroscopy of Combed Double-Stranded DNA Bundles. *J. Phys. Chem. C*, *118*, 1174-1181.
- (102) Pinheiro, A.V., Han, D., Shih, W.M. and Yan, H. (2011) Challenges and opportunities for structural DNA nanotechnology. *Nature Nanotechnology*, *6*, 763-772.
- (103) Aldaye, F.A., Palmer, A.L. and Sleiman, H.F. (2008) Assembling Materials with DNA as the Guide. *Science*, *321*, 1795-1799.
- (104) Hu, J., Wang, M., Frantz, P., Kolbe, W., Ogletree, D.F. and Salmeron, M. (1996) Imaging of Single Extended DNA Molecules on Flat (Aminopropyl) triethoxysilane-Mica by Atomic Force. *Langmuir*, *12* (7), 1697–1700.
- (105) Nečas, D. and Klapetek, P. (2012) Gwyddion: an open-source software for SPM data analysis. *Central European Journal of Physics*, *10*, 181-188.
- (106) Mikhaylov, A., Sekatskii, S.K.; and Dietler, G. (2013) DNA Trace: A Comprehensive Software for Polymer Image Processing. *Journal of Advanced Microscopy Research*, *8*(4), 241-245.
- (107) Conner, B.N., Takano, T., Tanaka, S., Itakura, K. and Dickerson, R.E. (1982) The molecular structure of d(<sup>13</sup>CpCpGpG), a fragment of right-handed double helical A-DNA. *Nature*, *295*, 294-299.
- (108) Fang, Y. and Hoh, J.H., (1998) Surface-directed DNA condensation in the absence of soluble multivalent cations. *Nucleic Acids Res.*, *26*, 588–593
- (109) Santos, S., Stefancich, M., Hernandez, H., Chiesa, M. and Thomson, N. H. (2012) Hydrophilicity of a Single DNA Molecule. *J. Phys. Chem. C*, *116*, 2807–2818.
- (110) Banavali, N. K. and Roux, B. (2005) Free Energy Landscape of A-DNA to B-DNA Conversion in Aqueous Solution. *J. Am. Chem. Soc.* *127*, 6866–6876.
- (111) Mazur, A. K. (2003) Titration in Silico of Reversible B $\leftrightarrow$ A Transitions in DNA. *J. Am. Chem. Soc.* *125*, 7849–7859.
- (112) Tolstorukov, M. Y., Ivanov, V. I., Malenkov, G. G., Jernigan, R. L. and Zhurkin, V. B. (2001) Sequence-Dependent B $\leftrightarrow$ A Transition in DNA Evaluated with Dimeric and Trimeric Scales. *Biophys. J.*, *81*, 3409–3421.
- (113) Nguyen, T. H., Choi, S. S., Kim, D. W. and Kim, Y. U. (2007) Study on the Binding Force Between -DNA and Various Types of Substrates. *J. Korean Phys. Soc.*, *50*, 1942.

- (114) Manohar, S., Mantz, A. R., Bancroft, K. E., Hui, C. Y., Jagota, A. and Vezenov, D. V. (2008) Peeling Single-Stranded DNA from Graphite Surface to Determine Oligonucleotide Binding Energy by Force Spectroscopy. *Nano Lett.*, 8, 4365–4372.
- (115) Cuenot, S., Gabriel, S., Jérôme, C., Jérôme, R. and Duwez, A. S. (2005) Are Electrografted Polymers Chemisorbed or Physisorbed onto Their Substrate? *Macromol. Chem. Phys.*, 206, 1216–1220.
- (116) Fink, H.W. and Schönenberger, C. (1999) Electrical conduction through DNA molecules. *Nature*, 398, 407–410.
- (117) Kasumov, A.Y., Kociak, M. and Gue, S. (2001) Proximity-Induced Superconductivity in DNA. 291, 280–283.
- (118) Legrand, O., Côte, D. and Bockelmann, U. (2006) Single molecule study of DNA conductivity in aqueous environment. *Phys. Rev. E - Stat. Nonlinear, Soft Matter Phys.*, 73, 1–6.
- (119) Bonthuis, D. J., Meyer, C., Stein, D. and Dekker, C. (2008) Conformation and Dynamics of DNA Confined in Slitlike Nanofluidic Channels. *Phys. Rev. Lett.* 101, 108303
- (120) Kounovsky-Shafer, K.L., Hernández-Ortiz, J.P., Jo, K., Odijk, T., de Pablo, J.J. and Schwartz, D.C. (2013) Presentation of large DNA molecules for analysis as nanoconfined dumbbells. *Macromolecules*, 46, 8356–8368.
- (121) Jones, J. J., van der Maarel, J. R. C. and Doyle, P. S. (2013) Intrachain Dynamics of Large dsDNA Confined to Slitlike Channels. *Phys. Rev. Lett.* 110, 068101
- (122) Manneschi, C., Angeli, E., Ala-Nissila, T., Repetto, L., Firpo, G. and Valbusa, U. (2013) Conformations of DNA in Triangular Nanochannels. *Macromolecules*, 46, 4198–4206.
- (123) Strychalski, E. A., Geist, J., Gaitan, M., Locascio, L. E. and Stavis, S. M. (2012). Quantitative Measurements of the Size Scaling of Linear and Circular DNA in Nanofluidic Slitlike Confinement. *Macromolecules* 45, 1602–1611
- (124) Fanzio, P., Manneschi, C., Angeli, E., Mussi, V., Firpo, G., Ceseracciu, L., Repetto, L. and Valbusa, U. (2012) Modulating DNA translocation by a controlled deformation of a PDMS nanochannel device. *Sci. Rep.*, 2, 791.
- (125) Micheletti, C. and Orlandini, E. (2012) Knotting and metric scaling properties of DNA confined in nano-channels: a Monte Carlo study. *Soft Matter* 8, 10959–10968.
- (126) Micheletti, C. and Orlandini, E. (2012) Numerical Study of Linear and Circular Model DNA Chains Confined in a Slit: Metric and Topological Properties. *Macromolecules* 45, 2113–2121.
- (127) Odijk, T. (1983) The Statistics and Dynamics of Confined or Entangled Stiff Polymers, 16 (8), 1340–1344.
- (128) Tegenfeldt, J.O., Prinz, C., Cao, H., Chou, S., Reisner, W.W., Riehn, R., Wang, Y.M., Cox, E.C., Sturm, J.C., Silberzan, P., *et al.* (2004) From the Cover: The dynamics of genomic-length DNA molecules in 100-nm channels. *Proc. Natl. Acad. Sci. U. S. A.*, 101, 10979–10983.
- (129) Reisner, W., Morton, K.J., Riehn, R., Wang, Y.M., Yu, Z., Rosen, M., Sturm, J.C., Chou, S.Y., Frey, E. and Austin, R.H. (2005) Statics and dynamics of single DNA molecules confined in nanochannels. *Phys. Rev. Lett.*, 94, 1–4.
- (130) Castillo-Fernandez, O., Salieb-Beugelaar, G.B., van Nieuwkasteele, J.W., Bommer, J.G., Arundell, M., Samitier, J., van den Berg, A. and Eijkel, J.C.T. (2011) Electrokinetic DNA transport in 20 nm-high nanoslits:

- Evidence for movement through a wall-adsorbed. *Electrophoresis*, 32, 2402–2409.
- (131) Lin, P., Hsieh, C.-C., Chen, Y.-L. and Chou, C.-F. (2012) Effects of Topology and Ionic Strength on Double-Stranded DNA Confined in Nanoslits. *Macromolecules* 45, 2920–2927.
- (132) Yeh, J.-W., Taloni, A., Chen, Y.-L. and Chou, C.-F. (2012) Entropy-Driven Single Molecule Tug-of-War of DNA at Micro–Nanofluidic Interfaces. *Nano Lett.* 12, 1597–1602.
- (133) Fanzio, P., Mussi, V., Manneschi, C., Angeli, E., Firpo, G., Repetto, L. and Valbusa, U. (2011) DNA detection with a polymeric nanochannel device. *Lab Chip*, 11, 2961–6.
- (134) Persson, F., Utko, P., Reisner, W., Larsen, N. B. and Kristensen, A. (2009) Confinement Spectroscopy: Probing Single DNA Molecules with Tapered Nanochannels. *Nano Lett.* 9, 1382–1385.
- (135) Jo, K., Dhingra, D. M. Odijk, T., de Pablo, J. J. Graham, M. D., Runnheim, R. Forrest, D. and Schwartz, D. C. (2007) A single-molecule barcoding system using nanoslits for DNA analysis. *PNAS* 104, 2673–2678
- (136) Japaridze, A., Benke, A., Renevey, S., Benadiba, C. and Dietler, G. (2015) Influence of DNA Binding Dyes on Bare DNA Structure Studied with Atomic Force Microscopy. *Macromolecules* 48, 1860–1865.
- (137) Kundukad, B., Yan, J. and Doyle, P. S. (2014) Effect of YOYO-1 on the mechanical properties of DNA. *Soft Matter* 10, 9721–9728.
- (138) Günther, K., Mertig, M. and Seidel, R. (2010) Mechanical and structural properties of YOYO-1 complexed DNA. *Nucl. Acids Res.* 38, 6526–6532.
- (139) Witz, G., Rechendorff, K., Adamcik, J. and Dietler, G. (2011) Conformation of Ring Polymers in 2D Constrained Environments. *Phys. Rev. Lett.* 106, 248301.
- (140) Mason, D. J. and Powelson, D. M. (1956) Nuclear division as observed in live bacteria by a new technique. *J Bacteriol* 71, 474–479.
- (141) Cairns, J. (1963) The Chromosome of Escherichia coli. *Cold Spring Harb Symp Quant Biol* 28, 43–46.
- (142) Sobetzko, P., Glinkowska, M., Travers, A. and Muskhelishvili, G. (2013) DNA thermodynamic stability and supercoil dynamics determine the gene expression program during the bacterial growth cycle. *Molecular BioSystems* 9, 1643–1651.
- (143) Voineagu, I., Narayanan, V., Lobachev, K. S. and Mirkin, S. M. (2008) Replication stalling at unstable inverted repeats: Interplay between DNA hairpins and fork stabilizing proteins. *PNAS* 105, 9936–9941.
- (144) Green, S. J., Lubrich, D. and Turberfield, A. J. (2006) DNA Hairpins: Fuel for Autonomous DNA Devices *Biophysical Journal* 91, 2966–2975.
- (145) Murade, C., Subramaniam, V., Otto, C. and Bennink, M.L. (2009) Interaction of oxazole yellow dyes with DNA studied with hybrid optical tweezers and fluorescence microscopy. *Biophys. J.*, 97, 835–843.
- (146) Keyser, U.F., Koeleman, B.N., van Dorp, S., Krapf, D., Smeets, R.M.M., Lemay, S.G., Dekker, N.H. and Dekker, C. (2006) Direct force measurements on DNA in a solid-state nanopore. *Nature Physics* 2, 473 – 477
- (147) Doyle, P.S., Ladoux, B. and Viovy, J.L. (2000) Dynamics of a tethered polymer in shear flow. *Phys. Rev. Lett.*, 84, 4769–4772
- (148) He, Q., Ranchon, H., Carrivain, P., Viero, Y., Lacroix, J., Blatché, C., Daran, E., Victor, J.-M. and Bancaud, A. (2013) Conformational Manipulation of DNA in Nanochannels Using Hydrodynamics. *Macromolecules*, 46 (15), pp 6195–6202

- (149) Ashley, N, Harris,D. and Poulton J. (2005) Detection of mitochondrial DNA depletion in living human cells using PicoGreen staining. *Exp Cell Res.*, 303(2):432-46
- (150) Smit, P.J., Wiltshire,M. and Errington, R.J. (2004) DRAQ5 Labeling of Nuclear DNA in Live and Fixed Cells . *Current Protocols in Cytometry*, 7.25.1-7.25.1
- (151) Martin, R.M., Leonhardt, H. and Cardoso, M.C. (2005) DNA Labeling in Living Cells .*Cytometry A* .67(1): 45–52
- (152) Benke, A. and Manley, S. (2012) Live-Cell dSTORM of Cellular DNA Based on Direct DNA Labeling. *ChemBioChem* 2012, 13, 298 – 301
- (153) Wojcik, K. and Dobrucki, J. W. (2008) Interaction of a DNA intercalator DRAQ5, and a minor groove binder SYTO17, with chromatin in live cells–influence on chromatin organization and histone-DNA interactions. *Cytometry. A* 73, 555–562
- (154) Dragan, A.I., Casas-Finet,J.R., Bishop,E.S., Strouse, R.J., Schenerman, M.A. and Geddes, C.D. (2010) Characterization of PicoGreen interaction with dsDNA and the origin of its fluorescence enhancement upon binding. *Biophys. J.* 99, 3010–3019
- (155) Portugal, J. and Waring, M. J. (1988) Assignment of DNA binding sites for 4',6-diamidine- 2-phenylindole and bisbenzimidazole (Hoechst 33258). A comparative footprinting study. *Biochim. Biophys. Acta* 949 (2), 158–168
- (156) Gudnason, H., Dufva, M., Bang, D. D. and Wolff, A. (2007) Comparison of multiple DNA dyes for real-time PCR: effects of dye concentration and sequence composition on DNA amplification and melting temperature. *Nucleic Acids Res.* 35 (19) e127
- (157) Sischka, A., Toensing, K., Eckel, R., Wilking, S.D., Sewald, N., Ros, R. and Anselmetti, D. (2005) Molecular mechanisms and kinetics between DNA and DNA binding ligands. *Biophys. J.* 88, 404–411
- (158) Bennink, M.L., Schärer,O.D., Kanaar, R., Sakata-Sogawa, K., Schins, J.M., Kanger, J.S., de Grooth, B.G. and Greve, J. (1999) Single-molecule manipulation of double-stranded DNA using optical tweezers: interaction studies of DNA with RecA and YOYO-1. *Cytometry.* 36(3) :200-8
- (159) Kaji,N., Ueda,M. and Baba,Y. (2001) Direct measurement of conformational changes on DNA molecule intercalating with a fluorescence dye in an electrophoretic buffer solution by means of atomic force microscopy. *Electrophoresis*, 22, 3357.
- (160) Gurrieri, S., Wells, K.S., Johnson, I.D. and Bustamante, C. (1997) Direct Visualization of Individual DNA Molecules by Fluorescence Microscopy: Characterization of the Factors Affecting Signal/Background and Optimization of Imaging Conditions Using YOYO. *Anal Biochem.* 249(1):44-53
- (161) Ahn, S.J., Costa, J. and Emanuel, J.R. (1996) PicoGreen quantitation of DNA: effective evaluation of samples pre- or post-PCR. *Nucleic Acids Research.* 24 (13) 2623–2625,
- (162) Nyberg, L., Persson,F., Akerman,B. and Westerlund,F. (2013) Heterogeneous staining: a tool for studies of how fluorescent dyes affect the physical properties of DNA. *Nucleic Acids Res.*, 41, e184.
- (163) Eckel,R., Ros,R., Ros,A., Wilking,S.D., Sewald,N. and Anselmetti,D. (2003) Identification of binding mechanisms in single molecule-DNA complexes. *Biophys. J.*, 85, 1968–1973.
- (164) Vladescu,I.D., McCauley,M.J., Nuñez,M.E., Rouzina,I. and Williams,M.C. (2007) Quantifying force-dependent and zero-force DNA intercalation by single-molecule stretching. *Nat. Methods*, 4, 517–522.

- (165) Kleimann,C., Sischka,A., Spiering,A., Tönsing,K., Sewald,N., Diederichsen,U. and Anselmetti,D. (2009) Binding kinetics of bisintercalator Triostin A with optical tweezers force mechanics. *Biophys. J.*, 97, 2780–2784.
- (166) Bates, A.D., Maxwell, A. DNA topology; Oxford University Press, New York, 2005
- (167) Holm, C., Joanny, J.F., Kremer, K., Netz, R.R., Reineker, P., Seidel,C., Vilgis,T.A, Winkler, R. G. (2004) Polyelectrolyte Theory, *Adv. Polym. Sci.* 2004, 166, 67–111
- (168) Singer,V.L., Jones,L.J., Yue,S.T. and Haugland,R.P. (1997) Characterization of PicoGreen reagent and development of a fluorescence-based solution assay for double-stranded DNA quantitation. *Anal. Biochem.*, 249, 228–238
- (169) Larsen, T. A.; Goodsell, D. S.; Cascio, D.; Grzeskowiak, K.; Dickerson, R. E. (1989) The Structure of DAPI Bound to DNA *J. Biomol. Struct. Dyn.* 7, 477-491.
- (170) Kapuscinski,J. (1979) DAPI : a DNA-Specific Fluorescent Probe. *Biotech Histochem.* 70(5), 220-233.
- (171) Trotta, E., D’Ambrosio, E., Del Grosso, N., Ravagnan, G., Cirillin, M. and Paci, M. (1993) H NMR Study of [ d ( GCGATCGC ) ]<sub>2</sub> and Its Interaction with Minor Groove Binding 4’,6-Diamidino-2-phenylindole *The Journal of Bio. Chem.* 268 (6), 3944-3951
- (172) Eriksson,S., Kim,S.K., Kubista,M. and Nordtn, B. (1993) Binding of 4’,6-Diamidino-2-phenylindole (DAPI) to AT Regions of DNA: Evidence for an Allosteric Conformational Change. *Biochemistry.* 32, 2987–2998
- (173) Larsson, A., Åkerman, B. and Jonsson, M. (1996) DAPI Staining of DNA : Effect of Change in Charge , Flexibility , and Contour Length on Orientational Dynamics and Mobility of the DNA during Agarose Gel Electrophoresis. *J. Phys. Chem.*, 100, 3252-3263
- (174) Njoh, K.L., Patterson, L.H., Zloh, M., Wiltshire, M., Fisher, J., Chappell, S., Ameer-Beg, S., Bai, Y., Matthews, D., Errington, R.J. and Smith, P.J. (2006) Spectral Analysis of the DNA Targeting Bisalkylaminoanthraquinone DRAQ5 in Intact Living Cells, *Cytometry Part A.* 69A, 805–814
- (175) Raghavan, S., Manzanillo, P., Chan, K., Dovey, C. and Cox, J.S. (2008) Secreted transcription factor controls Mycobacterium tuberculosis virulence. *Nature* 454:717–721.
- (176) Chen, J.M., Boy-Rottger, S., Dhar, N., Sweeney, N., Buxton, R.S., Pojer, F., Rosenkrands, I. and Cole, S.T. (2012) EspD is critical for the virulencemediating ESX-1 secretion system in Mycobacterium tuberculosis. *J. Bacteriol.* 194:884–893.
- (177) Fortune, S.M., Jaeger, A., Sarracino, D.A., Chase, M.R., Sasseti, C.M., Sherman, D.R., Bloom, B.R. and Rubin, E.J. (2005) Mutually dependent secretion of proteins required for mycobacterial virulence. *Proc. Natl. Acad. Sci. U. S. A.* 102:10676–10681.
- (178) Blasco, B., Chen, J.M., Hartkoorn, R., Sala, C., Uplekar, S., Rougemont, J., Pojer, F. and Cole, S.T. (2012) Virulence regulator EspR of Mycobacterium tuberculosis is a nucleoid-associated protein. *PLoS Pathog.* 8:e1002621.
- (179) Blasco, B., Stenta, M., Alonso-Sarduy, L., Dietler, G., Peraro, M.D., Cole, S.T. and Pojer, F. (2011) Atypical DNA recognition mechanism used by the EspR virulence regulator of Mycobacterium tuberculosis. *Mol. Microbiol.* 82: 251–264.
- (180) Dillon, S.C. and Dorman, C.J. (2010) Bacterial nucleoid-associated proteins, nucleoid structure and gene expression. *Nat. Rev. Microbiol.* 8:185–195.

- (181) Hunt, D.M., Sweeney, N.P., Mori, L., Whalan, R.H., Comas, I., Norman, L., Cortes, T., Arnvig, K.B., Davis, E.O., Stapleton, M.R., Green, J. and Buxton, R.S. (2012) Long-range transcriptional control of an operon necessary for virulence-critical ESX-1 secretion in *Mycobacterium tuberculosis*. *J. Bacteriol.* 194:2307–2320.
- (182) Rosenberg, O.S, Dovey, C., Tempesta, M., Robbins, R.A., Finer-Moore, J.S., Stroud, R.M. and Cox, J.S. (2011) EspR, a key regulator of *Mycobacterium tuberculosis* virulence, adopts a unique dimeric structure among helix-turnhelix proteins. *Proc. Natl. Acad. Sci. U. S. A.* 108:13450–13455.
- (183) Gordon, B.R., Li, Y., Wang, L., Sintsova, A., van Bakel, H., Tian, S., Navarre, W.W., Xia, B. and Liu, J. (2010) Lsr2 is a nucleoid-associated protein that targets AT-rich sequences and virulence genes in *Mycobacterium tuberculosis*. *Proc. Natl. Acad. Sci. U. S. A.* 107:5154–5159.
- (184) Rickman, L., Scott, C., Hunt, D.M., Hutchinson, T., Menendez, M.C., Whalan, R., Hinds, J., Colston, M.J., Green, J. and Buxton, R.S. (2005) A member of the cAMP receptor protein family of transcription regulators in *Mycobacterium tuberculosis* is required for virulence in mice and controls transcription of the *rpfa* gene coding for a resuscitation promoting factor. *Mol. Microbiol.* 56:1274 –1286.
- (185) Gonzalo-Asensio, J., Mostowy, S., Harders-Westerveen, J., Huygen, K., Hernandez-Pando, R., Thole, J., Behr, M., Gicquel, B., Martin, C. (2008) PhoP: a missing piece in the intricate puzzle of *Mycobacterium tuberculosis* virulence. *PLoS One* 3:e3496.
- (186) Walters, S.B., Dubnau, E., Kolesnikova, I., Laval, F., Daffe, M. and Smith, I. (2006) The *Mycobacterium tuberculosis* PhoPR two-component system regulates genes essential for virulence and complex lipid biosynthesis. *Mol. Microbiol.* 60: 312–330.
- (187) Pang, X., Samten, B., Cao, G., Wang, X., Tvinnereim, A.R., Chen, X.L. Howard, S.T. (2013) MprAB regulates the *espA* operon in *Mycobacterium tuberculosis* and modulates ESX-1 function and host cytokine response. *J. Bacteriol.* 195:66–75.
- (188) Buxton, R.S., Green, J., Hunt, D.M., Kahramanoglou, C., Stapleton, M.R., Sweeney, N.P. (2012) Long range transcriptional control of virulence critical genes in *Mycobacterium tuberculosis* by nucleoid-associated proteins? *Virulence* 3:408–410.
- (189) Chen, J.M., Pojer, F., Blasco, B. and Cole, S.T. (2010) Towards anti-virulence drugs targeting ESX-1 mediated pathogenesis of *Mycobacterium tuberculosis*. *Drug Discov. Today Dis. Mech.* 7:e25– e31.
- (190) Kim, J., Yoshimura, S.H., Hizume, K., Ohniwa, R.L., Ishihama, A. and Takeyasu, K. (2004) Fundamental structural units of the *Escherichia coli* nucleoid revealed by atomic force microscopy. *Nucleic Acids Res.*, 32(6), 91982-92.
- (191) Rimsky, S. and Travers, A. (2011) Pervasive regulation of nucleoid structure and function by nucleoid-associated proteins. *Curr Opin Microbiol.*, 14, 136-141.
- (192) Ali Azam, T., Iwata, A., Nishimura, A., Ueda, S. and Ishihama, A. (1999) Growth phase-dependent variation in protein composition of the *Escherichia coli* nucleoid. *J Bacteriol.*, 181, 6361-6370.
- (193) Luijsterburg, M.S., Noom, M.C., Wuite, G.J. and Dame, R.T. (2006) The architectural role of nucleoid-associated proteins in the organization of bacterial chromatin: a molecular perspective. *J Struct Biol.*, 156(2), 262-72.
- (194) Maurer, S., Fritz, J. and Muskhelishvili, G. (2009) A systematic *in vitro* study of nucleoprotein



- complexes formed by bacterial nucleoid associated proteins revealing novel types of DNA organization *J Mol Biol.*, 387, 1261-1276.
- (195) Dürrenberger, M., La Teana, A., Citro, G., Venanzi, F., Gualerzi, C.O. and Pon, C.L. (1991) Escherichia coli DNA-binding protein H-NS is localized in the nucleoid. *Res Microbiol.*, 142(4), 373-80.
- (196) Dorman, C.J. (2007) H-NS, the genome sentinel. *Nat Rev Microbiol.*, 5(2), 157-61.
- (197) Dorman, C.J., Ni Bhriain, N. and Higgins, C.F. (1990) DNA supercoiling and environmental regulation of virulence gene expression in *Shigella flexneri*. *Nature*, 344(6268),789-92.
- (198) O'Byrne, C.P. and Dorman, C.J. (1994) Transcription of the *Salmonella typhimurium* spv virulence locus is regulated negatively by the nucleoid-associated protein H-NS. *FEMS Microbiol Lett.*, 121(1),99-105.
- (199) Porter, M.E. and Dorman, C.J. (1994) A role for H-NS in the thermo-osmotic regulation of virulence gene expression in *Shigella flexneri*. *J Bacteriol.*, 176(13),4187-91.
- (200) Madrid, C., Nieto, J.M., Paytubi, S., Falconi, M., Gualerzi, C.O. and Juárez, A. (2002) Temperature- and H-NS-dependent regulation of a plasmid-encoded virulence operon expressing *Escherichia coli* hemolysin. *J Bacteriol.*, 184(18),5058-66.
- (201) Blädel, I., Wagner, K., Beck, A., Schilling, J., Schmidt, A.M. and Heusippa G. (2013) The H-NS protein silences the pyp regulatory network of *Yersinia enterocolitica* and is involved in controlling biofilm formation. *FEMS Microbiol Lett.*, 340(1),41-8.
- (202) Eijkelkamp, B.A., Stroehler, U.H., Hassan, K.A., Elbourne, L.D., Paulsen, I.T. and Brown M.H. (2013) H-NS plays a role in expression of *Acinetobacter baumannii* virulence features. *Infect Immun.*, 81(7),2574-83.
- (203) Mou, X., Spinard, E.J., Driscoll, M.V., Zhao, W. and Nelson, D.R. (2013) H-NS is a negative regulator of the two hemolysin/cytotoxin gene clusters in *Vibrio anguillarum*. *Infect Immun.*, 81(10),3566-76
- (204) Reverchon, S. and Nasser, W. (2013) *Dickeya* ecology, environment sensing and regulation of virulence programme. *Environ Microbiol Rep.*, (5),622-36.
- (205) Kahramanoglou, C., Seshasayee, A.S., Prieto, A.I., Ibberson, D., Schmidt, S., Zimmermann, J., Benes, V., Fraser, G.M. and Luscombe, N.M. (2011) Direct and indirect effects of H-NS and Fis on global gene expression control in *Escherichia coli*. *Nucleic Acids Res.*, 39(6),2073-91.
- (206) Spurio, R., Dürrenberger, M., Falconi, M., La Teana, A., Pon, C.L. and Gualerzi, C.O. (1992) Lethal overproduction of the *Escherichia coli* nucleoid protein H-NS: ultramicroscopic and molecular autopsy. *Mol Gen Genet.*, 231(2),201-11.
- (207) Wang, W., Li, G.W., Chen, C., Xie, X.S. and Zhuang, X. (2011) Chromosome organization by a nucleoid-associated protein in live bacteria. *Science*, 333(6048),1445-9.
- (208) Owen-Hughes, T.A., Pavitt, G.D., Santos, D.S., Sidebotham, J.M., Hulton, C.S., Hinton, J.C. and Higgins, C.F. (1992) The chromatin-associated protein H-NS interacts with curved DNA to influence DNA topology and gene expression. *Cell*, 71, 255–265.
- (209) Spurio R, Falconi M, Brandi A, Pon CL, Gualerzi CO (1997) The oligomeric structure of nucleoid protein H-NS is necessary for recognition of intrinsically curved DNA and for DNA bending. *EMBO J.* 16(7):1795-805.
- (210) Rimsky, S., Zuber, F., Buckle, M. and Buc, H. (2001) A molecular mechanism for the repression of transcription by the H-NS protein. *Mol Microbiol.*, 42, 1311–1323

- (211) Lang, B., Blot, N., Bouffartigues, E., Buckle, M., Geertz, M., Gualerzi, C.O., Mavathur, R., Muskhelishvili, G., Pon, C., Rimsky, S., Stella, S., Babu, M.M. and Travers, A. (2007) High affinity DNA binding sites for H-NS provide a molecular basis for selective silencing within proteobacterial genomes. *Nucl Acids Res.*, 35, 6330-6337
- (212) Dame, R.T., Wyman, C. and Goosen, N. (2000) H-NS mediated compaction of DNA visualised by atomic force microscopy. *Nucleic Acids Res.*, 28(18),3504-10.
- (213) Schneider, R., Lurz, R., Lüder, G., Tolksdorf, C., Travers, A. and Muskhelishvili, G. (2001) An architectural role of the *Escherichia coli* protein FIS in organising DNA. *Nucl Acids Res.*, 29, 5107-5114.
- (214) Travers, A. and Muskhelishvili, G. (2005) DNA supercoiling – a global transcriptional regulator for enterobacterial growth? *Nature Rev Microbiol.*, 3, 157-169.
- (215) Blot, N., Mavathur, R., Geertz, M., Travers, A. and Muskhelishvili G (2006) Homeostatic regulation of supercoiling sensitivity coordinates transcription of the bacterial genome. *EMBO rep* 7, 710-715.
- (216) Tupper, A.E., Owen-Hughes, T.A., Ussery, D.W., Santos, D.S., Ferguson, D.J., Sidebotham, J.M., Hinton, J.C. and Higgins, C.F. (1994) The chromatin-associated protein H-NS alters DNA topology in vitro. *EMBO*, 13(1), 258-68.
- (217) Falconi, M., Colonna, B., Prosseda, G., Micheli, G. and Gualerzi, C.O. (1998) Thermoregulation of *Shigella* and *Escherichia coli* EIEC pathogenicity. A temperature-dependent structural transition of DNA modulates accessibility of virF promoter to transcriptional repressor H-NS. *EMBO J.*, 17, 7033–7043.
- (218) Bouffartigues, E., Buckle, M., Badaut, C., Travers, A. and Rimsky, S. (2007) H-NS cooperative binding to high-affinity sites in a regulatory element results in transcriptional silencing. *Nat Struct Mol Biol.*, 14(5),441-8.
- (219) Ouafa, Z.A., Reverchon, S., Lautier, T., Muskhelishvili, G. and Nasser, W. (2012) Bacterial nucleoid-associated proteins modulate the DNA supercoiling response of major virulence genes in the plant pathogen *Dickeya dadantii*. *Nucl Acids Res.*, 40,4306-4319 .
- (220) Shin, M., Lagda, A.C., Lee, J.W., Bhat, A., Rhee, J.H., Kim, J.S., Takeyasu, K., Choy, H.E. (2012) Gene silencing by H-NS from distal DNA site. *Mol Microbiol.*, 86(3),707-19.
- (221) Liu, Y., Chen, H., Kenney, L.J. and Yan, J. (2010) A divalent switch drives H-NS/DNA-binding conformations between stiffening and bridging modes. *Genes Dev.*, 24, 339–344
- (222) Afflerbach, H., Schröder, O. and Wagner, R. (1999) Conformational changes of the upstream DNA mediated by H-NS and FIS regulate *E. coli* RnB P1 promoter activity. *J Mol Biol.*, 286(2),339-53.
- (223) Lim, C.J., Lee, S.Y., Kenney, L.J. and Yan, J. (2012) Nucleoprotein filament formation is the structural basis for bacterial protein H-NS gene silencing. *Sci Rep.*, 2:509.
- (224) Kotlajich, M.V., Hron, D.R., Boudreau, B.A., Sun, Z., Lyubchenko, Y.L. and Landick, R. (2015) Bridged filaments of histone-like nucleoid structuring protein pause RNA polymerase and aid termination in bacteria. *eLife*, 4:e04970.
- (225) Schneider, R., Travers, A. and Muskhelishvili, G. (1997) FIS regulates the bacterial growth phase-dependent topological transitions in DNA. *Mol Microbiol.*, 26, 519-530
- (226) Gowrishankar, J. (1989) Nucleotide sequence of the osmoregulatory proU operon of *Escherichia coli* *J Bacteriol* 171: 1923-1931.
- (227) Lazarus, L.R., Travers, A.A. (1993) The *Escherichia coli* FIS protein is not required for the activation

- of tyrT transcription on entry into exponential growth. *EMBO J.* 12(6):2483-94.
- (228) Dorman C.J. (2013) Co-operative roles for DNA supercoiling and nucleoid-associated proteins in the regulation of bacterial transcription. *Biochem Soc Trans.*, 41,542-7.
- (229) Ishihama, A. (2000) Functional modulation of *Escherichia coli* RNA polymerase. *Annu. Rev. Microbiol.* 54, 499–518
- (230) Ishihama, A. (2012) Prokaryotic genome regulation: a revolutionary paradigm. *Proc. Jpn. Acad. Ser. B Phys. Biol. Sci.* 88, 485–508
- (231) Tse-Dihn, Y. C., and Beran, R. K. (1988) Multiple promoters for transcription of the *Escherichia coli* DNA topoisomerase I gene and their regulation by DNA supercoiling. *J. Mol. Biol.* 202, 735–742
- (232) Lesley, S. A., Jovanovich, S. B., Tse-Dinh, Y. C., and Burgess, R. R. (1990) Identification of a heat shock promoter in the topA gene of *Escherichia coli*. *J. Bacteriol.* 172, 6871–6874
- (233) Goodrich, J. A., and McClure, W. R. (1991) Competing promoters in prokaryotic transcription. *Trends Biochem. Sci.* 16, 394–397
- (234) Liebig, B., and Wagner, R. (1995) Effects of different growth conditions on the *in vivo* activity of the tandem *Escherichia coli* ribosomal RNA promoters P1 and P2. *Mol. Gen. Genet.* 249, 328–335
- (235) Qi, H., Menzel, R., and Tse-Dinh, Y. C. (1997) Regulation of *Escherichia coli* topA gene transcription: involvement of a  $\sigma$ S-dependent promoter. *J. Mol. Biol.* 267, 481–489
- (236) Govantes, F., Orjalo, A. V., and Gunsalus, R. P. (2000) Interplay between three global regulatory proteins mediates oxygen regulation of the *Escherichia coli* cytochrome d oxidase (cydAB) operon. *Mol. Microbiol.* 38, 1061–1073
- (237) Cameron, A. D., Kröger, C., Quinn, H. J., Scally, I. K., Daly, A. J., Kary, S. C., and Dorman, C. J. (2013) Transmission of an oxygen availability signal at the *Salmonella enterica* serovar *Typhimurium* fis promoter. *PLoS One* 8, e84382
- (238) Le Grice, S. F., and Sonenshein, A. L. (1982) Interaction of *Bacillus subtilis* RNA polymerase with a chromosomal promoter. *J. Mol. Biol.* 162, 551–564
- (239) Hanamura, A., and Aiba, H. (1991) Molecular mechanism of negative autoregulation of *Escherichia coli* crp gene. *Nucleic Acids Res.* 19, 4413–4419
- (240) González-Gil, G., Kahmann, R., and Muskhelishvili, G. (1998) Regulation of crp transcription by oscillation between distinct nucleoprotein complexes. *EMBO J.* 17, 2877–2885
- (241) Nasser, W., Rochman, M., and Muskhelishvili, G. (2002) Transcriptional regulation of fis operon involves a module of multiple coupled promoters. *EMBO J.* 21, 715–724
- (242) Li, M., Wang, J., Geng, Y., Li, Y., Wang, Q., Liang, Q., and Qi, Q. (2012) A strategy of gene overexpression based on tandem repetitive promoters in *Escherichia coli*. *Microb. Cell Fact.* 11, 19
- (243) Strainic, M. G. Jr., Sullivan, J. J., Collado-Vides, J., and deHaseth, P. L. (2000) Promoter interference in a bacteriophage lambda control region: effects of a range of interpromoter distances. *J. Bacteriol.* 182, 216–220
- (244) El-Robh, M. S., and Busby, S. J. (2002) The *Escherichia coli* cAMP receptor protein bound at a single target can activate transcription initiation at divergent promoters: a systematic study that exploits new promoter probe plasmids. *Biochem. J.* 368, 835–843

- (245) Palmer, A. C., Ahlgren-Berg, A., Egan, J. B., Dodd, I. B., and Shearwin, K. E. (2009) Potent transcriptional interference by pausing of RNAPolymerases over a downstream promoter. *Mol. Cell* 34, 545–555
- (246) Liu, L. F., and Wang, J. C. (1987) Supercoiling of the DNA template during transcription. *Proc. Natl. Acad. Sci. U.S.A.* 84, 7024–7027
- (247) Opel, M. L., and Hatfield, G. W. (2001) DNA supercoiling-dependent transcriptional coupling between the divergently transcribed promoters of the *ilvYC* operon of *Escherichia coli* is proportional to promoter strengths and transcript lengths. *Mol. Microbiol.* 39, 191–198
- (248) Yamada, M., Kabir, M. S., and Tsunedomi, R. (2003) Divergent promoter organization may be a preferred structure for gene control in *Escherichia coli*. *J. Mol. Microbiol. Biotechnol.* 6, 206–210
- (249) Bae, J. Y., Laplaza, J., and Jeffries, T. W. (2008) Effects of gene orientation and use of multiple promoters on the expression of *XYL1* and *XYL2* in *Saccharomyces cerevisiae*. *Appl. Biochem. Biotechnol.* 145, 69–78
- (250) Nakagawa, H., Tategu, M., Yamauchi, R., Sasaki, K., Sekimachi, S., and Yoshida, K. (2008) Transcriptional regulation of an evolutionary conserved intergenic region of *CDT2-INTS7*. *PLoS One* 3, e1484
- (251) Seila, A. C., Core, L. J., Lis, J. T., and Sharp, P. A. (2009) Divergent transcription: a new feature of active promoters. *Cell Cycle* 8, 2557–2564
- (252) Uesaka, M., Nishimura, O., Go, Y., Nakashima, K., Agata, K., and Imamura, T. (2014) Bidirectional promoters are the major source of gene activation-associated non-coding RNAs in mammals. *BMC Genomics* 15,35
- (253) Lepoivre, C., Belhocine, M., Bergon, A., Griffon, A., Yammine, M., Vanhille, L., Zacarias-Cabeza, J., Garibal, M. A., Koch, F., Maqbool, M. A., Fenouil, R., Loriod, B., Holota, H., Gut, M., Gut, I., Imbert, J., Andrau, J. C., Puthier, D., and Spicuglia, S. (2013) Divergent transcription is associated with promoters of transcriptional regulators. *BMC Genomics* 14, 914
- (254) Grainger, D. C., Hurd, D., Harrison, M., Holdstock, J., and Busby, S. J. (2005) Studies of the distribution of *Escherichia coli* cAMP-receptor protein and RNA polymerase along the *E. coli* chromosome. *Proc. Natl. Acad. Sci. U.S.A.* 102, 17693–17698
- (255) Reppas, N. B., Wade, J. T., Church, G. M., and Struhl, K. (2006) The transition between transcriptional initiation and elongation in *E. coli* is highly variable and often rate limiting. *Mol. Cell* 24, 747–757
- (256) Mooney, R. A., Davis, S. E., Peters, J. M., Rowland, J. L., Ansari, A. Z., and Landick R. (2009) Regulator trafficking on bacterial transcription units *in vivo*. *Mol. Cell* 33, 97–108
- (257) Shavkunov, K. S., Masulis, I. S., Tutukina, M. N., Deev, A. A., and Ozoline, O. N. (2009) Gains and unexpected lessons from genomes-scale promoter mapping. *Nucleic Acids Res.* 37, 4919–4931
- (258) Wade, J. T., and Grainger, D. C. (2014) Pervasive transcription: illuminating the dark matter of bacterial transcriptomes. *Nat. Rev. Microbiol.* 12, 647–653
- (259) Huerta, A. M., Francino, M. P., Morett, E., and Collado-Vides, J. (2006) Selection for unequal densities of 70 promoter-like signals in different regions of large bacterial genomes. *PLoS Genetics* 2, e185
- (260) Murley, L. L., and Grindley, N. D. (1998) Architecture of the  $\gamma$ -resolvase synaptosome: oriented heterodimers identity interactions essential for synapsis and recombination. *Cell* 95, 553–562

- (261) Biswas, T., Aihara, H., Radman-Livaja, M., Filman, D., Landy, A., and Ellenberger, T. (2005) A structural basis for allosteric control of DNA recombination by lambda integrase. *Nature* 435, 1059–1066
- (262) Rice, P. A., Mouw, K. W., Montañó, S. P., Boocock, M. R., Rowland, S. J., and Stark, W. M. (2010) Orchestrating serine resolvases. *Biochem. Soc. Trans.* 38, 384–387
- (263) Ninnemann, O., Koch, C., and Kahmann, R. (1992) The *E. coli* *fis* promoter is subject to stringent control and autoregulation. *EMBOJ.* 11, 1075–1083
- (264) Schneider, R., Travers, A., and Muskhelishvili, G. (2000) The expression of the *Escherichia coli* *fis* gene is strongly dependent on the superhelical density of DNA. *Mol. Microbiol.* 38, 167–175
- (265) Ball, C. A., Osuna, R., Ferguson, K. C., and Johnson R. C. (1992) Dramatic changes in Fis levels upon nutrient upshift in *Escherichia coli*. *J. Bacteriol.* 174, 8043–8056
- (266) Mallik, P., Pratt, T. S., Beach, M. B., Bradley, M. D., Undamatla, J., and Osuna, R. (2004) Growth phase-dependent regulation and stringent control of *fis* are conserved processes in enteric bacteria and involve a single promoter (*fis* P) in *Escherichia coli*. *J. Bacteriol.* 186, 122–135
- (267) Nasser, W., Schneider, R., Travers, A., and Muskhelishvili, G. (2001) CRP modulates *fis* transcription by alternate formation of activating and repressing nucleoprotein complexes. *J. Biol. Chem.* 276, 17878–17886
- (268) Pratt, T. S., Steiner, T., Feldman, L. S., Walker, K. A., and Osuna, R. (1997) Deletion analysis of the *fis* promoter region in *Escherichia coli*: antagonistic effects of integration host factor and Fis. *J. Bacteriol.* 179, 6367–6377
- (269) Meng, W., Belyaeva, T., Savery, N. J., Busby, S. J., Ross, W. E., Gaal, T., Gourse, R. L., and Thomas, M. S. (2001) UP element-dependent transcription at the *Escherichia coli* *rrnB* P1 promoter: positional requirements and role of the RNA polymerase  $\sigma$  subunit linker. *Nucleic Acids Res.* 29, 4166–4178
- (270) González-Gil, G., Bringmann, P., and Kahmann, R. (1996) FIS is a regulator of metabolism in *Escherichia coli*. *Mol. Microbiol.* 22, 21–29
- (271) Kelly, A., Goldberg, M. D., Carroll, R. K., Danino, V., Hinton, J. C., and Dorman, C. J. (2004) A global role for Fis in the transcriptional control of metabolism and type III secretion in *Salmonella enterica* serovar Typhimurium. *Microbiology* 150, 2037–2053
- (272) Richardson, J. P. (1966) Some physical properties of RNA polymerase. *Proc. Natl. Acad. Sci. U.S.A.* 55, 1616–1623
- (273) Chamberlin, M., McGrath, J., and Waskell, L. (1970) New RNA polymerase from *Escherichia coli* infected with bacteriophage T7. *Nature* 228, 227–231
- (274) Savochkina, L. P., and Bibilashvili, R. Sh. (1979) Influence of ionic strength on RNA-polymerase structure. *Mol. Biol. (Mosk)* 13, 509–518
- (275) Shaner, S. L., Piatt, D. M., Wensley, C. G., Yu, H., Burgess, R. R., and Record, M. T., Jr. (1982) Aggregation equilibria of *Escherichia coli* RNA polymerase: evidence for anion-linked conformational transitions in the promoters of core and holoenzyme. *Biochemistry* 21, 5539–5551
- (276) Hu, H. Y., He, L., and Khaitovich, P. (2014) Deep sequencing reveals a novel class of bidirectional promoters associated with neuronal genes. *BMC Genomics* 15, 457
- (277) Bystrenova, E., Facchini, M., Cavallini, M., Cacace, M. G. and Biscarini, F. (2006) Multiple Length-Scale Patterning of DNA by Stamp-Assisted Deposition. *Angew. Chemie - Int. Ed.*, 45, 4779–4782.

- (278) Camacho, C. J. and Fisher M.E. (1990) Tunable Fractal Shapes in Self-Avoiding Polygons and Planar Vesicles Carlos, *Phys. Rev. Lett.* 65,9
- (279) Sherratt,D.J. (2003) Bacterial chromosome dynamics. *Science*, 301, 780–785.
- (280) Travers,A. and Muskhelishvili,G. (2005) Bacterial chromatin. *Curr. Opin. Genet. Dev.*, 15, 507–514.
- (281) Dillon,S.C. and Dorman,C.J. (2010) Bacterial nucleoid-associated proteins, nucleoid structure and gene expression. *Nat. Rev. Microbiol.*, 8, 185–195.
- (282) Trun, N.J. and Marko, J.F. (1998) Architecture of a bacterial chromosome. *ASM News*, 64, 276–283.
- (283) Ohniwa, R.L., Ushijima,Y., Saito,S. and Morikawa,K. (2011) Proteomic analyses of nucleoid-associated proteins in escherichia coli, pseudomonas aeruginosa, bacillus subtilis, and staphylococcus aureus. *PLoS One*, 6.
- (284) Peter, B.J., Arsuaga, J., Breier, A.M., Khodursky, A.B., Brown, P.O. and Cozzarelli, N.R. (2004) Genomic transcriptional response to loss of chromosomal supercoiling in Escherichia coli. *Genome Biol.*, 5, R87.
- (285) Schneider, R., Travers, A, Kutateladze, T. and Muskhelishvili,G. (1999) A DNA architectural protein couples cellular physiology and DNA topology in Escherichia coli. *Mol. Microbiol.*, 34, 953–964.
- (286) Bordes, P., Conter, A., Morales, V., Bouvier, J., Kolb, A. and Gutierrez, C. (2003) DNA supercoiling contributes to disconnect sigmaS accumulation from sigmaS-dependent transcription in Escherichia coli. *Mol. Microbiol.*, 48, 561–571.
- (287) Crozat, E., Philippe, N., Lenski, R.E., Geiselman, J. and Schneider, D. (2005) Long-term experimental evolution in Escherichia coli. XII. DNA topology as a key target of selection. *Genetics*, 169, 523–532.
- (288) Sinden, R.R. and Pettijohn, D.E. (1981) Chromosomes in living Escherichia coli cells are segregated into domains of supercoiling. *Proc. Natl. Acad. Sci. U. S. A.*, 78, 224–228.
- (289) Postow, L., Hardy, C.D., Arsuaga, J. and Cozzarelli, N.R. (2004) Topological domain structure of the Escherichia coli chromosome. *Genes & Dev.* 18, 1766–1779
- (290) Deng, S., Stein, R. A. and Higgins, N.P. (2005) Organization of supercoil domains and their reorganization by transcription. *Mol. Microbiol.*, 57, 1511–1521.
- (291) Samorí, B., Siligardi, G., Quagliariello, C., Weisenhorn, A. L., Vesenka, J. and Bustamante, C.J. (1993) Chirality of DNA supercoiling assigned by scanning force microscopy. *Proc. Natl. Acad. Sci. U. S. A.*, 90, 3598–3601.
- (292) Fathizadeh, A., Schiessel, H. and Ejtehadi, M.R. (2015) Molecular Dynamics Simulation of Supercoiled DNA Rings.
- (293) Benedetti, F., Japaridze, A., Dorier, J., Racko, D., Kwapich, R., Burnier, Y., Dietler, G. and Stasiak, A. (2015) Effects of physiological self-crowding of DNA on shape and biological properties of DNA molecules with various levels of supercoiling. *Nucleic Acids Res.*, 10.1093/nar/gkv055.
- (294) Vologodskii, A.V., Levene,S.D., Klenin, K.V., Frank-Kamenetskii, M. and Cozzarelli, N.R. (1992) Conformational and thermodynamic properties of supercoiled DNA. *J. Mol. Biol.*, 227, 1224–1243.
- (295) Yoshinaga, N., Yoshikawa, K. and Kidoaki, S. (2002) Multiscaling in a long semiflexible polymer chain in two dimensions. *J. Chem. Phys.*, 116, 9926–9929.
- (296) Vologodskii, A. V., Cozzarelli, N. R. (1994) *Annu. Rev. Biophys. Biomol. Seruel.* 23, 609--43.
- (297) Schlick, T. (1995) Modeling superhelical DNA: Recent analytical and dynamic approaches. *Curr. Opin. Struct. Biol.*, 5, 245–262.

- (298) Balke, V.L. and Gralla, J.D. (1987) Changes in the linking number of supercoiled DNA accompany growth transitions in *Escherichia coli*. *J. Bacteriol.*, 169, 4499–4506.
- (299) Alonso-Sarduy, L.; De Los Rios, P.; Benedetti, F.; Vobornik, D.; Dietler, G.; Kasas, S.; Longo, G. (2014) Real-Time Monitoring of Protein Conformational Changes Using a Nano-Mechanical Sensor. *PLoS One*, 9, e103674.
- (300) Bloomfield, V.A. (1998) DNA Condensation by Multivalent Cations, John Wiley & Sons, Inc.
- (301) Widom, J. and Baldwin R.L. (1980) Cation-induced toroidal condensation of DNA: Studies with  $\text{Co}^{3+}(\text{NH}_3)_6$ , *Journal of Molecular Biology*, 144, 4, pg 431-453
- (302) Gosule, L.C. and Schellman, J. A (1976) Compact form of DNA induced by spermidine. *Nature*, 259, 333–335.
- (303) Chatteraj, D. K., Gosule, L.C. and Schellman, J. A (1978) DNA condensation with polyamines: II. Electron microscopic studies, *Journal of Molecular Biology*, 121, 3, pg 327-337
- (304) Mann, A., Richa, R. and Ganguli, M. (2008) DNA condensation by poly-l-lysine at the single molecule level: Role of DNA concentration and polymer length. *J. Control. Release*, 125, 252–262.
- (305) Ross, W., Thompson, J. F., Newlands, J. T. and Gourse, R. L. (1990) *E. coli* Fis Protein Activates Ribosomal RNA Transcription in Vitro and in Vivo. *EMBO J.* 9, 3733–3742.
- (306) Maurer, S., Fritz, J., Muskhelishvili, G. and Travers, A. (2006) RNA polymerase and an activator form discrete subcomplexes in a transcription initiation complex. *EMBO J.*, 25, 3784–90.
- (307) Jacquet, M., Cukier-Kahn, R., Pla, J. & Gros, F. (1971). A thermostable protein factor acting on in vitro DNA transcription. *Biochem. Biophys. Res. Commun.* 45, 1597–1607.
- (308) Dorman, C. J. (2004). H-NS: a universal regulator for a dynamic genome. *Nat. Rev., Microbiol.* 2, 391–400
- (309) Ueguchi, C. & Mizuno, T. (1993). The *Escherichia coli* nucleoid protein H-NS functions directly as a transcriptional repressor. *EMBO J.* 12, 1039–1046.
- (310) Coste, F., Hervouet, N., Oberto, J., Zelwer, C. and Castaing, B. (1999) Crystallization and preliminary X-ray diffraction analysis of the homodimeric form  $\alpha_2$  of the HU protein from *Escherichia coli*. *Acta Cryst. D* 55, 1952-1954.
- (311) Bahloul, A. Boubrik, F., Rouviere-Yaniv, J., Roles of *Escherichia coli* histone-like protein HU in DNA replication: HU-beta suppresses the thermosensitivity of dnaA46ts. *Biochimie*, 83 (2001) 219-229.
- (312) Durrenberger, M., Bjornsti, M. A., Uetz, T., Hobot, J. A. and Kellenberger, E. (1988). Intracellular location of the histone-like protein HU in *Escherichia coli*. *J. Bacteriol.* 170, 4757–4768.
- (313) Kobryn, K., Lavoie, B. D. & Chaconas, G. (1999) Supercoiling-dependent site-specific binding of HU to naked Mu DNA. *J. Mol. Biol.* 289, 777–784
- (314) van Noort, J., Verbrugge, S., Goosen, N., Dekker, C. and Dame, R.T. (2004) Dual architectural roles of HU: formation of flexible hinges and rigid filaments. *Proc. Natl. Acad. Sci. U. S. A.*, 101, 6969–6974.
- (315) Swinger, K. K., Lemberg, K. M., Zhang, Y. & Rice, P. A. (2003) Flexible DNA bending in HU–DNA cocrystal structures. *EMBO J.* 22, 3749–3760.
- (316) Japaridze, A., Vobornik, D., Lipiec, E., Cerreta, A., Szczerbinski, J., Zenobi, R. and Dietler, G. (2015) Towards an effective control of DNA's sub-molecular conformation on a surface, Submitted in *ACS Macromolecules*

- (317) Japaridze, A., Micheletti, C., Orlandini, E., Smith, K., Valle, F. and Dietler G. (2015) Conformational properties of DNA inside narrow slits, In preparation
- (318) Blasco, B., Japaridze, A., Stenta, M., Wicky, B. I. M., Dietler, G., Dal Peraro, M., Pojer F. and Cole, S. T. (2014) Functional Dissection of Intersubunit Interactions in the EspR Virulence Regulator of *Mycobacterium tuberculosis*, *Journal of Bacteriology*, Vol. 196, num. 10, p. 1889-1900, 2014
- (319) Japaridze, A., Renevey, S., Sobetzko, P., Stoliar, L., Dietler, G. and Muskhelishvili, G. (2015) DNA sequence organization directs the assembly of distinct higher-order H-NS filaments, Submitted in JBC
- (320) Adamcik, J., Jeon, J.-H., Karczewski, K.J., Metzler, R. and Dietler, G. (2012) Quantifying supercoiling-induced denaturation bubbles in DNA. *Soft Matter*, **8**, 8651.
- (321) Jeon, J.-H., Adamcik, J., Dietler, G. and Metzler, R. (2010) Supercoiling Induces Denaturation Bubbles in Circular DNA. *Phys. Rev. Lett.*, **105**, 208101.
- (322) Hartschuh, A., Sánchez, E.J., Xie, X.S. and Novotny, L. (2003) High-Resolution Near-Field Raman Microscopy of Single-Walled Carbon Nanotubes. *Phys. Rev. Lett.*, **90**, 095503.



# CURRICULUM VITAE – Aleksandre JAPARIDZE

Date of birth: 27.04.1988

Nationality: Georgian

Address: Rte de la Sorge  
BSP 410 (Cubotron UNIL)  
EPFL SB IPSB LPMV  
CH-1015 Lausanne, Switzerland

E-mail: [aleksandre.japaridze@epfl.ch](mailto:aleksandre.japaridze@epfl.ch)

## Education

---

- 2011-Present      **EPFL , Lausanne , Switzerland**  
Enrolled at the Doctoral School of Physics , Member of the Laboratory Of Physics of Living Matter
- 2009 – 2011      **Jacobs University Bremen, Bremen, Germany**  
Molecular Life Sciences Master Program, MSc in Molecular Biophysics and Molecular Genetics
- 2008 July-September      **EPFL , Lausanne , Switzerland**  
Summer Project at the Laboratory Of Physics of Living Matter
- 2007 Spring Semester      **Saarland University, Saarbrücken, Germany**  
Department of Natural Sciences and Technology II

2005 - 2009      **Tbilisi State University, Tbilisi, Georgia**  
Department of Exact and Natural Sciences, BSc in Physics

## **Work experience**

---

---

2011 - 2015      **EPFL , Lausanne , Switzerland**  
PhD in Physics (ongoing) in the Group of Prof. G. Dietler,  
Laboratory of the Physics of Living Matter

2010 Sep-2011      **Jacobs University Bremen, Bremen, Germany**  
Jul      Group of Prof. J. Fritz in collaboration with Prof. G Muskhelishvili,  
*AFM study of Protein-DNA Complexes*

2010 May-Jul      **Jacobs University Bremen, Bremen, Germany**  
Group of Prof. G. Muskhelishvili , Molecular Genetics  
*Molecular Cloning of ProV-UAS fragment in E.coli*

2010 Feb-Apr      **Jacobs University Bremen, Bremen, Germany**  
Group of Prof. J. Fritz, Biophysics  
*AFM study of solid supported bilayers on mica*

2009 Sep-      **Jacobs University Bremen, Bremen, Germany**  
2010 Jan      Group of Prof. M. Winterhalter in collaboration with Prof. D. Gabel, Biophysics  
*Interaction of Boron-Clusters with liposomes*

2008 Jul-  
Sep                    **EPFL, Lausanne, Switzerland**  
Group of Prof. G. Dietler,  
Laboratory of the Physics of Living Matter  
*AFM study of circular DNA on Graphite Surface*

***Research Topics :***

*Scaling behavior of DNA molecules;*

*Protein-DNA Complexes;*

*Bacterial Chromatin Organization;*

*Development of new experimental methods for DNA confinement;*

*Structural Role in Genetic Regulation*

Experimental Techniques/ Experience

---

Biophysical	Atomic Force Microscopy, Ultra High Vacuum AFM, Dynamic light scattering
Molecular Biology	Molecular Cloning, Polymerase Chain Reaction, DNA isolation/purification, Agarose gel electrophoresis, Liposome Preparation and characterization

Participation in scientific conferences

---

**Poster Contributions**

2015                    DNA topoisomerases, DNA topology and human health, Les-Diablerets.  
Switzerland

- Integrating Genomics within hierarchical physical models of DNA and chromosomes, ENS Lyon, France
- 2014 1st course on Multiscale Integration in Biological Systems, Paris Curie Institute, Paris France
- Swiss Physical Society, University of Fribourg, Fribourg, Switzerland
- Biophysical Society conference, Significance of Knotted Structures for Function of Proteins and Nucleic Acids, Warsaw, Poland
- 2013 Swiss Soft Days 10<sup>th</sup> Edition , PSI, Villigen, Switzerland
- Swiss Soft Days 11<sup>th</sup> Edition , University of Fribourg, Fribourg, Switzerland
- International Soft Matter Conference 2013, Sapienza Università di Roma, Italy
- 2012 Workshop on Virology, ICTP, Trieste, Italy
- Swiss Soft Days 9<sup>th</sup> Edition, Nestle Research Center, Lausanne
- 2010 German Physical Society Spring Meeting,  
Regensburg University, Poster session,  
Topic : "Interaction of Boron-Clusters with liposomes : Influence on the Zeta-potential"
- Oral Presentations**
- 2015 INSA, Lyon, France

Topic : ***“Hyperplectonemes - Novel type of DNA structures”***

SISSA, Trieste, Italy

Topic : ***“Long range RNA-Polymerase binding sensing by DNA topology”***

Free University of University, Tbilisi, Georgia

Topic : ***“Investigation of DNA structure by atomic force microscopy”***

2014

Swiss Soft Days XV , EPFL, Switzerland

Topic : ***“DNA in confinement ”***

2013

IPSB Sandwich Seminar, EPFL, Switzerland

Topic : ***“EspR-DNA complexes visualized by AFM”***

University of Padova, Padova, Italy

Topic: ***“DNA scaling in confined space”***

LAAS-CNRS , Toulouse, France

Topic: ***“Scaling properties of circular DNA molecules at high concentrations and in confined space”***

BioPhysics Workshop, Trieste, Italy

Topic: ***“Scaling properties of DNA molecules studied by AFM”***

CCMX Summerschool, EPFL, Switzerland

Topic: ***“Characterisation of Materials by Atomic Force Microscopy”***

EPFL-LANEF Nanomechanics Workshop, EPFL, Switzerland

Topic: ***“Study of Scaling Properties of DNA by AFM”***

CCMX Winterschool, Kandersted, Switzerland

Topic: *"Nanoparticle Drug delivery for Cancer treatment"*

Tbilisi State University, Tbilisi, Georgia

2012 Topic : *"Scaling Properties of DNA"*

The Young Scientists and Students Scientific Conference,

2008 Tbilisi State University, Tbilisi, Georgia First place.

Topic: *" Observation of circular DNA on Highly Ordered Pyrolytic Graphite with AFM"*

Awards Best Poster Presentation Award at Biophysical Society conference,  
2014

## Teaching assignments

---

---

**2011-2012:** Assistant for Computational Physics III (Prof. G. Foffi)

**2012-2013:** Assistant for Physics Laboratories TP (Prof. R. Schaller)

### Assistant for Master student's lab projects:

**2012:** Ali Aghebatrafat, TP project : "Scalin properties of pUC19 DNA"

**2013:** Kathleen Smith, TP project: "AFM study of DNA in confined geometry"

**2013-2014:** Sylvain Renevey, TP project: "Nucleoprotein assemblies studied with AFM"  
"DNA-DYE interaction studied by AFM"

**2014-2015:** Amine El Amrani, TP project: "DNA trapping in Nano-wells"

---

---

## Publications

---

2015

- **Influence of DNA Binding Dyes on Bare DNA Structure Studied with Atomic Force Microscopy.**

**A. Japaridze**, A. Benke, S. Renevey, C. Benadiba and G. Dietler.

in ACS Macromolecules, vol. 48, num. 6, p. 1860-1865, 2015.

- **Effects of physiological self-crowding of DNA on shape and biological properties of DNA molecules with various levels of supercoiling.**

F. Benedetti, **A. Japaridze**\*, J. Dorier, D. Racko, R. Kwapich, Y. Burnier, G. Dietler and A. Stasiak.

in Nucleic Acids Research, vol. 43, num. 4, p. 2390-2399, 2015.

\* **Co-first author**

- **Upstream Binding of Idling RNA Polymerase Modulates Transcription Initiation from a Nearby Promoter**

V. Gerganova, S. Maurer, L. Stoliar, **A. Japaridze**, G. Dietler W. Nasser, T. Kutateladze, A. Travers and G. Muskhelishvili

in Journal of Biological Chemistry, vol. 290, num. 13, p. 8095-8109,

- **Structure of EspB, a secreted substrate of the ESX-1 secretion system of Mycobacterium tuberculosis**

N. Korotkova, J. Piton, J. M. Wagner, S. Boy-Röttger, **A. Japaridze**, T. J. Evans, S. T. Cole, F. Pojer, K. V. Korotkov

In Journal of Structural Biology, 191, 236-244

2014

- **Functional Dissection of Intersubunit Interactions in the EspR Virulence Regulator of Mycobacterium tuberculosis.**

B. Blasco, A. Japaridze, M. Stenta, B. I. M. Wicky, G. Dietler, M. Dal Peraro, F. Pojer and S. T. Cole

In Journal of Bacteriology, Vol. 196, num. 10, p. 1889-1900, 2014.

2012

- **Nanoaggregates of micropurified lipopolysaccharide identified using dynamic light scattering, Zeta-potential measurement and TLR4 signaling activity.**

E. Hardy, T. Kamphuis, A. Japaridze, J. C. Wilschut and M. Winterhalter

In Analytical Biochemistry: Vol. 430, Issue 2, p. 203–213, 2012

Publications Submitted/ In Submission

- **DNA sequence organization directs the assembly of distinct higher-order H-NS filaments**

A. Japaridze, S. Renevey, P. Sobetzko, L. Stoliar, G. Dietler and G. Muskhelishvili

Submitted in Journal of Biological Chemistry

- **Towards an effective control of DNA's sub-molecular conformation on a surface**

A. Japaridze, D. Vobornik, E. Lipiec, A. Cerreta, J. Szczerbinski, R. Zenobi and G. Dietler

Submitted in ACS Macromolecules



- **Conformational properties of DNA inside narrow slits**

**A. Japaridze**, C. Micheletti, E. Orlandini, K. Smith, F. Valle and G. Dietler

In preparation

- **DNA Hyperplectonemes**

**A. Japaridze**, F. Benedetti, A. Stasiak<sup>2</sup>, F. Pojer, S. Cole, P. De Los Rios, G. Muskhelishvili, G. Longo and G. Dietler

In preparation

## **Language skills**

---

Georgian – native

English – fluent

German – fluent (Deutsches Sprachdiplom, Zweite Stufe)

Russian – fluent

French – beginner

## **Computer skills**

---

MS Office, Mathematica, WSxM , Gwyddion, Image J, Ellipse

## **Hobbies and interests**

---

Sports: Rock climbing, Alpinism, Martial arts   Arts: Music, Photography